Metallicity-Dependent Isotopic Abundances and the Impact of Helium Rate Uncertainties in Massive Stars

A DISSERTATION
SUBMITTED TO THE FACULTY OF THE GRADUATE SCHOOL
OF THE UNIVERSITY OF MINNESOTA
BY

Christopher West

IN PARTIAL FULFILLMENT OF THE REQUIREMENTS
FOR THE DEGREE OF
Doctor of Philosophy

Alexander Heger

December, 2013

Acknowledgements

I would like to first thank my adviser, Alexander Heger, for all his help and guidance over these several years. I must express my appreciation to Yong-Zhong Qian for his support, very useful discussions, and advice. I thank also all my other teachers who contributed to my learning, within the classroom and without. They made this journey possible, and revealed the true rewards along the way.

I am very grateful to my mother and fathers, who inspired in me a passion and drive for learning. They have always supported my academic efforts, carrying my courage for me in times of doubt, and being there in times of need.

I thank my sister, Geneviève West, for keeping me humble. I thank my brother, Louis Teerlinck, for keeping me honest. Both of whom also provided the valuable service of holding me intellectually accountable.

I thank Catherine Katt for helping me discover this journey, and sharing with me the life of the spirit. I thank Kathy and LuLu Manus, for encouraging me to reach for the stars, in many different ways, throughout my entire life.

A special thanks to Vince Froehlich for freely sharing the language of the heart, for walking the path at eye level, and for other things left unstated.

Finally, I thank with all my heart, my sweet Jellybean. Her patience and sacrifice through this process were so lovingly given. She is my inspiration, and always reminds me to see also the Sun, when studying the stars.

Dedication

To those who anonymously serve. May we all forever meet on the Broad Highway.

Abstract

All stellar evolution models for nucleosynthesis require an initial *isotopic* abundance set to use as a starting point, because nuclear reactions occur between isotopes. Generally, our knowledge of isotopic abundances of stars is fairly incomplete except for the Solar System. We develop a first model for a complete average isotopic decomposition as a function of metallicity. Our model is based on the underlying nuclear astrophysics processes, and is fitted to observational data, rather than traditional forward galactic chemical evolution modeling which integrates stellar yields beginning from big bang nucleosynthesis. We first decompose the isotopic solar abundance pattern into contributions from astrophysical sources. Each contribution is then assumed to scale as a function of metallicity. The resulting total isotopic abundances are summed into elemental abundances and fitted to available halo and disk stellar data to constrain the model's free parameter values. This procedure allows us to use available elemental observational data to reconstruct and constrain both the much needed complete isotopic evolution that is not accessible to current observations, and the underlying astrophysical processes. Our model finds a best fit for Type Ia supernovae contributing $\simeq 0.7$ to the solar Fe abundance, and Type Ia onset occurring at [Fe/H] $\simeq -1.2$, in agreement with typical values. The completed model can be used in future nucleosynthesis studies.

We also perform a preliminary analysis to assess the impact of our isotopic scaling model on the resulting nucleosynthesis of massive stars, compared to a linear interpolation method. Using these two input methods we compute a limited grid of stellar models, and compare the final nucleosynthesis to observations. The compactness parameter was first used to assess which models would likely explode as successful supernovae, and contribute explosive nucleosynthesis yields. We find a better agreement to solar observations using the scaling model compared to the linear interpolation method, for the six *s*-only isotopes along the weak *s*-process path.

As a second project, we study the sensitivity of presupernova evolution and supernova nucleosynthesis yields of massive stars to variations of the helium-burning reaction rates within the range of their uncertainties. The current solar abundances from Lodders (2010) are used for the initial stellar composition. We compute a grid of 12 initial

stellar masses and 176 models per stellar mass to explore the effects of independently varying the $^{12}C(\alpha,\gamma)^{16}O$ and 3α reaction rates, denoted $R_{\alpha,12}$ and $R_{3\alpha}$, respectively. The production factors of both the intermediate-mass elements ($A = 16 - 40$) and the s-only isotopes along the weak s-process path (^{70}Ge, ^{76}Se, ^{80}Kr, ^{82}Kr, ^{86}Sr, and ^{87}Sr) were found to be in reasonable agreement with predictions for variations of $R_{3\alpha}$ and $R_{\alpha,12}$ of $\pm 25\,\%$; the s-only isotopes, however, tend to favor higher values of $R_{3\alpha}$ than the intermediate-mass isotopes. The experimental uncertainty (one standard deviation) in $R_{3\alpha}(R_{\alpha,12})$ is approximately $\pm 10\,\%(\pm 25\,\%)$. The results show that a more accurate measurement of one of these rates would decrease the uncertainty in the other as inferred from the present calculations. We also observe sharp changes in production factors and standard deviations for small changes in the reaction rates, due to differences in the convection structure of the star. The compactness parameter was used to assess which models would likely explode as successful supernovae, and hence contribute explosive nucleosynthesis yields. We also provide the approximate remnant masses for each model and the carbon mass fractions at the end of core-helium burning as a key parameter for later evolution stages.

Contents

List of Tables

List of Figures

Chapter 1

Stellar Evolution

1.1 Introduction

In this work, we address two problems with initial conditions in stellar modeling. The first problem is that the initial isotopic abundances are poorly estimated for sub-solar models. Secondly, the present uncertainties in the helium burning reaction rates result in different nucleosynthesis and evolution. By addressing these two initial conditions, we seek to improve stellar modeling results, which will aid future investigations and enable better model predictions. Moreover, some results from our efforts can be extended to additional nucleosynthesis studies.

The pioneering works of Cameron (1957), and Burbidge et al. (1957) identified nuclear reactions as being responsible for the energy production in stars, and since that time nuclear physics has become integral for understanding stellar environments. Its contemporary application in stellar models permits the investigation of the evolution and nucleosynthesis of stars across a broad range of initial masses and compositions, furthering our understanding of not only galactic and chemical evolution, but also the origins of the isotopes essential for life.

This work has two purposes. The first is to improve initial compositions used as inputs into stellar modeling. In principle, any composition can be chosen. Observations give the necessary information to study stellar models with compositions similar to the Sun, but for compositions containing a lower (or higher) fraction of metals (isotopes

heavier than helium) the needed observations of the isotopic abundances are not available — and the isotopic composition is *crucial* for understanding the nucleosynthesis. Hence, if one wishes to choose compositions representative of the Galaxy sometime in its chemical history or future, it is necessary to model the Galactic isotopic abundances as a function of metallicity (mass fraction of all elements heavier than helium) to get the input composition. Historically, this modeling has been done rather crudely, typically by linearly interpolating isotopic abundances between their big bang nucleosynthesis and the solar abundance values. More refined efforts modify these interpolations to increase the intermediate-mass isotope contributions from massive stars at sub-solar metallicities (α-enhanced compositions; e.g., Salasnich et al., 2000; Coelho et al., 2007). It is unknown in detail how these approximations affect the final nucleosynthesis. We thus make a more careful attempt at modeling the history of these isotopic abundances by constructing a metallicity-dependent scaling model.

Later, we also perform a preliminary analysis to assess the impact of our model on the resulting nucleosynthesis compared to the linear interpolation method. Using these two input methods we compute a limited grid of stellar models, and compare the final nucleosynthesis to to observations. This first attempt will pave the way for future, more detailed investigations.

The second objective of this work is to study the impact of uncertainties in the helium (He) burning reaction rates on massive star evolution and nucleosynthesis. The $^{12}\mathrm{C}(\alpha,\gamma)^{16}\mathrm{O}$ and 3α reactions dominate the energy production of massive stars during core-He burning and later in He-shell burning phases, and their rates compete to determine the subsequent carbon abundance and affect later nucleosynthesis. A limited study of the impact of varying these rates across their present 2σ uncertainty exists in a previous work (Tur et al., 2007), which concluded that a more refined grid for the uncertainty of the rates was necessary to assess the effects of independently varying them. In this work, we extend the previous study using a greater resolution in both the He reaction rate grid and the number initial masses considered, and succeed in constraining the overall uncertainty better than theoretical/experimental efforts to date.

In other words, we studied two different things. First, we wanted to improve the methodology for generating abundances for stellar simulations. Our phenomenological approach, whereas more complex, fits well to data and better represents the abundances

in the Galaxy. Second, we wanted to improve the present uncertainties on the He burning rates. Since massive stars make nearly the entire solar abundance of certain isotopes, we can isolate which He rates reproduce these solar abundances by running massive star simulations.

This work has the following outline. The present chapter introduces the relevant stellar physics and modeling. Chapter 2 discusses the nuclear physics and chemical evolution. Chapter 3 describes the isotopic scaling model used for generating the initial compositions. Chapter 4 describes the study on varying the He burning reaction rates. In Chapter 5, we study the impact of varying the initial compositions of a grid of massive stars at various metallicities, using the isotopic scaling model and the interpolated solar model as inputs. Finally, Chapter 6 gives a summary and remarks for future extensions.

The rest of this chapter is organized as follows. In Section 1.2, the relevant stellar physics is introduced, and general stellar evolution is explained. In Section 1.3, the stellar model used in the present work is discussed.

1.2 Stellar Physics

There are two sets of coordinates common in stellar physics. Eulerian coordinates use time and the radial coordinate from the star's center as independent variables, whereas the Lagrangian description replaces the radius with the mass coordinate (defined below). The latter is often more useful in the case of spherical symmetry: Throughout stellar evolution many important features of the star, such as nuclear burning shells, experience large changes in their radial coordinates but typically much smaller changes in their mass coordinate. Hence, this coordinate choice facilitates discussion of such features, as the total mass is fairly invariant compared to the total radius. The Lagrangian description will be used throughout the present work (e.g., Clayton, 1968; Cox, 1968; Sackmann and Anand, 1970; Rolfs and Rodney, 1988; Kippenhahn and Weigert, 1990).

1.2.1 Basic Equations

The fundamental hydrodynamic equations for stellar evolution (in Lagrangian coordinates) are given as (Kippenhahn and Weigert, 1990; Heger, 1998),

$$\frac{\partial m}{\partial r} = 4\pi r^2 \rho, \tag{1.1}$$

$$\frac{\partial P}{\partial m} = -\frac{Gm}{4\pi r^4} - \frac{1}{4\pi r^2}\frac{\partial^2 r}{\partial t^2}, \tag{1.2}$$

$$\frac{\partial L}{\partial m} = \varepsilon_n - \varepsilon_\nu - c_P \frac{\partial T}{\partial t} + \frac{\delta}{\rho}\frac{\partial P}{\partial t}, \tag{1.3}$$

$$\frac{\partial T}{\partial m} = -\frac{GmT}{4\pi r^4 P}\nabla\left(1 + \frac{r^2}{Gm}\frac{\partial^2 r}{\partial t^2}\right), \tag{1.4}$$

$$\frac{\mathrm{d}Y_i}{\mathrm{d}t} = \sum_{\alpha_k,\alpha_l,\ldots,\alpha_i,\ldots\beta_k,\beta_l,\ldots,\beta_i,\ldots} \lambda_{\alpha_k k+\alpha_l l+\ldots\rightarrow\beta_k k+\beta_l l+\ldots} \frac{\beta_i - \alpha_i}{\alpha_k!\alpha_l!\ldots} Y_k^{\alpha_k} Y_l^{\alpha_l} \ldots. \tag{1.5}$$

Note that the radius is (implicitly) a function of mass. Equation 1.1 is a statement of mass conservation and defines the Lagrangian mass coordinate, where m is the mass enclosed at radius r, and ρ is the density. Equation 1.2 is a statement of momentum conservation and defines the equation of motion, where P is the pressure, and G is the gravitational constant. When the star is in hydrostatic equilibrium, the acceleration of the radial variable vanishes and Equation 1.2 reduces to the familiar relation, $\partial P/\partial m = -Gm/4\pi r^4$. Equation 1.3 describes the conservation of energy, with L as the total luminosity, and ε_n and ε_ν being energy generation (per unit mass per second) due to nuclear reactions and neutrino cooling, respectively. The third and fourth terms of Equation 1.3 together give the gravitational internal energy, where T is the temperature. Equation 1.4 is the transport of energy equation, with $\nabla \equiv \mathrm{d}\ln T/\mathrm{d}\ln P$ unless the region of interest is radiative, in which case,

$$\nabla \rightarrow \nabla_{\mathrm{rad}} = \frac{3}{16\pi acG}\frac{\kappa l P}{mT^4}\left[1 + \frac{r^2}{Gm}\frac{\partial^2 r}{\partial t^2}\right]^{-1}, \tag{1.6}$$

where κ is the opacity, c is the speed of light, l is the local luminosity, and $a = 7.57 \times 10^{-15}\,\mathrm{erg\,cm^{-3}\,K^{-4}}$ is the radiation-density constant. If the region is convective, ∇ is found by applying *mixing length* theory (discussed briefly in Section 1.3.2, and for greater detail see Clayton, 1968; Kippenhahn and Weigert, 1990). Equation 1.5 gives the variation of the composition with time due to nuclear interactions, where Y_i is the abundance (in mole fractions) of isotope i, and λ is the reaction rate. The summation includes all species (denoted by, k, l, ...) of all possible reactants (α_k, α_l, ...) and all possible products (β_k, β_l, ...) that are involved in interactions with Y_i. The mass fraction of isotope i, X_i, is related to the mole fraction by, $Y_i = X_i/A_i$, where A_i is the mass of isotope i in atomic mass units (amu). Further discussion and derivation of these equations can be found in Kippenhahn and Weigert (1990).

This set of equations governs the evolution of stars. Solving these equations allows the modeling of the dynamics and nucleosynthesis of stellar evolution. Note that we use modified equations in KEPLER (discussed below in Section 1.3). An important additional concept is needed for describing energy transfer, and will be discussed next.

1.2.2 Convection

Convection is the salient dynamical instability in stellar environments. If the local temperature gradient is sufficiently large then a convective instability will occur, mixing the composition and transporting heat. The criterion for "sufficient" is determined by the mitigating effects of gradients in the adiabatic temperature and mean molecular weight. Specifically, a region is convectively stable under the condition,

$$\nabla_{\mathrm{rad}} < \nabla_{\mathrm{ad}} + \frac{\varphi}{\delta}\nabla_{\mu}, \tag{1.7}$$

where $\varphi \equiv (\partial \ln\rho/\partial \ln\mu)$, $\delta \equiv -(\partial \ln\rho/\partial \ln T)$, and using the following common definitions,

$$\nabla_{\mathrm{rad}} \equiv \left(\frac{\mathrm{d}\ln T}{\mathrm{d}\ln P}\right)_{\mathrm{rad}}, \qquad \nabla_{\mathrm{ad}} \equiv \left(\frac{\mathrm{d}\ln T}{\mathrm{d}\ln P}\right)_{\mathrm{ad}}, \qquad \nabla_{\mu} \equiv \frac{\mathrm{d}\ln\mu}{\mathrm{d}\ln P}. \tag{1.8}$$

This is the *Ledoux criterion* for convection and is preferred since it is often not the case that the composition is chemically homogeneous, $\nabla_\mu \neq 0$. If the composition *would* be convectively stable except for the contribution from the composition gradient, that is, Equation 1.7 is not satisfied but $\nabla_{\mathrm{rad}} < \nabla_{\mathrm{ad}}$ (the *Schwarzchild criterion* for convection)

then the system experiences semi-convection, which can be interpreted as an oscillatory instability that begins as a secular instability and grows dynamically unstable if it persists over a time scale longer than the thermal/radiative diffusion time (Kato, 1966). Hence, semi-convection is most pronounced in massive stars during the long periods of core H and He burning at the interface of the core and the inner-most burning shell, although can also occur in subsequent core and shell burning phases to a lesser degree.

In summary, convection and semi-convection are critical for understanding the energy transport in stars. They can affect not only the stellar structure and evolution, but also the nucleosynthesis.

1.2.3 Stellar Evolution by Mass

1.2.3.1 Low and Intermediate Mass Stars

Most stars spend the majority of their lives on the main sequence burning hydrogen (H) in their core, but those with mass below $M \lesssim 0.08\,\mathrm{M}_\odot$ cannot reach sufficient core temperatures to ignite H burning (Cohen, 1988). These "brown dwarfs" evolve nearly at constant temperature as they burn deuterium during the star's contraction. This contraction is eventually halted by degeneracy pressure, and the star does not participate in any further nucleosynthesis (Iliadis, 2007).

Stars with slightly higher masses, $0.08 \lesssim M/\mathrm{M}_\odot \lesssim 0.4$, are able to burn H in the core but cannot reach the needed temperatures to ignite helium (He). These "red dwarfs" stay on the main sequence for longer than the current age of the Universe, remaining convective for much of this time, and eventually end their life as He white dwarfs (Adams et al., 2004).

Stars with masses between $0.4 \lesssim M/\mathrm{M}_\odot \lesssim 2.0$ burn H in the core during the main sequence through the *pp chains* (proton-proton reactions) and *CNO cycles* (see Section 2.6.1), however, those with masses below $M \lesssim 1.5\,\mathrm{M}_\odot$ favor the former and stars with $M \gtrsim 1.5\,\mathrm{M}_\odot$ favor the latter, due to the efficiency of these processes at different stellar temperatures (both H burning processes are equally efficient at $T \sim 10^7\,\mathrm{K}$; Kippenhahn and Weigert, 1990; Adelberger et al., 2011). Upon core-H depletion, H burning continues in a shell until the envelope becomes convective, and the star enters the red giant branch (RGB). Knowledge of the evolution beyond the RGB phase suffers

uncertainty, due to incomplete understanding of convection and mass loss (see for e.g., observational evidence: Castellani and Renzini, 1968; Soker et al., 2001, observational constraints: Momany et al., 2012, theoretical estimates: Fusi-Pecci and Renzini, 1975). Generally, as the core temperature continues to rise, core-He burning ignites (at $T \approx 0.1\,\mathrm{GK}$) and the star enters the horizontal giant branch (HGB). Note this stage is reached only once *quiescent* He burning is achieved, which may follow a core-He flash (a runaway fusion episode on the degenerate He material). Once the He in the core is depleted, the star then enters the asymptotic giant branch (AGB) phase. Here, shell-He burning supports the envelope until the fuel depletes, at which point the outer H shell contracts, raising temperatures and igniting shell-H burning. This restores the He abundance in the shell, until it is sufficient to once again ignite in a shell-He flash (fusion on non-degenerate He material leading to a thermal pulse), depleting the He shell of fuel once more (Iben, 1977; Chiosi et al., 1992). These cyclical episodes last a few hundred years and can happen several times with $\approx 10,000\,\mathrm{yrs}$ occurring between flashes. During this phase the stars sheds significant mass in stellar winds, forming planetary nebulae. The burning episodes terminate after the AGB phase, due to insufficient mass to ignite core-carbon (C) burning. The star then dies as a carbon/oxygen (C/O) white dwarf.

Stars with masses $2.0 \lesssim M/\mathrm{M}_\odot \lesssim 8.0$ are thought to evolve similarly to those with masses between $0.4 \lesssim M/\mathrm{M}_\odot \lesssim 2.0$ with some notable differences. For example, above $M \gtrsim 2.0\,\mathrm{M}_\odot$, the He core during the RGB phase is not degenerate, hence no He flash precedes quiescent burning (Iliadis, 2007). There are also additional mixing episodes during the AGB phase for stars above $M \gtrsim 4.0\,\mathrm{M}_\odot$ (Iliadis, 2007), and indeed the higher mass stars in this range, $M \approx 8.0\,\mathrm{M}_\odot$, are assumed to ignite C during or after the *second dredge-up phase* (Eldridge and Tout, 2004), resulting in super asymptotic branch stars (discussed further below). This dredge-up phase occurs during the AGB phase, when the convective envelope reaches down into the H burning shell, mixing the products of shell-H burning outward. This process can occur for stars with initial masses greater than $M \gtrsim 3.0\,\mathrm{M}_\odot$ (Lambert, 1992).

1.2.3.2 Massive Stars

Less is known about the evolution of stars with initial masses in the range $9 \lesssim M/\mathrm{M}_\odot \lesssim 10$ (Iliadis, 2007). Their evolution is thought to proceed through core-H and (non-degenerate) He burning. Subsequent H and He shell burning phases increase the C/O core until enough C accumulates to ignite a *shell-C burning flash*, at which point the star enters the super asymptotic branch (SAGB) phase (e.g., Siess, 2007). Note that the exact mass range to enter this phase depends on the initial metallicity and treatment of convection (Lau et al., 2012). As with the AGB phase in lower mass stars, the SAGB is cyclical with continued C depletion and restoration from shell burning for $\approx 20,000\,\mathrm{yrs}$. The resulting oxygen-neon-magnesium (ONeMg) core from these cycles is degenerate, and if the core mass reaches the critical value of $\approx 1.36\,\mathrm{M}_\odot$, the Fermi energy becomes sufficiently high for electron capture on Mg to occur. This reduces the available electrons that contribute to the degeneracy pressure, further increasing the temperature, and a runaway is triggered with the star exploding as an electron capture supernova (ECSN). Whether the star can achieve the critical value for explosion depends greatly on the third dredge-up phase (Siess, 2008), which impacts both the mass and chemical composition of the core. Fairly recent SAGB models suggesst the strong He enrichment from the dredge-up phases may be enough to provide non-negligible contributions to the Galactic He production (Siess, 2007). Stars unable to reach the critical mass necessary for explosion die as ONe white dwarfs (Eldridge and Tout, 2004; Lau et al., 2011). We have discovered an $11\,\mathrm{M}_\odot$ solar metallicity star model that produced an ECSN event *without* a prior SAGB phase. The model experienced a complete third dredge-up phase, removing the He shell entirely, with no more burning beyond the He region and only minor C burning toward the edge of the core. Such instances have also been observed by others, but it is unclear whether they are physical results or follow instead from the approximate treatment of convection in 1D stellar modeling .

Stars with initial masses in the range $10 \lesssim M/\mathrm{M}_\odot \lesssim 40$ are the primary focus of the stellar models in the present work. They have enough mass to complete all possible hydrostatic core burning phases, and following core-C burning, Ne, O, and finally Silicon (Si) are burned to leave an Iron (Fe) core. An example of these phases, including the main reactions involved, burning time scales, and core temperatures is given for a $20\,\mathrm{M}_\odot$ in Fig. 1.1. The result from hydrostatic burning is the well-known

onion-layer structure, where the H, He, C, Ne, O, and Si shells are typically convective and separated by sharp density and entropy gradients that prevent (convective) mixing across them. An example of the entire pre-supernova evolution of a typical massive star is given in Fig. 1.2, showing all core and shell burning phases, energy production and loss, and convective regions.

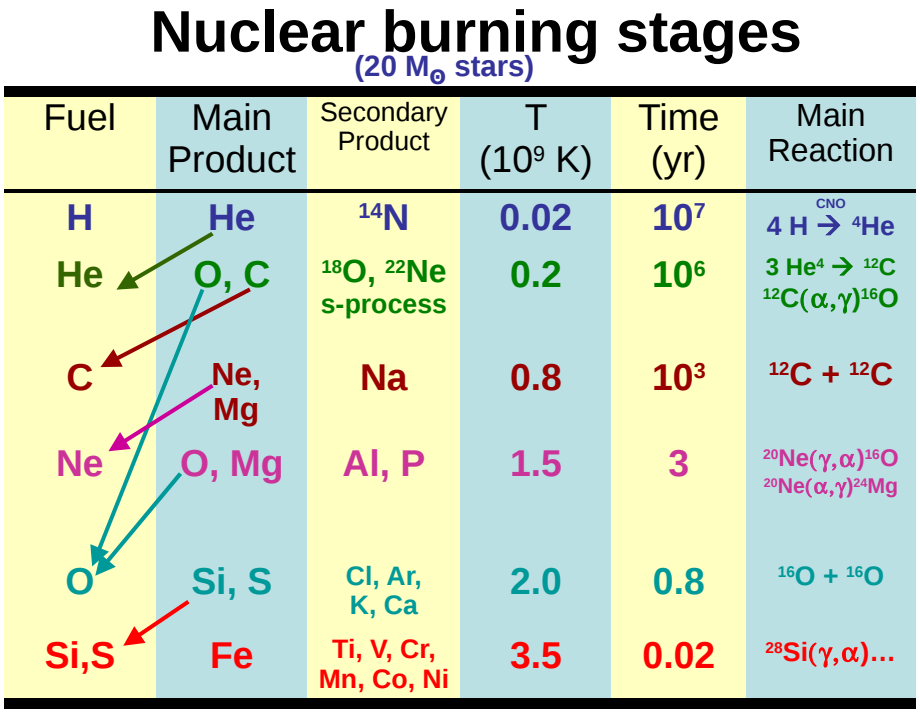

Figure 1.1: The core nuclear burning stages for a $20\,\mathrm{M}_\odot$ star (provided by Heg, 2012).

The binding energy per nucleon reaches a maximum at Fe, and no further core burning phases are possible that will contribute to the positive energy generation of the star (Rolfs and Rodney, 1988). The mass of the degenerate Fe core will continue to grow though subsequent shell burning episodes, however, until the Chandrasekhar limit is reached. The value of this limit discovered by Chandrasekhar in 1938 was, $M_{\mathrm{Ch0}} \approx 5.83 Y_e^2\,\mathrm{M}_\odot$, where $Y_e = n_e/\rho N_A$ is the electron fraction, with n_e being the electron number density, ρ the mass density, and N_A is Avagadro's number (Chandrasekhar, 1939). The current value modifies M_{Ch0} to account for thermal core structure, non-zero

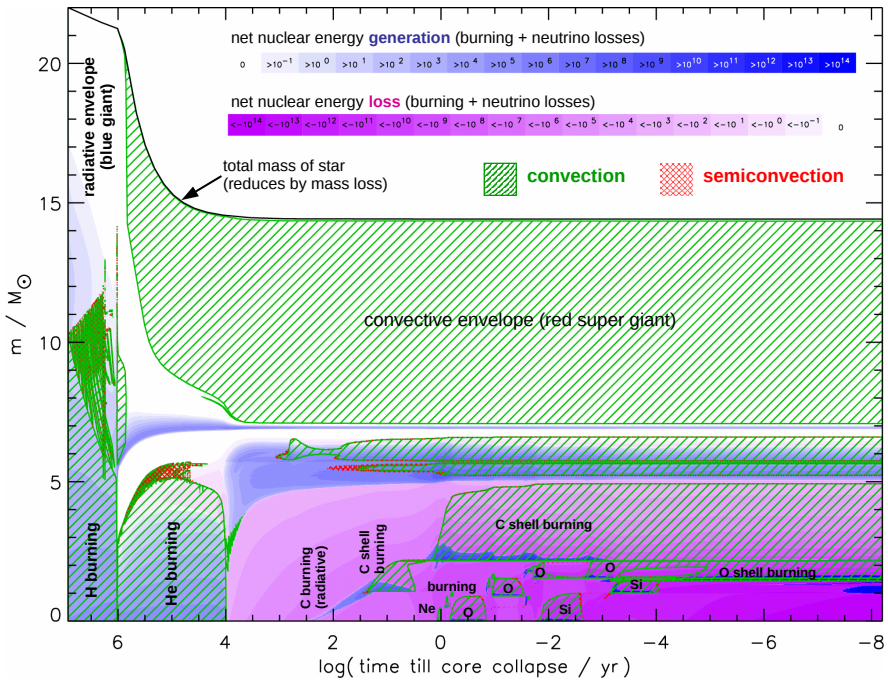

Figure 1.2: The evolution of a $22\,M_\odot$ star as a function of mass coordinate. All hydrostatic burning are shown (taken from Heg, 2012).

entropy, coulomb corrections, and relativistic corrections (Timmes et al., 1996; Shapiro and Teukolsky, 1983), and takes the form,

$$M_{\rm Ch} \approx M_{\rm Ch0}\left[1+\left(\frac{S_e}{k\pi N_A Y_e}\right)^2\right], \tag{1.9}$$

where S_e is the electron entropy, and k is Boltzmann's constant. Intuitively, this limit must exist since the mass dependence in the expressions for gravitational pressure and degeneracy pressure is different, hence there is some mass for which they balance.

Beyond this mass limit the star cannot support itself against gravitational collapse with a degenerate core, and the core begins to collapse on thermal time scales as neutrinos carry away the binding energy (Woosley et al., 2002). The increasing densities promote electron captures and photo-disintegration of ^{56}Fe into α-particles and neutrons. This of course serves to accelerate the collapse by decreasing the degeneracy

pressure and removing thermal photons that also provide support. The collapse continues and the core overshoots nuclear densities, and the strong nuclear force releases the potential energy of this compression in a *core bounce* that impacts infalling material, driving a shock wave and leaving behind a proto-neutron star. This shock is insufficient to explode the star, however, and it eventually stalls after losing energy by photo-disintegrating the infalling outer Fe layers. Re-energizing this stalled shock in order to produce a successful supernova explosion had been a long standing problem in stellar modeling (e.g., Arnett, 1996). At first, artificial remedies were used which included energy injection, where the needed energy deposition to drive the shock past the infalling material was simply inserted (Aufderheide et al., 1991), and parametrizing the explosion using a mechanical piston (discussed in Section 1.3.3).

It was suggested as early as 1966 that the immense neutrino flux from the proto-neutron star may in fact be responsible for re-energizing the shock (Colgate and White, 1966), but the details were not understood until later (Wilson, 1985; Bethe and Wilson, 1985). More recent investigations continue to support the neutrino-heating mechanism (e.g., Marek and Janka, 2009), and it is presently the best known solution for modeling the energetics of supernova explosions.

Stars with initial masses in the range $40 \lesssim M/\mathrm{M}_{\odot} \lesssim 100$ also complete all stages of hydrostatic burning, and can incur heavy mass loses of their envelopes during a Wolf-Rayet phase (WR). Many will collapse directly to a black hole (BH) without an explosion, and hence not populate the interstellar medium (ISM) with metals except during the mass loss episodes. In fact, it is the amount of mass loss during the WR phase that dictates whether direct collapse will occur or whether a neutron star (NS) will result instead (e.g., Heger et al., 2003), and this mass loss is strongly dependent on the luminosity (Nugis and Lamers, 2000), and is also a function of metallicity (Heger et al., 2003).

1.2.3.3 Very Massive Stars

Stars in the mass range $100 \lesssim M/\mathrm{M}_{\odot} \lesssim 260$, have temperatures and densities sufficiently high after core-He burning so that pair-production by photons impacting on nuclei is energetically favorable (e.g., Heger and Woosley, 2002). This decreases the photon pressure, contracting the star and raising temperatures and densities higher still,

which further increases the pair-production events. For the subset of stars smaller than $M/\mathrm{M}_\odot \lesssim 140$, this contraction results in explosive O burning. This explosive burning does not unbind the star but incurs heavy mass loss followed by Kelvin-Helmholtz contraction, leading to further explosions. Such "pulsations" (contraction followed by explosive burning) can happen multiple times until the stars burns Si to Fe and ultimately dies as a BH, after ejecting its outer layers, without a final supernova (SN) explosion (Heger and Woosley, 2002). Conversely, the subset of stars greater than $M/\mathrm{M}_\odot \gtrsim 140$ die as pair-instability supernovae (PSNe). For these cases, the runaway from pair-production is halted by implosive O and Si burning, which destroys the star and leaves no remnant (Heger and Woosley, 2002; Heger et al., 2003).

Stars more massive than $M \approx 260\,\mathrm{M}_\odot$, if non-rotating, are believed to collapse directly to a BH without an explosion (Heger and Woosley, 2002). A non-zero rotation may prevent direct BH formation if a sufficient accretion disk can develop (Shibata and Shapiro, 2002), with material ejected in the polar jets. Finally, it is believed that stars more massive than $M \approx 10^5\,\mathrm{M}_\odot$ (*supermassive* stars) are too heavy to support themselves with any known burning process, and collapse directly to a BH before achieving hydrostatic equilibrium. The full story of stars in this extreme mass range is still being pieced together. Recent models, for example, suggest some fraction of supermassive stars may explode as successful supernovae (see e.g., (Johnson et al., 2013), for the case of a $55,000\,\mathrm{M}_\odot$ star, and references therein). A summary of the ranges of initial stellar masses and their remnants is given in Fig. 1.3 for the case of solar metallicity.

In the previous sections, we have discussed the general evolution of stars as a function of their initial mass. The effects of metallicity on the nucleosynthesis have not been addressed here, but will be discussed in Chapters 2 and 3. We shall now introduce stellar modeling, specifically in the context of the codes used throughout in this work.

1.3 Stellar Models

Since the development of computers, modeling stellar evolution has been achieved by iteratively solving the fundamental equations for stellar evolution numerically. Many codes for stellar evolution exist, such as the 1D simulation MESAstar that is open-sourced to the community (`http://mesa.sourceforge.net/`, Paxton et al., 2011), as

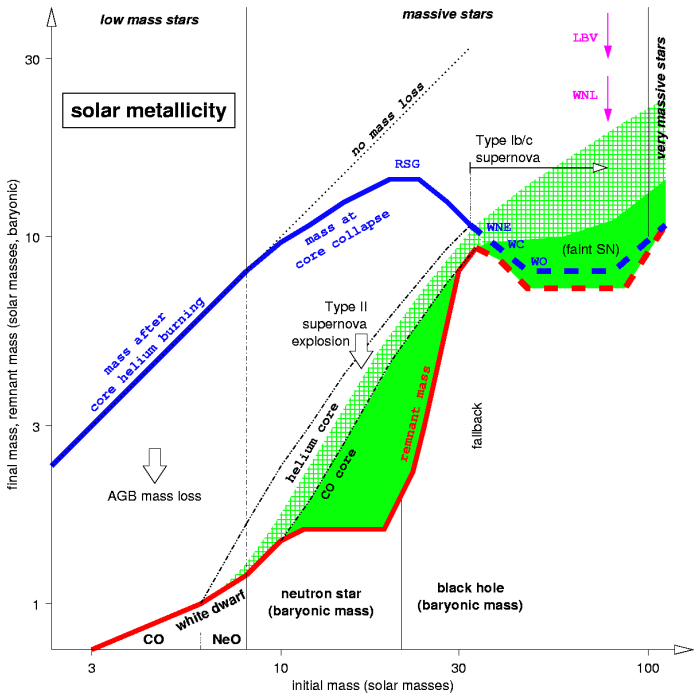

Ejected "metals"

Figure 1.3: The fates of stars as a function of the initial mass, for the case of solar metallicity (taken from Heger et al., 2010).

well as a recent 3D simulation CASTRO (`https://ccse.lbl.gov/Research/CASTRO/index.html`, Almgren et al., 2010) that enables improved investigations of phenomena such as convection, which has previously been constrained to lower-dimensional, approximate treatments. The stellar simulation used throughout this work is KEPLER, a time-implicit one-dimensional hydrodynamics package for stellar evolution (Weaver et al., 1978).

1.3.1 The Basic Equations

The KEPLER code integrates the following equations, assuming a non-rotating spherical symmetry (Weaver et al., 1978),

$$\frac{dv}{dt} = -4\pi r^2 \frac{\partial P}{\partial m} - \frac{Gm}{r^2} + \frac{4\pi}{r}\frac{\partial Q}{\partial m}, \tag{1.10}$$

$$\frac{d\epsilon}{dt} = -4\pi P \frac{\partial}{\partial m}\left(vr^2\right) - \frac{\partial L}{\partial m} + \dot{S} + 4\pi Q \frac{\partial}{\partial m}\left(\frac{v}{r}\right), \tag{1.11}$$

where the independent variable m is the mass interior to a given radius r, $v = dr/dt$ is the velocity, P is the pressure, ϵ is the internal energy per unit mass, L is the luminosity through a shell at radius r, $\dot{S}$ is the local energy generation rate per unit mass, G is the gravitational constant, and $Q \equiv (4/3)\,\eta_v r^4 \partial\left(v/r\right)/\partial r$, where η_v is the dynamic viscosity coefficient, as defined in Landau and Lifshitz (1959). Viscosity is generally small in stellar environments unless shocks are present, which can introduce spatial gradient discontinuities and numerical complications. To avoid such problems, the dynamic viscosity coefficient is taken to be,

$$\eta_v = \eta_R + \frac{3}{4} l_1 \rho c_s + \frac{3}{4} l_2^2 \rho \max\left[0, -\nabla \cdot \mathbf{v}\right], \tag{1.12}$$

where η_R is the physical viscosity coefficient, and c_s is the sound speed, and l_1 and l_2 are parametrized lengths used in the second and third terms to provide viscous stresses that serve to dissipate strong shock transitions.

To summarize, the terms in Equation 1.10 give the accelerations of mass elements due to pressure gradients, gravity, and viscous stresses, respectively. The terms in Equation 1.11 give the rate of change of the internal energy due to the local dynamics (either compression or expansion), heat flow, nuclear energy generation (including neutrino losses), and viscous dissipation.

1.3.2 Convection

Convection is treated in KEPLER using mixing length theory (see, Clayton, 1968), where a mass element is assumed to rise or fall a distance l before thermalizing with the local environment. The average velocity of the mass elements is given (through a treatment of the buoyancy) by,

$$v_c = \frac{1}{2}\left(\frac{GM}{Tr^2}\Delta\nabla T\right)^{\frac{1}{2}} l, \tag{1.13}$$

where $\Delta\nabla T$ is defined as the difference of the absolute magnitude of the adiabatic temperature gradient from the absolute magnitude of the temperature gradient, G is

the gravitational constant, M is the mass, r is the radial coordinate, and T is the temperature. The final expression for the heat flux due to convection is then given as,

$$H = c_P \rho \left(\frac{GM}{Tr^2}\right)^{\frac{1}{2}} (\Delta\nabla T)^{\frac{3}{2}} \frac{l^2}{2}, \tag{1.14}$$

where c_P is the heat capacity at constant pressure, and ρ is the density. In KEPLER, the mixing length l is taken to be the pressure scale-height, which takes the following form when the system is in hydrostatic equilibrium,

$$H_P \equiv -\frac{\mathrm{d}r}{\mathrm{d}\ln P} = \frac{P}{\rho g}, \tag{1.15}$$

where g is the local gravity, and P is the pressure. The mixing due to convection is then addressed by solving the time-dependent diffusion equation once the mixing length is found,

$$\frac{\mathrm{d}\,Y_\mathrm{i}}{\mathrm{d}t} = \frac{\partial}{\partial m}\left[\left(4\pi r^2\right)^2 \rho^2 D \frac{\partial Y_i}{\partial t}\right], \tag{1.16}$$

where Y_i is the abundance of ion species i, and D is the diffusion coefficient, given by $D_c = v_c l/3$ for *Ledoux* convection. In the case of semi-convection, $D = D_s = q_r D_c D_R / (D_c + D_R)$, where D_R is the radiation diffusion constant, and the adjustable parameter q_r is set to 0.1. Further details on the treatment of convection and mixing can be found in Woosley and Weaver (1988), and Woosley et al. (2002).

1.3.3 Explosion Mechanism

The explosion mechanism is modeled as a mechanical piston that imparts an acceleration at constant Lagrangian mass coordinate to provide the desired total kinetic energy of the ejecta, taken throughout this work to be $1.2\,\mathrm{B}$ ($1\,\mathrm{B} = 10^{51}\,\mathrm{erg}$) at 1 year after the explosion. The value for the acceleration is found iteratively until the desired final energy is produced. The mass cut is evaluated at $S/N_A k = 4.0$, where S is the entropy (roughly the edge of the Fe core). Further discussion of the parametrization of the explosion used in KEPLER can be found in Weaver et al. (1978); Woosley and Weaver (1995); Woosley and Heger (2007), and references therein. A discussion of the mass cut is given in Tur et al. (2007) and Heger and Woosley (2010).

This discussion is not exhaustive; further details of the KEPLER code can be found

in previous citations and references therein. We aim to develop the features salient to the present work only. In the following chapter, we address the relevant nucleosynthesis and astrophyiscal processes.

Chapter 2

Nucleosynthesis

2.1 Introduction

Nucleosynthesis is the study of nuclear species, the reactions and processes that create them, and their properties. There are several astrophysical processes responsible for nucleosynthesis, and understanding these processes is essential for describing the isotopic and elemental abundances of the Galaxy, both now and in the past. One goal of nucleosynthesis studies is to understand the isotopic abundance pattern of the solar neighborhood (Fig. 2.1), its chemical origin and evolution.

Understanding these abundances requires a broad range of physics that describes everything from primordial matter and the stellar furnaces that process it, to large scale structures within galaxies, such as globular clusters, and entire galaxies themselves. Indeed, nucleosynthesis intersects astrophysics, nuclear physics, and cosmology. The present work will draw on many astrophysical processes responsible for explaining the features in Fig 2.1. These astrophysical processes will now be introduced, organized roughly by isotopic mass.

2.2 Big-Bang Nucleosynthesis

The first isotopes were created shortly after the Big Bang. When the Universe was less than ∼100 seconds old, protons and neutrons were in thermal equilibrium with each other by weak interactions with neutrinos, preventing the stable construction

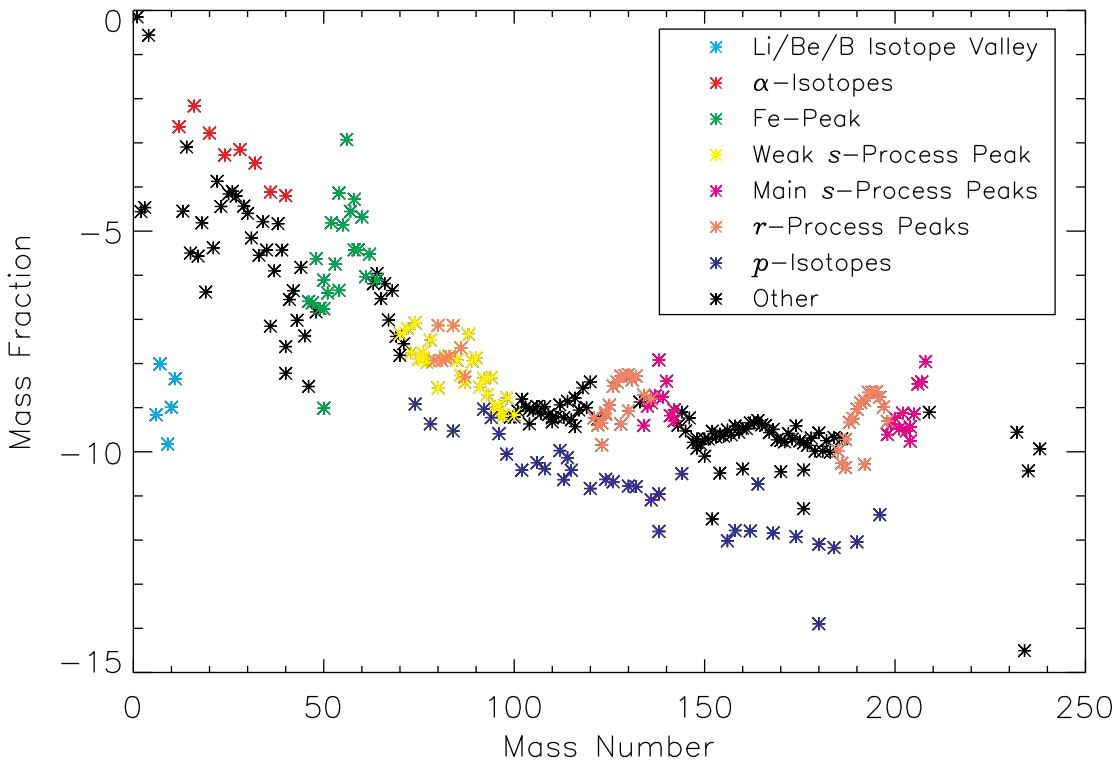

Figure 2.1: The isotopic abundance pattern of the solar neighborhood and its salient features. The abundances are taken from Lodders, 2010. The isotopes given by *black asterisks* do not fall into only one of the categories above, and are made in a variety of processes.

of atomic nuclei. Upon continuing expansion the temperature dropped sufficiently to "freeze out" neutrino interactions. At this "freeze-out" temperature, corresponding to $k_B T \sim 0.8\,\mathrm{MeV}$, the weak interaction rate became slower than the Hubble expansion, and the neutron-to-proton ratio (after subsequent β decay) was fixed to $n/p \simeq 1/7$ (Yao et al., 2006). At this point big bang nucleosynthesis (BBN) began with strong interactions among the nucleons, first leading to deuterium (^{2}H) formation, and proceeding to produce non-negligible abundances of ^{3}He, ^{4}He, ^{7}Li, minute abundances of ^{6}Li, and trace amounts of isotopes up through oxygen (Cyburt et al., 2001; Fields, 2006).

BBN isotope network calculations give an isotopic abundance pattern that provides

the initial conditions of the Universe's chemical evolution, consisting of only a few species. The rest of the periodic table of elements and (more importantly for the nuclear astrophysicist) the complete table of isotopes is synthesized in stellar environments from a variety of processes.

2.3 General Classification of Processes

Isotopic production proceeds from BBN abundances and falls generally into two categories. Astrophysical processes that are "primary" make isotopes directly from BBN material, and thus do not require pre-existing metals (isotopes heavier than He). Note that this does not imply the production channel must be absent of metals, merely that any metals participating in the reaction(s) are made *in situ*. Since no pre-existing metals are needed, the rate of production of isotopic abundances of primary processes are a constant function of metallicity, implying,

$$\frac{\partial X_{i,\mathrm{p}}}{\partial Z} = const. \Rightarrow X_{i,\mathrm{p}} \propto Z, \tag{2.1}$$

where $X_{i,\mathrm{p}}$ is the abundance of some isotope i made in a primary process, and Z is the total metallicity. Thus as the metallicity increases, so too (in proportion) must the abundances of isotopes made in primary processes that comprise the aggregate.

Astrophysical processes that are "secondary" make isotopes from pre-existing metals. Here the rates of isotopic abundances are proportional to their parent isotopic abundances, made from *primary* processes, implying,

$$\frac{\partial X_{i,\mathrm{s}}}{\partial Z} \propto X_{j,\mathrm{p}} \Rightarrow X_{i,\mathrm{s}} \propto Z^2, \tag{2.2}$$

where the subscript s denotes secondary process. As the metallicity increases, so too (in proportion) does the abundance of isotopes made in secondary processes that comprise the aggregate, *as well as* the abundance of isotopes made in primary processes from which the secondary isotopes are made, hence the additional factor of Z.

Alternately, these relations may be motivated by noting that primary processes produce isotopes with a rate independent of time, and the average Z of the Galaxy should increase monotonically with time (e.g., Timmes et al., 1995; Prochaska et al.,

2003; Bensby et al., 2004; Li et al., 2008), although such relations are dependent on selection effects (Edvardsson et al., 1993; Feltzing et al., 2001). Similarly, secondary processes produce isotopes at a rate proportional to abundances from primary processes. The relations above hold for individual astrophysical events.

There does exist a known tertiary process, photo-disintegration events (the γ-process), that can be synthesized from parent isotopes made in secondary processes. Such events would generate abundances cubic in Z, and although this process contributes very little to the *overall* distribution of isotopic abundances relative to primary and secondary processes, there are isotopes that have dominant abundance contributions from photo-disintegration (e.g., ^{130,132}Ba, ^{174}Hf). Note that the ν-process (discussed below), which is typically considered primary for light isotopic production, can have contributions to some heavy isotopes (e.g., ^{138}La, ^{180}Ta) that are *also* secondary or tertiary in nature, for the same reasons as photo-disintegration events.

2.4 Light Isotopes

2.4.1 Helium

Almost all He made after BBN is believed to be constructed during H burning in stars of masses above $M_{\odot} > 0.08$. Objects below this limit cannot generate sufficient temperatures to begin nuclear fusion of H. They are held up against gravitational collapse by electron degeneracy pressure, after some initial deuterium burning, and exit chemical evolution as brown dwarfs (Iliadis, 2007). From a chemical evolution perspective, such stars serve only to remove isotopic material from the interstellar medium (ISM) from future nucleosynthesis.

2.4.2 ν-Process

Neutrino-induced nucleosynthesis can be separated in two categories. The "light" ν-process involves interactions among neutrinos and lighter nuclei in the NeO layer during core-collapse supernovae (CCSNe; Woosley et al., 1990; Yoshida et al., 2004; Heger et al., 2005). The neutrinos elevate nuclei to excited states through inelastic collisions, which then decay by nucleon emission (Woosley, 1977; Hartmann et al., 1991). The target

nuclei for these interactions are CNO isotopes made from H and He, hence this is a primary process. This process produces abundances for ^{11}B, ^{7}Li, and ^{19}F isotopes (Timmes et al., 1995; Heger et al., 2005; Prantzos, 2010b). The "heavy" ν-process also involves neutrino interactions, but with target nuclei made from either the s- or r-processes (discussed in Section 2.7), and is responsible for heavy nuclei production such as ^{180}Ta and ^{138}La. Due to the requirement of pre-existing s- or r-process metals to serve as the target nuclei, the "heavy" ν-process behaves like the γ-process (discussed in Section 3.2.5.4) with respect to metallicity.

2.4.3 Galactic Cosmic Ray Spallation

Galactic Cosmic Ray (GCR) spallation events occur when energetic protons or α-particles impact on existing CNO nuclei in the ISM (Reeves, 1970; Meneguzzi et al., 1971). GCR spallation contributes to ^{6}Li, ^{9}Be, ^{10}B, and ^{11}B abundances (Prantzos, 2007, 2010a). Since spallation occurs on pre-existing CNO nuclei in the ISM, this process was traditionally considered secondary. Observations, however, show a primary dependence on metallicity for ^{9}Be (Prantzos, 2007; Boesgaard et al., 2011), which is in conflict with the understanding of traditional spallation events. A solution to this problem was proposed by Prantzos (2012, 2010a), who suggested that GCRs accelerated by the winds of rotating massive stars could be abundant in CNO isotopes. If these GCRs then hit ISM protons or α-particles, this would satisfy the condition of a primary event. A more recent investigation by Banerjee et al. (2013) identified neutrino-induced reactions in the He shells during CCSNe events as an additional possible source for primary ^{9}Be. It is not yet clear what the relative contributions to primary ^{9}Be would be from both primary GCR spallation and neutrino-induced reactions, if indeed both contribute. In the present work we assume that primary GCR spallation is the mechanism for LiBeB production, along with secondary GCR spallation (Prantzos, 2007, 2010a, 2012), but acknowledge that future efforts may require modification.

2.4.4 Classical Novae

In binary star systems, white dwarfs that accrete material from its companion star can undergo outbursts powered by a thermonuclear runaway in the accreted layer (Truran,

1982; Starrfield, 1989). Nucleosynthesis occurs on both the accreted material, that is rich in H and He, and on primary CNO (and ONeMg for ONeMg novae) dredged-up into the envelope, hence this process is primary. Unlike most other primary processes that immediately begin to enrich the ISM (compared to galactic chemical evolution timescales), there is a delay between the formation of the novae progenitors and their contributions to the ISM, as is also the case with Type Ia SNe. Simulations show differences in isotopic production below the iron peak, depending on the composition of the core and its mass (José and Hernanz, 2008, 2007; Gehrz et al., 1998). Hence, precise abundance determinations are difficult to isolate. Many CO novae simulations show production of ^{7}Li, ^{13}C, ^{15}N, ^{17}O, and ^{19}F that dominate the ejecta, whereas ONeMg novae show additionally contributions of other metals up to ^{40}K (José and Hernanz, 2007), both of these cases are subject to core mass and the treatment of mixing.

2.5 Low and Intermediate-Mass Star Contributions

Stellar winds from low and intermediate-mass stars are rich in C and N isotopes (Arnould et al., 2003), and provide significant contributions to their solar abundances. Fitting the contributions from these sources to data is problematic, since contamination from massive stars is always present and difficult to separate out. Hence, we do not independently address stellar wind contributions in the present work and instead combine their contributions with those from massive stars, both of which are primary processes.

2.6 Intermediate-Mass and Iron Group Isotopes

The majority of the metals by mass fall into this category and are made in different types of supernovae. Simulations of electron-capture supernovae (ECSNe), for example, show large productions of ^{64}Zn, ^{70}Ge, and ^{90}Zr, however, the ^{90}Zr overproductions vanish with a change in Y_e of only $1\,\% - 2\,\%$ (Wanajo et al., 2009). Light p-isotopes (^{74}Se, ^{78}Kr, ^{84}Sr, and ^{92}Mo) are also shown to be produced in appreciable quantities, but very little α-isotopes and iron group isotopes are produced in this environment (Wanajo et al., 2009). In our model we do not address ECSNe contributions differently from CCSNe, and this is left for future work.

2.6.1 Hydrostatic Burning

Hydrostatic burning in massive stars ($\sim 10 - 100\,\mathrm{M}_{\odot}$) synthesizes most isotopes from He up to the iron peak (Burbidge et al., 1957; Rauscher et al., 2002). Stellar winds can eject some of this material over the star's life, but the subsequent SNe provides the salient contributions to ISM for intermediate-mass and iron group isotopes. Massive stars that experience heavy mass loss, which is typical for those with $M \gtrsim 30\,\mathrm{M}_{\odot}$, are thought to play important roles in chemical enrichment at low metallicities. Specifically, stellar models have shown significant contributions to CNO isotopes with moderate productions of Na and Al, although the latter require fast rotating models, which may also influence the C production (Chiappini et al., 2006; Meynet et al., 2006).

Main sequence hydrogen burning proceeds with the 4 CNO cycles,

$$\mathrm{CNO\,I}: {}^{12}\mathrm{C}\,(\mathrm{p},\gamma)^{13}\,\mathrm{N}\left(\beta^{+}\nu_{\mathrm{e}}\right){}^{13}\mathrm{C}\,(\mathrm{p},\gamma)^{14}\,\mathrm{N}\,(\mathrm{p},\gamma)^{15}\,\mathrm{O}\left(\beta^{+}\nu_{\mathrm{e}}\right){}^{15}\,\mathrm{N}\,(\mathrm{p},\alpha)^{12}\,\mathrm{C}, \tag{2.3}$$

$$\mathrm{CNO\,II}: {}^{16}\mathrm{O}\,(\mathrm{p},\gamma)^{17}\,\mathrm{F}\left(\beta^{+}\nu_{\mathrm{e}}\right){}^{17}\,\mathrm{O}\,(\mathrm{p},\alpha)^{14}\,\mathrm{N}\,(\mathrm{p},\gamma)^{15}\,\mathrm{O}\left(\beta^{+}\nu_{\mathrm{e}}\right){}^{15}\,\mathrm{N}\,(\mathrm{p},\gamma)^{16}\,\mathrm{O}, \tag{2.4}$$

$$\mathrm{CNO\,III}: {}^{15}\mathrm{N}\,(\mathrm{p},\gamma)^{16}\,\mathrm{O}\,(\mathrm{p},\gamma)^{17}\,\mathrm{F}\left(\beta^{+}\nu_{\mathrm{e}}\right){}^{17}\,\mathrm{O}\,(\mathrm{p},\gamma)^{18}\,\mathrm{F}\left(\beta^{+}\nu_{\mathrm{e}}\right){}^{18}\,\mathrm{O}\,(\mathrm{p},\alpha)^{15}\,\mathrm{N}, \tag{2.5}$$

$$\mathrm{CNO\,IV}: {}^{16}\mathrm{O}\,(\mathrm{p},\gamma)^{17}\,\mathrm{F}\left(\beta^{+}\nu_{\mathrm{e}}\right){}^{17}\,\mathrm{O}\,(\mathrm{p},\gamma)^{18}\,\mathrm{F}\left(\beta^{+}\nu_{\mathrm{e}}\right){}^{18}\,\mathrm{O}\,(\mathrm{p},\gamma)^{19}\,\mathrm{F}\,(\mathrm{p},\alpha)^{16}\,\mathrm{O}, \tag{2.6}$$

Despite the many reactions involved in the CNO cycles, the net result of each is,

$$4\mathrm{H} \rightarrow^{4} \mathrm{He} + 2\mathrm{e}^{+} + 2\nu_{\mathrm{e}}. \tag{2.7}$$

Hence, whereas this does not contribute to the metallicity of the star, it is responsible for ^{14}N, and some ^{13}C and ^{15}N abundances, which participate in later nucleosynthesis (Woosley and Weaver, 1995; Prantzos, 2003). Note that the overall CNO abundance

does not change, but the distribution of CNO isotopes achieves an equilibrium abundance determined by the relative cross-sections — hence the dominant result from the CNO cycles is ^{14}N. Note further that whereas the CNO I cycle is the most relevant for energy generation, the other cycles can be relevant for nucleosynthesis, by providing isotopes that participate in the CNO I cycle.

Once the star leaves the main sequence, the salient core-He burning reactions are $^{4}\mathrm{He}\,(\alpha,\gamma)^{8}\,\mathrm{Be}\,(\alpha,\gamma)^{12}\,\mathrm{C}$, which is often denoted simply by $3\alpha \rightarrow ^{12}$ C due to the short timescales required for the second two-body interaction (^{8}Be has $\tau_{1/2} \sim 10^{-17}$ s; Audi et al., 2003), and $^{12}\mathrm{C}\,(\alpha,\gamma)^{16}\,\mathrm{O}$. These rates compete to affect the O/C ratio at the end of core-He burning, in addition to indirectly affecting subsequent burning episodes and the structure of the pre-supernova star. A study investigating the effects of varying these rates across their known 2σ uncertainty range is discussed in Chapter 4. Additional He burning reactions relevant for nucleosynthesis include $^{15}\mathrm{N}\,(\alpha,\gamma)^{19}\,\mathrm{F}$ which contributes to the ^{19}F abundance (Meynet and Arnould, 2000), and $^{14}\mathrm{N}\,(\alpha,\gamma)^{18}\,\mathrm{F}\,(\beta^{+}\nu_{\mathrm{e}})^{18}\,\mathrm{O}\,(\alpha,\gamma)^{22}\,\mathrm{Ne}$, which contributes to ^{18}O and ^{22}Ne abundances (Woosley and Weaver, 1995), the latter being crucial for the weak *s*-process (discussed in Section 2.7.2).

Due to higher temperatures that enable a greater variety of nuclear reactions, the nucleosynthesis beyond core-He burning becomes complicated enough to warrant the use of nuclear reaction networks to solve for the final composition (Woosley et al., 2002). Such networks consist of coupled, linear differential equations that are solved numerically in stellar evolution codes. In addition to the more complicated nucleosynthesis, neutrino losses now play a much larger role in balancing the energy budget (Arnett, 1972). In fact, the evolution of massive stars beyond He burning has been described as a "neutrino-mediated Kelvin-Helmholtz contraction of a carbon-oxygen core" (Woosley et al., 2002), that is interrupted only when subsequent burning phases are able to balance the neutrino losses.

The main reactions during core-C burning are, with almost equal branchings,

$$^{12}\mathrm{C}\left(^{12}\mathrm{C},\alpha\right)^{20}\mathrm{Ne},\ ^{12}\mathrm{C}\left(^{12}\mathrm{C},\mathrm{n}\right)^{23}\mathrm{Mg},\ \text{and}\ ^{12}\mathrm{C}\left(^{12}\mathrm{C},\mathrm{p}\right)^{23}\mathrm{Na}.$$

Two other isotopes of Ne can be produced by,

$$^{20}\mathrm{Ne}\,(\mathrm{p},\gamma)^{21}\,\mathrm{Na}\,(\beta^{+}\nu_{\mathrm{e}})^{21}\,\mathrm{Ne},\ \text{and}\ ^{21}\mathrm{Ne}\,(\mathrm{p},\gamma)^{22}\,\mathrm{Na}\,(\beta^{+}\nu_{\mathrm{e}})^{22}\,\mathrm{Ne}.$$

Much of the ^{23}Na is processed by,

$$^{23}\mathrm{Na}\,(\mathrm{p},\alpha)^{20}\,\mathrm{Ne},\ ^{23}\mathrm{Na}\,(\mathrm{p},\gamma)^{24}\,\mathrm{Mg},\ \text{and}\ ^{23}\mathrm{Na}\,(\alpha,\mathrm{p})^{26}\,\mathrm{Mg}\,(\mathrm{p},\gamma)^{27}\,\mathrm{Al}.$$

There is also the processing of ^{21}Ne into ^{26}Mg by,

$$^{21}\mathrm{Ne}\,(\mathrm{p},\gamma)^{22}\,\mathrm{Na}\,(\beta^{+})^{22}\,\mathrm{Ne}\,(\alpha,\mathrm{n})^{25}\,\mathrm{Mg}\,(\mathrm{n},\gamma)^{26}\,\mathrm{Mg},$$

in addition to some others (Arnett and Thielemann, 1985). These latter reactions have rates about an order of magnitude smaller than the main reactions.

Core-Ne burning occurs next, with the photo-disintegration reaction, $^{20}\mathrm{Ne}\,(\gamma,\alpha)^{16}\,\mathrm{O}$ followed by $^{20}\mathrm{Ne}\,(\alpha,\gamma)^{24}\,\mathrm{Mg}$. Other reactions (with rates of about two orders of magnitude less) also include (Thielemann and Arnett, 1985),

$$^{24}\mathrm{Mg}\,(\alpha,\gamma)^{28}\,\mathrm{Si},\ ^{25}\mathrm{Mg}\,(\alpha,\mathrm{n})^{28}\,\mathrm{Si},\ ^{26}\mathrm{Mg}\,(\alpha,\mathrm{n})^{28}\,\mathrm{Si},\ ^{26}\mathrm{Mg}\,(\mathrm{p},\mathrm{n})^{26}\,\mathrm{Al},\ ^{26}\mathrm{Mg}\,(\alpha,\gamma)^{30}\,\mathrm{Si},$$
$$^{27}\mathrm{Al}\,(\alpha,\mathrm{p})^{30}\,\mathrm{Si},\ \text{and}\ ^{30}\mathrm{Si}\,(\mathrm{p},\gamma)^{31}\,\mathrm{P}.$$

The main reactions of core-O burning are (e.g., Clayton, 1968),

$$^{16}\mathrm{O}\left(^{16}\mathrm{O},\mathrm{n}\right)^{31}\,\mathrm{S},\ ^{16}\mathrm{O}\left(^{16}\mathrm{O},\mathrm{p}\right)^{31}\,\mathrm{P},\ ^{16}\mathrm{O}\left(^{16}\mathrm{O},\mathrm{d}\right)^{30}\,\mathrm{P},\ \text{and}\ ^{16}\mathrm{O}\left(^{16}\mathrm{O},\alpha\right)^{28}\,\mathrm{Si}.$$

Other important reactions include (Thielemann and Arnett, 1985),

$$^{31}\mathrm{P}\,(\mathrm{p},\alpha)^{28}\,\mathrm{Si}\,(\alpha,\gamma)^{32}\,\mathrm{S},\ ^{32}\mathrm{S}\,(\alpha,\gamma)^{36}\,\mathrm{Ar}\,(\alpha,\mathrm{p})^{39}\,\mathrm{K},\ ^{32}\mathrm{S}\,(\alpha,\gamma)^{36}\,\mathrm{Ar}\,(\mathrm{n},\gamma)^{37}\,\mathrm{Ar}\,(\beta^{+})^{37}\,\mathrm{Cl},$$

and long reaction chains producing ^{40}Ca and ^{46}Ti from ^{35}Cl.

Since Silicon (Si) is very tightly bound, its burning proceeds differently than the typical fusion reactions in core-O and core-C burning. New nuclei are synthesized by α-capture on ^{28}Si, with the α-particle abundance replenished from photo-disintegration of heavier nuclei. Since the nuclei capture and release α-particles at a high rate, the abundance pattern between ^{28}Si and ^{56}Ni does not change over times sufficient for large numbers of individual reactions. Such a system can be said to be *close* to equilibrium (in this isotope range), a condition called quasi-nuclear statistical equilibrium (QSE) (see, Bodansky et al., 1968; Meyer et al., 1998). Indeed this phase has been described as core-Si "melting" to ^{56}Ni rather than burning (Clayton, 1968). Eventually the Si composition reaches the Fe group nuclei, but the exact path is highly dependent on the neutron excess, temperature, density, and convection. For this reason stellar modeling often requires a separate QSE network coupled to the reaction network, and Si burning

is thus more computationally expensive and potentially numerically unstable (Woosley et al., 2002).

In summary, the main reactions of each core burning phase have been discussed that provide the needed energy generation. Hence, these are important for understanding the evolution of the star. Additionally, there are many other reactions given which are important contributors to the nucleosynthesis.

2.6.2 Core Collapse Supernovae

Upon core collapse the Fe core disappears into the remnant, and the passage of the shock through the interior layers of the star leaves the composition α-rich by photo-disintegration. The material subsequently expands and cools to form the majority of the observed α-isotopes and nuclei up to the Fe peak. It is believed that CCSNe likely produces between 1/3 and 2/3 of the solar abundance of iron peak isotopes (Timmes et al., 1995). The products of explosive O and Si burning are similar to their hydrostatic counterparts, but may vary due to the higher temperatures (Truran and Arnett, 1970). From explosive Si burning many isotopes are made between ^{43}Ca and ^{66}Zn. The explosive O burning makes most of the observed isotopic abundances between ^{28}Si and ^{42}Ca. Explosive Ne/C burning makes lower mass isotopes between ^{23}Na and ^{31}P, and additionally many neutron-rich isotopes with mass numbers between $\approx 36 - 88$. The latter are made from neutron capture reactions, with the neutrons provided by (α, n) reactions from the Ne/C explosive burning (Woosley et al., 2002).

2.6.3 Pair-Instability Supernovae

Pair-instability supernovae (PISNe) have been shown in simulations to overproduce even nuclei relative to odd nuclei due to the small neutron excess in their interiors, as well as over-productions of Si and S due to the extensive O burning (e.g., Heger and Woosley, 2002; Umeda and Nomoto, 2002). In our model we do not address PISNe contributions differently from CCSNe, and this effect is left for future work.

2.6.4 Type Ia Supernovae

The standard model for Type Ia SNe is thermonuclear explosions of CO white dwarfs (Hoyle and Fowler, 1960). Many different progenitor models are being investigated. The double degenerate channel involves the merger of two WDs (e.g., Iben and Tutukov, 1984; Toonen et al., 2012; Wang and Han, 2012). Within this channel there is also a possible sub-Chandrasekhar progenitor model, where the explosion occurs below the Chandrasekhar mass limit due to carbon detonation near the WD surface (e.g., Nomoto et al., 2013). In the single degenerate channel, a white dwarf accretes material from a red giant companion (e.g., Nomoto et al., 1997; Hillebrandt and Niemeyer, 2000; Woosley, 2001). Note that there is also a possible sub-Chandrasekhar progenitor model for this channel as well, if a helium detonation is induced in the accreting WD by strong He flashes (e.g., Nomoto et al., 2013). Even in the single degenerate Chandrasekhar models, however, there are discrepancies between the delay time distribution and the corresponding time-integrated supernova Ia rate (e.g., Bours et al., 2013). It is clear the progenitors of Type Ia are still not well known, however, it should be noted that the Chandrasekhar mass models better explain the observed features of SNe Ia (e.g., spectra, composition) compared to the sub-Chandrasekhar models (e.g., Livio, 2000).

These SNe provide the remaining iron peak abundances not produced in massive stars, with some enrichment of other metals (Travaglio et al., 2004b; Maeda et al., 2010). In fact, simulations show Type Ia production of minute trace contributions to all isotopes below the iron peak (Nomoto et al., 1997), with the exception of ^{40}K — dependent, however, on the initial metallicity of the progenitor. The burning occurs in nuclear statistical equilibrium (NSE), and because of the balancing of forward and backward reactions, the final abundances are not determined by cross-sections but rather by the binding energies (Hoyle, 1946; Burbidge et al., 1957; Cameron, 1957). Both CCSNe and Type Ia SNe produce their isotopic yields explosively, which destroys much of the initial metal composition. The evolutions of their isotopic products are considered primary.

2.7 Heavy Isotopes

Isotopes heavier than Fe cannot be made through fusion reactions. Different mechanisms must then be operative to produce the heavy isotopes. We now introduce these mechanisms, and describe the isotopic approximate ranges to which they contribute.

2.7.1 The Main *s*-Process

The *s*-process is one of the four trans-iron processes for making the heavier nuclides. It synthesizes isotopes via slow neutron capture (Burbidge et al., 1957), and is responsible for approximately half the heavy isotopes beyond iron (Pignatari et al., 2010; Heil et al., 2007). Since this process is characterized by neutron capture rates that are slow compared to the β decay rate of the target nucleus, $\tau_\beta \ll \tau_{n\gamma}$, production proceeds along the path of isotopic stability, with ^{56}Fe playing the role of the seed nucleus (e.g., Fig. 2.2). In reality many metals can seed this process, but in practice ^{56}Fe is often used as the sole target nucleus due to both its large abundance and neutron capture cross section relative to other potential seeds.

The main component of the *s*-process occurs in the thermally pulsating (TP) AGB stellar phase for stars with $M \lesssim 1.5 M_\odot$ [1]. The TP-AGB phase (e.g., Habing and Olofsson, 2003) occurs once the He shell has depleted its fuel. The next energy source is then provided by burning H in a thin shell next to the depleted He shell. This slowly builds up the He shell abundance once more, and eventually the He ignites explosively in a He flash or thermal pulse. After termination of this pulse, protons from the H shell can be mixed (H-ingestion) into the top layers of the intershell (e.g., Iliadis, 2007), perhaps by semi-convection or overshooting (e.g., Lattanzio and Lugaro, 2005). The star then contracts enough to once again ignite H shell burning, and the cycle begins again. The protons that have been mixed downward into the intershell region can be captured on synthesized ^{12}C to form a ^{13}C pocket by the reactions, $^{12}\mathrm{C}\,(\mathrm{p},\gamma)^{13}\,\mathrm{N}\,(\beta^{+}\nu_{\mathrm{e}})^{13}\,\mathrm{C}\,(\mathrm{p},\gamma)^{14}\,\mathrm{N}$ (Busso et al., 1999). Existing α-particles can then produce a neutron source by the reaction, ^{13}C(α,n)^{16}O. The neutrons facilitate main *s*-process production throughout several helium flashes by capture on pre-existing metals contained in the star. Due to

[1] Production for this component is also possible in SAGB stars with a $^{22}\mathrm{Ne}(\alpha,\mathrm{n})^{25}\mathrm{Mg}$ neutron source, although the yields are highly dependent on the $^{12}\mathrm{C}(\alpha,\gamma)^{16}\mathrm{O}$ and 3α reaction rates (Lau et al., 2011).

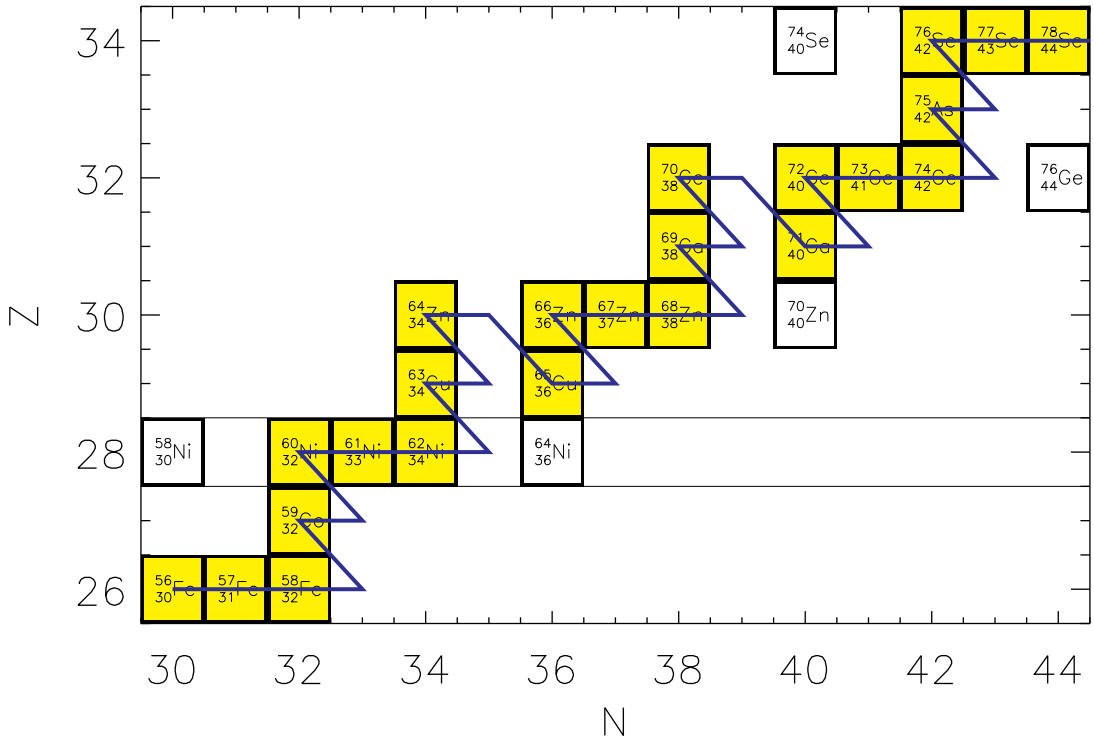

Figure 2.2: An example *s*-process path (*blue line*), from ^{56}Fe to ^{78}Se. Stable isotopes are shown, and those along the *s*-process path are given in *yellow*. Branching points are not shown.

the larger neutron exposures possible in the main *s*-process (relative to the weak component of the *s*-process), heavy isotopes can be produced, with salient contributions between mass numbers $A \geq 88$ (Truran and Iben, 1977; Iben, 1975).

Analytic calculations of *s*-process abundances are possible. The relevant differential equations are linear and coupled. The abundance evolution of a stable nuclide denoted by its mass A can be expressed as (e.g., Clayton, 1968),

$$\frac{dN_A}{dt} = -N_n N_A \langle \sigma \mathrm{v} \rangle_A + N_n N_{A-1} \langle \sigma \mathrm{v} \rangle_{A-1} \,, \tag{2.8}$$

where N_A is the number density of nuclide with mass A, N_n is the neutron number

density (typically $\sim 10^8\,\mathrm{cm}^{-3}$), and $\langle \sigma \mathrm{v} \rangle_A$ is the Maxwellian-averaged neutron capture thermonuclear reaction rate, given by,

$$\langle \sigma v \rangle = \left(\frac{8}{\pi \mu} \right)^{\frac{1}{2}} \frac{1}{(kT)^{3/2}} \int_0^\infty E\sigma\,(E) e^{-\mathrm{E}/kT} \mathrm{d}E, \tag{2.9}$$

where μ is the reduced mass, E is the energy, T is the temperature, k is Boltzmann's constant, and $\sigma(E)$ is the cross-section. Under the *classical model approximation*, the temperature is assumed constant during neutron irradiation, hence the Maxwellian-averaged thermonuclear reaction rate can be simplified,

$$\langle \sigma v \rangle_A \approx \langle \sigma \rangle_A \, v_T, \tag{2.10}$$

where v_T is the thermal neutron velocity, and only the cross-section is averaged. It is typical to then define the neutron exposure,

$$\tau = v_T \int N_n(t) \mathrm{d}t. \tag{2.11}$$

The neutron exposure, or time-integrated neutron flux, has characteristic values depending on environment (discussed further below). This definition then allows the recasting of the original abundance evolution equation, and the entire system can be written as (e.g., Iliadis, 2007),

$$\begin{aligned} \tfrac{dN_A}{d\tau} &= -N_A \langle \sigma \rangle_A + N_{A-1} \langle \sigma \rangle_{A-1} \\ \tfrac{dN_{A-1}}{d\tau} &= -N_{A-1} \langle \sigma \rangle_{A-1} + N_{A-2} \langle \sigma \rangle_{A-2} \\ &\vdots \\ \tfrac{dN_{56}}{d\tau} &= -N_{56} \langle \sigma \rangle_{56}\,, \end{aligned} \tag{2.12}$$

where N_{56} is the ^{56}Fe number density. Bottlenecks in the reaction flow exist at closed neutron shells, where the neutron capture cross-sections are small, and the abundances at these corresponding mass numbers accumulate into peaks. Three such peaks exist at approximate mass numbers, 88, 138, and 208, thus Sr, Ba, and Pb are signature s-process elements. In between closed neutron shells the flow is in equilibrium, hence

$dN_A/d\tau \approx 0$ and thus $N_A \langle\sigma\rangle_A \approx N_{A-1} \langle\sigma\rangle_{A-1} \approx const.$ Additionally, there are unstable nuclei along the s-process path that have β decay rates comparable to either the neutron capture rate or the β^+ decay rate. These nuclei create branching points in the reaction flow, and the relation between the products of the abundance and the cross sections must be modified to, $N_A \langle\sigma\rangle_A + N_{A'} \langle\sigma\rangle_{A'} \approx N_{A+1} \langle\sigma\rangle_{A+1}$, where A' stands for the unstable branching point nuclei.

The system given in Equation 2.12 can be solved analytically. It is unlikely that the neutron exposure will remain constant throughout successive dredge-up episodes during the AGB phase of the star. One would expect the neutrons to decrease at a rate proportional to the available ^{13}C. Hence, it is common to assume an exponential distribution of neutron exposures of the form (e.g., Clayton, 1968; Käppeler et al., 1990),

$$p(\tau) = \frac{f N^{\text{seed}}}{\tau_0} e^{-\tau/\tau_0}, \tag{2.13}$$

where f is the fraction of ^{56}Fe seed nuclei, denoted as N^{seed}, that has been subjected to the neutron exposure, and τ_0 is the mean or characteristic neutron exposure, which can serve as a parameter in s-process calculations. The abundances averaged over $p(\tau)$ can then be expressed in the standard way (e.g., Iliadis, 2007),

$$\overline{N_A(\tau_0)} = \frac{\int_0^\infty N_A(\tau)\, p(\tau)\, d\tau}{\int_0^\infty p(\tau)\, d\tau} = \int_0^\infty \frac{N_A(\tau)}{\tau_0} e^{-\tau/\tau_0} d\tau, \tag{2.14}$$

and the system given in Equation 2.12 can be iteratively solved to yield (e.g., Käppeler et al., 1990, 2011a),

$$\langle\sigma\rangle_A \overline{N_A(\tau_0)} = \frac{f N^{\text{seed}}}{\tau_0} \prod_{i=56}^{A} \left(1 + \frac{1}{\tau_0 \langle\sigma\rangle_i}\right). \tag{2.15}$$

This type of analysis has been used very successfully to fit the s-process abundances of s-only isotopes (isotopes made only by the s-process) to their observed solar abundances (e.g., Käppeler et al., 1990, 2011b). In AGB stars at high metallicities, typical fit values for the mean neutron exposure are $\tau_0 \simeq 0.3\,\text{mb}^{-1}$ (Käppeler et al., 1990). It was found from such a fitting that one τ_0 value could not fit all observed s-only isotopes in the solar abundance pattern, and in fact three distinct neutron exposure distributions were

required (e.g., Lamb et al., 1977; Iben and Renzini, 1982a,b; Busso and Gallino, 1985; Iliadis, 2007). This motivated postulating two additional types of *s*-processes, occurring in different astrophysical environments.

2.7.2 The Weak *s*-Process

The weak component of the *s*-process occurs in massive stars, during convective core-He burning and C shell burning (Pignatari et al., 2010). The neutron source in core-He burning is from the reaction $^{22}\mathrm{Ne}(\alpha,\mathrm{n})^{25}\mathrm{Mg}$. The ^{22}Ne nuclei are produced from the burning of ^{14}N (that was made previously in the CNO cycle) by,

$$^{14}\mathrm{N}\,(\alpha,\gamma)^{18}\,\mathrm{F}\,(\beta^{+}\nu_{\mathrm{e}})^{18}\,\mathrm{O}\,(\alpha,\gamma)^{22}\,\mathrm{Ne}.$$

Subsequent C shell burning can produce neutrons by, $^{13}\mathrm{C}(\alpha,\mathrm{n})^{16}\mathrm{O}$, and also provide α-particles to reignite the $^{22}\mathrm{Ne}(\alpha,\mathrm{n})^{25}\mathrm{Mg}$ neutron source. These neutrons are captured on initial ^{56}Fe present in the star, and typical neutron exposure values are $\tau_0 \simeq 0.07\,\mathrm{mb}^{-1}$ (Käppeler et al., 1990). The weak *s*-process component can only synthesize isotopes along the line of stability up to a mass number of $A{\approx}\,100$ (Raiteri et al., 1993), due its smaller neutron exposures relative to the main component. Although typically considered for its isotopic production beyond Fe, this process may also contribute significant amounts of ^{36}S, ^{37}Cl, ^{40}Ar, ^{40}K, and ^{45}Sc by neutron capture on lighter isotopes (Woosley et al., 2002), although we neglect these contributions in the present work.

Both the main and weak components of the *s*-process rely on the existence of metals in the initial composition of the star, and therefore are considered secondary processes. The *neutron source* for the main *s*-process, however, is primary (Clayton, 1988) — as well as some of the C shell burning contributions to the weak *s*-process, which could result in a behavior between that of a primary and secondary process.

2.7.3 The Strong *s*-Process

Originally a strong component of the *s*-process was introduced to address the underproduction of lead not accounted for by the main component at solar metallicities (Clayton and Rassbach, 1967), and it was believed that a third type of neutron exposure was needed to generate the remaining Pb, with typical values estimated at $\tau_0 \sim 7\,\mathrm{mb}^{-1}$ (Käppeler et al., 1990). Sufficient production was later found in the low metallicity

regime of the main component, and the strong s-process component has since been re-interpreted as a low metallicity effect of the main component (Gallino et al., 1998). This can be understood in the following way. As the metallicity (and hence Fe) decreases the neutron-to-seed ratio increases, since the neutron source is primary, whereas Fe has significant contributions from Type Ia SNe (which do not contribute at low metallicities). This increased neutron-to-seed ratio appears to provide sufficient neutron exposure to make the heavy Pb and Bi isotopes underproduced by the main s-process. Simulations of low metallicity AGB stars show production of "strong" s-process isotopes at [Fe/H] $= -2.6$ that exceed production at solar metallicities by several *dex*, depending on ^{13}C pocket efficiencies (Bisterzo et al., 2010). This implies nearly all of the solar "strong" s-process abundances are made at low metallicities.

2.7.4 Lighter Element Primary Process

Indication for the need of an additional primary process separate from the r-process is implied by observations of ultra-metal poor (UMP) stars, and was first implemented by Qian and Wasserburg (2001) in a two component phenomenological model. This process, sometimes referred to as the weak r-process (Truran and Cowan, 2000) or charged-particle reaction process (Qian and Wasserburg, 2007), was named in more general terms by Travaglio et al. (2004a) as the lighter element primary process (LEPP), and is needed to explain an observed excess of some lower mass ($A < 130$) elements, notably Sr, Y, and Zr, that cannot be accounted for by neutron capture processes, photo-disintegration, or CCSNe. Investigation of the triple-α and $^{12}\mathrm{C}(\alpha, \mathrm{n})^{16}\mathrm{O}$ rates indicates that their present 2σ uncertainty cannot account for the necessary production of Sr, Y, and Zr by the weak s-process in massive stars (Tur et al., 2009). A more recent nucleosynthesis calculation by Arcones and Montes (2011) suggests the interesting possibility of the needed abundances being produced in the neutrino-driven winds of ultra-metal poor CCSNe, although their yields suffer over-productions of additional isotopes in order to provide the necessary Sr, Y, and Zr.

2.7.5 The *r*-Process

The r-process synthesizes isotopes beyond the iron peak using rapid neutron capture relative to the beta decay rate, $\tau_\beta \gg \tau_{n\gamma}$, with high neutron density on order of $n \gtrsim 10^{21}\,\mathrm{cm}^{-3}$ (Burbidge et al., 1957). The astrophysical location of this process is still a matter of debate, but was first thought to occur in CCSNe environments (Hoffman et al., 1997). More recently it has been postulated to occur in shocked surface layers of O-Mg-Ne proto-neutron stars (Ning et al., 2007; Qian and Wasserburg, 2007), and simulations have also shown success in reproducing r-process signatures from ν-driven nucleosynthesis in the He-shell during CCSNe in the low metallicity regime (Z < -3.0; Banerjee et al., 2011). Yet other possibilities include neutron star mergers and r-process production in winds from accretion disks of BHs (e.g., Qian, 2012, and references therein). A recent principle component analysis has linked r-process elemental abundances with α-isotopes, however, further suggesting CCSNe as a possible site for this process (Ting et al., 2012).

The r-process proceeds far beyond the neutron-rich side of stability due to the high neutron densities (e.g., Fig. 2.3). Abundances accumulate towards higher neutron numbers until the rate between neutron capture and photo-disintegration balances, $\lambda_{n,\gamma} = \lambda_{\gamma,n} \gg \lambda_\beta$. This equilibrium (called the "waiting point") is not disturbed by subsequent β decays, which serve to send the flow to higher proton numbers where neutron capture can continue to a new equilibrium specific to that isotopic chain. In this fashion abundances flow and pile up until the neutron exposure terminates, when all unstable isotopes then β decay back to the line of stability.

As with the s-process, the r-process also bottlenecks at closed neutron shells. Since the closed neutron shells are encountered on the neutron rich side of stability, however, the proton number is lower at these bottlenecks for the r-process than it is for the s-process, hence after decay to stability the r-process peaks always occur at lower mass numbers relative to the s-process peaks, at approximately 80, 130, and 195 (see Fig. 2.1). Elements of interest for representing r-process elements that have r-only isotopes include Ge, Eu, and Pt. The explosive environment of the r-process does not *directly* depend on the initial metallicity of the star, and therefore is primary (although stellar populations that could be responsible for the r-process could depend on metallicity).

The abundance evolution for the r-process can be described by the set of differential

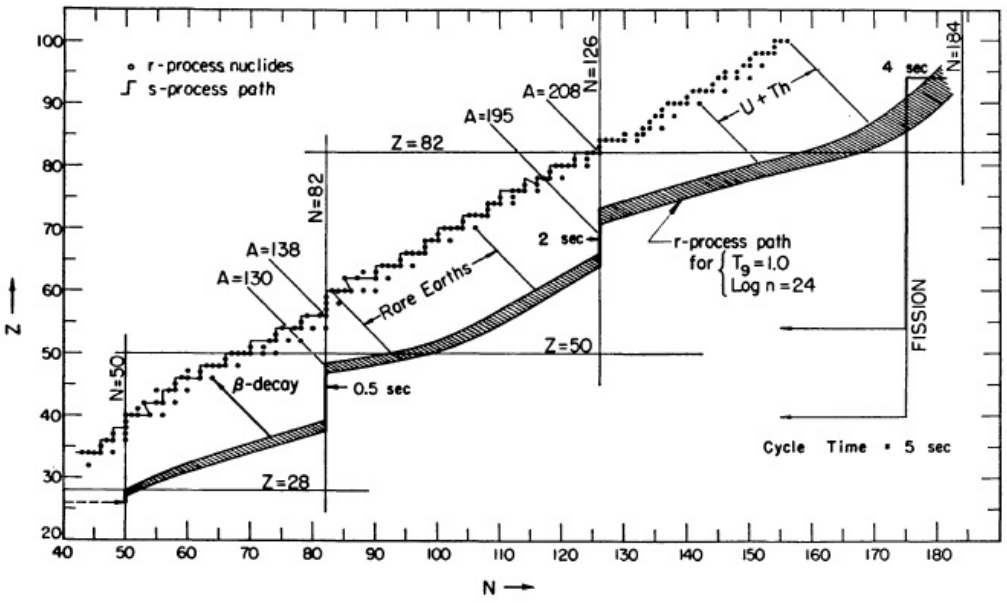

Figure 2.3: An example r-process path (*hatched region*). Stable isotopes are given by *dots*. The r-process path was calculated at a temperature of $T = 10^9\,\mathrm{K}$ with a neutron density of $n = 10^{24}\,\mathrm{cm}^{-3}$. The s-process path (*black line*) is shown for comparison (taken from Seeger et al., 1965).

equations of the form,

$$\frac{dN_A(Z)}{dt}dt = -N_n N_A(Z)\langle\sigma\nu\rangle_{Z,A} + N_{A+1}(Z)\lambda_{\gamma,A+1}(Z), \tag{2.16}$$

where Z is the elemental charge, $\lambda_{\gamma,A+1}$ is the photo-disintegration decay constant of N_{A+1}, and the remaining variables follow the convention of Equation 2.8. In between waiting points, where thermal equilibrium is established, the final abundances are given by the Saha equation for each isotope chain (e.g., Qian, 2003; Iliadis, 2007). Modeling the r-process can be done in principle, but requires knowledge of neutron capture

Q-values, α and β decay rates, the branching ratios for neutron emission, normalized partition functions, and fission probabilities (Iliadis, 2007). Unfortunately this information is not experimentally accessible, as most of the nuclei on the r-process path are highly unstable and cannot presently be produced in a laboratory. Hence, this process does not enjoy the same success as s-process modeling. Note that uncertainties in the r-process site and the key properties of it also contribute to this lack of success.

2.7.6 The *i*-Process

Another type of neutron capture process has been identified, with neutron densities intermediate to the s- and r-processes. This i-process was first suggested by Cowan and Rose (1977); Truran et al. (1978); Hillebrandt et al. (1981) and later observed in massive star models by Rauscher et al. (2002) (who named it "n-process"). More recently, it has been found in low metallicity AGB and SAGB models (Herwig et al., 2011; Bertolli et al., 2013). This process is characterized by reaction flows that drive the composition only slightly to the neutron-rich side of stability ($\sim$1–6 mass numbers) before β-decay, and can produce light r-process isotopes. It is not presently known what contributions this process makes to the solar abundances.

2.7.7 *p*-Isotopes

Isotopes that lie on the proton-rich side of stability (p-isotopes) mostly cannot be made by the s-process. There are a few proton rich isotopes that do either lie on the s-process path or are sufficiently close to the path to have non-negligible contributions from s-process branching points, for example, ^{108}Cd, ^{94}Mo, and ^{115}Sn. This is likely dependent on the specific modeling of the s-process, the specific treatment of branching points and values used for the cross-sections. The majority of p-isotopes, however, cannot be made by slow neutron capture; nor can they made by the r-process, since stable isotopes "block" the decay path from unstable isotopes to them (e.g., Fig. 2.4). Two additional processes are believed responsible for generating the observed p-isotopes.

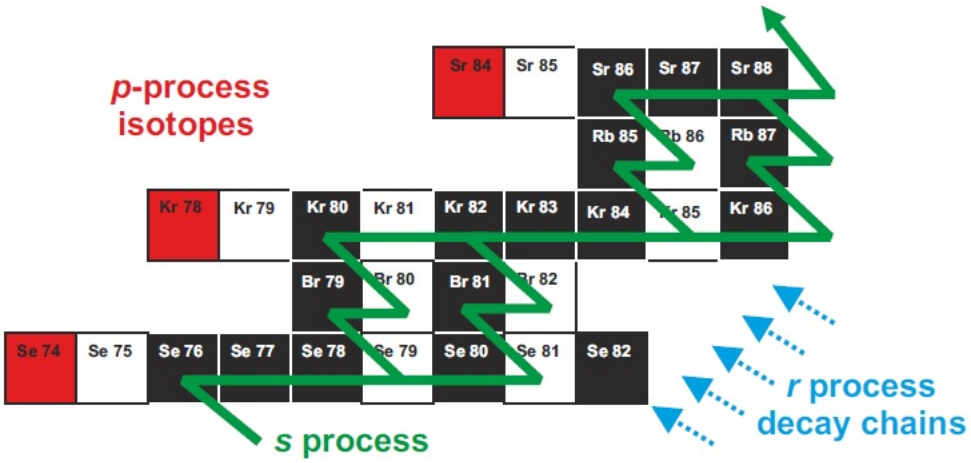

Figure 2.4: An example of proton-rich isotopes relative to the path of isotopic stability and the r-process decay chains. *Red*: Proton-rich isotopes. *Black*: Stable isotopes along the s-process path. *White*: Unstable isotopes (taken from Rauscher et al., 2013). Note that a few of the branching points along the s-process path are shown at ^{79}Se, ^{81}Se, and ^{85}Kr.

2.7.7.1 The νp-Process

The νp-process occurs in CCSNe environments, where high neutrino fluxes create proton rich ejects via weak reactions with neutrons and protons (Fröhlich et al., 2006). Additional neutrino interactions with the left-over protons from α-rich freeze-out produce a neutron abundance, which then undergo (n, p) strong reactions. The resulting protons can then be captured allowing the synthesis of proton rich isotopes up to mass number of $A \simeq 100$ (Fröhlich et al., 2006; Martinez-Pinedo et al., 2006). Since the evolution of this process depends upon ν-interactions with free nucleons, it is independent of the

initial star's metallicity, and is considered a primary process.

2.7.7.2 The γ-Process

Proton-rich isotopes beyond mass number $A \simeq 100$ are believed to be created by the γ-process, where successive photodisintegration events on pre-existing metals occur in the interior layers of supernovae (Woosley and Howard, 1978; Rayet et al., 1990). The target nuclei for such events are previously synthesized metals from the r- or s-processes. This process generally begins with (γ, n) reactions moving the target nuclei to the proton rich side of the stability line, where the rate of (γ, p) and (γ, α) start to dominate. Whereas all p-isotope abundances are relatively small and do not dominate their respective elemental abundances, they cannot be accounted for by s- or r-process production, and so both of the p-isotope production processes discussed are required to provide a complete galacto-chemical history.

2.8 Galactic Chemical Evolution

The metallicity-dependent isotopic scaling model discussed in Chapter 3 is similar to Galactic Chemical Evolution (GCE) models in a few ways. For example, both give the average isotopic ratios for the Galaxy as a function of metallicity. Note that there is some dispersion of abundances at any given metallicity — the Galaxy is not homogeneous or well-mixed. The *purpose* between our scaling model and GCE, however, is quite different, and some of the assumptions present in the scaling model, which are sufficient for generating stellar simulation inputs, would be inadequate for describing GCE. Therefore, it is important to give a brief overview of typical GCE models and concepts so that distinctions between them and our scaling model can be discussed.

The purpose of GCE is to describe the chemical history of galaxies using observations of stellar abundances in order to investigate earlier epochs in the Universe, to probe the mechanisms of galaxy formation, and to gain insight into stellar evolution by constraining the stellar yields. The chemical evolution of a system can be described by the following coupled equations (e.g., Tinsley, 1980; Pagel, 1997; Prantzos, 1998),

$$M_T = M_g + M_s, \tag{2.17}$$

$$\frac{dM_T}{dt} = F - E, \tag{2.18}$$

$$\frac{dM_s}{dt} = \psi - e, \tag{2.19}$$

$$\frac{dM_g}{dt} = F - E + e - \psi, \tag{2.20}$$

where M_T is the total mass of the system composed of gas (M_g) and stars (M_s), the rate of accretion and ejection of material from the the system is given by F and E, the ejection rate of matter from stars is given by e, and the star formation rate (by mass) is given by ψ. Equation 2.20 holds for each isotopic abundance i, and the rate of ejection from stars takes the form,

$$e_i = \int_{m_t}^{m_u} \psi(t - \tau(m)) \cdot \varphi(m) \cdot Y_i(m) dm, \tag{2.21}$$

where $\tau(m)$ is the lifetime of a star with mass m, the initial mass function (IMF) is given by $\varphi(m)$, and $Y_i(m)$ is the stellar yield of isotope i. The integral runs from the mass of the lightest star dying at time t to the upper limit of the IMF, the latter being effectively constrained by available yields (estimated or otherwise).

Typical GCE models integrate Equation 2.20 to obtain the isotopic abundances as a function of time for some model composition. In principle, one could begin with a BBN composition and numerically integrate Equation 2.20 across discrete time-steps, while also computing the star ejecta integrals over a reasonable mass range. The results would then depend on the resolution of both the time-steps and the grid of stellar model abundances used. Indeed, after each time-step, one should run stellar models with the present composition as the input, and then use the output stellar yields, Y_i, to run the next GCE step. These yields are functions not only of the initial stellar mass, but also the star's initial metallicity, which increases monotonically with Δt (Wheeler et al., 1989). Ideally, complete yields would be taken from stellar simulations, but in practice the number of simulations needed even for a subset of the mass range (such as focusing only on massive stars) across the all time-steps is prohibitive. Hence, many GCE models

interpolate between a manageable number of stellar models to estimate the yields at different metallicities and masses. Despite this approximation, models have found success in reproducing the solar abundance pattern (e.g., Timmes et al., 1995). Even successful models, however, address only a subset of the total stable isotopes and astrophysical processes that contribute to the chemical evolution. Not every astrophysical process (e.g., the *r*-process) or dynamics of the environment (e.g., the accretion functions) are well understood or known. Regardless of these difficulties, progress in GCE modeling has grown more sophisticated with the inclusion of realistic galactic dynamics, with recent attempts being made to incorporate hierarchical merger models (e.g., Calura and Menci, 2009).

In a sense, every stable isotope is on equal footing in GCE models. Whereas some contribute to the overall Galactic abundances more than others, describing the evolution of each is the salient purpose. Therefore, assumptions in the modeling process that neglect easily destroyed isotopes (e.g., ^{3}He or ^{6}Li) are unfavorable; one can argue that understanding the stellar processing of these isotopes is necessary to construct a complete picture. In comparison, calculating an isotopic abundance pattern for use as inputs into stellar models *can* more safely neglect these fragile isotopes, as they mostly will not survive stellar processing to impact the final yields, and do not largely affect stellar nucleosynthesis. In the following chapter, we address the details of our scaling model.

Chapter 3

Isotopic Scaling Model

3.1 Introduction and Motivation

Yields from stellar simulations depend on the initial isotopic composition of the star. For example, the initial composition is important during hydrostatic burning phases for neutron capture reactions on initial metals, affecting odd-z nuclei abundances. In massive stars the weak s-process yields are constrained by both the initial CNO abundance, which is responsible for providing a neutron source, and also the initial Fe abundance, which supplies the seeds for neutron capture (Pignatari et al., 2010). The initial Fe abundance is also important in intermediate and low-mass AGB stars for seeding the main s-process yields (Käppeler et al., 1989; Lattanzio and Lugaro, 2005; Käppeler et al., 2011b). The detailed stellar abundances affect the opacity of the star (e.g., Seaton, 1995), which in turn will affect the structure as well as mass and angular momentum loss, changing the late stellar evolution.

Initial isotopic abundances are also important in the ν-process (Section 2.4.2). This process is responsible for the synthesis of several p-isotopes through charged-particle reactions such as $^{180}\mathrm{Hf}\,(\nu_\mathrm{e},\mathrm{e}^-)^{180}\,\mathrm{Ta}$ and $^{138}\mathrm{Ba}\,(\nu_\mathrm{e},\mathrm{e}^-)^{138}\,\mathrm{La}$, as well as neutral current interactions such as $^{181}\mathrm{Ta}\,(\nu,\nu'\mathrm{n})^{180}\,\mathrm{Ta}$ and $^{139}\mathrm{La}\,(\nu,\nu'\mathrm{n})^{138}\,\mathrm{La}$. This process can also contribute to lighter isotopic production, examples of which include, $^{20}\mathrm{Ne}\,(\nu,\nu'\mathrm{n})^{19}\,\mathrm{F}$, $^{12}\mathrm{C}\,(\nu,\nu'\mathrm{p})^{11}\,\mathrm{B}$, $^{20}\mathrm{Ne}\,(\nu,\nu'\mathrm{p})^{19}\,\mathrm{Ne}\,(\beta^+)^{19}\,\mathrm{F}$, and $^{12}\mathrm{C}\,(\nu,\nu'\mathrm{n})^{11}\,\mathrm{C}(\beta^+)^{11}\mathrm{B}$. All parent nuclei involved in these lighter isotopic reactions are produced in a primary fashion in the star, hence understanding the initial metal composition is less important in these

cases. The heavy p-isotope production by this process, however, requires initial metals to seed the reactions, therefore the initial isotopic distribution does affect the resulting abundances for those cases.

Additionally, there are several reaction flows that synthesize p-isotopes from existing s- or r-process material in photo-disintegration (γ-process) events (Woosley and Howard, 1978). The isotope ^{204}Pb is entirely produced in the s-process, and can undergo several (γ, n) reactions to yield the unstable isotope, ^{196}Pb, which then β^+ decays to the p-isotope, ^{196}Hg. This p-isotope can also be made more directly by (γ, n) reactions from another s-process isotope, ^{198}Hg. Additionally, ^{196}Hg can be made from stable isotopes created both by the s- and r-process, ^{199}Hg and ^{200}Hg. The several origins for ^{196}Hg production illustrate the importance of knowing the initial abundances of all the potential parent isotopes, otherwise the final abundance for this p-isotope cannot be reliably calculated.

Other parent nuclei that make p-isotopes by (γ, n) reactions include, ^{182,183,184}W, ^{186,187,188}Os, and ^{192,194}Pt, which (through similar reactions) can yield the following p-isotopes, ^{180}W, ^{184}Os, and ^{190}Pt respectively. The situation becomes even more complicated, however, since once synthesized, ^{190}Pt can also make ^{184}Os by (γ, n) reactions followed by a β^+decay. Likewise, ^{184}Os can also synthesize ^{180}W in the same fashion. The conclusion is that not only are the initial abundances of the s- and r-process parent nuclei important, but also the initial p-isotope abundances themselves, without which one cannot hope to account for all the possible reactions that will affect the final abundance pattern once the γ-process terminates. Moreover, additional reaction chains are possible by introducing (γ, α) events accompanied with (γ, n) reactions, which can also produce p-isotopes such as ^{144}Sm from ^{152}Gd, for example (Woosley et al., 1990). Knowing the initial abundances of heavy isotopes is hence crucial for understanding γ-process abundances, which use s- and r-process isotopes, and sometimes *themselves*, as seeds (Rauscher et al., 2002; Arnould and Goriely, 2003). See Fig 3.1 for an example of photo-disintegration reactions.

Finally, knowing the initial stellar composition is important since some fraction of it is not processed and will return to the ISM unchanged, hence the final abundance pattern will directly inherit any poorly estimated initial abundances. This is complicated by the fact that, in many cases, what is made in the stars and what was there initially

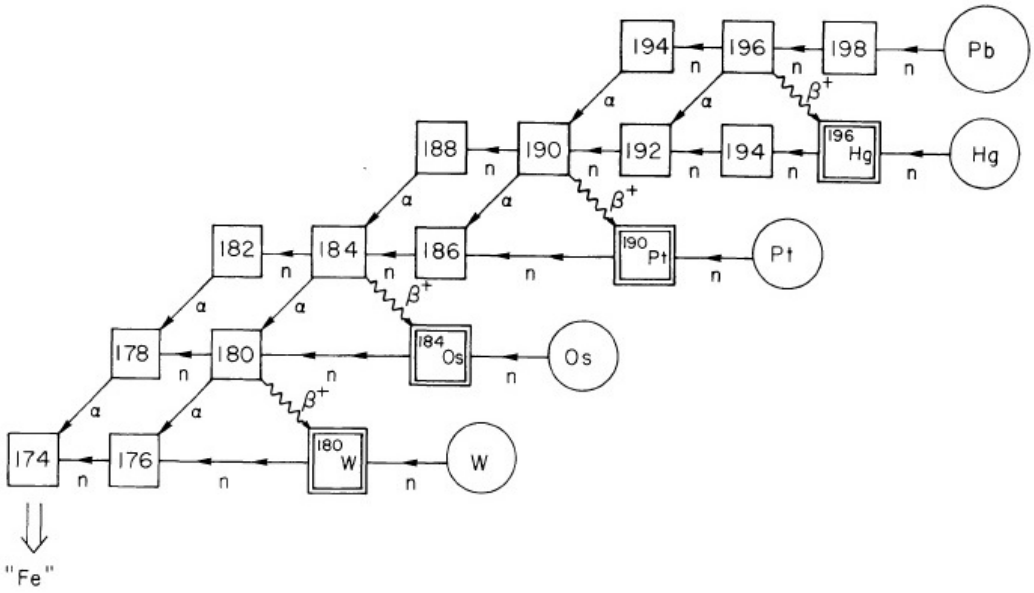

Figure 3.1: Example of photo-disintegration flows near heavy p-isotopes (*double squares*). The circles labeled with elemental symbols represent all the stable isotopes of that element. Arrows denote photo-neutron and photo-alpha reactions. The wavy arrows denote β^+ decay (taken from Woosley and Howard, 1978).

is difficult to disentangle.

Now it would be ideal to directly use stellar abundance observations to construct the initial isotopic abundance pattern for stellar simulations. Unfortunately, observations do not provide a complete elemental and isotopic history. Whereas elemental data does exist across a reasonable metallicity range for very abundant elements, it is scarce or absent for most rare elements. Spectroscopy currently does not give elemental abundances for all the elements for stars other than the Sun — except a few cases of light isotopes and some molecular lines. Even if complete elemental observations became possible, perhaps through improved instruments or observational techniques, one cannot simply

take the average values at some metallicity and use it to derive isotopic abundances, since it is unclear how to distribute elemental abundances into isotopic abundances at every metallicity. In general, isotopic ratios are not a constant function of metallicity.

The majority of isotopic data is limited to measurements from meteorites and solar spectroscopy, which gives us an abundance pattern for the solar system and Sun. Samples that would yield isotopic information at lower metallicities would necessarily originate from ouside the solar system, and are scarce on Earth. Instead, observers rely on very limited spectral isotopic information for isotopic abundances at lower metallicities. There are some isotopic measurements that are known, such as the $^{12}C/^{13}C$ and $^{6}Li/^{7}Li$ ratios (Shetrone et al., 1993; Prantzos, 2010a) or the $^{16}O/^{17}O$ ratio (Harris et al., 1988), but the aggregate is small. In most cases, the isotopic ratios are simply not known, and the few isotopic observations that do exist provide little information beyond the iron peak (except in the solar neighborhood).

Barring observations, the next choice is to employ galactic chemical evolution modeling to obtain the isotopic abundances to use for stellar simulation inputs. Modern GCE models typically split a model galaxy into one or more zones that require functional forms for infall and star formation rates (Timmes et al., 1995; Chiappini et al., 1997; Costa et al., 2009; Henry et al., 2010). Other processes such as ISM mixing, and galaxy mergers are often not addressed, although there have been fairly recent efforts to incorporate mergers in a hierarchical model (Tumlinson, 2006). The model galaxy is then typically evolved by integrating stellar yields over time, hence these models require nucleosynthesis yields from stellar simulations as inputs. The difficulty with this approach is that in order to provide self-consistent nucleosynthesis yields, the stellar simulations need a complete initial set of isotopic abundances, because nuclear reactions occur between isotopes, not elements.

Ideally, such a set would come directly from the GCE simulation itself. This would require knowledge of the complete set of stellar yields for the specific abundances of the GCE model at each time step and for each zone: the complicating factor is in reality composition is *not* just a function of metallicity, but also a function of environment, i.e., time and space. Instead, the inputs for the stellar simulations often use scaled solar abundances or the results of some other approximation. Furthermore, most GCE models usually evolve only a subset of the stable isotopes, such as just the iron peak

isotopes (Henry et al., 2010) or everything from hydrogen up to the iron peak (Timmes et al., 1995; Kobayashi et al., 2006), or only elements. An approach different than GCE modeling to describe chemical abundances has been done recently by Ting et al. (2012). They perform a principle component analysis on elemental data that takes correlations among elemental ratios and roughly delineates different processes responsible for these correlations, as well as identify likely sites and metallicity regimes congruent with them. These efforts offer verification of the established paradigm concerning many astrophysical processes, and may help constrain others whose properties are not completely known. In contrast to this principle component analysis, our model could be interpreted as a "physical component analysis."

The approach taken here is complementary to traditional GCE methods, however, one must take care not to confuse our model with a proper GCE model. We construct an astrophysical model of all stable isotopes, based on physical principles for the production sites and mechanisms. Effectively, we scale isotopic abundances as a function of a chosen model parameter. This isotopic model is then mapped to an elemental model by summing the isotopic abundances to their respective elements. Next, we fit the elemental abundances against available observational data to obtain numerical values for the free parameters of the model. Our completed model then gives the average *isotopic* history of the Galaxy, subject to the approximations employed. The benefit of this approach is that it is not necessary to know or model dynamic and galactic evolution processes employed in traditional GCE models such as infall, ISM mixing, and galaxy mergers, whose uncertainties are poorly constrained.

Compared to full GCE calculations our approach is rather simplistic and approximate, precisely because we do not integrate stellar yields or address dynamic and galactic evolution processes employed in traditional GCE models, and we assume a unique and *typical* abundance distribution for a given metallicity rather than allowing for a spread in distribution as found in nature. The intention here is to improve upon the typical standard of scaling isotopic solar abundances by a constant factor, which effectively treats all isotopic production as primary. Our improvements to this standard is to incorporate secondary processes and Type Ia contributions with separate scalings, to better approximate their relative values at desired input metallicities for nucleosynthesis studies, and the resulting isotopic histories from our model can be used both as inputs

in stellar models, and for comparison to abundances from other sources like damped Lyman-α systems and dwarf galaxies. This model is an improvement over the previous standard of guessing *ad-hoc* assumptions for the interpolation between the known endpoints of solar and BBN, or the use of scaled solar abundances. This could also be seen as a first iteration step for more sophisticated first principle GCE models, but at a higher order approximation than just scaled solar abundances, but not a replacement for them. Hence, whereas the approximations and comparisons of our model are sufficient for this purpose, they would be quite unsatisfactory for describing GCE itself.

The first task is to evaluate the contribution from each astrophysical process to the isotopic solar abundance pattern, which is explained in Section 3.2. In Section 3.3, the model itself is introduced and the scaling of the processes as a function of our parametrization is given, using the relative solar contributions and the BBN abundance pattern as fixed boundary conditions. This also defines the relevant free parameters for fitting the elemental abundances to stellar data. In Section 3.4, the elemental model is fit to available data and the best fit parameter values are found. In Section 3.5, the resulting elemental model is discussed along with additional results given by the isotopic model. Section 3.6 addresses the constraints of the model and discusses possible extensions for future work.

3.2 Solar Abundance Decomposition

This model attempts to cover the essential key astrophysical processes responsible for the production of the isotopes in the Galaxy (discussed in Chapter 2). First, these processes are used to decompose the solar system abundances. The isotopic solar abundance pattern was taken from a new data set by Lodders (2010) which gives updated values relative to their 2003 publication (Lodders, 2003). In the following, the decomposition is explained, and the processes are organized roughly by the mass range of isotopes to which they contribute.

3.2.1 Big-Bang Nucleosynthesis

A theoretical BBN abundance pattern from Cyburt et al. (2001) and provided by Fie (2002) was used for the zero metallicity boundary condition. Isotopic contributions from

this BBN pattern are taken for ^{1}H, ^{2}H, ^{3}He, ^{4}He, and ^{7}Li. The remaining negligible contributions of ^{6}Li and the isotopes heavier than ^{7}Li were not used. A constant ^{7}Li abundance at low metallicities has been observed that suggests a primordial abundance, but whose value is much smaller than the predicted BBN abundance (Spite and Spite, 1982). This "Spite plateau" is still a mystery (Cyburt et al., 2008; see also for recent efforts: Meléndez et al., 2010a,b,c), hence the present model uses the theoretical BBN abundance for ^{7}Li.

3.2.2 Light Isotopes

The remaining helium not made during BBN is a product of hydrogen burning and is assigned to evolve as a primary process. The "release time scale" of helium can vary depending on the stellar mass, and relative to metallicity it may evolve slightly slower than a true primary process (the same is true for C and N). This delay is not accounted for in the present work.

This model addresses the primary "light" ν-process but does not distinguish between the "heavy" ν-process and γ-process contributions, since the latter two both contribute to isotopes in a similar mass range and with a similar metallicity dependence. Hereafter, the ν-process shall stand for the "light" ν-process, and the γ-process includes the "heavy" ν-process contributions. This model does, however, distinguish between primary and secondary GCR spallation events.

Identifying the precise (non-BBN) Li, Be, and B contributions presents a challenge. At present, there is no consensus for explaining the solar abundance pattern for the isotopes of these elements using the processes that could be responsible. Due to the difficulty in determining what fraction each actually contributes to the light isotope solar abundance pattern, novae, the ν-process, and primary GCR spallation are placed into a single category due to their shared primary nature, hence we scale the abundances from these processes identically. Standard GCR spallation is treated separately since it is secondary. The relative solar abundance decomposition between novae/ν-process/primary GCR spallation and secondary GCR spallation for ^{6,7}Li, ^{9}Be, and ^{10,11}B is estimated from Prantzos (2012). Both Li isotopes are given $\approx 30\,\%$ secondary contributions, and the ^{9}Be, and ^{10,11}B isotopes are given $25\,\%$ secondary contributions. The remaining non-BBN contributions for all LiBeB isotopes are assigned the novae/ν-process/primary

GCR spallation category. Note the decomposition for these light isotopes are *at best* known to within $\approx 5\,\%$ (Pra, 2013).

The onset delay of classical novae is not addressed in this model. Novae contributions beyond ^{7}Li are taken to be negligible compared to massive star contributions. This approximation holds well for CNO isotopes that have large contributions from massive stars, but for isotopes such as ^{19}F the approximation is less than ideal. In fact, it believed that ^{19}F may also be produced by the ν-process in CCSNe (Woosley and Haxton, 1988), during hydrostatic nucleosynthesis in He shell of thermally pulsating AGB stars (Forestini et al., 1992), and in the He core of heavy mass loss Wolf-Rayet stars (Meynet and Arnould, 2000). The decomposition from these sources is still a matter of debate (Abia et al., 2010, and references therein), and this complication is beyond the scope of the current model.

3.2.3 Low and Intermediate-Mass Stars

Stellar winds from low and intermediate-mass stars are rich in C and N isotopes (Arnould et al., 2003), and provide significant contributions to the solar abundances for these isotopes. As previously mentioned in Chapter 2, fitting the contributions from these sources to data is problematic, since contamination from massive stars is always present and difficult to separate. This model does not independently address stellar wind contributions and instead combines them with contributions from massive stars, both of which are primary processes.

3.2.4 Intermediate-Mass and Iron Group Isotopes

Decomposing the abundances in the intermediate-mass range involves fitting contributions from massive stars and Type Ia SNe. Yields for Type Ia supernovae were taken from the W7 model (Nomoto et al., 1997) for isotopes with mass numbers $12 \leq A \leq 56$. The category of "massive star contributions" is defined in this context to be the collection of all primary isotopic production with mass numbers $12 \leq A \leq 68$ not attributed to Type Ia SNe. This includes all isotopic enrichment to the ISM driven by massive star stellar winds and production from CCSNe, the r-process, the ν-process, novae yields, and stellar winds from low and intermediate-mass stars, with production from CCSNe

dominating the isotopic abundances in this category. The solar contributions from massive stars were taken from the yields of a Population III (PopIII; stars that have a BBN initial composition) massive star simulation (Heger and Woosley, 2010) fitted to stars in the range $-3.1 \leq [\mathrm{Fe/H}] \leq -2.9$ taken from the Frebel data set (Frebel, 2010). We use the common definition: $[\mathrm{X}] \equiv \mathrm{Log}(\mathrm{X}/\mathrm{X}_{\odot})$. Note that the "iron metallicity" (relative to solar), [Fe/H], should be distinguished from the "total metallicity", [Z]: The former is a conventional proxy for the latter. The simulation included stars in the mass range $10 - 100\,\mathrm{M}_{\odot}$, with a Salpeter initial mass function (IMF) and a low mixing of 0.02512 (Joggerst et al., 2008) employed in a running boxcar method (Heger and Woosley, 2010). The explosion energy of the supernovae was set to be $E = 1.2\,\mathrm{B}$, where $1\,\mathrm{B} = 10^{51}\,\mathrm{erg}$.

The fit of the yields to the Frebel (2010) data set gave a χ value of 2.218 (for fitting procedure see, Heger and Woosley, 2010), and is shown in Fig 3.2. Many elements are fitted to within their uncertainties, however, exceptions include N and Al, which have fits over two standard deviations away from the data. Whereas it would be ideal to fit all elements of interest to within their uncertainties, these results will later be subject to scalings (discussed below), which are needed to fit to the solar abundances, and will thus change to some degree anyway. We are confident that our effort here is reasonable, given the extensive mass range of models considered and large data compilation used, but acknowledge that future improvements are possible. The heavier massive star contributions for mass numbers $57 \leq A \leq 68$ were not taken from the PopIII simulation (Heger and Woosley, 2010), and were instead calculated as residuals from the main and weak *s*-processes, discussed below in Section 3.2.5.

Under the assumption that Type Ia are responsible for some fraction f of the observed solar ^{56}Fe abundance, each W7 yield was scaled by this factor: $f \cdot X_{56}^{\odot}/X_{56}^{Ia}$, where $X_{56}^{\odot}$ is the solar abundance of ^{56}Fe, and X_{56}^{Ia} is the W7 yield for ^{56}Fe. This shifts the entire Type Ia SNe abundance pattern (preserving ratios) until the yield for ^{56}Fe is equal to $f \cdot X_{56}^{\odot}$. The fraction f represents a free parameter in the model, which is determined by fitting the elemental scalings against available data (in Section 3.4). The massive star yields were scaled to the remaining contribution to solar ^{56}Fe not accounted for by Type Ia. This factor is given as: $(1 - f) \cdot X_{56}^{\odot}/X_{56}^{\mathrm{massive}}$, where $X_{56}^{\mathrm{massive}}$ is the massive star yield for ^{56}Fe.

An additional scaling of both types of SNe data in the range $12 \leq A \leq 56$ was then

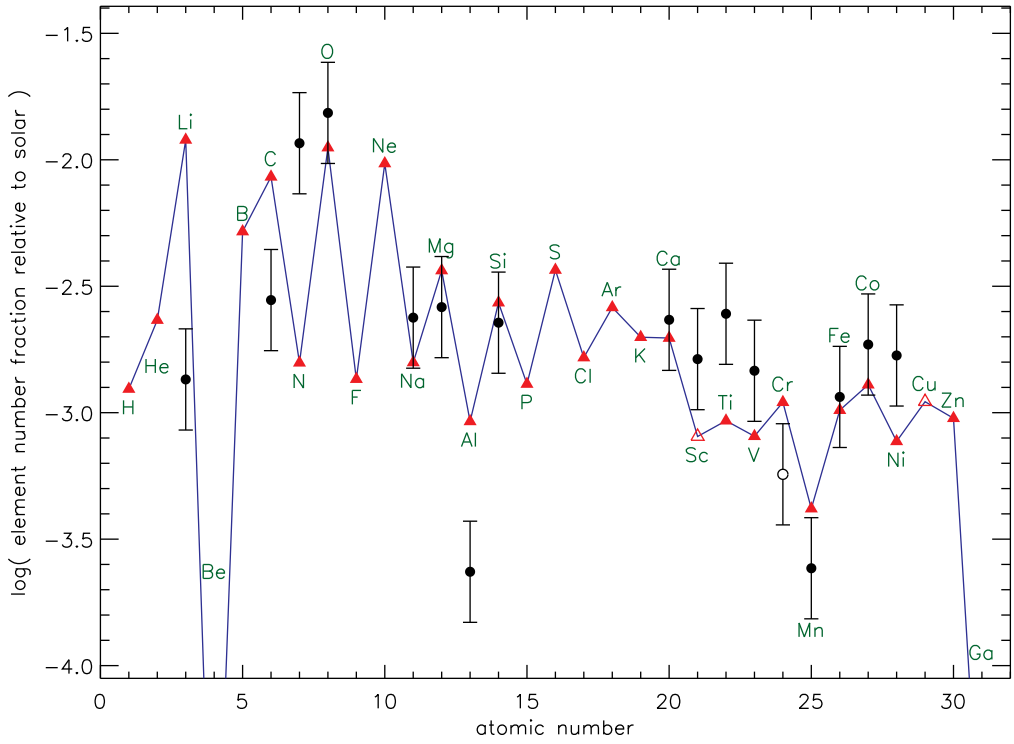

Figure 3.2: The fits of the CCSNe yields from Heger and Woosley (2010) to the Frebel (2010) data set. *Circles*: the elemental averaged data values with uncertainties. *Triangles*: the fit values from the massive star simulation. *Hollow Circles*: elemental data ignored in the fit. *Hollow Triangles*: elements fitted only to the data as upper bounds.

required to ensure that the massive star and Type Ia contributions summed to the solar abundance for every isotope, since the first scaling using f would only guarantee that ^{56}Fe satisfied this requirement. This additional scaling preserved the ratio of each isotopic contribution between the W7 and massive star yields,

$$X_{i,\mathrm{f}}^{\mathrm{massive}} = \left(\frac{X_i^{\odot}}{X_{i,0}^{\mathrm{massive}} + X_{i,0}^{\mathrm{Ia}}} \right) X_{i,0}^{\mathrm{massive}}, \tag{3.1}$$

$$X_{i,\mathrm{f}}^{\mathrm{Ia}} = \left(\frac{X_i^{\odot}}{X_{i,0}^{\mathrm{massive}} + X_{i,0}^{\mathrm{Ia}}} \right) X_{i,0}^{\mathrm{Ia}}, \tag{3.2}$$

where $X_{i,0}$, $X_{i,\mathrm{f}}$ are the original and (scaled) fitted abundances of isotope i, for either the massive or Type Ia contributions (identified with superscripts), and $X_i^{\odot}$ is the solar abundance of isotope i. For clarity of presentation, this procedure has been explained using two successive scalings, but in practice this can be done with a single scaling that achieves both. This second scaling preserves the isotopic ratios *across* each model, but the ratios *within* each model undergo some distortion. That is, the overall abundance patterns of the W7 and massive star simulations are altered. Nevertheless, the final abundance patterns we use still show Type Ia contributing mostly to the Fe peak, and massive stars contributing to CNO and α-elements up to the Fe peak. The abundance patterns from both sets of SNe data before and after scalings are shown in Figs. 3.3 and 3.4. As discussed in Section 2.6.4, there are different possible Type Ia progenitor scenarios, which may produce yields quite different than the W7 model used here. Due to the uncertainties in the status of Type Ia progenitors, we do not presently attempt to account for this, and revisions are left for future work.

The use of the solar metallicity W7 model is approximate. In our Galaxy, large contributions to the SN Ia yields may come from sub-solar progenitors. The exact nature and properties of these sources, however, are still uncertain (e.g., Timmes et al., 2003; Bours et al., 2013), and given these uncertainties, the inclusion of the W7 yields, while not a complete description, is also not unreasonable. To investigate the impact of this approximation, we also computed the solar abundance decomposition for the massive stars and Type Ia using a composition between that of the W7 and W70 (zero metallicity) models to estimate a sub-solar composition. We then compared the ratios of the isotopes between ^{12}C and ^{56}Fe from our original decomposition to this new one. Of the 53 isotopes in this range, 45 have ratios of the new abundance (W70) over the old abundance (W7) that are within 2.0. Of the 8 that remain, the largest differences are ^{40}K, which now has a nonzero abundance, and ^{15}N, ^{41}K, ^{43}Ca, and ^{47}Ti, which have ratios of $\approx$300, 15, 40, and 20, respectively (the others have ratios within 5). This does present non-trivial corrections to the solar abundance decomposition, but except for a few isotopes, the changes are quite minor (within a factor of 2). It is unlikely that these changes would noticeably impact the fittings to data we perform later.

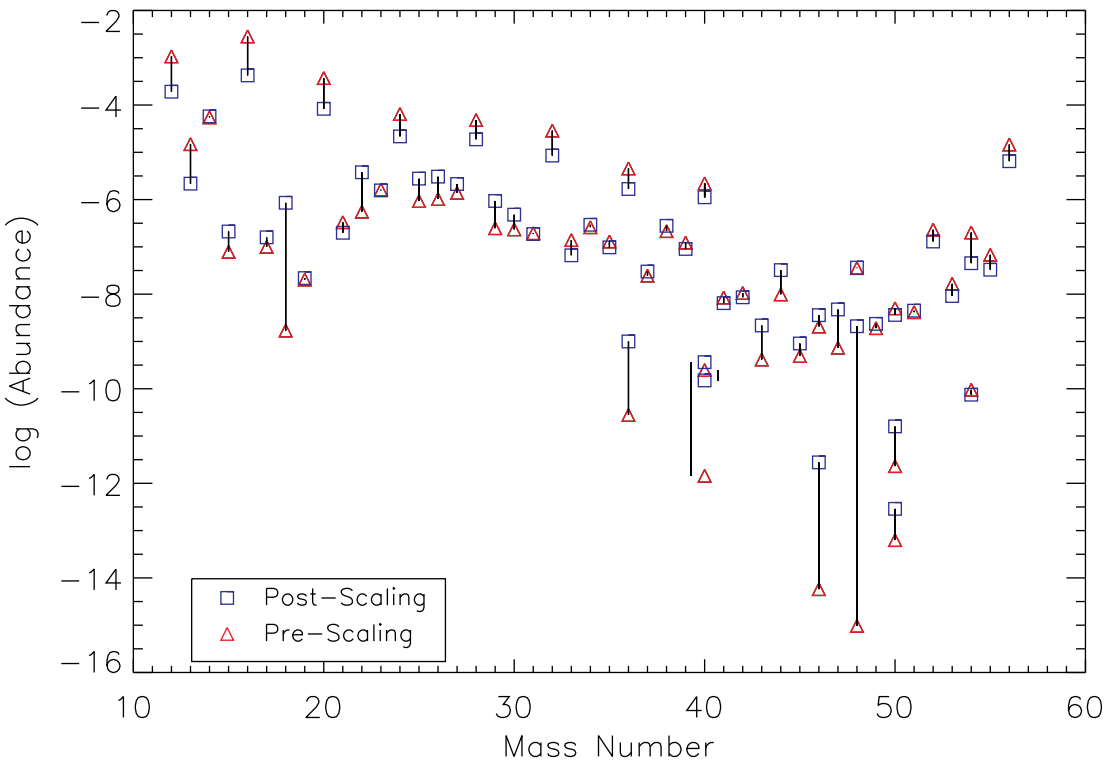

Figure 3.3: The CCSNe yields from Heger and Woosley (2010) fitted to Frebel (2010), and scaled to a nominal value of $(^{56}\mathrm{Fe}_{\mathrm{massive}}/^{56}\mathrm{Fe}_{\odot}) = 0.3$. Shown are the yields before (*Triangles*) and after (*Squares*) fitting with the W7 data.

3.2.5 Heavy Isotopes

3.2.5.1 Weak *s*-Process

Modeling the weak *s*-process has been less successful than models for the main component (Pignatari et al., 2010). Since flow equilibrium is not reached during the neutron exposure, uncertainties in the neutron capture cross-sections affect the yields of all subsequent isotopes (Heil et al., 2007). We need to reproduce the solar system abundances of the *s*-only isotopes for both the main and weak components. The weak *s*-process has 6 *s*-only isotopes, ^{70}Ge, ^{76}Se, ^{80}Kr, ^{82}Kr, ^{86}Sr, and ^{87}Sr that owe their solar abundances to *both* the main and weak components (Raiteri et al., 1993), and the relative

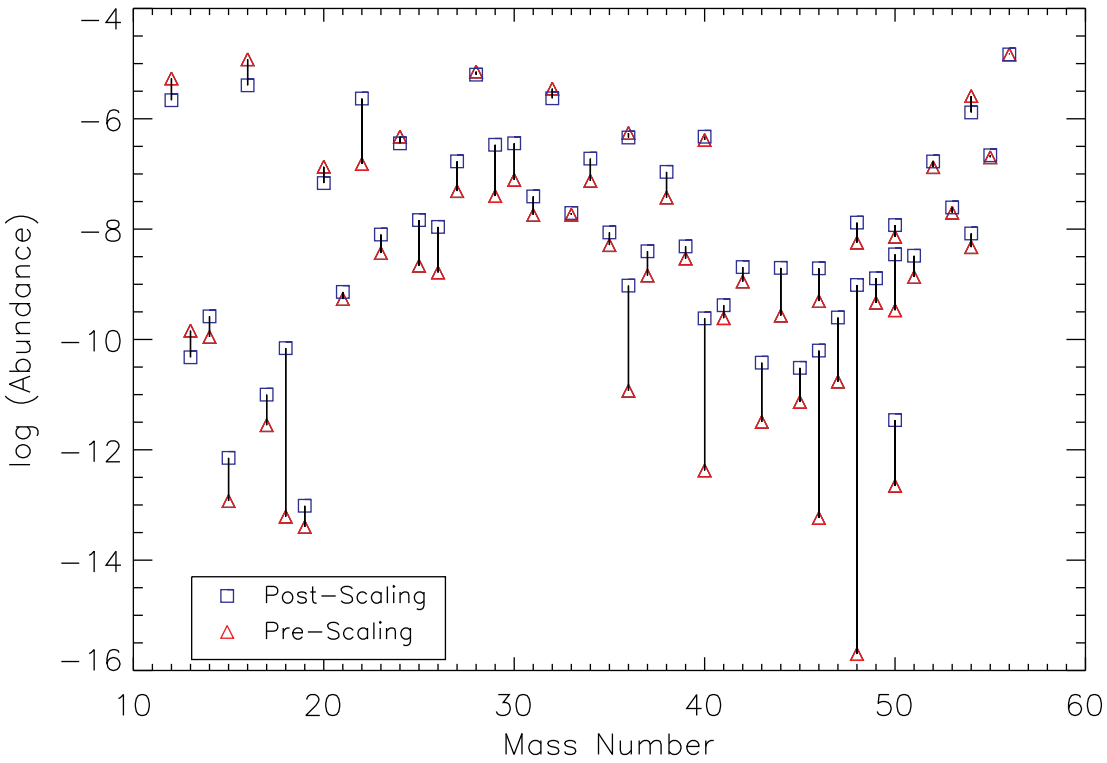

Figure 3.4: The Type Ia SNe yields from Nomoto et al. (1997), scaled to a nominal value of $(^{56}\mathrm{Fe}_{\mathrm{Ia}}/^{56}\mathrm{Fe}_{\odot}) = 0.7$. Shown are the yields before (*Triangles*) and after (*Squares*) fitting with the CCSNe data.

contributions from each represent a poorly known *a priori* constraint. Additionally, recent stellar model calculations for the weak *s*-process have difficulties in both producing sufficient *s*-only isotopic yields without at the same time overproducing many other isotopes beyond their solar abundances (Pignatari et al., 2010).

For the purposes of making a reasonable assessment of the weak *s*-process contributions to the solar system abundances, a calculation is performed using the updated online Maxwellian-averaged cross-sections (MACs) compilation from the KADoNIS project (`www.kadonis.org`, Dillmann et al., 2009). The branching points addressed in the calculation that lie along the weak *s*-process path are the unstable nuclei ^{64}Cu and ^{80}Br,

with corresponding β^+ and β^- thermal branching ratios that were taken from Takahashi and Yokoi (1987). The branching point at ^{79}Se was ignored, and was taken by β^- decay to ^{79}Br prior to any neutron capture (which would give a ^{80}Se population). This approximation is due to the high temperature dependence of the β^- decay rate of ^{79}Se (Walter et al., 1986; Heil et al., 2008; Makinaga et al., 2009). The isotope ^{93}Zr was treated as stable for this calculation, since the thermal β^- decay branching ratio is small relative to neutron capture rate (Takahashi and Yokoi, 1987). After the neutron exposure ended, the remaining ^{93}Zr abundance was taken to ^{93}Nb. The ^{85}Rb branching was omitted and it was assumed to entirely β^- decay to ^{86}Sr, again because the neutron capture branching ratio is negligible (Takahashi and Yokoi, 1987).

The differential equations for the weak *s*-process abundances under the classical approximation (Käppeler et al., 2011b) were solved numerically. The set of differential equations (see, Equation 2.12) can be written in vector form as,

$$\frac{\mathrm{d}\mathbf{X}}{\mathrm{d}\tau} = \mathrm{A} \cdot \mathbf{X}, \tag{3.3}$$

where $\mathbf{X}$ is a vector of the isotopic abundances, $\mathbf{X} = (X_{\mathrm{Fe56}}, X_{\mathrm{Fe57}}, \ldots, X_{\mathrm{Ru101}})$, τ is the neutron exposure, and A is the matrix of Maxwellian-averaged neutron capture cross-sections and branching ratios for beta decay, with components $\mathrm{A}_{ij} = -\sigma_i$ for $i = j$, with $\mathrm{A}_{i,j-1} = +\sigma_i$, $\mathrm{A}_{i+1,j} = \sigma_i\beta_i$, and $\mathrm{A}_{i+2,j} = \sigma_i(1-\beta_i)$, where β_i is the beta decay branching ratio for isotope i at branching points (where applicable). Note $(1-\beta_i)$ is the β^+ branching ratio, and all other elements in the sparse matrix A are zero.

In solving this system, a continuous neutron exposure distribution was not assumed. Instead, different values for single exposures were used. A linear combination of the yields from different single neutron exposures was sought that best fits the abundances of the *s*-only isotopes in the weak *s*-process range. In addition, to ensure that the sum of *s*-only isotopes for the weak and main components were not overproduced with respect to solar, the abundances to which the *s*-only isotopes were fit were taken as the residuals of the main s-process yields subtracted from the solar abundances. In addition, 15 % of the solar ^{80}Kr and 3 % of the solar ^{82}Kr were attributed to the νp-process (Käppeler et al., 1989; Pignatari et al., 2010) and likewise subtracted.

We found linear combination of five neutron exposures that reproduces the desired

s-only isotopic abundance residuals for ^{70}Ge, ^{80}Kr, and ^{86}Sr. The resulting abundances are shown in Fig. 3.5. The remaining *s*-only isotopes, ^{76}Se, ^{82}Kr, and ^{87}Sr were under-produced. The only resulting overproductions were for ^{65}Cu and ^{89}Y. The neutron exposures were found to be: $0.2, 0.25, 0.3, 0.35,$ and $0.4\,\mathrm{mb}^{-1}$. The respective coefficients the abundances from each of these exposures were weighted by were: $1.5, 0.2, 0.4, 0.6,$ and 0.7. The attempt here was to fit as many *s*-only isotopes to their residuals without generating overproductions, and using the numerical prescription employed, it was not possible to fit all *s*-only isotopes without causing additional isotopic over-abundances. The overproductions of ^{65}Cu and ^{89}Y as well as the underproductions of ^{76}Se, ^{82}Kr, and ^{87}Sr were scaled with the main *s*-process abundances, to fit with the solar abundances. This scaling was equivalent to the scaling done for massive stars and Type Ia yields: the isotopic ratios were preserved.

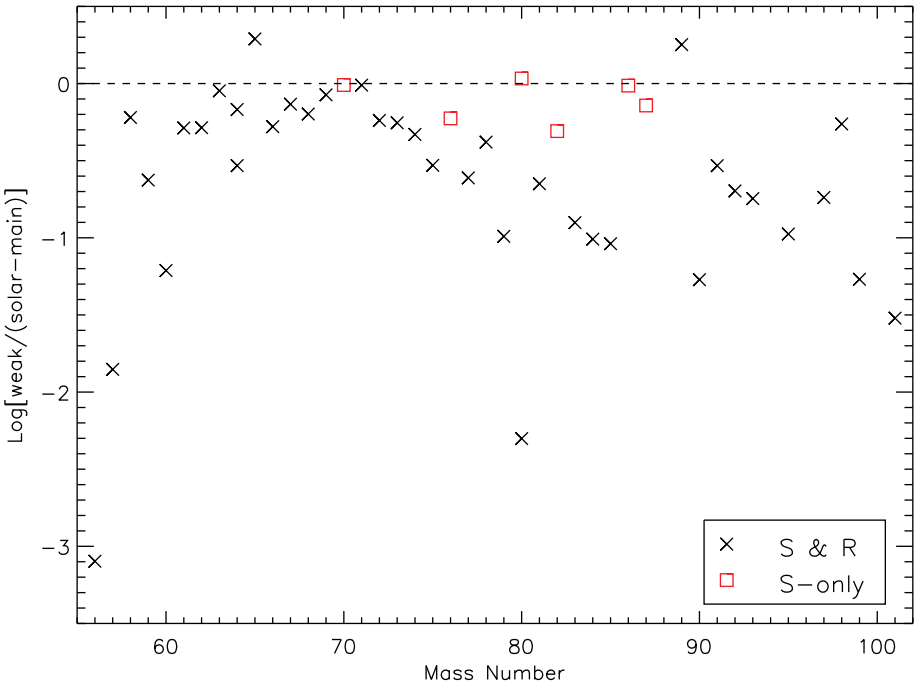

Figure 3.5: The calculated weak *s*-process contributions to the solar abundance pattern. *Red boxes*: *s*-only isotopes. *Black* ×*'s*: isotopes with contributions from the *r*- and *s*-processes. The yields for the *s*-only isotopes ^{70}Ge, ^{80}Kr, and ^{86}Sr are reproduced well, with underproductions for ^{76}Se, ^{82}Kr, and ^{87}Sr. The only overproductions were for the non *s*-only isotopes ^{65}Cu and ^{89}Y.

In addition to producing isotopes along the path of stability, there is indication that the weak s-process component in massive stars is responsible for seeding a non-negligible p-isotopic production component. The massive star yields from Rauscher et al. (2002) show significant isotopic productions for ^{74}Se, ^{78}Kr, and ^{84}Sr, which cannot be accounted for by the νp-process (since their stellar models include weak s-process and γ-process reactions, but do not include the νp-process). A possible mechanism for producing these p-isotopes are γ-process reactions on weak s-process seeds, where the weak s-process would enhance the abundances of unstable proton-rich isotopes, which would then undergo photo-distintegration events to give stable p-isotopes. The scaling of these p-isotopic yields should thus track the weak s-process, rather than the traditional γ-process (as far as its dependence on metallicity), since the abundances are made *in situ* from existing weak s-process seeds. It is unclear exactly how much this weak s-process enhanced p-process (WSEP) should contribute to the solar ^{74}Se, ^{78}Kr, and ^{84}Sr abundances. It was decided to attribute half of the solar abundances to each the WSEP isotopes and the νp-process for these three p-isotopes.

The uncertainties in our calculation are constrained by the errors of the MACs given in the compilation from the KADoNIS project (Dillmann et al., 2009), and vary by isotope. These uncertainties were not propagated through the equations, since the treatment of the weak s-process is only approximate.

3.2.5.2 Main *s*-Process

The main s-process contributions to the solar abundance pattern were taken from Bis (2011), and these yields were re-normalized to the Lodders (2010) abundances. Many of the s-isotopes with mass numbers $A \geq 88$ were consistent with their solar values, however, some were under-produced. The s-only isotopes under-produced by less than 0.1 dex below their solar abundance were considered to be within acceptable limits, given uncertainties in modeling, observations, etc., and were re-assigned to be their nominal solar values. This cutoff at 0.1 dex is admittedly somewhat arbitrary. The uncertainties in neutron capture cross-sections and modeling of the AGB stars introduces error, yet remarkably so many s-only isotopes are reproduced by Bis (2011) to within 25% ($\simeq$ 0.1 dex) of their solar values. This choice of cutoff value acknowledges the existence of errors that are often difficult to enumerate, while assuming that since so many s-only

isotopes are reproduced close to their solar values, the model is likely reliable.

The resulting abundance pattern is given in Fig. 3.6. Below a mass number of $A = 88$, the *s*-only isotopes show an explicit drop in their production, and the weak *s*-process has to contribute in this region to reproduce the needed solar abundances. For mass numbers above $A = 88$, three *s*-only isotopes are under-produced by more than 0.1 dex (Bis, 2011): ^{152}Gd, ^{187}Os, and ^{192}Pt. The residual abundances of these three isotopes are attributed to the γ-process. This treatment of the residuals is very approximate, and while ^{152}Gd and ^{192}Pt lie on the proton-rich side of the stability line, ^{187}Os is preceded by the more proton rich ^{184}Os and ^{186}Os, both of which would be more likely candidates for γ-process enrichment. The contribution of ^{152}Gd to elemental Gd is only $\sim$0.2 %, hence relatively little γ-process enrichment is needed to populate the residual abundance. The isotope ^{192}Pt contributes $\sim$0.79 % to elemental Pt, however, the *p*-isotope ^{190}Pt contributes even less at $\sim$0.01 %, so it is unlikely that a residual abundance from the γ-process would populate the needed $\sim$0.7 % ^{192}Pt without also raising the abundance of the more rare ^{190}Pt.

Since the main *s*-process produces three characteristic peaks at closed neutron shells, the abundances were divided into *ls*, *hs*, and "strong" components. The *ls* component was taken to be all abundances from Fig. 3 up to and including Sr, the *hs* component was taken to be all abundances after Sr and up to Pb. The strong component was assigned to Pb and Bi isotopes. Using the solar main *s*-process abundances given in Fig. 3.6 as a starting point, we scaled the *ls*, *hs*, and "strong" components separately due to the different neutron exposures required for their production.

We shall continue to refer to Pb and Bi *s*-process contributions as coming from the "strong" component, since they are evolved distinctly from the *hs* and *ls* parts of the main *s*-process, but it should be noted this is a convention introduced for clarity, and the strong *s*-process is indeed the low metallicity regime of the main *s*-process, having a distinctly stronger neutron-to-seed ratio.

3.2.5.3 *r*-Process

The *r*-process solar abundance contributions were determined using the residual method, in the mass range $69 \leq A \leq 238$. This method is often used since *s*-process modeling is more successful. Essentially, all solar abundances not accounted for by the *s*-process

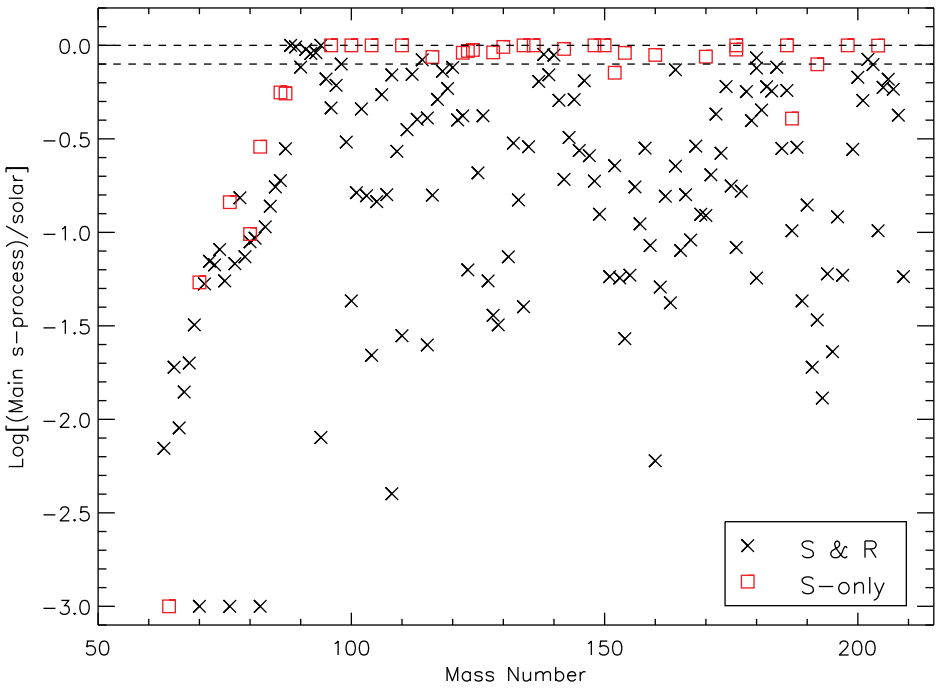

Figure 3.6: Adopted main s-process abundances from Bis, 2011, relative to the solar abundance pattern. *Red Boxes*: s-only isotopes. *Black* $\times$*'s*: isotopes with contributions from the r- and s-processes. Under-produced s-only isotopes that fell within 0.1 dex (*dashed line*) below their solar abundance were assumed to be their nominal solar values.

are allocated to the r-process, for the isotopes whose origins are from both,

$$X_{i,\mathrm{r}} = X_{i,\odot} - X_{i,\mathrm{s}}, \tag{3.4}$$

where $X_{i,\mathrm{r}}$ is the r-process abundance of isotope i, and similarly for the s-process and solar abundance. As previously stated, the r-process contributions in the lower mass range $56 \leq A \leq 68$ were *not* differentiated from the "massive star category." This choice was made to facilitate the decomposition of the solar abundance pattern in this range, where both CCSNe yields (from α-rich freeze-out, the α-process, and previous nuclear burning) and r-process yields contribute to abundances as primary processes, and are difficult to parse.

3.2.5.4 *p*-Isotopes

Similar to the main and weak components of the *s*-process, there is an expected transition region between the νp-process and γ-process. A calculation of νp-process yields for a 15 $M_\odot$ star was performed by Thielemann et al. (2010). Their results show sufficient production of Mo and Ru isotopes relative to their solar abundances, which is much needed due to well known deficiencies in the γ-process production of these isotopes. From their results, the νp-process yields are shown to decrease quite rapidly beyond mass number $A = 100$. This suggests that the region of overlap is fairly abrupt, with only ^{102}Pd beyond a peak at ^{98}Ru owing a non-negligible fraction of its abundance to the γ-process.

A more complete analysis perhaps using a grid of stellar masses, in order to determine the distribution in the transition region, would likely offer only minor corrections to the final elemental scalings. The complete isotopic decomposition for the solar abundance pattern is shown in Table B.2 of Appendix B and can be used for future isotopic reference. Charts for all stable isotopes, showing the contributions from all astrophysical processes considered, is given in Appendix C.

3.3 Model Description

Our simple model tries to describe a typical average galactic composition, where the initial state is a homogeneous BBN composition. The final state is taken as a homogeneous composition equivalent to the isotopic solar abundance pattern. Each process responsible for isotopic production (and depletion for the case of D and ^{3}He) is assumed to enrich (deplete) our model galaxy under the instantaneous mixing approximation, to preserve homogeneity across the entire metallicity range considered. Each isotope from our decomposition of the solar abundance pattern is scaled as a function of a chosen normalized dimensionless parameter ξ. At ξ=0 the galaxy is in the BBN composition, and at ξ=1 the galaxy has the solar composition. The benefit of this choice of parametrization is that its range is congruent with the total metallicity (relative to solar), $Z/Z_\odot$. A comparison between ξ and $Z/Z_\odot$ is shown in Section 3.5. This choice of parameter motivates choosing functional forms for the scalings of each process by addressing the predicted dependence on total metallicity these processes would obey.

Note that this comparison should not be interpreted as a physical condition imposed upon this parameter. Indeed the parameter ξ is not a physical quantity, rather it is a technical parameter that takes continuous values in the approximate range [0,3] (our range extends beyond solar metallicities), and is chosen to closely approximate Z for ease of discussion. Hence, we assume the relation between ξ and $Z/Z_{\odot}$ to be $\log(\xi) \approx [Z]$. This ansatz is checked later in Section 3.5.

The parametrization of our model is an attempt to scale the isotopic abundances characterized by typical trends in our Galaxy. For consistency we do not directly use metallicity as the argument of the scaling functions; indeed metallicity is an output of the model, and hence cannot be used as an input. In practice, normalized metallicity $Z/Z_{\odot}$ tracks ξ, see Fig. 3.15, with deviations less than 0.4 dex for $\log(\xi) \geq -3$. Whereas our model is not a traditional GCE model that uses scaled stellar yields, our parametrization allows us to improve upon the standard of scaling solar abundances by a constant factor, for use in nucleosynthesis studies. In the following we address the functional form for each process described in Section 3.2.

3.3.1 Massive Stars

The results of massive star simulations for Population III stars (discussed previously in Section 3.2.4), in addition to being used to compute the solar abundance decomposition, are also used to model the isotopic abundance pattern for $12 \leq A \leq 68$ at a low metallicity of $[\mathrm{Fe/H}] = -3$. The abundances from this simulation were normalized to the ^{56}Fe abundance at $[\mathrm{Fe/H}] = -3$, under assumption that Type Ia contributions to ^{56}Fe are negligible at this metallicity, hence each abundance was multiplied by the factor, $^{56}\mathrm{Fe}_{\odot}/X_i^{\mathrm{sim}}$, where X_i^{sim} is the abundance of isotope i from the PopIII simulation. These normalized abundances represent a third fixed point for the massive star isotope abundances (in addition to the solar abundances and BBN abundances). Then the massive abundances were interpolated linearly in log-space between their solar values (found in Section 3.2.4) and their respective abundances given by the normalized PopIII simulation. That is, for each isotope the abundances were scaled according to,

$$\log\left(X_i^*\left(\xi\right)\right) = m_i\left(\log\left(\xi\right) - \log\left(\xi_{\mathrm{low}}\right)\right) + \log\left(X_i^{\mathrm{sim}}\right), \tag{3.5}$$

where $X_i^*(\xi)$ is the massive abundance of isotope i as a function of the model parameter, and $\log(\xi_{\rm low}) = -2.5$ (corresponding to a metallicity of [Fe/H] $= -3$). The slope is defined as, $m_i \equiv \left(\log\left(X_{i,f}^{\rm massive}\right) - \log\left(X_i^{\rm sim}\right)\right) / \left(\log(\xi_\odot) - \log(\xi_{low})\right)$, where $X_{i,f}^{\rm massive}$ is the massive star contribution to the solar abundance (found in Equation 3.1), and $\log(\xi_\odot) = 0$ by definition. The interpolation given in Equation 3.5 is extrapolated in both directions from [Fe/H] $= -3$ to the BBN abundances (zero for these isotopes) and from [Fe/H] $= 0$ to super-solar values, which gives massive abundances for these isotopes across the entire metallicity range considered.

As mentioned above, the parameter ξ takes a value of $\log(\xi) = -2.5$ at [Fe/H] $= -3$. The reasoning behind this choice is as follows. At solar metallicity, massive stars are responsible for roughly 30 % of the total iron, but nearly 100 % of the alpha isotopes. So then $[{\rm Fe}]_{\rm massive} = -0.5$, and $[\alpha]_{\rm massive} = 0$. At lowest metallicities, alpha isotopes effectively comprise the aggregate of metals by mass, since secondary sources and Type Ia SNe do not provide enrichment until later. Hence $[Z] \simeq [\alpha]_{\rm massive}$ holds in low metallicity regimes and will trail [Fe/H] by a nearly constant 0.5 dex until Type Ia onset. We then use our model parameter ξ in place of $Z/Z_\odot$. This comparison between ξ and [Fe/H] is approximate, and relies on the normalized metallicity $Z/Z_\odot$ tracking ξ, see Fig. 3.15.

3.3.2 Type Ia Supernovae

There are three constraints for choosing a parametrization for Type Ia isotopes as a function of ξ. First, Type Ia contributions experience a delay before they begin to enrich the ISM. This is due to the time necessary for, in the accreting white dwarf model, an intermediate to low mass star to evolve through its main sequences and then accrete sufficient material to surpass the Chandrasekhar mass limit. In the meanwhile, massive stars continue to enrich the ISM, making the galaxy more metal rich. The metallicity at which Type Ia are able to begin contributing to ISM enrichment is typically constrained to the interval $-2 <$ [Fe/H] < -1 depending on environment, galaxy size, etc., but is usually favored towards the upper bound. The time delay of Type Ia SNe is dependent on progenitor model, and a combination of single and double degenerate channels may be required to match observations (see, for e.g., observations: Totani et al., 2008; fitting to progenitor models: Mennekens et al., 2010). Moreover, the delay may be somewhat

dependent on metallicity as well, as lower metallicity stars could make more massive WDs due to decreased mass loss (Kistler et al., 2013). Nevertheless, Type Ia contributions should be negligible below some value of ξ. Second, upon crossing the Type Ia onset value, contributions should gradually rise to their solar values. Third, at high ξ the scalings should behave essentially like a primary process. Note that this last constraint is an assumption of our model and could be true only for a flat star formation rate (SFR). In fact, investigation into Type Ia progenitors by Mannucci et al. (2006) predicts that the ratio of CCSNe to Type Ia rates to be increasing with redshift, a conclusion reached by posing a two component delay time distribution (DTD) progenitor model. If indeed there exists a Type Ia progenitor that operates at low redshifts and experiences a longer delay between the formation of the WD and the later Type Ia explosion (named 'tardy' by Mannucci et al., 2006), a larger number of CCSNe relative to number of CCSNe at the birth of the WD contaminate the ISM, thus increasing the metallicity at a faster rate than it was increasing at the birth of the WD. Hence, once the Type Ia SNe do explode, their products would have a metallicity dependence different than linear, due to this increasing rate ratio of CCSNe to SNe Type Ia. We are careful to note that it is unclear exactly how a non-flat SFR would impact our scaling for Type Ia SNe, since the above discussion relies on time, and a relation between our model parameter and time cannot be formed. We simply note that there may indeed be an effect. The analogy presented above with respect to flat SFRs serves to construct a rough behavior of Type Ia abundances, and does not mean to attach the physical quantity of time to our model parameter. Furthermore, Type Ia onset may not occur at one unique metallicity, there may be a spread — in how far the different environments have evolved in terms of Z (and O as its main tracer) — when Type Ia sets in. Hence, the corresponding parameter value ξ for Ia onset is not unique for all constituents, but rather just a typical average that fits the different environments that we sample as function of it.

One specific form which satisfies all three constraints discussed is given, e.g., by a scaled and shifted hyperbolic tangent base function,

$$X_i^{\rm Ia}(\xi) = X_{i,\odot}^{\rm Ia} \cdot \xi \cdot [\tanh(a \cdot \xi - b) + \tanh(b)]/[\tanh(a - b) + \tanh(b)]. \qquad (3.6)$$

The specific value for Type Ia onset is determined by fitting the free parameters, a and

b, against available data. Note the hyperbolic tangent function is tempered with a linear factor of ξ to ensure the behavior is linear near solar, where otherwise the tanh(x) function would asymptote. Note further that whereas this function is phenomenologically motivated it is not unique. The arctan(x) and erf(x) also satisfy the above constraints, however, the erf(x) is more computationally expensive than the arctan(x) and tanh(x) functions.

3.3.3 Neutron Capture and *p*-Isotopes

The main s-process (*ls, hs,* and "strong" components), weak s-process, r-process, νp-process, and γ-process contributions are parametrized as follows,

$$X_i^{\rm strong}(\xi) = X_{i,\odot}^{\rm strong} \cdot [\tanh(d \cdot \xi + g) + \tanh(g)]/[\tanh(d + g) + \tanh(g)], \tag{3.7}$$

$$X_i^{\rm ls}(\xi) = X_{i,\odot}^{\rm ls} \cdot \xi^l, \tag{3.8}$$

$$X_i^{\rm hs}(\xi) = X_{i,\odot}^{\rm hs} \cdot \xi^h, \tag{3.9}$$

$$X_i^{\rm ws}(\xi) = X_{i,\odot}^{\rm ws} \cdot \xi^w, \tag{3.10}$$

$$X_i^{\rm r}(\xi) = X_{i,\odot}^{\rm r} \cdot \xi^p, \tag{3.11}$$

$$X_i^{\nu{\rm p}}(\xi) = X_{i,\odot}^{\nu{\rm p}} \cdot \xi^p, \tag{3.12}$$

$$X_i^{\gamma}(\xi) = X_{i,\odot}^{\gamma} \cdot \xi^{\frac{h+p}{2}+1}, \tag{3.13}$$

The free parameters p and h denotes the exponent of the ξ-dependence for primary and secondary (hs) processes, respectively. The weak component of the s-process was given its own parameter w. The motivation for choosing a power law dependence on these

parameters lies in the relations between abundance and metallicity for primary and secondary events, namely that primary events produce abundances linear in metallicity, and secondary produce abundances quadratic in metallicity. The chosen model parameter ξ takes the place of total metallicity (as discussed in the beginning of this section), and the exponents are parametrized for fitting with data. The metallicity dependence for the γ-process is less clear. It is possible for the target nuclei for this process to be either secondary or primary in origin, and produced in a previous astrophysical environment by the s- or r-process. Hence, photo-disintegration events can potentially be a tertiary process. All γ-process isotopes have low ($\leq$1-10 %) contributions to their respective elemental abundances, hence we chose not to assign a separate free parameter for this process, since the fit to data would likely be poorly constrained. Instead a compromise was struck between the possible s- or r-process origins and the chosen exponent for the γ-process represents an equal primary and secondary seed; about half the metals which might be target nuclei for this process are created by the s-process, and the other half from the r-process. Note that the proposed γ-process abundances enhanced from weak s-process seeds in the WSEP process (discussed at the end of Section 3.2.5.1) are scaled the same as the weak s-process, not as γ-process yields.

The choice for the "strong" s-process function is motivated phenomenologically. At low metallicities ([Fe/H] $\lesssim -2.0$), essentially all of the solar abundances for the "strong" s-process have been made. Hence the abundances should be close to constant between $-2.0 \lesssim$ [Fe/H] $\lesssim 0$. Additionally, since AGB stars experience a time delay in their contributions, at some point below [Fe/H] $\lesssim -2.0$ the abundances drop smoothly, hitting zero at some unknown, low metallicity. The free parameters d and g are used to adjust the shape of the hyperbolic tangent function, and constrain the peak abundance achieved at low metallicity and the metallicity at which the abundances begin to drop to zero.

3.3.4 Hydrogen Burning, Classical Novae, ν-Process, and Galactic Cosmic Ray Spallation

The scaling of secondary GCR spallation abundances has the same functional form as the s-process scaling. Novae, primary GCR spallation, νp-process, deuterium, and helium (from hydrogen burning) abundances were scaled the same as the r-process, but

with an offset added to reflect BBN abundances at $\xi = 0$. The remaining isotope of hydrogen, ^{1}H, was scaled according to,

$$X_i^{\mathrm{H}}(\xi) = X_{i,\odot}^{\mathrm{H}} \cdot [1.0 - \xi \cdot Z_\odot - Y(\xi) - D(\xi)], \tag{3.14}$$

where $Y(\xi)$ is the mass fraction of the helium isotopes, $D(\xi)$ is the mass fraction of deuterium, and $\mathrm{Z}_\odot$ is the solar value of total metallicity, given as $\mathrm{Z}_\odot$=0.0153 (Lodders, 2010). Effectively, this scaling is simply a restatement of the sum of mass fractions, $\mathrm{X} + \mathrm{Y} + \mathrm{Z} = 1$.

3.4 Fitting Scaling Model to Observational Data

The isotopic scaling functions were summed into elemental scaling functions for the purpose of fitting the free parameters. An example of this algorithm is given in Appendix A. Two compilations of stellar abundance data were used for the fitting. The Frebel (2010) low metallicity data set contains over 1000 stars from the Milky Way (MW) halo and dwarf galaxies. Note that this set is a compilation from various sources and there is hence an unknown source of varying systematic errors. Nevertheless, the spread of the averages of this data (described below) is much bigger than the provided errors and likely spans these systematic errors, though may be subject to systematic offsets. The dwarf galaxy abundances were removed from the set, since it is likely that dwarf galaxies exhibit a different GCE than the MW. In fact a future extension of the current model could be applied to dwarf galaxies to give insight into their GCE relative to the MW. Additionally, the Frebel (2010) data from stars in binary systems was removed from the [Ba/Fe] and [Sr/Fe] data, since binary systems experience more enriched s-process abundances due to accretion. Binary stars were identified from the online CHARA catalog, `http://www.chara.gsu.edu/~taylor/catalogpub/catalogpub.html` (Taylor et al., 2003), and were removed from the data set. In addition to removing the known binaries identified by the CHARA catalog, stars that simultaneously satisfied the following criteria: [Fe/H] < -2.0, [Eu/Fe] > 0.5, and [Ba/Fe] > 0.0 were also removed, since they are likely also candidates for binary systems not covered by the CHARA catalog. The other compilation used was the data set from Soubiran and Girard (2005), which contains, in part, 725 stars with magnesium abundances. This data set is needed for high

metallicity abundances which fill a paucity of Mg data in the range $-1 < \text{[Fe/H]} < 0$ offered by Frebel (2010).

All data is given in units of [X/Fe] as a function of [Fe/H]. The [Fe/H] axis was split into 300 bins in the range $-5 < \text{[Fe/H]} < 1$, and the [X/Fe] axis was split into 1500 bins in the range of the elemental data. Each data point was then assigned a Gaussian distribution using nominal values for the errors in the observations,

$$\mathrm{f_i} = \exp\left\{-0.5 \cdot \left([(x_i - x_0)/\sigma_\mathrm{x}]^2 + [(y_i - y_0)/\sigma_\mathrm{y}]^2\right)\right\}, \tag{3.15}$$

where $\mathrm{f_i}$ is the value of the distribution at bin x_i on the [Fe/H] axis and bin y_i on the [X/Fe] axis, x_0 and y_0 are the [Fe/H] and [X/Fe] values of each data point, and σ_x and σ_y are the nominal errors for each x_0 and y_0. A nominal error of 0.1 dex was assumed for [Fe/H] and [Mg/Fe], and a nominal error of 0.15 dex was assumed for [Ba/Fe], [Sr/Fe], [Eu/Fe], and [O/Fe] (Fre, 2011). The Gaussian contributions were summed for each bin, and assigned an average and standard deviation for each bin. These binned averages and standard deviations were used for sampling the parameter spaces. We note that all fitting is done in the logarithmic space as is common practice. One could argue that abundances and yields are "additive," hence the linear space should be used. This is left for future work. Indeed, fitting in the linear space would be impractical for large dynamic ranges on the one hand; for ratios and small ranges the logarithmic space should suffice.

3.4.1 SNe Type Ia Parameters

For fitting the Type Ia parameters a, b, and the fraction of the solar ^{56}Fe abundance attributed to Type Ia SNe, f, [Mg/Fe] data was chosen due the large number of data points that exist for this element as well as its contribution from both massive stars and Type Ia SNe. The parameter value for a, b, and f were chosen to minimize χ^2_r between the [Mg/Fe] scaling model and the averages of the binned data. The results are given in Fig. 3.7.

As shown in Fig. 3.7, the magnesium scaling falls within the standard deviation of the data, and tracks the average well. The determined best fit parameter values are $a = 5.024$, $b = 2.722$, and $f = 0.693$, with a resulting $\chi^2_\mathrm{r} = 0.0317$. This low χ^2_r reflects

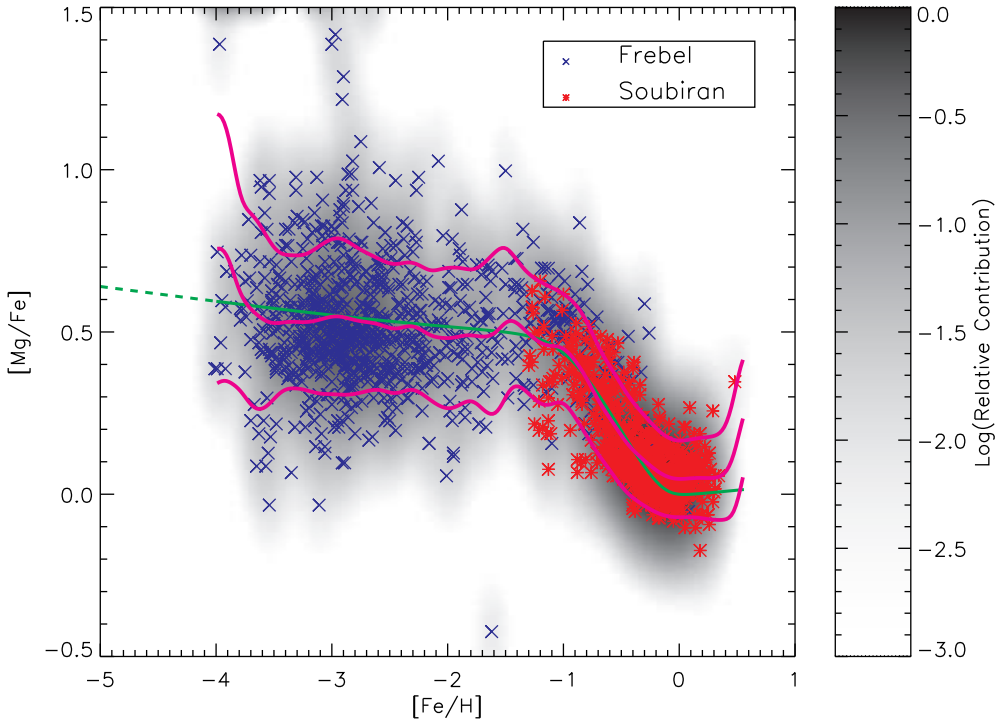

Figure 3.7: The resulting model for [Mg/Fe] found by parameter fitting. *Blue* ×*'s*: data from Frebel, 2010. *Red asterisks*: data from Soubiran and Girard, 2005. The dark shadow background shows the errors in the data, depicted by a Gaussian distribution about the data points. The averages and standard deviations for the Gaussian contributions per bin are given by the central and exterior pink lines, and the model itself is shown as a green line. There are a couple outlying data points on the graph whose Gaussian contributions can be seen at the upper limit of the [Mg/Fe] axis.

the large spread inherent in stellar abundances and the observational uncertainties that exist, and also the fact that the bins (and data) are not uncorrelated, as each star is "spread" out over many bins due to the assigned Gaussians. The drop of the curve to solar values from its peak at $[\mathrm{Fe/H}] \simeq -1$ is caused by Type Ia onset, when Fe production begins to dominate over magnesium.

The relatively flat line (only ≈ 0.1 dex drop in [Mg/Fe] over 2 dex in [Fe/H]) depicted

in the figure below [Fe/H] $\lesssim -4$ describes magnesium and iron abundances scaling together. This is a consequence of our model assuming massive stars are the sole and unique source of metals at low metallicity. Whereas it is likely that magnesium and iron co-evolve in this range, due to their shared primary (massive star) origin that dominates at low metallicities, it is unsubstantiated from the data that the correlation is as exact as the model finds it to be. Indeed, the model cannot predict abundances below [Fe/H] $\simeq -4$ with any reliability, given the paucity of data at such low metallicities. It could be argued that "average" scaling of abundances is not even a well-defined concept in this range, since individual astrophysical events can have a large stochastic effect on the metallicity content. In this sense, our model assumes "scaling" is a consequence of varying amounts of mixing with BBN from the same stellar sources, and until sufficient stellar events can reliably produce an average, our model is not a statistically accurate description of this mixing.

3.4.2 *r*-Process and *hs* Parameters

For determining the value for the r-process parameter p, the chosen data was [Eu/Fe]. Europium is an r-process peak element with two isotopes, ^{151}Eu and ^{153}Eu, both of which have dominant ($\sim 85\,\%$ its solar value) contributions from the r-process. We determined the optimized value for p using data from the Frebel (2010) data. The best fitting scaling for [Eu/Fe] is given in Fig. 3.8.

The best fit parameter value was found to be $p = 0.938$ with $\chi^2_{\rm r} = 0.040$. The previously found best fit values for a, b, and f (from Section 4.1) were used for Fe. Note that a nominal value of $h = 1.5$ for the s-process parameter was assigned to the s-process contributions to Eu for the purpose of fitting the [Eu/Fe] model. The choice of this nominal value for h has a negligible impact on the best fit value for p due to the small s-process component of Eu, and for comparison an optimization of the parameter space for p with an h value of 2 yields a best fit value of $p = 0.935$ with $\chi^2_{\rm r} = 0.041$, a difference of $0.3\,\%$ in p, and a difference of $2.5\,\%$ in $\chi^2_{\rm r}$.

For fitting the values for the heavy main s-process parameter h, the chosen data was [Ba/Fe]. This element has two s-only isotopes, ^{134}Ba and ^{136}Ba, along with three isotopes with contributions from both the s- and r-processes, ^{135}Ba, ^{137}Ba, and ^{138}Ba, and a small overall elemental contribution ($\sim 0.2\,\%$ its solar value) from two γ-process

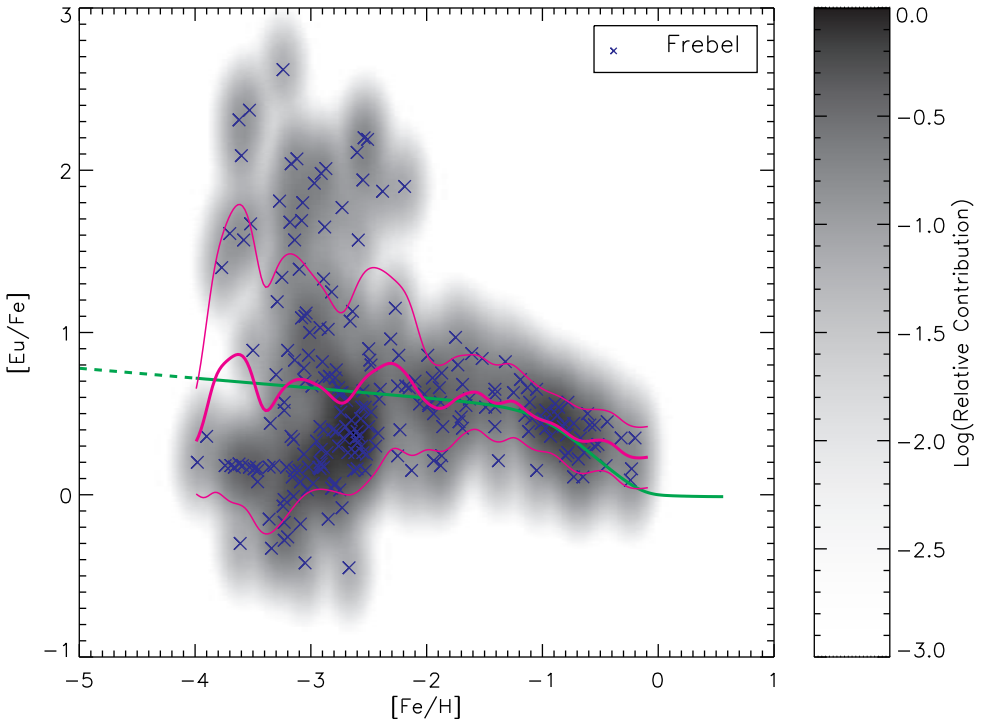

Figure 3.8: The resulting model for [Eu/Fe] found by parameter fitting. The full scaling is shown in green. *Blue* ×*'s*: data from Frebel, 2010. The rest of the figure follows the convention of Fig. 3.7.

isotopes, ^{130}Ba, and ^{133}Ba. In Fig. 3.9, we plot results for the scaling of barium with the best fit value for h. The previously found best fit values (from Section 4.1) for a, b, f, and p were used for Fe and the r-process contributions to Ba.

The minimized value of $\chi^2_{\rm r} = 0.134$ was obtained from the parameter value $h = 1.509$. The trend of our barium model at low ($\lesssim -2.0$) metallicities implies abundances that begin to track iron. At these low metallicities, iron production is dominated by primary massive star contributions, as is barium production dominated by the primary r-process, hence the [Ba/Fe] encounters a "floor" in its abundances, which is expected (e.g., Truran, 1981).

Above [Fe/H] $= -1.793$, secondary contributions from the s-process exceed r-process contributions, and begin to drive [Ba/Fe] upward to a local maximum, before Type Ia contributions take the ratio back down to solar. This metallicity value of [Fe/H] $= -1.793$

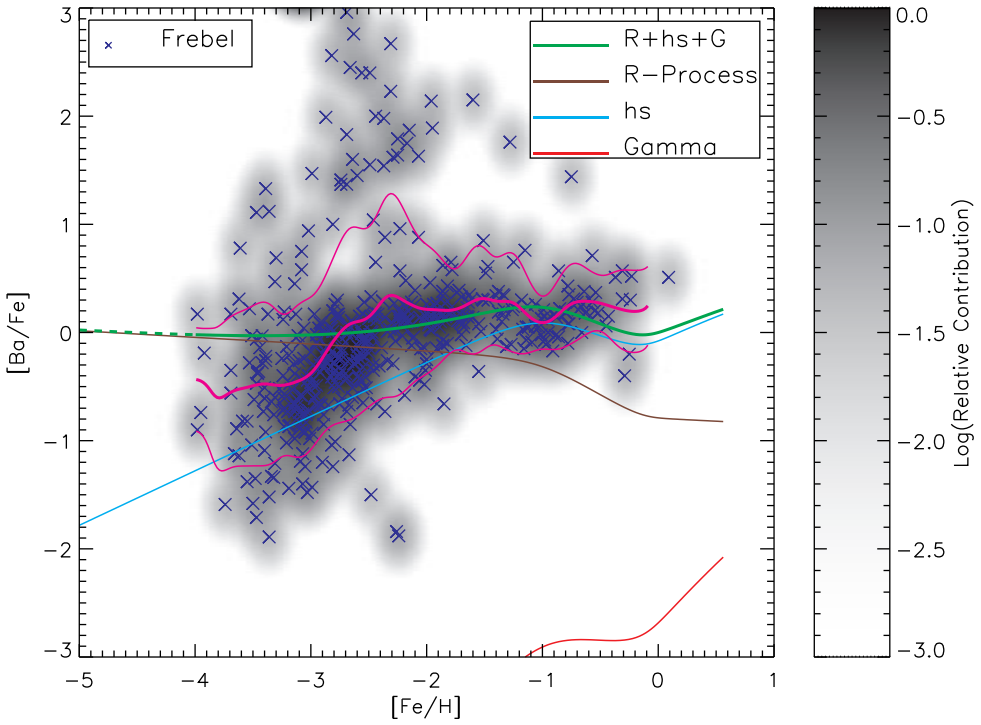

Figure 3.9: The resulting model for [Ba/Fe] found by parameter fitting. The full scaling is shown in green, with the heavy s-process, r-process, and γ-process components plotted in teal, brown, and red, respectively. *Blue* $\times$*'s*: data from Frebel, 2010. The rest of the figure follows the convention of Fig. 3.7.

where heavy s-process contributions equal r-process contributions is lower than the typical value of [Fe/H] ≈ -1.5 (e.g., Truran, 1981; Travaglio et al., 1999), and is due to our main heavy s-process exponent being smaller than the theoretical value of 2. Note that at all metallicities, the γ-process contributions to elemental abundances are negligible.

3.4.3 Weak *s*-Process and *ls* Parameter

The parameters constraining the weak s-process and ls scalings are w and l. Ideally one would wish to use [Ga/Fe] or [Se/Fe] elemental data, both of which have significant weak s-process isotopic contributions to their elemental abundances (≈ 0.61 for Ga, ≈ 0.21 for Se), as well as also lying on the first main s-process peak. Unfortunately data across a sufficient metallicity range for these elements is sparse, and [Sr/Fe] data

is used instead, which has ≈ 0.09 of its elemental abundance due to the weak s-process. In addition to data from Frebel (2010), two additional sources were used that provide observations of higher metallicity stars (Taylor et al., 2003). Sr has two s-only isotopes along the weak s-process path, ^{86}Sr and ^{87}Sr, along with one mixed isotope of r- and s-process origin, ^{88}Sr (although the r-process component is small), and one νp-process isotope, ^{84}Sr. Possible binary contamination of the data was removed according to the same prescription adopted for the [Eu/Fe] data. In Fig. 3.10, we plot results of the model for strontium with the best fit value for w and l. The previously found best fit values for a, b, f, and h (from Section 4.1 and 4.2) were used for Fe and the main s-process contributions to Sr.

The value of $\chi^2_{\rm r} = 0.061$ was obtained from the parameter value $w = 1.230$ and $l = 1.227$. At all metallicities, contributions from the light s-process exceed weak s-process contributions, and the νp-process and r-process contributions are negligible.

3.4.4 "Strong" s-Process Parameter

The final free parameter constrains the third s-process peak. Pb data was taken from Frebel (2010), and binary stars were removed. The remaining data set consists of four points only. Due to the paucity of data, our usual standard of optimizing the elemental scaling using a $\chi^2_{\rm r}$ analysis very poorly constrains [Pb/Fe]. Instead, the functional form given in Section 3.3.3 was used to fit the free parameters d and g by hand to the four data points. The result is given in Fig. 3.11.

As shown in Fig. 3.11, [Pb/Fe] peaks at [Fe/H] ≈ -3, which is about 0.5 dex lower than found in the AGB simulations by Bisterzo et al. (2010). Below [Fe/H] $= -3$, [Pb/Fe] drops until the "strong" s-process component is negligible, and the elemental scaling is determined only by the r-process. The free parameters were found to be $d = 140$, and $g = -0.05$. It should be noted that the few data points used only constrain the approximate location of the peak for the [Pb/Fe] fit, and the drop of the abundance at [Fe/H] ≈ -3.5 is not motivated by the data, but is an artifact of our chosen function for the "strong" s-process scaling. It is clear that [Pb/Fe] should indeed drop, as AGB stars do not produce isotopes at arbitrary low metallicities, but the exact nature of the drop to the r-process floor may not be well represented by our model. This very rough treatment of the "strong" s-process results in larger uncertainties for

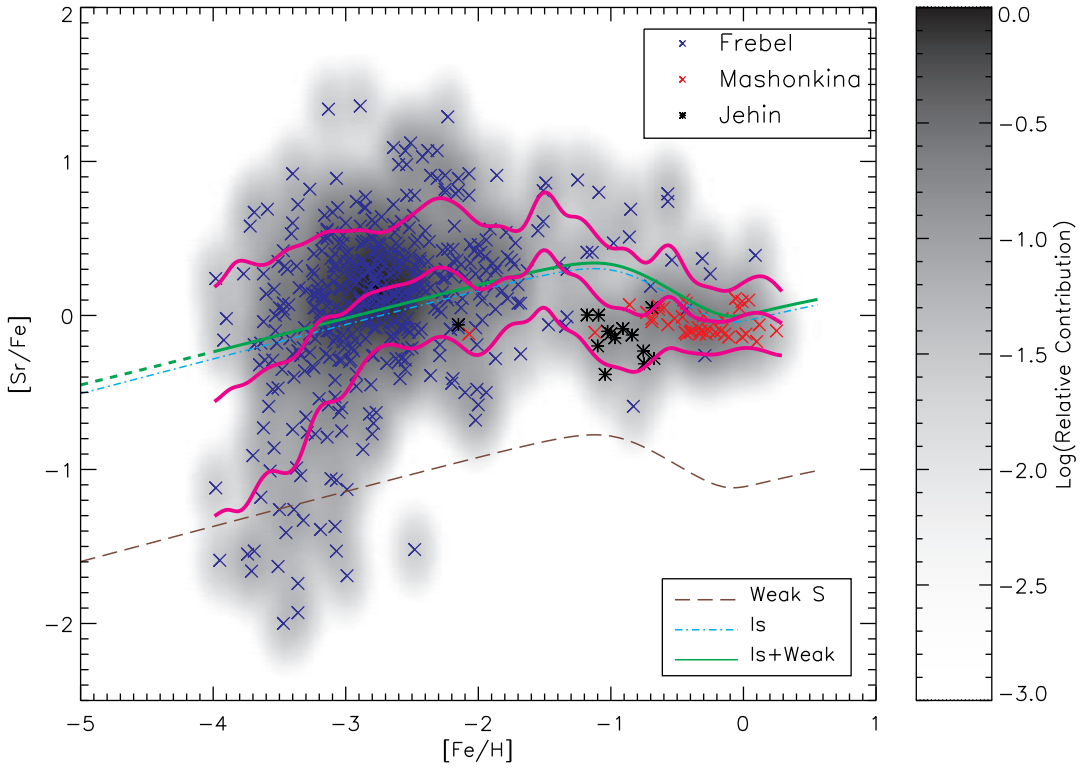

Figure 3.10: The resulting model for [Sr/Fe] found by parameter fitting. The full scaling is shown in green, with the light *s*-process and weak *s*-process components plotted in cyan and brown, respectively. *Blue* ×*'s*: data from Frebel, 2010. *Red* ×*'s*: data from Mashonkina and Gehren, 2001. *Black asterisks*: data from Jehin et al., 1999. The rest of the figure follows the convention of Fig. 3.7.

the *s*-process contributions to Pb and Bi isotopes from our model, and further revision is left to future work.

3.5 Results and Discussion

The functional forms for all scalings are now fixed by adjusting the model to optimally fit the observational data. A comparison is given in Fig. 3.12. Since each isotopic contribution in the "massive" category is independently interpolated between solar and

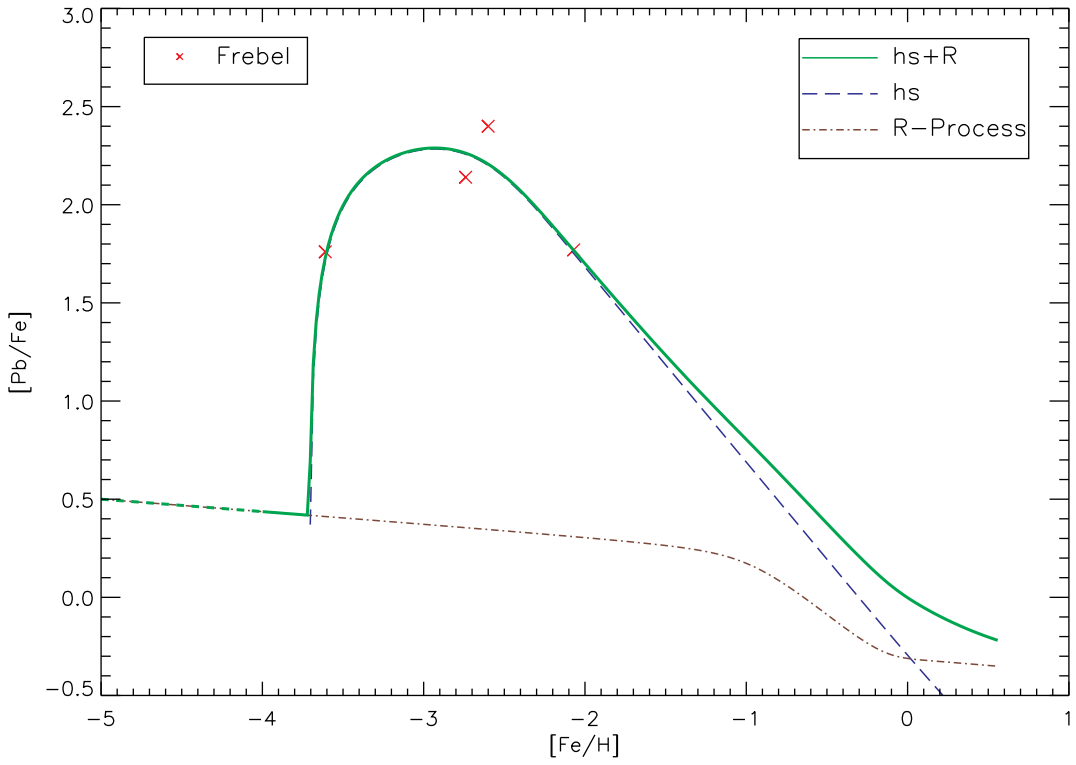

Figure 3.11: The resulting model for [Pb/Fe] found by parameter fitting by hand. The full scaling is shown in green, with the heavy *s*-process and r-process components plotted in cyan and brown, respectively. *Red* ×*'s*: data from Frebel, 2010.

[Fe/H], the "massive" (*brown solid line*) scaling shown in Fig. 3.12 is an example, and what is shown is the scaling for the massive contribution to ^{56}Fe only. Hence, this scaling gives,

$$[^{56}\mathrm{Fe}_{\mathrm{massive}}/\mathrm{O}] = \log\left(^{56}\mathrm{Fe}_{\mathrm{massive}}/^{56}\mathrm{Fe}_{\mathrm{massive},\odot}\right) - \log\left(\mathrm{O}/\mathrm{O}_{\odot}\right), \tag{3.16}$$

where $^{56}\mathrm{Fe}_{\mathrm{massive},\odot}$ is the massive contribution to the solar abundance of ^{56}Fe.

Type Ia SNe (*yellow long-dashed line*) contributions are negligible ($< 1\,\%$ the solar value) below the Type Ia onset identified by our model. After Type Ia onset at [Fe/H] ≈ -1.1, the contributions climb smoothly to solar. It is concerning that the

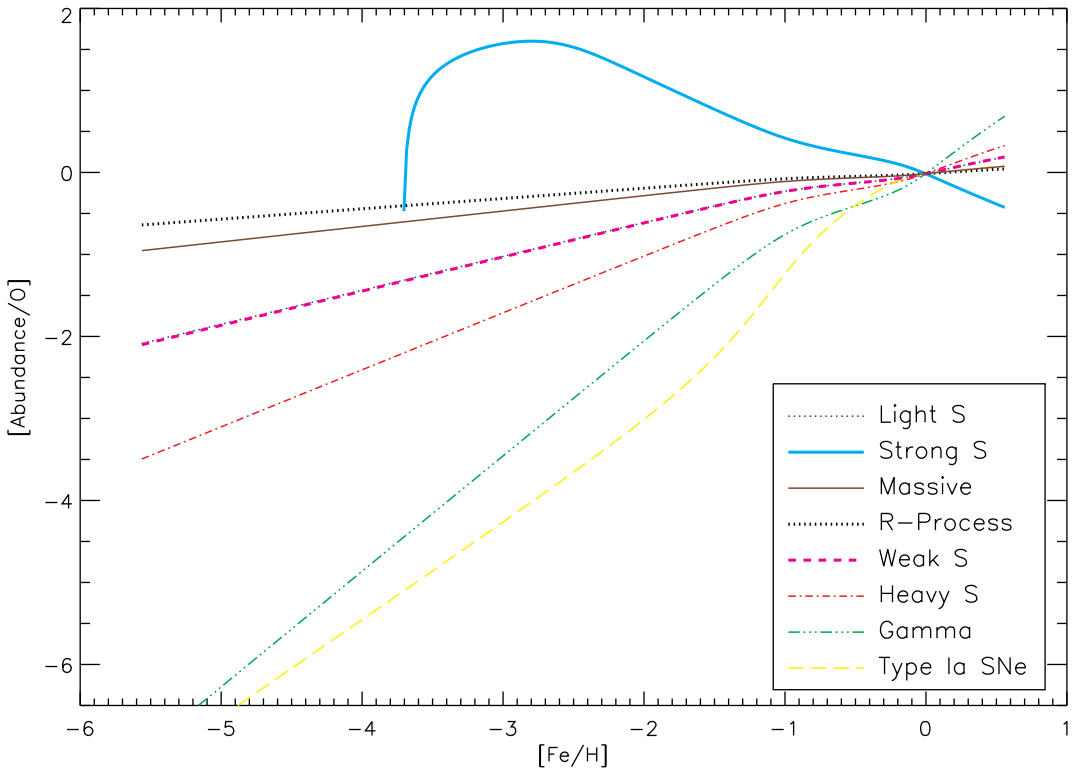

Figure 3.12: The scaling functions of the model contributions relative to oxygen as functions of metallicity. The "Massive" line shows the scaling of the massive category's contribution to ^{56}Fe, and is normalized to the solar contribution from this category only.

Type Ia scaling begins to flatten at low metallicities until its slope becomes less than the γ-process (*green dot-dot-dot-dashed line*). Whereas contributions are negligible at these metallicities, the tanh(x) function chosen for Type Ia fails to describe the accurate physical picture, as the slope ideally should increase sharply below onset to reflect Type Ia "turning on." We accept this behavior for the Type Ia scaling in part because contributions are already negligible and would offer insignificant corrections to the isotopic abundances if changed. Even though our Type Ia scaling has a negligible impact on the abundances below the onset value, its description in this range is not constrained at low metallicities. In the present model it is only important for [Fe/H] > -1.1. Furthermore, the elemental data ends at [Fe/H] ≈ -4, and hence the only constraint on Type

Ia scaling below this metallicity (where it flattens out) is that there is no contribution from the BBN composition.

Both the massive star (*brown solid line*) and r-process (*black dotted line*) scalings show similar trends at all metallicities, due to their shared primary nature. Abundances for the, νp-process, primary GCR spallation, novae contributions, and He production are scaled the same as the r-process, whereas secondary GCR spallation is scaled the same as the heavy s-process. The γ-process is scaled with an exponent given as the average of the heavy s- and r-processes plus one, $(h + p)/2 + 1$ (see Equation 3.13).

Both components of the s-process do not show the typical behavior of secondaries. The heavy component (*red dot-dashed line*) shows a higher drop off at lower metallicities than the primary processes, but with a slower exponent of 1.509 compared to the theoretical value of 2. The light s-process (*teal solid line*) and weak s-process (*pink dashed line*) scalings behave similarly at all metallicities, with an exponent intermediate between the heavy s-process and primary processes. The "strong" component displays supra-primary behavior above [Fe/H] ≈ -3.5, as is expected from its high abundance at low metallicities. Below [Fe/H] ≈ -3.5, it decreases at a rate larger than any other process, and its contributions quickly become negligible and the scaling is no longer plotted. In this range [Fe/H] $\lesssim -3.5$ it is unlikely that our model correctly describes the "strong" component, as only the peak of the scaling function is constrained by data.

The failure of our model to reproduce the theoretical secondary nature is not new, and this discrepancy has been previously observed in the data (Prantzos, 2010b). It may be possible to alleviate this discrepancy by noting that at low metallicities rotating massive stars may have an increased neutron exposure in two different ways. The first is enhanced nitrogen production from CNO burning, which then burns into neon to seed the neutron source (Pignatari et al., 2008; Frischknecht et al., 2010). The second is an earlier ^{22}Ne ignition due to higher core temperatures (Frischknecht et al., 2010). The effect of this larger neutron exposure is enhanced weak s-process production at low metallicities, driving an increase in the abundance and resulting in a parameter value that is closer to a primary rather than secondary process.

Explaining the discrepancy for the heavy and light components is more challenging. It may be plausible, however, that we are observing the net result of a mixed isotopic history. That is, one could imagine a composition with a given abundance of an isotope

made from a primary process in some astrophysical environment, that is then processed in a different astrophysical environment at a later time. If another abundance of this isotope is then made from a secondary process in the new astrophysical environment, its history would change from primary to secondary. Our model offers no way to track this effect. Indeed the aggregate of these effects may be in fact what we observe, and hence may be why our model gives an averaged main component parameter that deviates from the theoretical value of 2.0 (e.g., Prantzos, 2010b). Of course, this only applies to elements whose isotopic contributions can be made from both primary and secondary sources. In Table B.1 of Appendix B we summarize our optimized parameter values. The complete scaling model for all elements is shown in Fig. 3.13. Note that for illustration, we provide the elemental scalings in Fig. 3.13 to a metallicity lower than our model is fitted to data.

The traditional method of linearly interpolating solar abundances for inputs into stellar simulations is equivalent to treating the Galaxy as though all isotopic production is primary. This approximation is similar to Fig. 3.13, but with all metals changing their relative abundances at the same [Fe/H], which would manifest as a type of "flag" pattern, with all colors (representing relative abundances) changing together. In contrast to this approximation, Fig. 3.13 shows the corrections offered by our model to the traditional approximation due to the inclusion of Type Ia onset and secondary processes. These corrections are identifiable as "fingers" which protrude in the horizontal axis, distorting the otherwise clean "flag" pattern, and occurring at elements that either lie on the Fe-peak or that have strong secondary or other Type Ia contributions.

The scalings that notably stand apart from the others are the light elements: H, He, and Li. These begin with a much higher relative abundance (compared to the metals) due to BBN, and so change less relative to their solar values, compared to the other elements that begin with zero BBN contributions. Additionally, Pb displays a relative higher abundance at low metallicities due to the "strong" s-process. The sharp drop of Pb at [Fe/H] ≈ -3.8 is consistent with Fig. 3.11, and is a very approximate treatment.

In Table B.3 of Appendix B, we give the ratios of the isotopic abundances from our scaling model over the abundances generated from a linear interpolation between BBN and solar. The ratios are computed for two sub-solar total metallicities ($[Z] = -1$ and $[Z] = -3$), and illustrate the corrections the model provides to a standard approach.

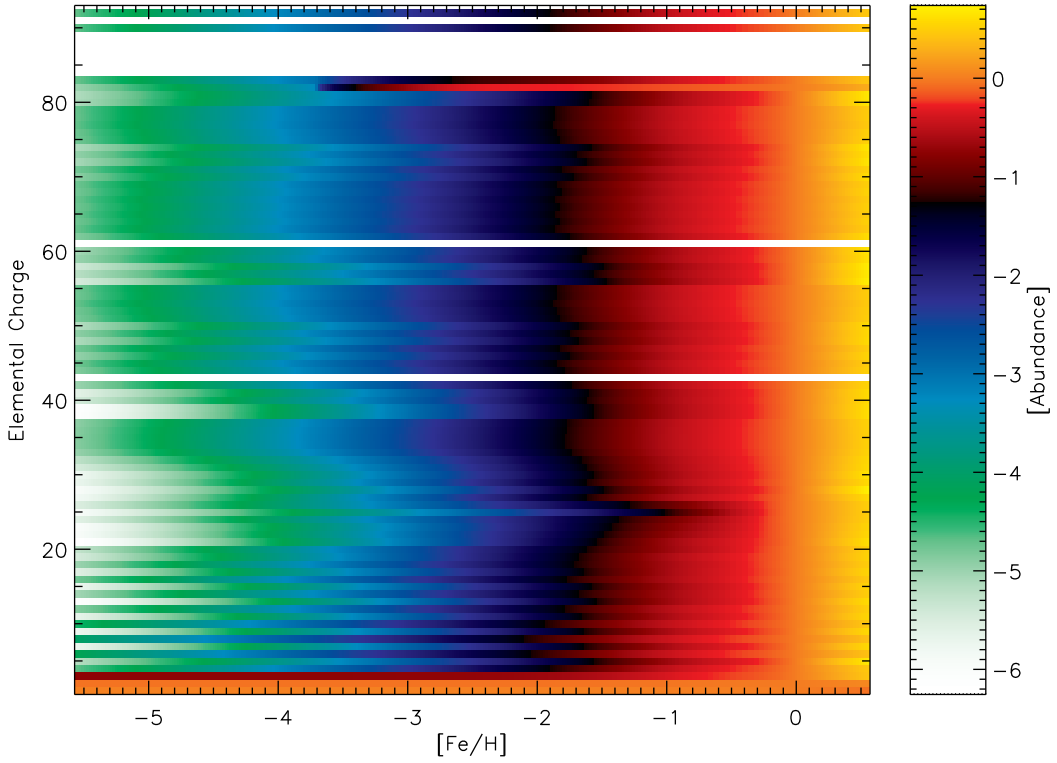

Figure 3.13: The complete elemental scaling of the model. The abundances are given relative to their solar values.

Elemental abundance ratios, [X/Fe], that are above zero at sub-solar metallicities generally indicates elements, X, that have strong contributions from primary sources. Specifically, [X/Fe] > 0 will hold if an element X has a larger primary contribution to its solar abundance than Fe has to its own solar abundance. Similarly, if an element X has a larger secondary or Type Ia contribution to its solar abundance than Fe has to its solar abundance, [X/Fe] < 0 will hold. In contrast, the method of linearly interpolating abundances from their solar values to BBN results in [X/Fe] $= 0$ for all metal elemental *and isotopic* abundances — all metals are scaled at the same rate. We can, therefore, compare the corrections that our scaling model produces to the abundances, relative to the linear interpolation method. This comparison is shown in Fig. 3.14.

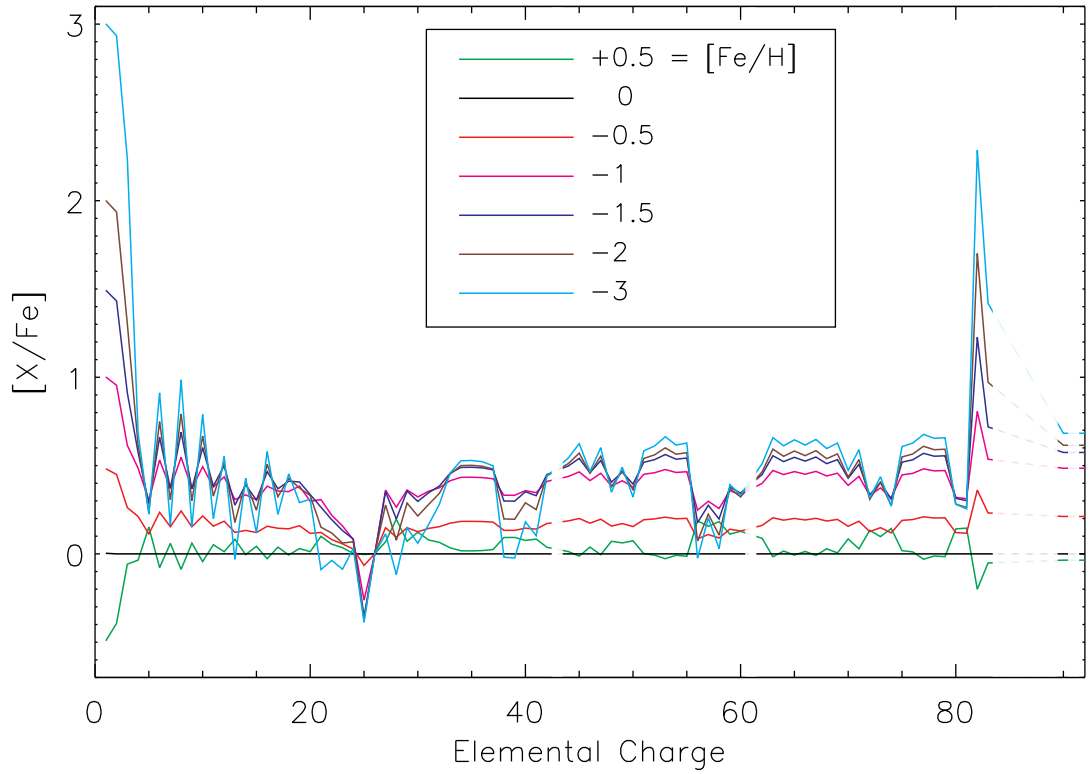

Figure 3.14: The elemental ratios against iron ([X/Fe]) at various metallicities for the scaling model. In contrast, the ratios produced from the linear interpolation method are a constant line at [X/Fe] = 0 for all elements, at all metallicities.

Finally, our choice for the model parameter, ξ, can now be compared to the normalized total metallicity, $Z/Z_\odot$ (Fig. 3.15). As shown in Fig. 3.15, our choice for the model parameter indeed corresponds to $[Z]$ to within 0.4 dex for $\log(\xi) \geq -3$ (below which our model is not constrained by data). The deviation from true linear is greatest at low metallicities and improves closer to solar metallicities. This comparison verifies our motivation for choosing functions for primary and secondary processes as being proportional to a polynomial of ξ. The deviation from linear is a result of the fixed point at [Fe/H] $= -3$ calculated from the massive star simulation, and the scaling of the massive contributions from the solar abundances through this fixed point in log-space (rather than linear-space). If the massive scalings were done in linear-space instead,

the massive isotopic ratios would be similar to the fixed point abundance ratios for metallicities well above [Fe/H] = −3, and these ratios would approach solar ratios only just before [Fe/H] = 0. This should not be the case, since enrichment from massive stars should produce ratios close to solar much earlier. For this reason a linear scaling in log-space was adopted, which impacts the isotopic ratios at a lower metallicity, and creates smooth transitions to the solar ratios.

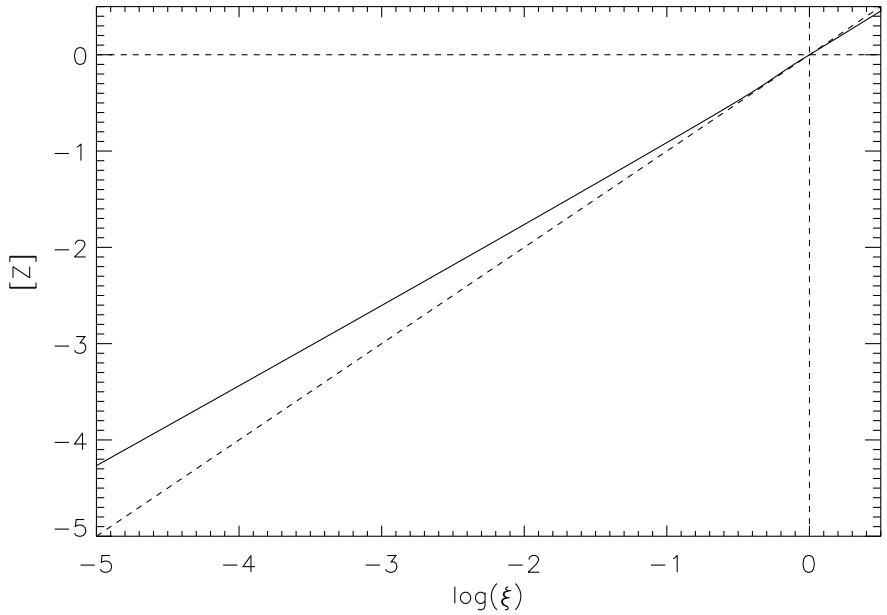

Figure 3.15: Comparison of our model parameter with [Z]. The behavior is linear to within 0.4 dex for all values of log(ξ) and [Z] considered by the model. The dashed lines demarcate the origin, and display the unity line for comparison.

The best-fit parameters (exponents of the scaling relations defined in Section 3.3.3) for the *ls*-, *hs*-, *r*-, and weak *s*-processes (l, h, p, and w, respectively) represent the rate of change of an abundance (in log-space) made by these processes as a function of ξ (see Equations 3.8-3.11). Of more interest for comparings with observations, however, are the *physical* exponents, which give the rates as a function of metallicity. Since a relation between ξ and Z exists (Fig. 3.15), we can now compute these new exponents,

using the following relations,

$$x^*_{\rm Z} = \frac{{\rm d}\ln P\left(\xi(Z)\right)}{{\rm dln}[Z]}, \tag{3.17}$$

$$x^*_{\rm Fe} = \frac{{\rm d}\ln P\left(\xi(Z)\right)}{{\rm dln}[Fe]}, \tag{3.18}$$

where x^* is the physical exponent of the scaling function $P\left(\xi(Z)\right)$, which is defined as the functions given by Equations 3.8-3.11, relative to their solar value, $P\left(\xi(Z)\right) \equiv X_i(\xi)/X_{i,\odot}$. Note that ξ is a function of Z, $\xi = \xi\left(Z\right)$. Using Equations 3.17-3.18, we compute the physical exponents for the *ls*-, *hs*-, *r*-, and weak *s*-processes. The results are shown in Fig. 3.16. In general, the exponents are nearly constant both at low values and close to solar values of $[Z]$ and $[Fe]$. The rate of change of $P\left(\xi(Z)\right)$ relative to $[Fe]$ is lower than the rate relative to $[Z]$, because the same change occurs in $P\left(\xi(Z)\right)$ over a wider range in $[Fe]$ compared to $[Z]$.

The Tables 3.1 and 3.2 give the physical exponents for a selection of [Z] and [Fe] values. At $Z = Z_\odot$, the physical exponents in Table 3.1 are greater than our best-fit, technical exponents by about 10 %. For the *r*-process, this result agrees nicely with the theoretical exponent of 1. The exponents for the *hs*-, *ls*-, and weak *s*-processes likewise increase, but are still below their theoretical values of 2. Possible reasons for this were discussed above. Note that the units throughout are *mole fractions*. As mentioned previously, both massive star and *r*-process scaling rates are quite similar at all metallicities, due to their shared primary nature. The rates for the νp-process, primary GCR spallation, novae contributions, and He production are the same as the *r*-process, whereas secondary GCR spallation has the same rate as the heavy *s*-process. The γ-process rate is the average of the heavy *s*- and *r*-process rates plus one (see Equation 3.13).

Table 3.1: Physical Exponent Values at different values of [Z]

Parameter	0	-1	-2	-3	Description
l^*	1.335	1.431	1.457	1.471	*ls*-process Exponent
h^*	1.667	1.760	1.791	1.792	*hs*-process Exponent
r^*	1.036	1.094	1.114	1.113	Primary Process Exponent
w^*	1.358	1.435	1.460	1.475	Weak *s*-process Exponent

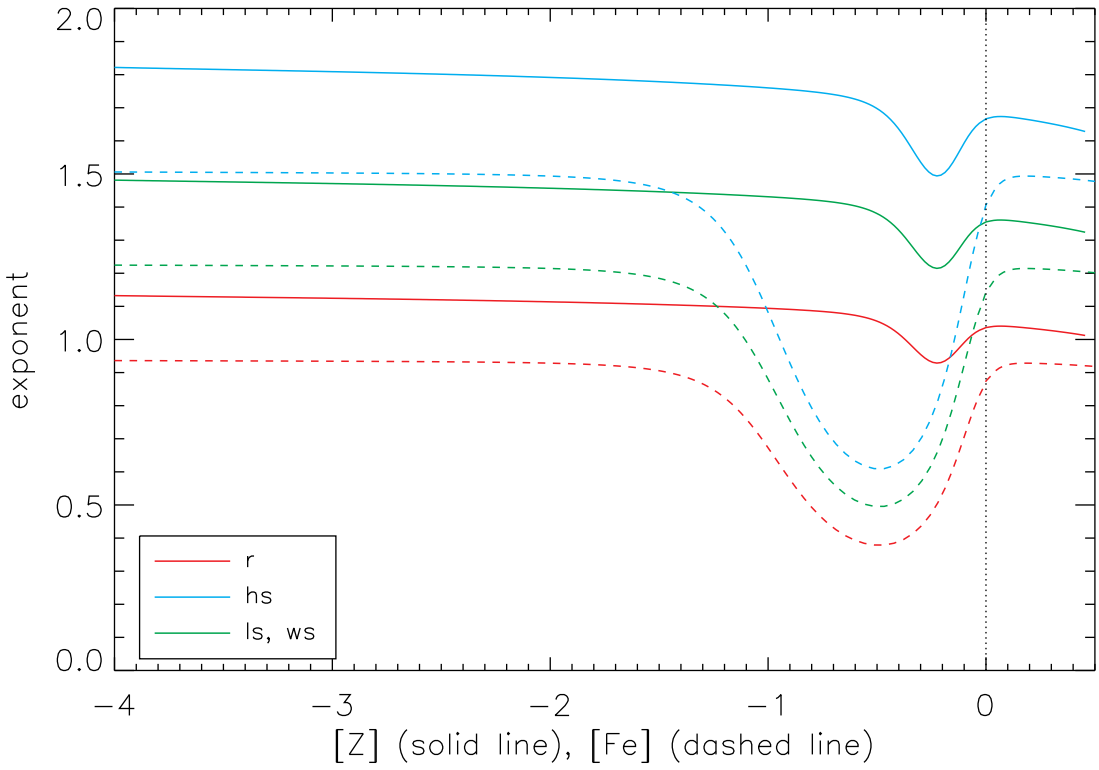

Figure 3.16: The physical exponent values (x^*) as functions of [Z] (*solid line*) and [Fe] (*dashed line*). Shown are the exponents for the *ls*-, *hs*-, *r*-, and weak *s*-processes.

Table 3.2: Physical Exponent Values at different values of [Fe]

Parameter	0	-1	-2	-3	Description
l^*	1.144	0.890	1.214	1.222	*ls*-process Exponent
h^*	1.407	1.094	1.493	1.503	*hs*-process Exponent
r^*	0.874	0.680	0.928	0.934	Primary Process Exponent
w^*	1.147	0.892	1.217	1.225	Weak *s*-process Exponent

3.6 Conclusions

A metallicity-dependent Galactic isotopic decomposition for all stable isotopes has been constructed. The solar abundance pattern was decomposed into several astrophysical

processes responsible for isotope synthesis. Parametric functions were chosen to scale the contributions from each astrophysical process to give isotopic abundances, with the solar abundance pattern and BBN used as boundary conditions. The isotopic scalings were summed into elemental scalings and compared with stellar data in the halo and disk to tune the fit parameters of the model. The final scalings provide a complete isotopic abundance pattern at any desired metallicity. The purpose of this work is to provide *isotopic* abundances that can be used as initial abundances for stellar models in future work, or other nucleosynthesis studies. Our model is a large improvement over approximating the input *isotopic* abundance pattern by simply scaling the solar abundances, and/or using solar isotopic ratios. This is the first time this has been done in a systematic way.

The interpretation of our offered solar abundance pattern decomposition is approximate, as different assumptions (of varying reliability) operate for different isotopes. The decompositions of the light isotopes (below carbon) likely reflect the best current understanding, however, the current understanding is admittedly an area of ongoing investigation. The decomposition from carbon up to the Fe peak from massive stars and Type Ia SNe are the result of scalings done on data from two models that preserve the isotopic ratios across the two models, which distorts the original abundance patterns taken from the simulations. Whereas this preserves the salient features of these two processes, it should be noted that the isotopes that are not CNO or Fe peak suffer a larger uncertainty in their decompositions due to this scaling. Furthermore we make no distinction between the several operative primary processes that fall under the category of "massive stars," which are dominated by CCSNe yields but also necessarily include yields from stellar winds of lower mass stars, ν-process, and classical novae.

The main s-process yields used show good agreement with the solar abundances, however, the weak s-process computation only reproduces the necessary abundances for three of the six s-only isotopes along the weak s-process path. The method for computing the weak s-process should ideally rely upon stellar models, unfortunately the results often display over-productions of several isotopes above their solar values. Our more simple approach, whereas less robust, has the advantage of only two isotopic over-productions, and is calculated directly from the neutron capture cross-sections and branching ratios.

In addition to providing isotopic abundances for input into stellar simulations, our methodology can also be applied to model other systems such as dwarf galaxies, and tailoring the free parameters to relevant data sets will then yield approximate chemical abundances for such systems. Yet another application lies with stellar model fits. Currently published stellar evolution models only give average yields for stars over certain mass ranges. These averages must be fitted to available observational data sets, as done for example by Heger and Woosley (2010). The need for this fit is evident, since stellar models only address the stellar nucleosynthesis part of GCE and neglect several processes which will ultimately influence the subsequent ISM abundances over many stellar lifetimes, processes such as infall and ISM mixing. The age of the Galaxy (or timescale of GCE) is much greater than the typical stellar lifetimes that contribute significantly to ISM enrichment; hence this fitting is required to give stellar yields a more precise physical meaning in a GCE context. Thus in addition to providing the initial isotopic abundances for input into stellar simulations, the abundances can also be used to fit the resulting stellar yields from the model in a consistent fashion.

This work has laid out a basic method of isotopic decomposition as a function of metallicity based on elemental observational data and underlying nucleosynthesis processes for a complicated environment like the Galaxy. Future work should have a more detailed look at specific and less complicated environments like, e.g., dwarf galaxies that have different contributions and would hence allow one to constrain model parameters more uniquely (such as Type Ia onset contributions). Another challenge will be to relate and identify the different nucleosynthesis processes with the principle components found in observational work like that of Ting et al. (2012), and help to improve such principle component analysis based on physical nucleosynthesis processes.

Chapter 4

The Impact of Helium-Burning Reaction Rates on Massive Star Evolution and Nucleosynthesis

4.1 Introduction

As discussed in Chapter 2, massive stars are responsible for the production of most intermediate-mass (A = 16−40) isotopes through hydrostatic burning phases and subsequent supernovae (Burbidge et al., 1957; Woosley et al., 2002). During core-He burning the $^{12}C(\alpha,\gamma)^{16}O$ and 3α reactions compete to determine the relative abundances of oxygen and carbon prior to core-C burning. Changes in these abundances have significant effects on subsequent stellar evolution and structure and on the resulting nucleosynthesis. The carbon abundance influences subsequent shell burning episodes and affects whether core-C burning will be radiative or convective. There is also a non-monotonic relation between the carbon abundance and the resulting remnant mass (Woosley et al., 2003; Sukhbold and Woosley, 2013), so that these reactions are important for understanding the populations of neutron stars (NS) and black holes (BH).

These rates can also affect weak *s*-process yields. The weak *s*-process is a slow neutron capture process occurring at the end of convective core-He burning and during shell carbon burning (Pignatari et al., 2010), and contributes to isotopic production along

the s-process path above iron and up to a mass number of A≈100 (Raiteri et al., 1993). A change in the helium-burning rates can induce a corresponding change in temperature to keep the star at constant luminosity, and the reaction for the neutron source for the weak s-process, ^{22}Ne$(\alpha, \mathrm{n})^{25}$Mg, is highly temperature-dependent. Additionally, the amounts of neutron poisons have been shown to vary with these rates (Rayet and Hashimoto, 2000; Tur et al., 2009).

Although not discussed in this work, the production of the important radioactive nuclei ^{26}Al, ^{44}Ti, and ^{60}Fe (Tur et al., 2010) is also sensitive to these rates. Gamma rays from these nuclei provide observational information that may help to test models of massive star internal structure and nucleosynthesis through the constraints imposed by the abundance ratios of ^{44}Ti/^{56}Co and ^{26}Al/^{60}Fe (Diehl et al., 2006; Leising and Diehl, 2009).

This study is an extension of the work by Tur et al. (2007) (see also, Tur et al., 2009), who calculated a limited subset of models of our full 2D parameter space. They concluded that across the 2σ uncertainty range standard deviations for the production factors sometimes vary non-monotonically with the rates, as do deviations in the remnant mass, indicating that both helium burning reactions are independently important (Tur et al., 2007). We extend upon their study by performing a much finer sampling of the 2σ uncertainty range to assess the effect of changing the rates *independently*, in order to map the whole 2D landscape to determine the true non-monotonic behavior with a higher resolution grid. The purpose is to: i) examine the effect of varying the helium burning reaction rates on the production factors of intermediate-mass isotopes, ii) examine the effect on the production factors of the six s-only isotopes along the weak s-process path, iii) assess the impact on i) and ii) of including only models that are likely to explode as successful supernovae, and iv) examine the effect on the remnant mass. We do not address the effect of varying the solar abundance set, which indeed has been shown to impact the final nucleosynthesis, and is studied in Tur et al. (2007) for the intermediate-mass isotopes and in Tur et al. (2009) for the weak s-process isotopes. We use an updated solar abundance set (Lodders, 2010) that was not yet available for the previous studies. It was corrected for the weak s-only isotopes by subtracting estimated main s-process contributions, as described in Section 4.2. We note that recent 3-body calculations of the 3α reaction show an increase in this rate at temperatures below

$\sim 0.07\,\mathrm{GK}$ (Nguyen et al., 2012). This will not impact the current study as He ignition in massive stars occurs beyond this threshold, at $T_{3\alpha} \sim 0.1\,\mathrm{GK}$.

This chapter has the following outline: in Section 4.2 we describe the stellar models and methods used in the analysis. In Section 4.3 we compare the intermediate-mass and weak *s*-process isotopes across all models, and for the subset of models likely to explode as supernovae rather than collapse to black holes (we ignore hypernovae and gamma ray bursts). This subset is chosen using a compactness parameter filter. We also discuss the remnant mass and carbon mass fractions at the end of core-He burning for the different stellar masses. Our conclusions are given in Section 4.4.

4.2 Stellar Models and Analysis

All models were computed using KEPLER, a time-implicit one-dimensional hydrodynamics package for stellar evolution (Weaver et al., 1978; Rauscher et al., 2002). A grid of 12 initial stellar masses $M_\odot$=12, 13, 14, 15, 16, 17, 18, 20, 22, 25, 27, and 30 was used, with the revised pre-solar abundances from Lodders (2010) for the initial composition. For each stellar mass, 176 models were computed to scan at least a 2σ uncertainty range for both the $^{12}\mathrm{C}(\alpha,\gamma)\,^{16}\mathrm{O}$ and 3α reaction rates, denoted $R_{\alpha,12}$ and $R_{3\alpha}$, respectively. This range was parametrized as a multiplier on the centroid values for the rates, as done by Tur et al. (2007). The centroid values used in KEPLER are taken from Caughlan and Fowler (1988) for $R_{3\alpha}$, and 1.2 times the rate recommended by Buc (2000) for $R_{\alpha,12}$. The range for the $R_{\alpha,12}$ multipliers was $(0.5, 2.0)$ with a resolution of $\Delta = 0.1$, and the range for the $R_{3\alpha}$ multipliers was $(0.75, 1.25)$ with a resolution of $\Delta = 0.05$. Commonly accepted uncertainties for $R_{3\alpha}$ and $R_{\alpha,12}$ are $\pm 10\,\%$ (Chernykh et al., 2010) and $\pm 25\,\%$. Our total range was, conservatively, slightly more than $\pm 2\sigma$. In Fig. 4.1 we show the grid of models computed both by Tur et al. (2007) and in the present work.

All stellar models were first evolved through hydrostatic burning until the Fe core collapsed, and an inward velocity of $10^8\,\mathrm{cm\,s^{-1}}$ was reached. The explosions were then modeled using the mechanical piston prescription (see Section 1.3.3). The final supernova yields for all models were then averaged by integrating over the Salpeter initial mass function (IMF) for each reaction rate multiplier pair in Fig. 4.1. The yields from stellar winds were included. Note the effects of rotation and magnetic fields are ignored.

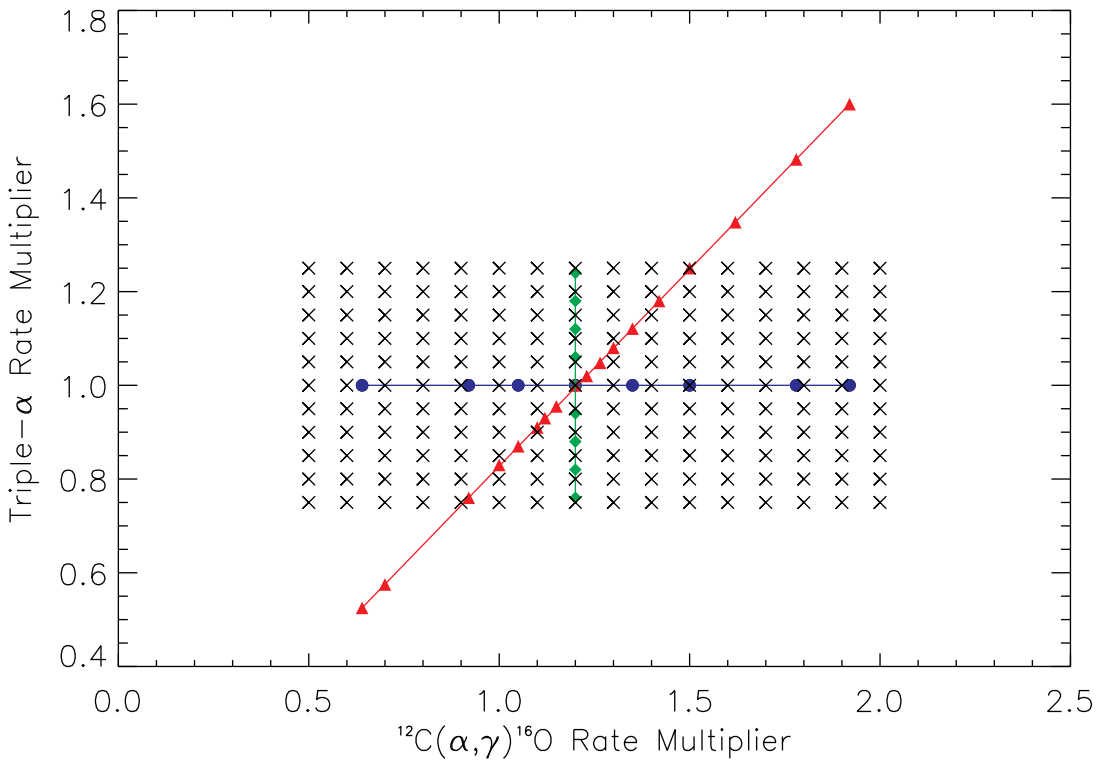

Figure 4.1: The $R_{\alpha,12}$ and $R_{3\alpha}$ reaction rate multiplier values used in the stellar models. The models using the reaction rate multiplier pairs given in *filled circles*, *triangles*, and *rhombuses* were performed by Tur et al., 2007. The $\times$'s show the models computed in the present work.

$$Y_i^* = \sum_j \int_{m_j}^{m_{j+1}} \xi\left(m\right) \cdot \left(s_{i,j} \cdot \left[m - m_j\right] + Y_{i,j}\right) \cdot dm \tag{4.1}$$

$$P_i = \frac{Y_i^*}{X_{i,\odot} \cdot \sum_k Y_k^*} \tag{4.2}$$

In Equation 5.1, the IMF interpolated yield mass for isotope i is given by Y_i^*, and the Salpeter mass spectrum is $\xi\left(m\right) = C \cdot m^{-2.35}$, where C is the proportionality constant. The mass grid used for the integrations are the *ejected* masses, defined as

the baryonic remnant masses subtracted from the initial stellar mass grid. Yields are linearly interpolated between adjacent masses in the integral, with the slope defined by, $s_{i,j} = (Y_{i,j+1} - Y_{i,j}) / (m_{j+1} - m_j)$, where $Y_{i,j}$ is the yield mass (*in grams*) of isotope i from a model with initial mass m_j. In Equation 5.2, the production factor for isotope i is given by P_i, the sum in the denominator runs over all isotopes, and the solar mass fraction of isotope i is given by $X_{i,\odot}$.

Massive stars are responsible for producing nearly the entire solar abundance of a subset of intermediate-mass isotopes, namely ^{16,18}O, ^{20}Ne, ^{23}Na, ^{24}Mg, ^{27}Al, ^{28}Si, ^{32}S, ^{36}Ar, and ^{40}Ca. Hence, in order to make the solar abundance pattern, massive near-solar metallicity stars need to produce these intermediate-mass isotopes in solar ratios. An analysis of the standard deviations of the production factors for this set of isotopes is used in the present work to identify helium reaction rate values that agree with solar observations. This agreement is an approximation that the above isotopes owe their entire solar abundance to massive, near-solar metallicity stars, and relies on sufficient sampling of the initial mass function (IMF) and understanding of the initial compositions. As mentioned, the impact of uncertainties in the initial composition is not addressed in this work, but an analysis of the effect of different compositions can be found in Tur et al. (2007).

For the weak s-process isotopes a correction is necessary, since the solar abundances of the six s-only isotopes along the weak s-process path (^{70}Ge, ^{76}Se, ^{80}Kr, ^{82}Kr, ^{86}Sr, and ^{87}Sr) have additional contributions from the main s-process, which occurs in asymptotic giant branch (AGB) stars, not massive stars. Hence what is needed are the production factors relative to the contributions from the weak s-process only, not relative to the entire solar abundance. To achieve this, the solar abundance decomposition from Chapter 3 was used, which gives, in part, the approximate solar contributions for the six weak s-only isotopes. This modifies Equation 5.1, with the substitution of $X_{i,\mathrm{w}}$ for $X_{i,\odot}$, where $X_{i,\mathrm{w}}$ denotes the contribution to the solar mass fraction of isotope i from the weak s-process.

4.3 Results and Discussion

4.3.1 Comparison of ^{12}C(α,γ) ^{16}O and 3α Reaction Rates

The production factors for the models were computed using Equations 5.1 and 5.2, and standard deviations were calculated for each model, using the intermediate-mass isotope set and the six s-only isotopes along the weak s-process path,

$$\sigma_P = \sqrt{\frac{\sum_{k=1}^{n} P_k^2}{n-1} - \left(\frac{\sum_{k=1}^{n} P_k}{n-1}\right)^2}, \tag{4.3}$$

where P_k are the production factors computed in Equation 5.2, and n is the number of entries in the isotope list: 10 for the intermediate-mass isotopes and 6 for the s-only isotopes along the weak s-process path. We distinguish σ_P (the standard deviation of the production factors) from σ (the uncertainty in the rates). Since massive stars contribute to most of the solar abundances for the intermediate-mass isotopes considered (or a fraction of them in the case of the s-only isotopes), low standard deviations should indicate combinations of $R_{\alpha,12}$ and $R_{3\alpha}$ that agree with observations. We first follow the type of analysis performed by Tur et al. (2007), for constant $R_{\alpha,12}$ and $R_{3\alpha}$ multipliers, shown in Fig. 4.2.

For a constant $R_{3\alpha}$ multiplier of 1.0 (Fig. 4.2, *top*), values for the $R_{\alpha,12}$ multiplier are favored within about $\pm 25\,\%$ of the centroid multiplier of 1.2. For a constant $R_{\alpha,12}$ multiplier of 1.2 (Fig. 4.2, *bottom*), values for the $R_{3\alpha}$ multiplier have a minimum standard deviation at 0.85, and vary across a similar range of standard deviation values for a $\pm 25\,\%$ change in $R_{3\alpha}$. Since $R_{3\alpha}$ is better experimentally determined, however, the extremes of this range are less likely than for $R_{\alpha,12}$. The results in Fig. 4.2 show approximate qualitative agreement with the findings of Tur et al. (2007), but care must be taken in a comparison as they do not use the (Lodders, 2010) abundances, and they have demonstrated that there is non-trivial variation among different solar abundance sets. The corresponding plot for the weak s-only isotopes is given in Fig. 4.3.

For a constant $R_{3\alpha}$ multiplier of 1.0 (Fig. 4.3, *top*), values for the $R_{\alpha,12}$ multiplier have a minimum standard deviation at 1.3. For a constant $R_{\alpha,12}$ multiplier of 1.2 (Fig. 4.3, *bottom*), the standard deviation has a minimum at the $R_{3\alpha}$ multiplier value of 0.95. Significant variations in the production factors exists across both multiplier

ranges.

4.3.2 Intermediate-Mass Isotopes

To address how changing the rate multipliers independently affects the nucleosynthesis, the entire set of models in $(R_{\alpha,12}, R_{3\alpha})$ space was mapped in a 2D grid, rather than restricting ourselves to 1D slices. Results are first given for just the $25\,M_\odot$ models (Fig. 4.4). The corresponding plots for all models can be found in Appendix E.

The best fit $R_{\alpha,12}$ and $R_{3\alpha}$ values occupy a region in the lower right-hand corner, and a strip running approximately though the centroid value for each rate. It is interesting that some adjacent models display significant differences in their nucleosynthesis despite a small change in the reaction rate multipliers, for example, $(R_{\alpha,12}, R_{3\alpha}) = (0.5, 0.9)$,$(0.6, 0.9)$, or $(R_{\alpha,12}, R_{3\alpha}) = (0.5, 1.05)$,$(0.6, 1.05)$. In some cases adjacent models can evolve with quite different shell burning episodes, whereas in other cases can be very similar, such as for $(R_{\alpha,12}, R_{3\alpha}) = (0.9, 0.9)$,$(1.0, 0.9)$ or $(R_{\alpha,12}, R_{3\alpha}) = (1.0, 1.1)$,$(1.1, 1.1)$. How this occurs can be understood by considering the convective history of adjacent models. First, the $(R_{\alpha,12}, R_{3\alpha}) = (0.5, 0.9)$ and $(R_{\alpha,12}, R_{3\alpha}) = (0.6, 0.9)$ models are given in Fig. 4.5, which have a difference in σ_P of 3 to 4 (Fig. 4.4).

In the $(0.5, 0.9)$ model we observe a convective region that extends past the C shell and into the above He layer, with subsequent He ingestion into the shell burning with C into O. In the $(0.6, 0.9)$ model the convective layer terminates before the He shell, and the mixing and subsequent nucleosynthesis seen in the $(0.5, 0.9)$ model does not occur.

In contrast, the $(R_{\alpha,12}, R_{3\alpha}) = (0.9, 0.9)$ and $(R_{\alpha,12}, R_{3\alpha}) = (1.0, 0.9)$ models are given in Fig. 4.6, which show a difference in σ_P of ≤ 1. In both Fig. 4.5 and Fig. 4.6 the $\Delta R_{3\alpha}$ is the same; however, in the latter the $R_{\alpha,12}$ values are sufficiently large to result in radiative core-C burning, and C shell burning episodes in the $(R_{\alpha,12}, R_{3\alpha}) = (0.9, 0.9)$ and $(1.0, 0.9)$ models (Fig. 4.6) that do not interact convectively with the He layer. Generally, larger carbon abundances at the end of core-He burning can support longer and more energetic carbon shell burning episodes, which can result in He ingestion leading to different nucleosynthesis.

The differences of adjacent models depend on the initial stellar mass, and it is expected that regions in the $(R_{\alpha,12}, R_{3\alpha})$ parameter space that have different standard deviations at one mass may not at another. To average these effects across the IMF,

Equations 5.1 and 5.2 were used for the entire set of models for all masses, and the standard deviations for the production factors are given Fig. 4.7.

Changes in the $^{12}\mathrm{C} + ^{12}\mathrm{C}$ reaction rate may also affect nucleosynthesis; rate uncertainties at low temperatures were thought to be large, perhaps orders of magnitude. A heavy ion fusion study by Jiang et al. (2007) reported a rate decrease at low energy. On the other hand, Spillane et al. (2007) found a strong increase in rates due to a low energy resonance. A still lower energy resonance at lower energy had weak experimental support. Possible effects have been studied by Pignatari et al. (2013) for a $25\,\mathrm{M}_{\odot}$ half-solar metallicity star. They found significant changes in the production of *s*-process elements. However, their calculations were not carried through to solar collapse and an explosion, which affects the production of these isotopes (Tur et al., 2009). In addition, recent measurements by Zickefoose (2011), reported by Notani et al. (2012) give an S-factor 50 times smaller than the previously reported value. For these reasons it is not clear how much the nucleosynthesis considered in this work would be affected.

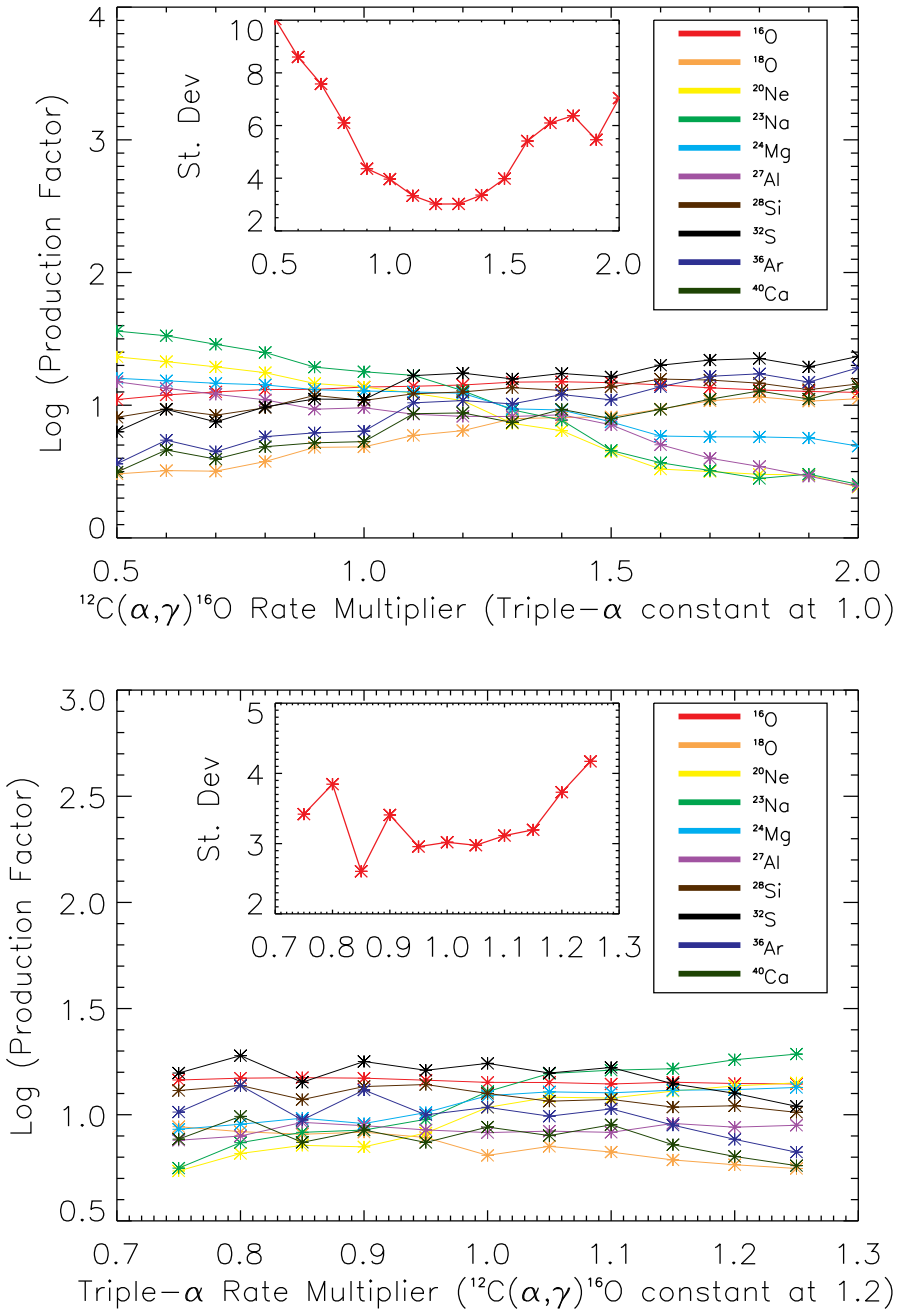

Figure 4.2: *Top*: The production factors for the intermediate-mass isotopes averaged over the IMF as a function of the $R_{\alpha,12}$ multiplier, at a constant $R_{3\alpha}$ multiplier of 1.0. *Bottom*: The production factors for the intermediate-mass isotopes averaged over the IMF as a function of the $R_{3\alpha}$ multiplier, at a constant $R_{\alpha,12}$ multiplier of 1.2. The inset graph shows the standard deviations.

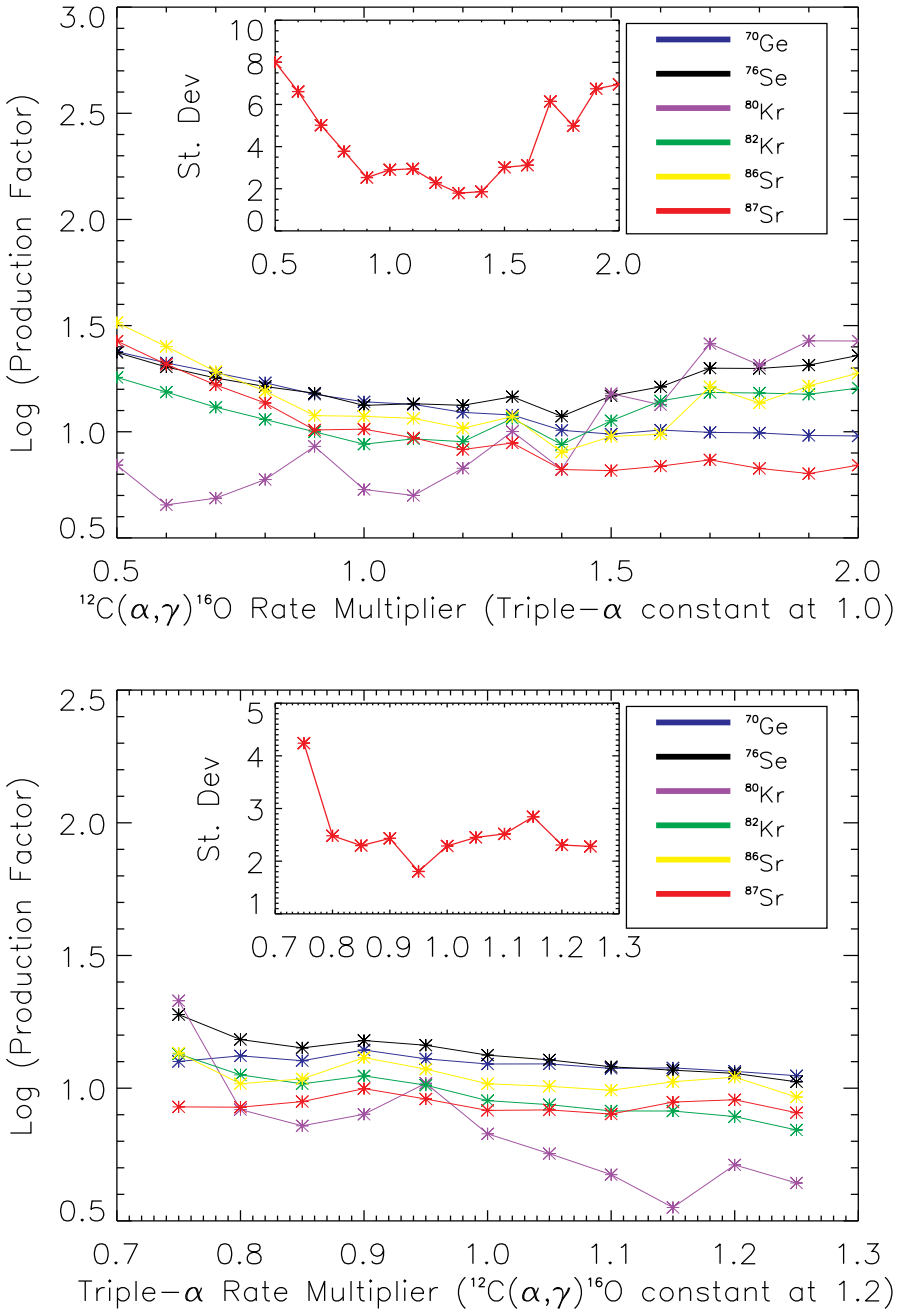

Figure 4.3: *Top*: The production factors for the weak *s*-only isotopes averaged over the IMF as a function of the $R_{\alpha,12}$ multiplier, at a constant $R_{3\alpha}$ multiplier of 1.0. *Bottom*: The production factors for the weak *s*-only isotopes averaged over the IMF as a function of the $R_{3\alpha}$ multiplier, at a constant $R_{\alpha,12}$ multiplier of 1.2. The inset graph shows the standard deviations.

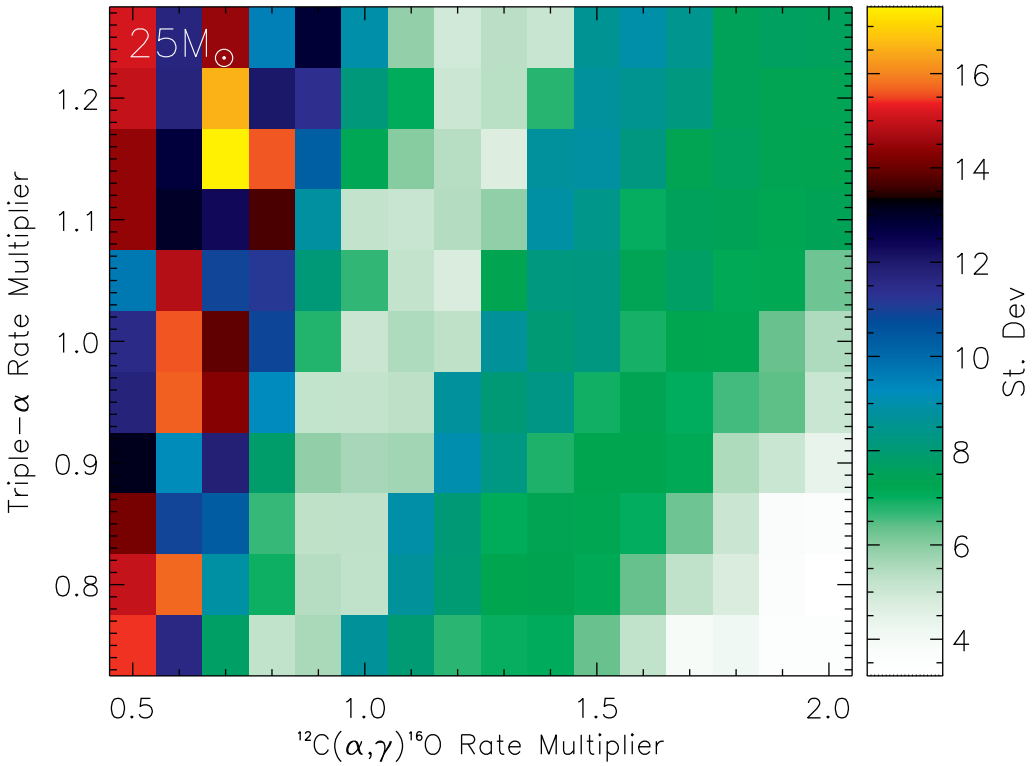

Figure 4.4: Standard deviations of the production factors as a function of the $R_{\alpha,12}$ and $R_{3\alpha}$ reaction rate multipliers for the 25 $M_\odot$ models. Each model is given by the $R_{\alpha,12}$ and $R_{3\alpha}$ reaction rate multiplier pair used for the helium rates.

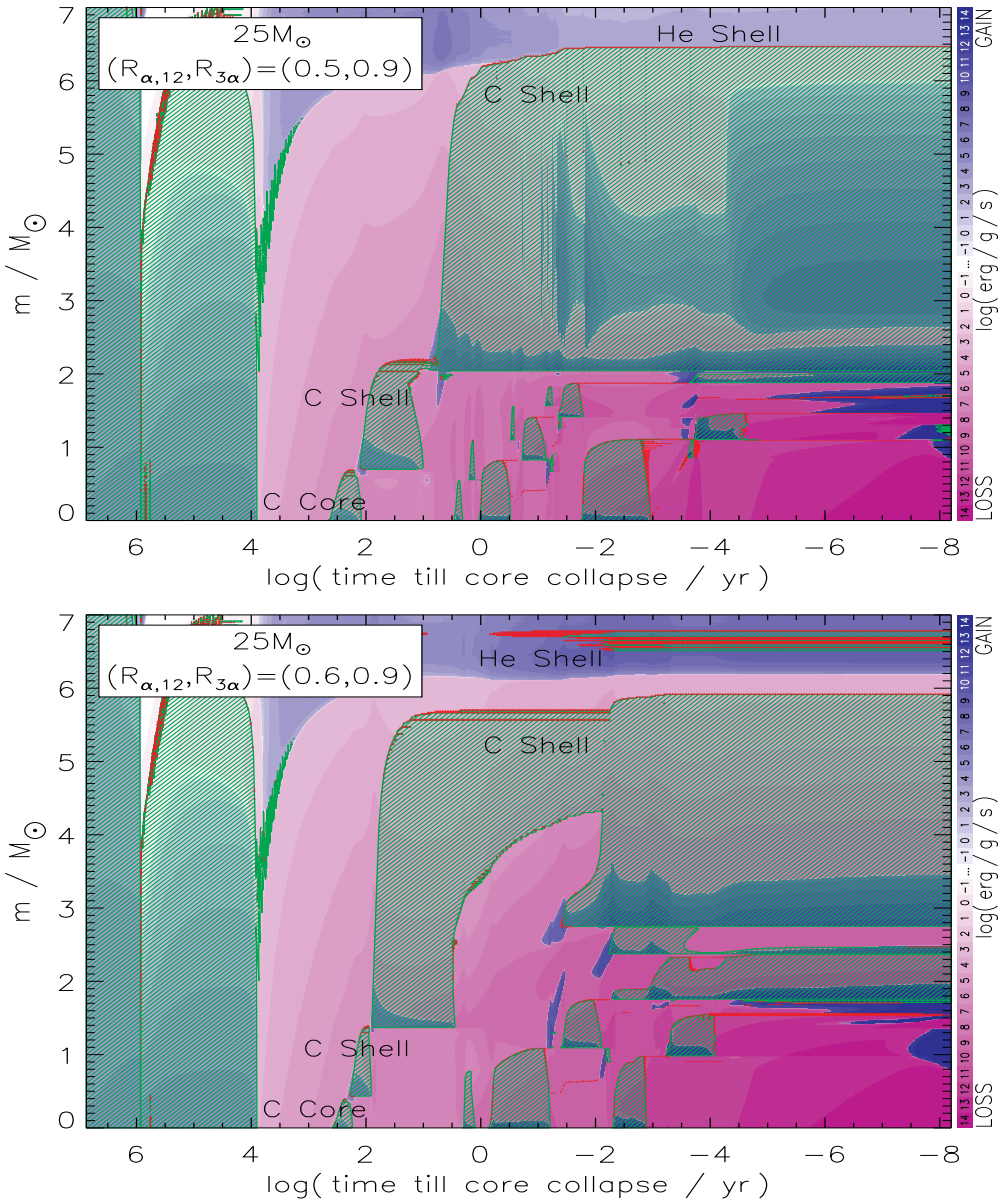

Figure 4.5: *Top*: The convection plot for the inner $7\,\mathrm{M}_\odot$ of the $(R_{\alpha,12}, R_{3\alpha}) = (0.5, 0.9)$ model. *Bottom*: The convection plot for the $(R_{\alpha,12}, R_{3\alpha}) = (0.6, 0.9)$ model. Shown are convective regions (hatch-marks), semi-convective (cross-hatching), and energy generation from nucleosynthesis given by the logarithm scale. The entire evolution from the main sequence to onset of core collapse is shown.

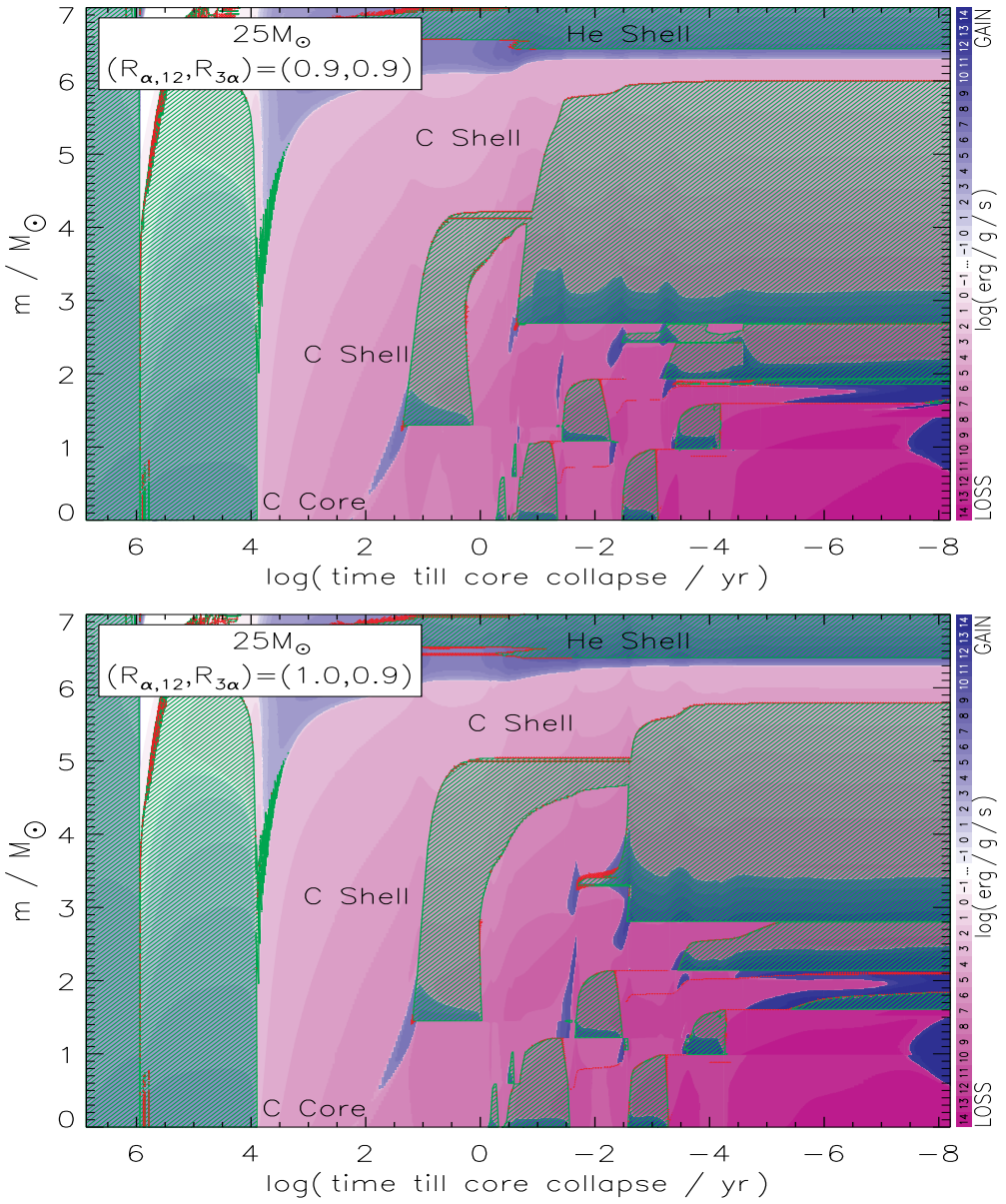

Figure 4.6: *Top*: The convection plot for the inner $7\,\mathrm{M}_\odot$ of the $(R_{\alpha,12}, R_{3\alpha}) = (0.9, 0.9)$ model. *Bottom*: The convection plot for the $(R_{\alpha,12}, R_{3\alpha}) = (1.0, 0.9)$ model. See Fig. 4.5 for a detailed description.

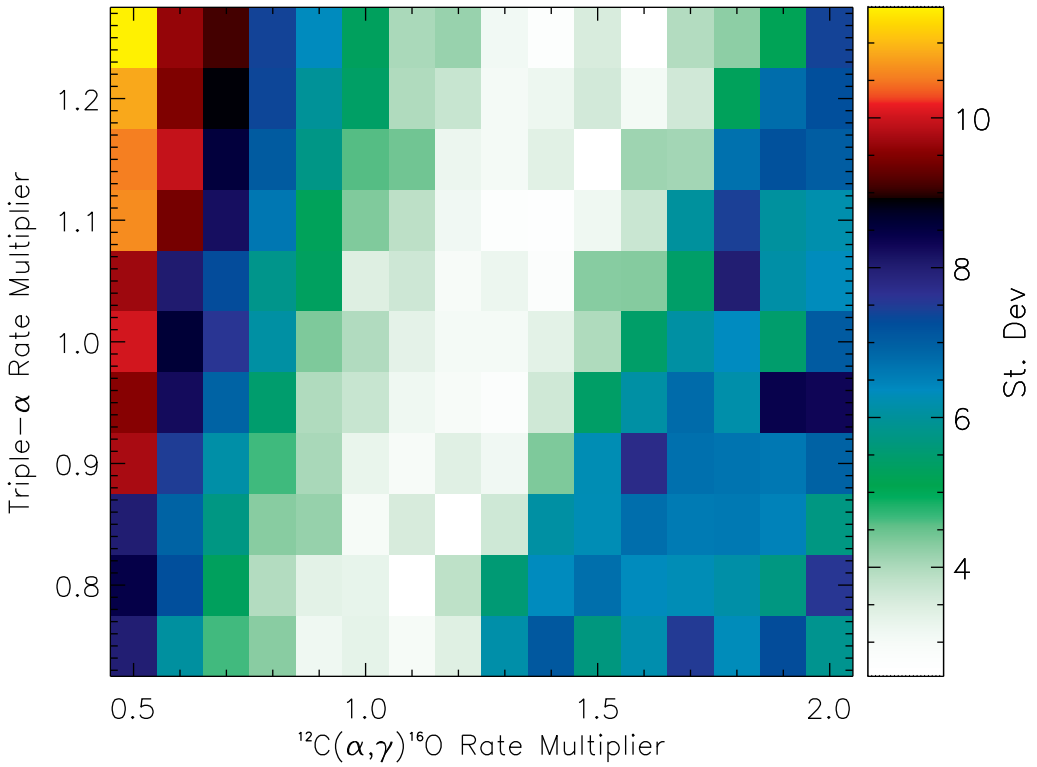

Figure 4.7: Standard deviations of the IMF averaged production factors for the intermediate-mass isotopes. The entire grid of initial masses was used.

The results in Fig. 4.7 show a region of small standard deviation ($\sigma_P \lesssim 4$) that extends across models within $(R_{\alpha,12}, R_{3\alpha}) = (1.0, 0.75)$ to $(1.6, 1.25)$ and defined with a slope (in rate multiplier ratios) close to unity with a spread of $\approx \pm 0.2$ in $R_{\alpha,12}$. The IMF averaged production factors for the weak s-process isotopes are shown in Fig. 4.8. The results for the individual masses can be found in the appendix for the weak s-only isotopes.

The results in Fig. 4.8 show a region of small standard deviation ($\sigma_P \lesssim 4$) that extends across models within $(R_{\alpha,12}, R_{3\alpha}) = (1.3, 1.0)$ to $(1.5, 1.25)$ and defined with a slope close to unity with a spread of $\approx \pm 0.1$ in $R_{\alpha,12}$. The production factors for all isotopes for the $(R_{\alpha,12}, R_{3\alpha}) = (1.3, 1.0)$ model are given in Fig. 4.9. This model lies within the region of minimum standard deviation for both the intermediate-mass and

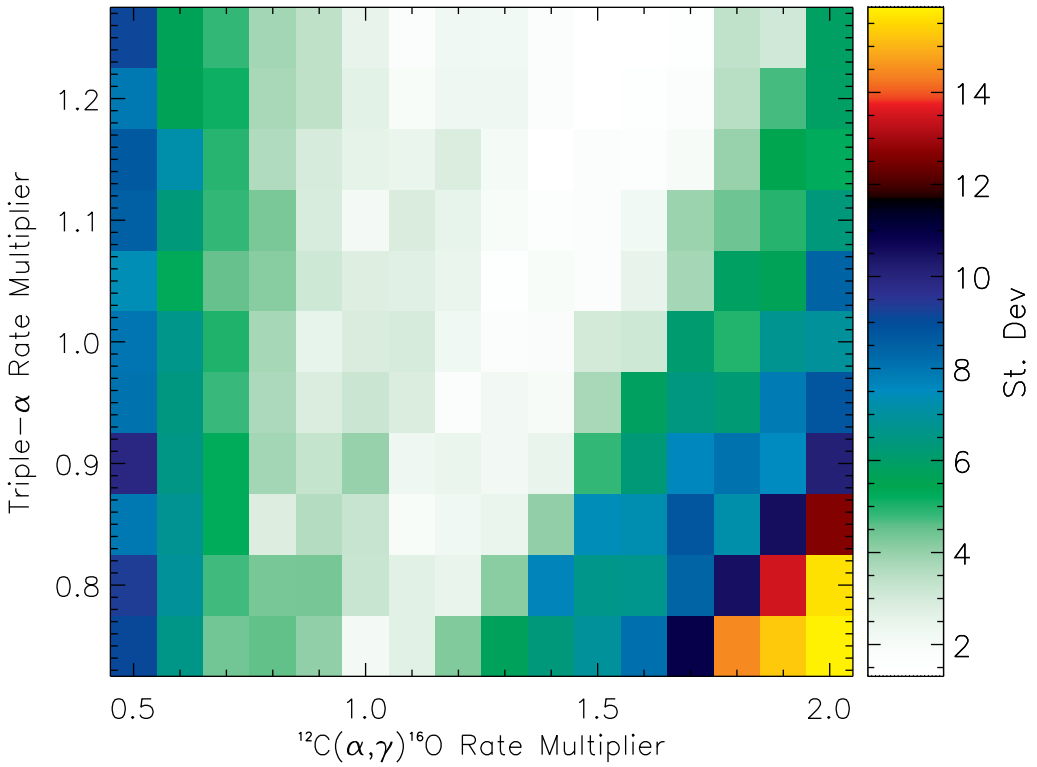

Figure 4.8: Standard deviations for the IMF averaged production factors for the weak *s*-only isotopes, using the entire grid of initial masses.

weak *s*-only isotopes. The neutrino-process isotopes, ^{7}Li, ^{11}B, ^{19}F, ^{138}La, and ^{180}Ta all show over-productions. Specifically, ^{11}B shows a production factor very close to ^{16}O ($P_{11B}/P_{16O} = 0.97$), which agrees with Austin et al. (2011); these authors also show that this ratio varies by more than a factor of 2 at different values of $R_{\alpha,12}$. The low values for most of the heavy nuclei in Fig. 4.9 are expected, as we did not include the *r*-process or *s*-process contributions from AGB stars.

4.3.3 Implications for Stellar Remnants

The analysis above assumed a perfect supernova success rate; i.e., abundances from all models were included even though some would collapse to a black hole without enriching the ISM with a SN event. We thus performed an additional analysis that removed the

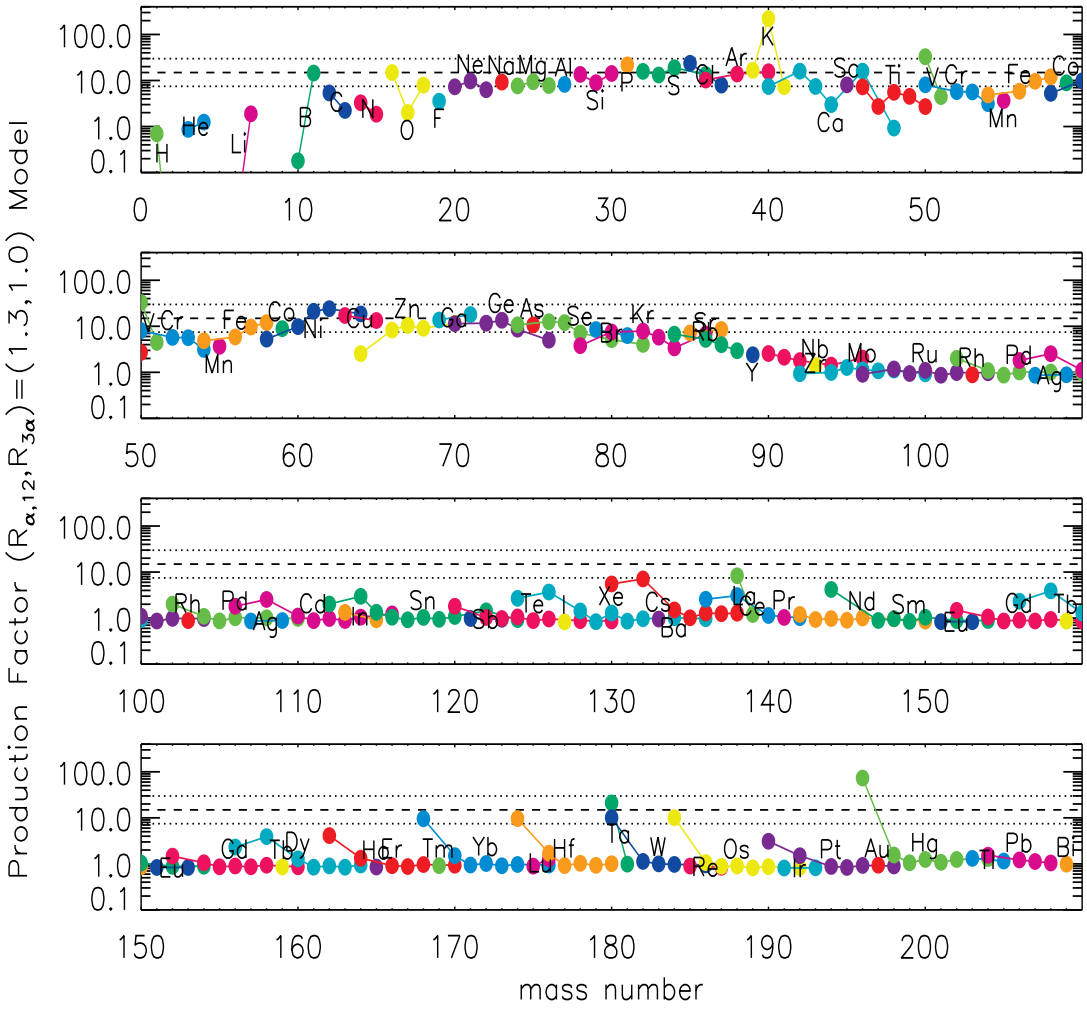

Figure 4.9: Production factors for all isotopes for the $(R_{\alpha,12}, R_{3\alpha}) = (1.3, 1.0)$ model. Shown are the ^{16}O production factor (dashed line) with ± 2 ranges (dotted lines).

models that may result in possible "failed" supernovae, prior to IMF averaging. Black hole formation following core collapse has been investigated recently by O'Connor and Ott (2011), who identified a single parameter that can be used to roughly infer the fate of the core collapse event, using 62 progenitors. This compactness parameter is defined

generally as,

$$\xi_M = \frac{M/\mathrm{M}_\odot}{R\left(M\right)/1000\,\mathrm{km}}, \tag{4.4}$$

where M is the baryonic mass, and $R\left(M\right)$ is the radial coordinate that encloses M at the time of core bounce. The relevant specific ξ_M for black hole formation is at a mass of $M = 2.5\,\mathrm{M}_\odot$, and $\xi_{2.5}$ is used by O'Connor and Ott (2011) to distinguish a possible boundary between successful and failed supernova explosions at the value of $\xi_{2.5} = 0.45$. Their models with $\xi_{2.5} < 0.45$ were concluded to be likely successful supernova, using considerations of the time-averaged neutrino heating efficiency and subject (albeit mildly) to the equation of state (EOS) employed.

A more recent analysis of over 100 supernova simulations by Ugliano et al. (2012) have resultant NS and BH mass ranges that are compatible with a possible paucity of low mass BHs, which may imply a lower $\xi_{2.5}$ value than used by O'Connor and Ott (2011). A more refined boundary of $\xi_{2.5} \approx 0.25$ has been proposed by Woo (2012) (see also, Brown and Woosley, 2013), and will be adopted in the present work.

In our analysis all models are assumed to have the same final kinetic energy for the ejecta (1.2 B), however, the explosion energies can vary. A larger explosion energy would cause successful SNe above $\xi_{2.5} = 0.25$, since now larger densities would be required to overcome this larger energy and prevent a successful SN explosion. It would also cause more material above the Fe core to escape the gravitational potential, resulting in a smaller mass cut and remnant mass for models already below this limit.

The $\xi_{2.5}$ values were computed for each model. The distribution of $\xi_{2.5}$ values for the $25\,\mathrm{M}_\odot$ models is given as an example in Fig. 4.10. Figures for the $\xi_{2.5}$ values of the other masses can be found in Appendix E. Since we do not calculate the compactness factor using an actual core bounce, but instead a piston model, we investigated the sensitivity of the compactness factor to this assumption by also calculating $\xi_{2.5}$ at a point in the pre-SN collapse when the inward velocity was $10^8\,\mathrm{cm\,s^{-1}}$. We found a small impact on the models, with 15 (out of 2112) models that successfully explode ($\xi_{2.5} \leq 0.25$) using the pre-SN structure that otherwise fail.

For the $25\,\mathrm{M}_\odot$ models, those with low $R_{\alpha,12}$ values are favored for successful SNe events, in addition to a local minimum in $\xi_{2.5}$ defined by a narrow strip close to the

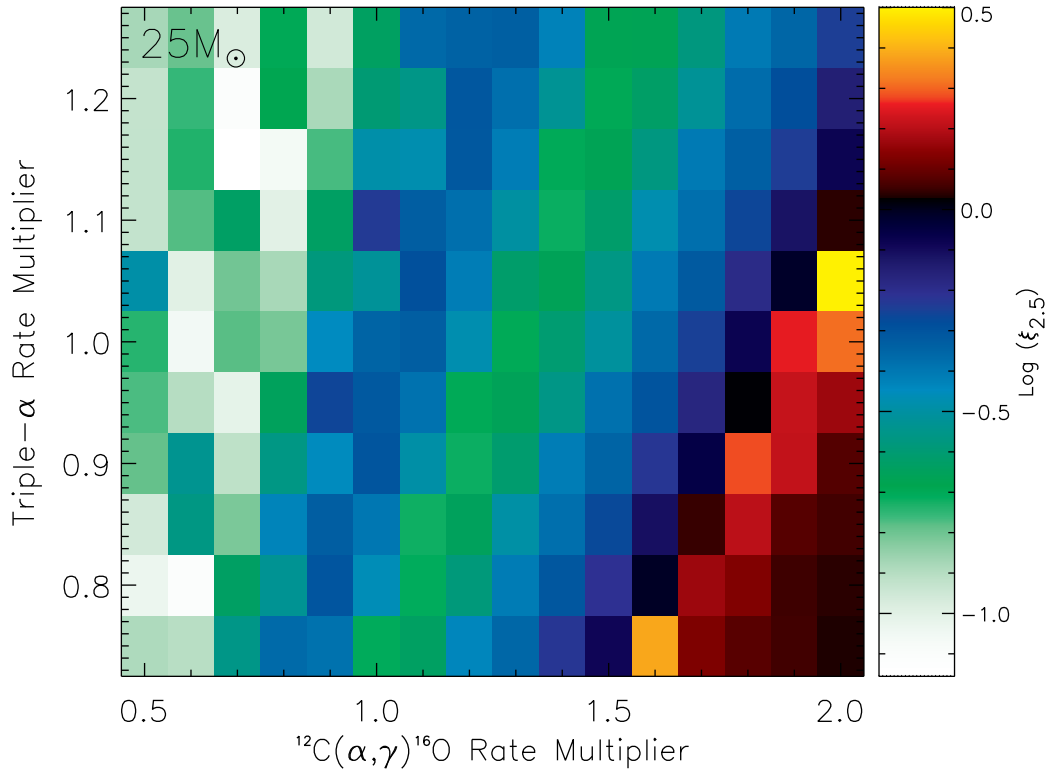

Figure 4.10: The distribution of the logarithm of $\xi_{2.5}$ values for the $25\,M_\odot$ models.

centroid value for this rate. In comparison, the $12\,M_\odot$, $13\,M_\odot$, $14\,M_\odot$, and $15\,M_\odot$ models *all* explode as successful SNe, whereas the $16\,M_\odot$ models have only 7 of 176 models that fail, and the $17\,M_\odot$ models have 10. The $18\,M_\odot$ models have 20 failed SNe, all above $R_{\alpha,12} \geq 0.9$ and spanning the whole range of $R_{3\alpha}$. Among our models of $20\,M_\odot$, several fail towards high $R_{\alpha,12}$ and low $R_{3\alpha}$ values, with a fairly delineated boundary between successful and failed SNe beginning at a multiplier pair value of $(R_{\alpha,12}, R_{3\alpha}) = (1.2, 0.75)$, and ending at $(1.8, 1.25)$. The $22\,M_\odot$ and $27\,M_\odot$ models show the same behavior as the $20\,M_\odot$ models but with a boundary favoring more BHs, delineated by a slope defined by $(1.0, 0.75)$ and $(1.4, 1.25)$ for the former, and $(0.5, 0.75)$ and $(0.8, 1.25)$ for the latter. Among our models of $30\,M_\odot$, there are 10 that explode at $R_{\alpha,12} = 0.5$ along with a strip of successful SNe from $(0.8, 0.75)$ to $(1.3, 1.25)$.

The yields from the stellar winds of all models, as well as the explosive yields of

the models that satisfy the condition $\xi_{2.5} < 0.25$ were then averaged over an IMF. The result is given in Fig. 4.11 for the intermediate-mass isotopes and in Fig. 4.12 for the weak s-only isotopes.

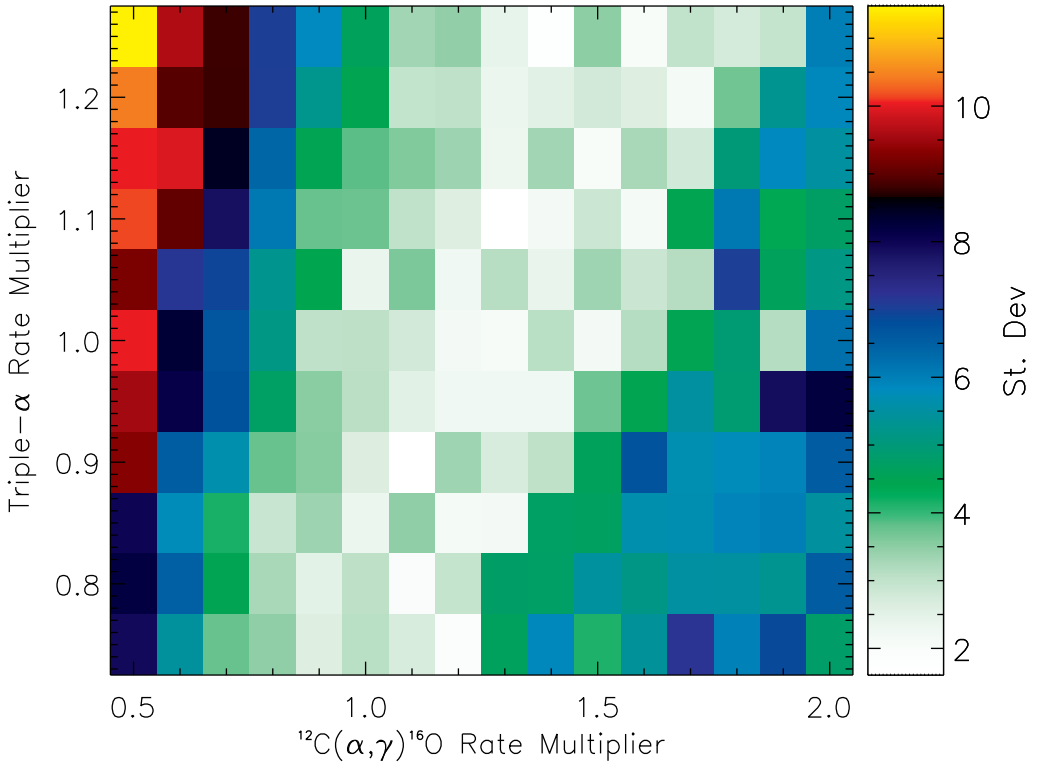

Figure 4.11: Standard deviations for the IMF-averaged production factors for the intermediate-mass isotopes. The yields from all stellar winds and the explosive yields from models that satisfy the condition $\xi_{2.5} < 0.25$ were used in the averaging.

As stated, Fig. 4.7 showed a small standard deviation region ($\sigma_P \lesssim 4$). This region extended across models within $(R_{\alpha,12}, R_{3\alpha}) = (1.0, 0.75)$ to $(1.5, 1.25)$ and was defined with a slope close to unity with a spread of $\approx \pm 0.2$ in $R_{\alpha,12}$. The impact of the compactness parameter for the intermediate-mass isotopes is that the ($\sigma_P \lesssim 4$) region from Fig. 4.7 is still observed in Fig. 4.11, but the latter has models in this region whose standard deviation has σ_P larger by 1, although this effect may be less if an even finer mass grid was used. We conclude that the current 25 % uncertainty range of $R_{\alpha,12}$

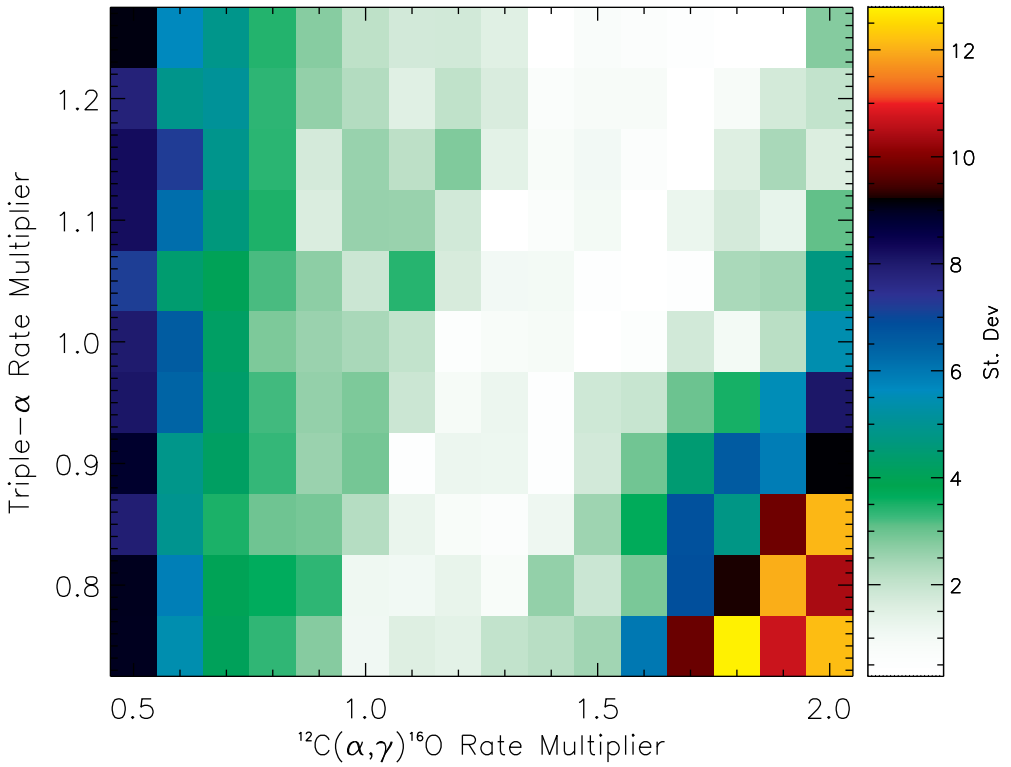

Figure 4.12: Standard deviations for the IMF-averaged production factors for the weak *s*-only isotopes. The yields from stellar winds and from the explosive yields of models that satisfy the condition $\xi_{2.5} < 0.25$ were used in the averaging.

agrees with observations. The region of small standard deviations for Fig. 4.11 has a slope defined approximately by $(R_{\alpha,12}, R_{3\alpha}) = (1.1, 0.75)$ to $(1.6, 1.25)$ with a spread of $\approx \pm 0.2$ in $R_{\alpha,12}$ for $R_{3\alpha} \lesssim 0.95$, and spread of $\approx \pm(0.3 - 0.4)$ in $R_{\alpha,12}$ for $R_{3\alpha} \gtrsim 0.95$. It is then possible to define the relation,

$$R_{\alpha,12} = 1.0 R_{3\alpha} + (0.25 \pm 0.3). \tag{4.5}$$

For a chosen $R_{3\alpha}$ value in the range 0.75 to 1.25, Equation 4.5 gives a range of $R_{\alpha,12}$ values that best match observations, taking into account only the intermediate-mass isotopes.

The impact of the compactness parameter on the weak *s*-only isotopes is that the

($\sigma_P \lesssim 4$) region from Fig. 4.8 becomes somewhat *more* sharply defined, in that the models above $R_{3\alpha} \approx 0.95$, from $R_{\alpha,12} \approx 1.0$ to 1.3 have increased standard deviations by $\approx 1-2$. In Fig. 4.12 there is a region of small σ_P with a slope defined by $(1.1, 0.75)$ to $(1.6, 1.25)$, with an average spread of $\approx \pm 0.2$ in $R_{\alpha,12}$. This result should be interpreted with care, however, since the IMF averaging is subject to the $X_{i,\mathrm{w}}$ values, taken from an approximate analysis of weak *s*-process contributions to the solar abundances (see Section 3.2.5.1) which uses only the relevant nuclear physics and does not employ stellar modeling. Furthermore, the decomposition of the weak *s*-process contributions does not address recent works that indicate possible evidence for an increase of the *s*-elements in the Galactic disk (Mashonkina et al., 2007; Maiorca et al., 2011, 2012; Jacobson and Friel, 2012). It is unclear what impact this would have on our analysis, however, since the weak *s*-isotopic abundances do not dominate their respective elemental abundances. Despite these issues, the weak *s*-process analysis in the present work is a step in the right direction; one simply cannot compare the weak *s*-process yields directly to the solar abundances (which contain main *s*-process abundances also). We thus caution the reader that whereas our weak *s*-process analysis is an improvement, it is also weakly constrained.

The best values for the helium rates from our analysis should agree with observations for *both* the intermediate-mass and weak *s*-only isotope sets. We thus computed the average of the standard deviation values for both sets (Fig. 4.13). Whereas the optimal values for the helium burning rates from our analysis should reproduce the observed abundance ratios for both the intermediate-mass and weak *s*-only isotope sets, the two sets will not be at the same level of production factor, because they have different astrophysical natures and galactic chemical evolution histories. For example, the weak *s*-process, being of secondary nature, is overproduced by a factor of ≈ 2.0 at solar metallicity and less is made at lower metallicities, yet their *relative* abundance ratio should be about solar - and this is what we match. In contrast, the intermediate-mass isotopes are primary and should be produced at a solar level, and again within this subgroup the isotope ratios should be at solar level. Hence, they were analyzed separately before the results were combined, instead of computing the standard deviations for all isotopes as a single group. The ratio of weak *s*-process to intermediate-mass isotopes is not the solar abundance ratio and not expected to be, so fitting both at once would be wrong.

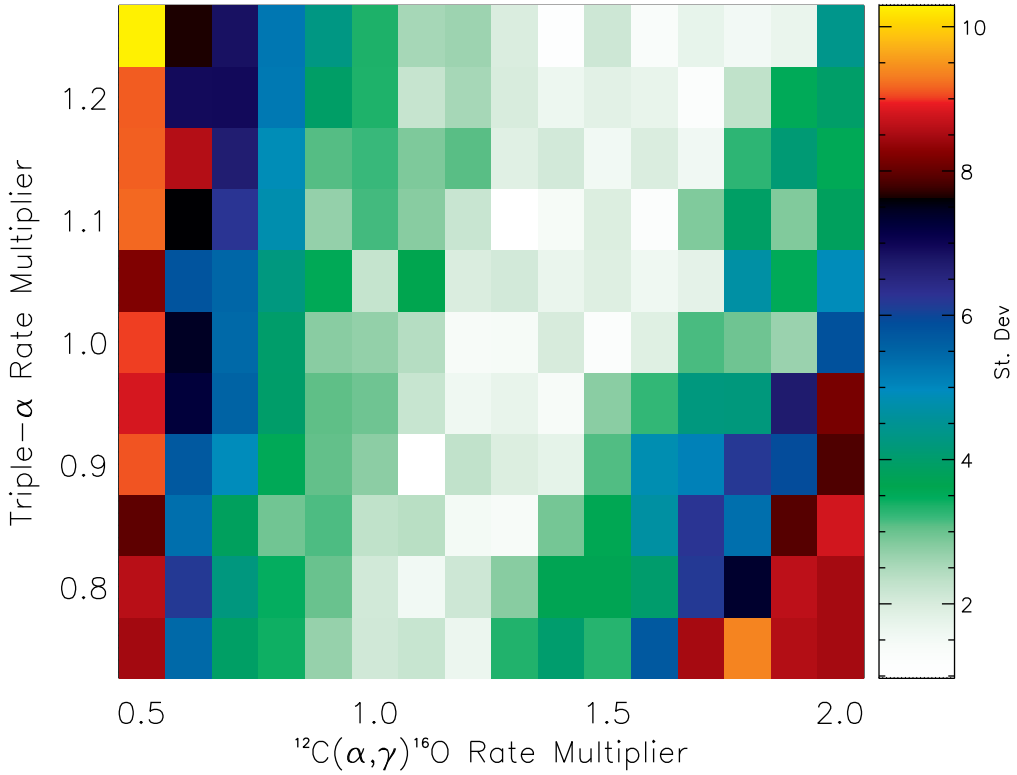

Figure 4.13: The average of the standard deviations for the production factors of the intermediate-mass (Fig. 4.11) and weak s-only isotopes (Fig. 4.12).

The region of small standard deviations for Fig. 4.13 has a slope defined approximately by $(R_{\alpha,12}, R_{3\alpha}) = (1.1, 0.75)$ to $(1.6, 1.25)$ with a spread of $\approx \pm 0.1$ in $R_{\alpha,12}$ for $R_{3\alpha} \lesssim 0.95$, and spread of $\approx \pm(0.2 - 0.3)$ in $R_{\alpha,12}$ for $R_{3\alpha} \gtrsim 0.95$. We then define the relation,

$$R_{\alpha,12} = 1.0 R_{3\alpha} + (0.35 \pm 0.2). \tag{4.6}$$

For a chosen $R_{3\alpha}$ value in the range 0.75 to 1.25, Equation 4.6 gives a range of $R_{\alpha,12}$ values that agree with observations, taking into account both the intermediate-mass and weak s-only isotopes. Note that this relation does not accurately define the regions of small standard deviation for either isotope set individually (see Fig. 4.11 and Fig. 4.12). Note further that the region of small σ_P in Fig. 4.13 is "noisy," and has values along

the line of best fit that are not minima of this region. We must re-emphasize that the analysis used is approximate, and the region contains values that may change if we change the parameters of the model or improve the completeness of the models included. Hence, whereas we can define this region, the analysis is likely insufficient to reliably distinguish between neighboring values within it. Subject to the approximations employed in the analysis, coordinate pairs for the reaction rate multipliers that satisfy this relation results in nucleosynthesis that equally agrees with current observations for both the intermediate and weak *s*-only isotopes, as far as the present study can determine.

We also explored the dependence of our results on the IMF used in Equation 5.1. We computed IMF averaged production factors for both the intermediate and weak *s* isotope list using two modified Salpeter IMFs (+0.3 and −0.3 added to the exponent). For the weak *s*-isotope list, both modified IMFs resulted in a difference in IMF-averaged production factors by $\leq 6\,\%$ in the region of best fit rates identified by Equation 4.6. For the intermediate-mass isotope list, both modified IMFs resulted in a difference in IMF averaged production factors by $\leq 4\,\%$ in the region of best fit rates. We thus believe the choice of IMF has only a small impact on the results, provided a reasonable IMF is chosen.

The stellar model KEPLER, however, is only approximate: convection is treated using mixing length theory, effects of rotation, binary star evolution, and magnetic fields are ignored, many reaction rates and mass loss rates are not well enough known, the opacities have uncertainties, etc. Some of these effects have been investigated. For example, Chieffi and Limongi (2012) studied the impact of rotation on solar metallicity massive stars in the range $13 - 120\,\mathrm{M}_{\odot}$, and found over-productions of F and slight over-productions of weak *s*-process isotopes. Another study by Iliadis et al. (2011) found several reaction rate uncertainties that influence massive star Al production, and found a range of ^{26}Al larger than those found by Tur et al. (2007). Although it was not the purpose of the present work to address the effects of the approximations in the stellar models, it is important to note that they can have a non-negligible impact on the results in some cases. Additionally, we interpolated yields across a finite IMF sampling and only for solar metallicity CCSNe stars instead of a full galactic chemical evolution model from big bang nucleosynthesis to the present Galaxy including all nucleosynthesis

sources. For the isotopes we compare in this work, however, the assumption that solar composition stars should produce about their solar ratios is reasonable.

4.3.4 Variations in Carbon Mass Fractions and Remnant Mass

The baryonic mass of the progenitor of the remnant depends on the central carbon mass at the end of core-He burning[1]. An increase in $R_{3\alpha}$ or decrease in $R_{\alpha,12}$ results in an increase in the carbon abundance. An example of the resulting trend in baryonic mass is given in Fig. 4.14, for the $25\,M_\odot$ models. Figures for the baryonic masses of the other models can be found in Appendix E.

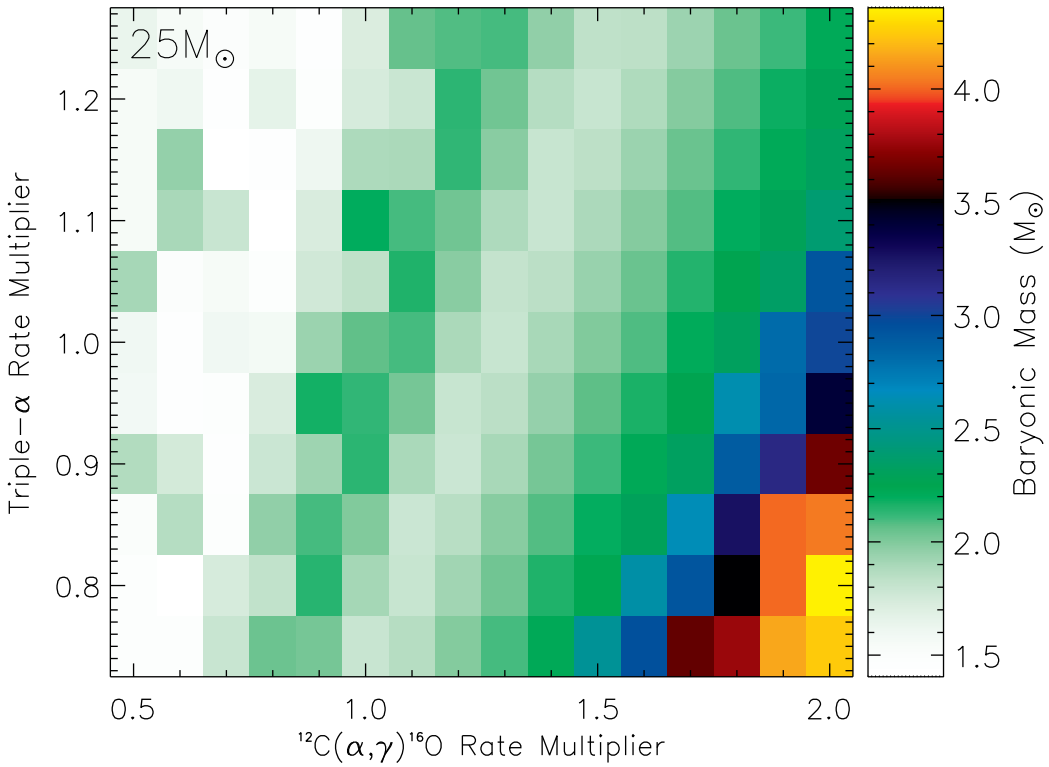

Figure 4.14: The baryonic mass of the progenitor of the remnant for the $25\,M_\odot$ models as a function of the $R_{3\alpha}$ and $R_{\alpha,12}$ multipliers.

[1]The gravitational mass of the remnant also depends on type, formation scenario (Zhang et al., 2008), and equation of state (Lattimer and Prakash, 2001).

Fig. 4.14 shows that there is a decrease in baryonic remnant mass for increasing $R_{3\alpha}$ and decreasing $R_{\alpha,12}$. This is because a larger carbon abundance at the end of core-He burning can support longer and more energetic carbon shell burning episodes, which allows the core to cool to lower entropy, yielding a smaller progenitor (Woosley et al., 2003; Tur et al., 2007). Note the apparent local maximum beginning at a $R_{\alpha,12}$ multiplier value of ~ 0.7 and extending to ~ 1.2, which coincides with the $\xi_{2.5}$ local maximum in Fig. 4.10. This may be caused by non-convective core-C burning that results in a more compact star and more massive baryonic remnant (Heger et al., 2001). This non-monotonicity has also been observed by Tur et al. (2007).

The cut-off mass for the remnant becoming a BH versus a NS is difficult to assess. A fraction of the NS progenitor is radiated away by neutrinos, which is dependent on the EOS (Lattimer and Prakash, 2001). A larger maximum for NS masses result from the "stiffest" EOS (those with largest pressures for a given density), and an upper limit of $M_{\rm high} = 2.9\,{\rm M}_\odot$ has been calculated by Tolos et al. (Tolos et al., 2012). Observational evidence places this limit between $2.0\ {\rm M}_\odot \lesssim M_{\rm high} \lesssim 2.5{\rm M}_\odot$, although this may only be an indication of the limit to the mass that can possibly be accreted in a binary system (Lattimer and Prakash, 2010).

An example of the correlation between baryonic mass and central carbon mass at the end of core-He burning can be seen by comparing Fig. 4.14 with Fig. 4.15 for the $25\,{\rm M}_\odot$ models. Figures for the carbon mass fractions of the other models can be found in Appendix E.

As shown in Fig. 4.15, high $R_{3\alpha}$ and low $R_{\alpha,12}$ multipliers result in higher carbon mass fractions as expected, whereas low $R_{3\alpha}$ and high $R_{\alpha,12}$ multipliers result in lower carbon mass fractions. Comparing Fig. 4.14 and Fig. 4.15 shows an overall inverse relation between the carbon mass fraction and the remnant mass (see also Figs. E.4 and Fig. E.5).

4.4 Conclusions

This chapter studies the effect of changing the helium burning rates $^{12}{\rm C}(\alpha,\gamma)^{16}{\rm O}$ and $^{4}{\rm He}(2\alpha,\gamma)^{12}{\rm C}$ independently to map the effects on stellar evolution and nucleosynthesis. We follow the entire evolution from hydrogen burning through the SN explosion,

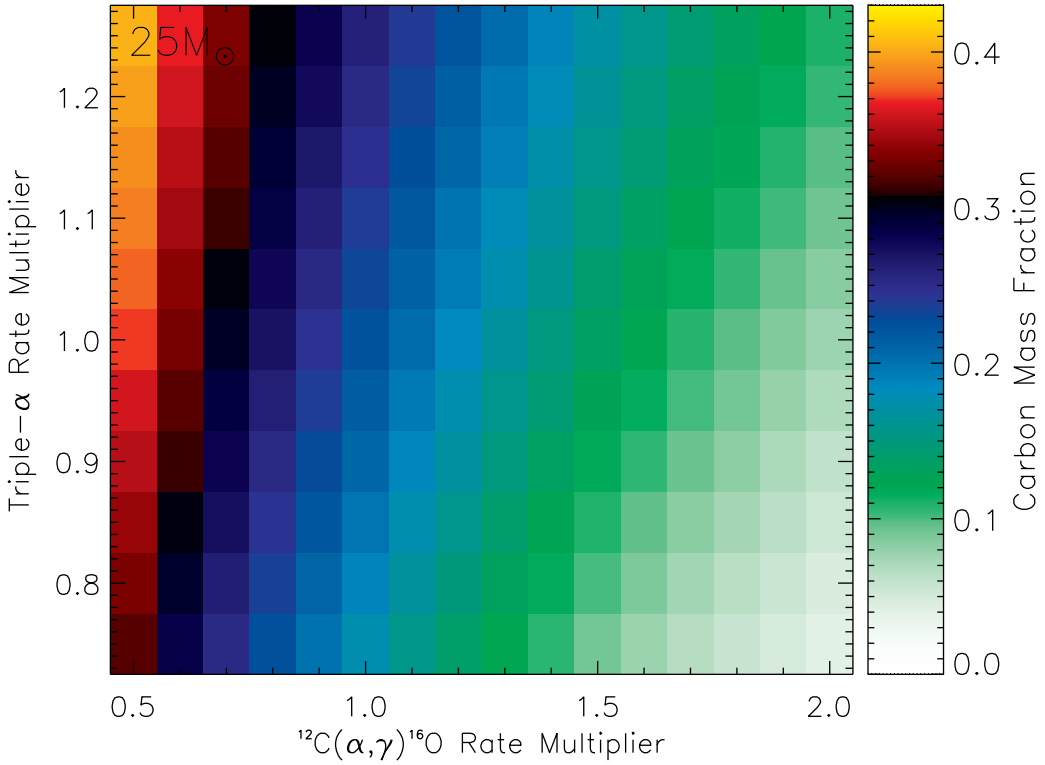

Figure 4.15: Central carbon mass fraction at the end of core-He burning for the $25\,M_\odot$ models as a function of the $R_{3\alpha}$ and $R_{\alpha,12}$ multipliers.

including wind and SN yields, and considering fallback, mixing, and which stars make SNe ($\xi_{2.5} < 0.25$) or collapse to BHs without SN, and finally integrating the yields over an IMF. In total, we calculated nucleosynthesis for a grid of 176 models for each of 12 stellar masses from $12\,M_\odot$ to $30\,M_\odot$ (2112 models). This is by far the most extensive investigation on the effects of rate variations for the helium burning reactions to date, and the first to use updated solar abundances (Lodders, 2010).

Combining constraints on intermediate-mass and weak *s*-only isotopes, we find a best fit for rate multipliers $(R_{\alpha,12}, R_{3\alpha}) = (1.1, 0.75)$ to $(1.6, 1.25)$ with an average spread of $\approx \pm 0.2$ in $R_{\alpha,12}$. More generally, we find a relation between $R_{\alpha,12}$ and $R_{3\alpha}$ for good fits to nucleosynthesis given by $R_{\alpha,12} = 1.0 R_{3\alpha} + (0.35 \pm 0.2)$ in the range $R_{3\alpha} = 0.75$ to 1.25. We also provide the line of best fit using only the intermediate-mass isotope list,

given by $R_{\alpha,12} = 1.0 R_{3\alpha} + (0.25 \pm 0.3)$.

In this analysis, all models are assumed to have a final kinetic energy of the ejecta of 1.2 B. Real supernovae have a range of explosion energies. A larger explosion energy would allow successful SNe above the $\xi_{2.5} = 0.25$ limit, since now larger densities would be required to overcome this larger energy to prevent a successful SN explosion. It would also cause more material above the Fe core to escape the gravitational potential, resulting in a smaller mass cut and remnant mass for models already below $\xi_{2.5} = 0.25$.

Small changes in the reaction rates can result in significant differences in the convection structure of the star, which is not just a numerical artifact but due to the physics of shell burning. This introduces "noise" into the comparisons, and is a warning for calculations done for specific cases; the general conclusion may be influenced by isolated processes. Given an astrophysical model that includes all the important physics with perfectly known physical input parameters, the values for the standard deviations shown in the figures should have a minimum region reflecting only the uncertainties in isotopic abundances. We know, however, that the stellar model used is only approximate and can affect the nucleosynthesis, as discussed in Section 4.3.3. These approximations result from parametrizing multi-dimensional mixing processes in 1D codes and also from uncertainties in the nuclear physics, hence they are inherent in all models. For the isotopes we compare in this work, however, the assumption that solar composition stars should produce about their solar ratios within each subgroup is reasonable.

If we change the parameters of the models or improve the completeness of the models, we expect the best fit rates to change also. Hence it is not necessarily the case that the best fit rate for an observable (in our case the abundances) coincides with the true rate. This suggests that the best reaction rates we obtain in our analyses are at some level effective rates. Analogous procedures have been used in many areas of physics. For example, in the shell model of nuclear physics, an effective nucleon-nucleon interaction (close to but not identical to the true interaction) is chosen to fit the low-lying spectra of many nuclei, and this reaction is very successfully used to predict other observables. Similarly, we think that the present procedure can provide better predictions of other astrophysical quantities, remnant masses or neutrinos synthesis of certain isotopes, for example.

Whereas our comparisons do not have the power to accurately determine the helium

burning reaction rates, they do show that the experimental values are not too far from the truth and that changes needed to compensate (in an effective interaction sense) for model uncertainties are not large. Thus, similar calculations necessary to assess the situation, as overall model uncertainties decrease, will be less demanding; we have shown that a significant part of the uncertainty space is irrelevant. It is also clear that if one of the two helium burning reactions is much better determined, the effective rate for the other will be much better determined. For example, if it is later determined that $R_{3\alpha}$ is near 1.25 times the present experimental centroid value, then the best fit $R_{\alpha,12}$ will be 33 % larger than the experimental centroid value. It may also happen that if both reactions become well determined, they would not agree with the effective interaction that best reproduces the abundances. In such an event, this work may still serve to provide an evaluation of other model uncertainties and point the way to improvements (Sukhbold and Woosley, 2013).

Chapter 5

Dependence of Stellar Nucleosynthesis on Initial Composition

5.1 Introduction

The final nucleosynthesis from massive star simulations depend on the initial isotopic composition. Ideally, the initial composition would come directly from observations, but unfortunately isotopic data is scarce except for the Sun. A second choice is to use galactic chemical evolution (GCE) models to provide the needed abundances. Since GCE models use different prescriptions, for not only estimated quantities such as infall, but also for stellar model yields, the sub-solar abundances computed by different GCE models are necessarily model-dependent. Additional limitations of GCE models were discussed in the previous Chapter.

A common estimation independent of GCE modeling is to linearly interpolate abundances as a function of metallicity between the known endpoints of their solar and big bang nucleosynthesis (BBN) values. This method effectively assumes that all metals are made in primary processes (i.e., directly from H and He), since primary processes produce abundances that scale linearly in metallicity. Such an approach is reasonable since the majority of metals by mass are indeed of primary origin, such as the light α-isotopes.

An obvious error in this method, however, is that isotopes made in secondary processes (i.e., from pre-existing metals) are approximated poorly, since they produce abundances that scale quadratically in metallicity. Using the linear interpolation method, secondary processes are *over-estimated* at sub-solar metallicities and possibly *under-estimated* at super-solar metallicities. Furthermore, this method also incorrectly over-approximates Type Ia SNe yields at low metallicities ($[Z] \lesssim -1$). Although Type Ia SNe are primary events, they cannot contribute to the ISM until sufficient time elapses for white dwarfs to evolve from a low mass star and then accrete enough material to explode (assuming the binary accretion model, e.g., Ruiter et al., 2010, and references therein). Hence, these events experience a time delay in their contributions to the ISM not accounted for with a simple linear interpolation — which implicitly assumes Type Ia contributions exist at all metallicities. It is presently unknown in detail how these errors impact the final nucleosynthesis.

In this chapter, we present a brief study on the dependence of the final massive star nucleosynthesis on changes in the initial composition. The initial composition for the stellar models is computed in two ways. The first is the scaled solar abundances discussed above (hereafter denoted SS), where abundances are linearly interpolated between their solar values (taken from Lodders, 2010) and BBN values (taken from Fie, 2002). In the second method, the initial composition is computed using the scaling model developed in Chapter 3 (hereafter denoted GG). As previously discussed, in this model secondary processes and Type Ia SNe abundances are treated separately from primary processes, which offers a correction to linearly interpolating all abundances. The purpose of this preliminary study is to make a first assessment of the impact of these corrections on the stellar models and nucleosynthesis yields. It is expected that since the GG compositions are matched to observational data, the models using them will produce abundances that do also, compared to SS.

This chapter has the following outline: In Section 5.2 we describe the stellar models and procedures used in the analysis, and in Section 5.3 we present the results of the models and general features of the differences in yields across the range of metallicities. In Section 5.4 we give a few concluding remarks.

5.2 Methodology

5.2.1 Initial Compositions

The initial composition affects the final stellar yields in two ways: it directly impacts the nucleosynthesis by constraining the abundances available for nuclear reactions, and it also affects the stellar structure and subsequent evolution. The latter is not an immediate effect of the initial composition on the final nucleosynthesis, but can affect the yields by changing how the star evolves (e.g., the regions that are convective). Ideally, we like to distinguish between these two effects. This would be implemented by running four grids of stellar models: i) using the scaling model abundances for the nucleosynthesis and for computing the structure (GG), ii) using the scaling model abundances for the nucleosynthesis but use the linear interpolation abundances for computing the structure (GS), iii) using the linear interpolation abundances for the nucleosynthesis and for computing the structure (SS), and iv) using the linear interpolation abundances for the nucleosynthesis but use the scaling model abundances for computing the structure (SG). A complete analysis using these four grids would allow us to isolate the differences in yields from both effects, for both input compositions. In the present study, we restrict our analysis to i) and iii) only; the full set of grids is left for future work.

The figures showing the ratio of initial compositions (GG/SS) for all initial metallicities are given in Appendix D. The initial compositions of SS and GG are identical for [Z] = 0, as here both are simply the solar abundance pattern Lodders (2010). When the metallicity decreases, the ratio GG/SS for many of the isotopic abundances becomes increasingly negative. This occurs because the GG compositions scale secondary and Type Ia SNe isotopic abundances at a larger rate than the linearly-scaled SS. The *s*-process peak isotopes (such as ^{134,136}Ba), γ-process isotopes (such as ^{156,158}Dy), and Fe-peak isotopic abundances all display this effect, which is greatest at the lowest initial metallicity considered ([Z] = -4). At super-solar metallicities the reverse is true. Here the increased scaling rate of *s*-process and γ-process isotopes pushes the GG/SS ratio more positive, however, the treatment of Type Ia SNe in the scaling model (a $\tanh(x)$ function scaling, see Equation 3.6) flattens the scaling rate for these relatively abundant isotopes upon reaching solar metallicities so as to not over-produce them relative to observations. The third *s*-process peak isotopes (^{204,206,207,208}Pb and ^{209}Bi) depart

from the aforementioned trend. These isotopes are presently understood to be from the main *s*-process at low metallicities Bisterzo et al. (2010), hence the GG/SS ratio is positive for these isotopes at low metallicities, and negative at super-solar metallicities in accordance with their believed mechanism for production (discussed further in Sections 2.7.3 and 3.3.3). A table giving numerical values for both SS and GG compositions for [Z] $= -1, -3$ is given in Table B.2 of Appendix B.

5.2.2 Stellar Models and Numerical Methods

All models were computed using the KEPLER code Weaver et al. (1978); Rauscher et al. (2002). We used 8 different initial stellar masses $M/M_{\odot} = 13,\ 15,\ 17,\ 20,\ 22,\ 25,\ 27,$ and 30. For each initial mass, a grid of 13 models were run with the following initial metallicities, [Z] $= +0.2, +0.1, 0.0, -0.2, -0.4, -0.6, -0.8, -1.0, -1.5, -2.0, -2.5, -3.0,$ and -4.0, where $[Z] \equiv \log(Z/Z_{\odot})$. This entire grid of 104 models was run for both the SS and GG methods. twice, once with the SS initial composition, and once with the GG.

All stellar models were first evolved through hydrostatic burning until the Fe-core collapsed, and an inward velocity of $10^8\,\mathrm{cm\,s^{-1}}$ was reached. The explosion mechanism in KEPLER for the resulting supernova is modeled as a mechanical piston that imparts an acceleration at constant Lagrangian mass coordinate to provide the desired total kinetic energy of the ejecta, taken in these models to be 1.2 B (1 B $= 10^{51}$ erg) at 1 year after the explosion. For details on the parametrization of the explosion used in KEPLER see Woosley and Heger Woosley and Heger (2007), and references therein. For details on the treatment of convection and mixing see Woosley and Weaver Woosley and Weaver (1988) and Woosley et al. Woosley et al. (2002), and a discussion of the mass cut is given by Tur et al., and Heger and Woosley Tur et al. (2007); Heger and Woosley (2010).

The final nucleosynthesis for all models includes yields from stellar winds. The explosive yields are taken only from models that are likely to successfully explode as SNe, using the compactness parameter filter cutoff ($\xi_{2.5} \leq 0.25$) discussed in Section 4.3.3. The final yields for the GG and SS models were then averaged at each metallicity, by

integrating over the Salpeter initial mass function (IMF),

$$Y_i^* = \sum_j \int_{m_j}^{m_{j+1}} \xi(m) \cdot (s_{i,j} \cdot [m - m_j] + Y_{i,j}) \cdot dm, \tag{5.1}$$

$$X_i = \frac{Y_i^*}{\sum_k Y_k^*}. \tag{5.2}$$

In Equation 5.1, the IMF interpolated yield mass for isotope i is given by Y_i^*, and the Salpeter mass spectrum is $\xi(m) = C \cdot m^{-2.35}$, where C is the proportionality constant. The mass grid used for the integrations are the *net* masses, defined as the baryonic remnant masses subtracted from the initial stellar mass grid. Yields are linearly interpolated between adjacent masses in the integral, with the slope defined by, $s_{i,j} = (Y_{i,j+1} - Y_{i,j}) / (m_{j+1} - m_j)$, where $Y_{i,j}$ is the yield mass (*in grams*) of isotope i from a model with initial mass m_j. In Equation 5.2, the mass fraction of isotope i is given by X_i, the sum in the denominator runs over all isotopes. Hence, at every initial metallicity of our grid, the yields from the GGM models computed at that initial metallicity were IMF averaged, and the resulting yields were expressed as mass fractions. The same was done for the SSM models.

We now address the final IMF averaged yields of the models, which for brevity shall hereafter be denoted simply as "yields."

5.3 Results and Discussion

Obviously, at solar metallicity both models have the same composition and therefore we get identical results. The interesting question, however, is which sub-solar models produce elemental ratios that agree with expected trends. We proceed by addressing different results between the models.

5.3.1 Iron Production and Neutron-to-Seed Ratio

Due to the treatment of Type Ia SNe in the GG models, the initial Fe abundance is less than the SS models at all sub-solar metallicities (Fig. 5.1, *Top*). We find quite similar final Fe yields for both models (Fig. 5.1, *Bottom*) — Fe is primary and dominated by

explosive yields, hence independent of the initial composition.

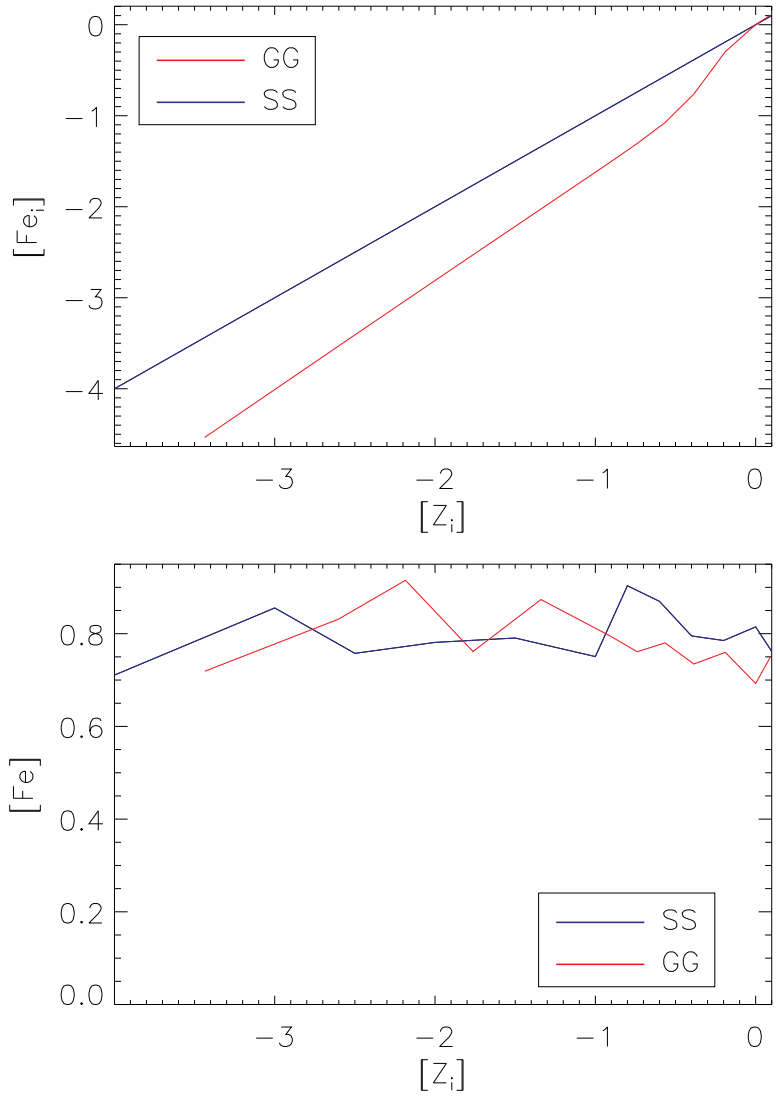

Figure 5.1: *Top*: The initial Fe abundance for both GG and SS models, as a function of the initial total metallicity. *Bottom*: The final Fe yields.

The initial Fe abundances serve as seed isotopes for the weak *s*-process. We thus expect differences in the weak *s*-only isotope production (^{70}Ge, ^{76}Se, ^{80}Kr, ^{82}Kr, ^{86}Sr, and ^{87}Sr). Moreover, such differences should not depend solely on the seed abundance, but also on the neutron source. As discussed in Section 2.7.2, the neutron-producing

reaction, $^{14}\mathrm{N}\,(\alpha,\gamma)^{18}\,\mathrm{F}\,(\beta^{+}\nu_{\mathrm{e}})^{18}\,\mathrm{O}\,(\alpha,\gamma)^{22}\,\mathrm{Ne}(\alpha,\mathrm{n})^{25}\mathrm{Mg}$, uses ^{14}N abundances made in the CNO cycle. Whereas CNO burning does not change the overall CNO content, it does re-distribute the abundance between the isotopes involved (see Section 2.6.1). Thus a larger initial CNO abundance will result in a corresponding larger ^{14}N abundance after CNO burning, which becomes the ^{22}Ne source for neutrons, and can potentially provide more neutrons given sufficient He.

In Fig. 5.2, we give the ratio of initial CNO to Fe for both GG and SS models. The GG models have a greater initial CNO/Fe ratio at all sub-solar metallicities, with the largest differences at the lowest metallicities considered. In general, a larger neutron-to-seed ratio can produce more *s*-process abundances, hence one might expect an overproduction of weak *s*-process abundances in the GG models relative to the SS models. In reality, the situation is more complicated. A very large neutron-to-seed ratio can drive the *s*-process abundances to increasingly higher mass numbers (e.g., Bisterzo et al., 2010). Indeed, this is precisely the description of how low metallicity AGB stars produce the heaviest *s*-only isotopes, where the neutron source, ^{13}C, is primary (Clayton, 1988). Hence, whereas a larger ratio is typically indicative of the *s*-process efficacy, it may not always result in a consistent increase of *s*-process abundances for all weak *s*-process isotopes.

5.3.2 Weak *s*-Process Production

In general, we do find greater *s*-process production in the GG models at low metallicities. A comparison is given in Fig. 5.3, for the six *s*-only isotopes along the weak *s*-process path. In the higher metallicity models, the *s*-only production becomes greater for SS, at different metallicities for each isotope.

To evaluate which set of models agrees with observations, we computed integrated yields for both models and compared the result to the solar abundances. The integrations were performed over the metallicity interval, and the weak *s*-process and Mg yields were linearly interpolated,

$$Y_i' = \sum_j \int_{z_j}^{z_{j+1}} \left(a_{i,j} \cdot [z - z_j] + Y_{i,j}^{*}\right) \cdot dz, \tag{5.3}$$

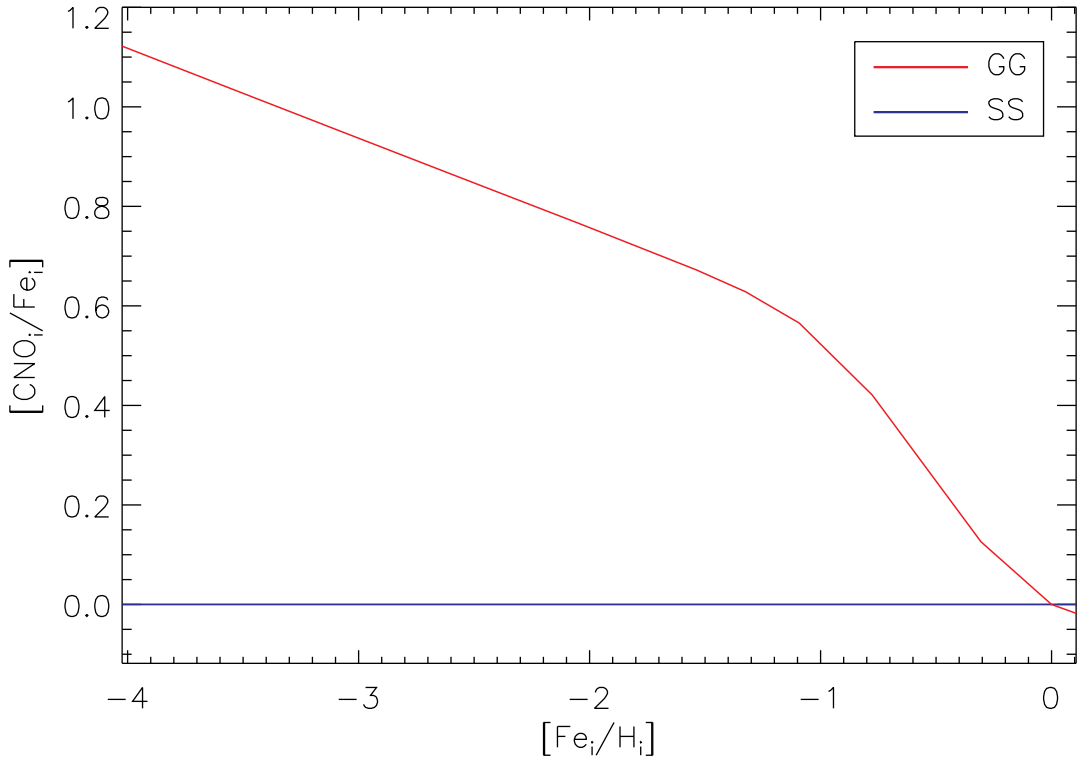

Figure 5.2: The initial CNO/Fe ratios as a function of initial [Fe/H] for both SS and GG models. At all sub-solar initial [Fe/H], a larger neutron-to-seed ratio is observed for the GG models.

where the IMF interpolated yield mass (*in grams*) for isotope i at metallicity z_j is given by $Y^*_{i,j}$, the integrated yield mass for isotope i is given by Y'_i, and the interpolated slopes are given by, $a_{i,j} = \left(Y^*_{i,j+1} - Y^*_{i,j}\right) / (z_{j+1} - z_j)$. The sum runs over the metallicity range of models, $[Z_i] \in (-4, -0.2)$. We computed integrated yields for the six weak s-only isotopes, as well as the three stable Mg isotopes. Using these results, we find a better agreement with solar observations in the GG models, with $[\mathrm{s/Mg}]_{\mathrm{GG}} = -0.69$ compared to $[\mathrm{s/Mg}]_{\mathrm{SS}} = -0.90$, where [s] is the logarithm of the sum of the six weak s-only isotopes relative to the fraction of their solar values attributed to this process (see Table B.2).

The idea here is that the solar abundances of the six weak s-only and Mg isotopes are made in several previous generations of stars. Hence, in order to compare with solar observations, it is necessary to account for all possible sub-solar stellar yields

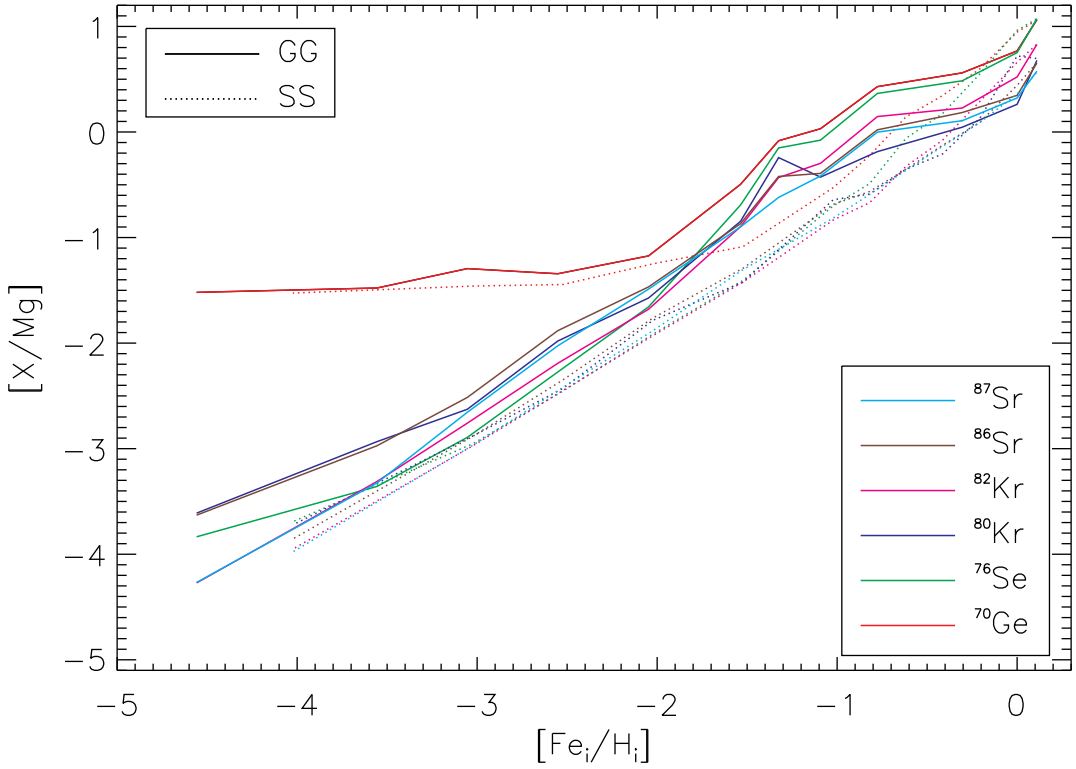

Figure 5.3: The produced weak *s*-only isotope yields over Mg as a function of initial [Fe/H] for both SS and GG models. In general, at sub-solar metallicities, the GG models have larger productions than the SS models.

that contribute. We only sample the nucleosynthesis, however, from models in a finite initial metallicity grid. Thus, we approximate the yields in between the models of our grid by interpolating across the entire sub-solar metallicity range. Note that this type of prescription has precedence in GCE models (e.g., Timmes et al., 1995). Our method assumes the yields are well-mixed, and do not raise the total metallicity of the surrounding environment much. We are also assuming the entire solar abundance of Mg isotopes comes from massive stars, which is reasonable. The comparison of the weak *s*-only isotopes to the fraction of their solar value attributed to massive stars is approximate, and is subject to the accuracy of the fitting described in Section 3.2.5.1. We caution that this analysis is a first step, and may require modification.

5.4 Conclusion

We performed a preliminary analysis for a grid of models across the initial metallicity range $-4.0 \leq [Z_i] \leq +0.1$ for 8 different initial masses, using inputs from our scaling model and linear interpolated solar abundances. Ideally, one would use a GCE model to compute the contributions to the solar abundances from sub-solar stars, using GG and SS as inputs, and our results would certainly benefit from comparison to full GCE calculations. These first results, however, are promising. We find better agreement for the weak *s*-process abundances in the GG models when compared to solar. We hope to continue this analysis in future work to address other massive star products, such as the α-isotopes. Additionally, we will extend the grid to include GS and SG models, and seek to distinguish between differences in yields caused by direct nucleosynthesis, and those caused by changes in the stellar structure and subsequent evolution.

Chapter 6

Summary

A scaling model for all stable isotopes as a function of metallicity has been developed. It takes into account the present understanding of all astrophysical processes responsible for isotopic production, which is the first time this has been achieved. The model also identifies, and uses, a new mechanism for p-isotope production in massive stars, the WSEP process (Section 3.2.5.1). The model is best-fit to a fairly representative data compilation, and describes on average the correct elemental ratios in the Galaxy. Additionally, the isotopic ratios are useful for future nucleosynthesis studies.

There are limitations of the model which are important to understand for future applications. The solar abundance decomposition is approximate for the weak s-process isotopes, as well as for intermediate-mass isotopes that have small contributions from either CCSNe and Type Ia SNe (low contributions typically experience the largest scaling factors, see Figs. 3.3 and 3.4). Additionally, the free parameters of the model are data-dependent, and would change if another data set is used in the fits. Nevertheless, for all "reasonable" data sets, the best-fit values will likely not change much — the trends in the scalings match our expectations of how abundances evolve. For comparison, we tested an alternate data set (Cayrel et al., 2004), and computed new best-fit values which agreed with our model's best-fits to within 10 %. We believe that the best-fit parameters are relatively stable for representative Galactic abundance data compliations. Another limitation is that the model relies on fits to massive star simulations to help extract the massive star contributions to the solar abundance pattern. Even with the rather extensive mass range sampled by the simulation ($10 - 100\,\mathrm{M}_{\odot}$), the fits to

observations suffered error for some elements, such as with nitrogen, for example.

Despite these limitations, our model is a step in the right direction. Previous attempts to construct isotopic abundances for use in stellar simulations have included performing crude linear interpolations. More refined efforts modify these interpolations to increase the intermediate-mass isotopic contributions from massive stars at sub-solar metallicities (α-enhanced compositions), and some methods additionally modify Fe-peak isotopes to address Type Ia SNe onset. In contrast, our model "modifies" *all* stable isotopes in a self-consistent fashion, and in agreement with observational data.

The present model assumes a homogeneous chemical evolution of the Galaxy. In reality, the components of the Galaxy (bulge, disk, and halo) have distinct stellar populations. A future extension of this model would be to address each component separately. The feasibility of this may be presently constrained by data needs, which may improve over time.

This work also represents a novel algorithm/procedure for modeling isotopic ratios, which can be applied to other systems in future works, such as dwarf galaxies. Using abundance data from these systems, the free parameters can be re-fitted to give the isotopic scalings. The isotopic ratios of the resulting fitted model can be compared to the present Galactic model, hopefully offering insight into how the relative chemical evolutions behave. This will also enable the modeling of stars within dwarf galaxies, with the resulting fitted model generating reliable input compositions.

We have also presented a study on the He-burning reaction rate uncertainties. We ran an extensive grid of 2112 solar metallicity stellar models, and fit the yields to expected abundances from the Sun. Our results improve future searches for He rate values in two ways. The best-fit rates occupy a region in the 2D parameter space of the 2σ uncertainty range, which dismisses a significant fraction of possible rate values from consideration. Secondly, the best-fit region allows us to couple the rates with a linear relation, leaving only one rate independent. In principle, this alone cuts future work in half — the experimenter need only improve one of the rates, and this will generate an automatic improvement in the other. Moreover, the experimenter has free-choice of which rate to improve, since the linear relation is invertible. Alternately, we may learn something about other uncertain physics when both rates are measured well.

Currently, the He-rate grid uses only solar metallicity models. A future extension

of this work would include stars at lower metallicities. The initial compositions of these sub-solar models can be generated using the isotopic scaling model. This would extend the 2D reaction rate grid with a "metallicity axis," and may improve the presently determined region of the uncertainty space that best-fits observations. Moreover, this approach might also be used to improve the ^{22}Ne(α,n)^{25}Mg reaction rate, which impacts the weak s-process abundances, and is poorly known (e.g., Longland et al., 2012). Extending the grid into yet another axis for ^{22}Ne would involve a very large number of stellar models, which may become prohibitive. Nevertheless, future refinements to the He rates may improve the situation, or conversely a reduced grid could be attempted.

Additionally, the effective best-fit reaction rates may improve predictions of other observables in massive stars. A collaborative investigation is presently underway to assess whether stellar models with our best-fit reaction rates can refine uncertainties of predicted ν-process yields (Austin et al., 2013, submitted). Preliminary results are promising, suggesting a tighter constraint on masssive star production of these isotopes than previously determined. Moreover, this approach may be applicable to other isotopes as well, such as the gamma ray and weak s-process nuclei.

The preliminary results of the study comparing our input compositions to linear interpolations suggest that the scaling model better reproduces the solar abundances for the six s-only isotopes along the weak s-process path. Presently, the analysis assumes the stellar yields do not significantly alter the overall metallicity of the surrounding ISM, and we interpolate between these yields at the initial metallicities of the models from which they come. Of course, this is not how chemical evolution really proceeds in the Galaxy — *especially* at low metallicities, where stellar events can have a larger impact on the overall metal abundances in the ISM. This study is a work in progress, and ongoing efforts are attempting to model the dilution that stellar yields might experience at different metallicities when mixed with the surroundings. If successful, this would change the metallicity of the ISM we use for the averaging in a consistent way. This dilution method may also allow us to make more direct comparisons to sub-solar observational data: the abundance rates should be similar for good models.

In summary, this work addresses two problems in stellar modeling. We improve the isotopic inputs for stellar simulations, a utility that should be of great use to the community, by enabling consistent inputs for GCE models and other nucleosynthesis

studies. We also improve the present uncertainties in the He burning reaction rates, by subtantially constraining the 2σ parameter space. In doing so, we enable better model predictions, and pave the way for future improvements. We discovered several useful extensions of these projects that may also contribute to our understanding of nucleosynthesis and stellar evolution. The ultimate goal of these endevours has a broad scope, and seeks to explain the origin of not only the isotopes that comprise the Universe, but also ourselves.

References

L. Buchmann. Personal communication, 2000.

B. Fields. Personal communication, 2002.

S. Bisterzo, R. Gallino, et. al. Personal communication, 2011.

A. Frebel. Personal communication, 2011.

A. Heger. Personal communication, 2012.

S. E. Woosley. Personal communication, 2012.

N. Prantzos. Personal communication, 2013.

C. Abia, K. Cunha, S. Cristallo, P. de Laverny, I. Domínguez, K. Eriksson, L. Gialanella, K. Hinkle, G. Imbriani, A. Recio-Blanco, V. V. Smith, O. Straniero, and R. Wahlin. Fluorine Abundances in Galactic Asymptotic Giant Branch Stars. *ApJ Letters*, 715: L94–L98, June 2010. doi: 10.1088/2041-8205/715/2/L94.

F. C. Adams, G. J. M. Graves, and G. Laughlin. Red Dwarfs and the End of the Main Sequence. In G. Garcia-Segura, G. Tenorio-Tagle, J. Franco, and H. W. Yorke, editors, *Revista Mexicana de Astronomia y Astrofisica Conference Series*, volume 22 of *Revista Mexicana de Astronomia y Astrofisica Conference Series*, pages 46–49, December 2004.

E. G. Adelberger, A. García, R. G. H. Robertson, K. A. Snover, A. B. Balantekin, K. Heeger, M. J. Ramsey-Musolf, D. Bemmerer, A. Junghans, C. A. Bertulani, J.-W. Chen, H. Costantini, P. Prati, M. Couder, E. Uberseder, M. Wiescher, R. Cyburt,

B. Davids, S. J. Freedman, M. Gai, D. Gazit, L. Gialanella, G. Imbriani, U. Greife, M. Hass, W. C. Haxton, T. Itahashi, K. Kubodera, K. Langanke, D. Leitner, M. Leitner, P. Vetter, L. Winslow, L. E. Marcucci, T. Motobayashi, A. Mukhamedzhanov, R. E. Tribble, K. M. Nollett, F. M. Nunes, T.-S. Park, P. D. Parker, R. Schiavilla, E. C. Simpson, C. Spitaleri, F. Strieder, H.-P. Trautvetter, K. Suemmerer, and S. Typel. Solar fusion cross sections. II. The pp chain and CNO cycles. *Reviews of Modern Physics*, 83:195–246, January 2011. doi: 10.1103/RevModPhys.83.195.

A. S. Almgren, V. E. Beckner, J. B. Bell, M. S. Day, L. H. Howell, C. C. Joggerst, M. J. Lijewski, A. Nonaka, M. Singer, and M. Zingale. CASTRO: A New Compressible Astrophysical Solver. I. Hydrodynamics and Self-gravity. *ApJ*, 715:1221–1238, June 2010. doi: 10.1088/0004-637X/715/2/1221.

A. Arcones and F. Montes. Production of Light-element Primary Process Nuclei in Neutrino-driven Winds. *ApJ*, 731:5, April 2011. doi: 10.1088/0004-637X/731/1/5.

D. Arnett. *Supernovae and Nucleosynthesis*. 1996.

W. D. Arnett. Hydrostatic Oxygen Burning in Stars. I. Oxygen Stars. *ApJ*, 173:393, April 1972. doi: 10.1086/151429.

W. D. Arnett and F.-K. Thielemann. Hydrostatic nucleosynthesis. I - Core helium and carbon burning. *ApJ*, 295:589–619, August 1985. doi: 10.1086/163402.

M. Arnould and S. Goriely. The p-process of stellar nucleosynthesis: astrophysics and nuclear physics status. *Physics Reports*, 384:1–84, September 2003. doi: 10.1016/S0370-1573(03)00242-4.

M. Arnould, L. Siess, and S. Goriely. The Nuclear Processes Responsible for the CNO Synthesis (invited review). In C. Charbonnel, D. Schaerer, and G. Meynet, editors, *CNO in the Universe*, volume 304 of *Astronomical Society of the Pacific Conference Series*, page 284, 2003.

G. Audi, O. Bersillon, J. Blachot, and A. H. Wapstra. The Nubase evaluation of nuclear and decay properties. *Nuclear Physics A*, 729:3–128, December 2003. doi: 10.1016/j.nuclphysa.2003.11.001.

M. B. Aufderheide, E. Baron, and F.-K. Thielemann. Shock waves and nucleosynthesis in type II supernovae. *ApJ*, 370:630–642, April 1991. doi: 10.1086/169849.

S. Austin, C. West, and A. Heger. Effective Helium Burning Rates and the Production of the Neutrino Nuclei. *ApJL*, 2013. Manuscript in preparation.

S. M. Austin, A. Heger, and C. Tur. B11 and Constraints on Neutrino Oscillations and Spectra from Neutrino Nucleosynthesis. *Physical Review Letters*, 106(15):152501, April 2011. doi: 10.1103/PhysRevLett.106.152501.

P. Banerjee, W. C. Haxton, and Y.-Z. Qian. Long, Cold, Early r Process? Neutrino-Induced Nucleosynthesis in He Shells Revisited. *Physical Review Letters*, 106(20): 201104, May 2011. doi: 10.1103/PhysRevLett.106.201104.

P. Banerjee, Y.-Z. Qian, W. C. Haxton, and A. Heger. New Primary Mechanisms for the Synthesis of Rare Be9 in Early Supernovae. *Physical Review Letters*, 110(14): 141101, April 2013. doi: 10.1103/PhysRevLett.110.141101.

T. Bensby, S. Feltzing, and I. Lundström. A possible age-metallicity relation in the Galactic thick disk? *Astronomy & Astrophysics*, 421:969–976, July 2004. doi: 10.1051/0004-6361:20035957.

M. G. Bertolli, F. Herwig, M. Pignatari, and T. Kawano. Systematic and correlated nuclear uncertainties in the i-process at the neutron shell closure N = 82. *ArXiv e-prints*, October 2013.

H. A. Bethe and J. R. Wilson. Revival of a stalled supernova shock by neutrino heating. *ApJ*, 295:14–23, August 1985. doi: 10.1086/163343.

S. Bisterzo, R. Gallino, O. Straniero, S. Cristallo, and F. Käppeler. s-Process in low-metallicity stars - I. Theoretical predictions. *Monthly Notices of the Royal Astronomical Society*, 404:1529–1544, May 2010. doi: 10.1111/j.1365-2966.2010.16369.x.

D. Bodansky, D. D. Clayton, and W. A. Fowler. Nuclear Quasi-Equilibrium during Silicon Burning. *ApJs*, 16:299, November 1968. doi: 10.1086/190176.

A. M. Boesgaard, J. A. Rich, E. M. Levesque, and B. P. Bowler. Beryllium and Alpha-element Abundances in a Large Sample of Metal-poor Stars. *ApJ*, 743:140, December 2011. doi: 10.1088/0004-637X/743/2/140.

M. C. P. Bours, S. Toonen, and G. Nelemans. Single degenerate supernova type Ia progenitors. Studying the influence of different mass retention efficiencies. *Astronomy & Astrophysics*, 552:A24, April 2013. doi: 10.1051/0004-6361/201220692.

J. M. Brown and S. E. Woosley. Nucleosynthetic Constraints on the Mass of the Heaviest Supernovae. *ArXiv e-prints*, February 2013.

E. Margaret Burbidge, G. R. Burbidge, William A. Fowler, and F. Hoyle. Synthesis of the elements in stars. *Rev. Mod. Phys.*, 29:547–650, Oct 1957. doi: 10.1103/RevModPhys.29.547. URL `http://link.aps.org/doi/10.1103/RevModPhys.29.547`.

M. Busso and R. Gallino. The production of neutron-rich isotopes during He burning in massive stars. *Astronomy & Astrophysics*, 151:205–214, October 1985.

M. Busso, R. Gallino, and G. J. Wasserburg. Nucleosynthesis in Asymptotic Giant Branch Stars: Relevance for Galactic Enrichment and Solar System Formation. *Annual Review of Astronomy and Astrophysics*, 37:239–309, 1999. doi: 10.1146/annurev.astro.37.1.239.

F. Calura and N. Menci. Chemical evolution of local galaxies in a hierarchical model. *Monthly Notices of the Royal Astronomical Society*, 400:1347–1365, December 2009. doi: 10.1111/j.1365-2966.2009.15440.x.

A. G. W. Cameron. Nuclear Reactions in Stars and Nucleogenesis. *Publications of the Astronomical Society of the Pacific*, 69:201, June 1957. doi: 10.1086/127051.

V. Castellani and A. Renzini. On the Evolution of the Horizontal Branch Stars of Metal-Poor Globular Clusters. *Astrophysics and Space Science*, 2:310–314, November 1968. doi: 10.1007/BF00650907.

G. R. Caughlan and W. A. Fowler. *At. Data Nucl. Data Tables*, 40(2):283 – 334, 1988.

R. Cayrel, E. Depagne, M. Spite, V. Hill, F. Spite, P. François, B. Plez, T. Beers, F. Primas, J. Andersen, B. Barbuy, P. Bonifacio, P. Molaro, and B. Nordström. First stars V - Abundance patterns from C to Zn and supernova yields in the early Galaxy. *Astronomy & Astrophysics*, 416:1117–1138, March 2004. doi: 10.1051/0004-6361:20034074.

S. Chandrasekhar. *An introduction to the study of stellar structure*. 1939.

M. Chernykh, H. Feldmeier, T. Neff, P. von Neumann-Cosel, and A. Richter. Pair Decay Width of the Hoyle State and its Role for Stellar Carbon Production. *Physical Review Letters*, 105(2):022501, July 2010. doi: 10.1103/PhysRevLett.105.022501.

C. Chiappini, F. Matteucci, and R. Gratton. The Chemical Evolution of the Galaxy: The Two-Infall Model. *ApJ*, 477:765, March 1997. doi: 10.1086/303726.

C. Chiappini, R. Hirschi, G. Meynet, S. Ekström, A. Maeder, and F. Matteucci. A strong case for fast stellar rotation at very low metallicities. *Astronomy and Astrophysics*, 449:L27–L30, April 2006. doi: 10.1051/0004-6361:20064866.

A. Chieffi and M. Limongi. The evolution of rotating solar metallicity stars extending in mass from 13 to 120 msun: the hydrostatic evolution and the explosive yields. *ArXiv e-prints*, December 2012.

C. Chiosi, G. Bertelli, and A. Bressan. New developments in understanding the HR diagram. *Annual review of astronomy and astrophysics*, 30:235–285, 1992. doi: 10.1146/annurev.aa.30.090192.001315.

D. D. Clayton. *Principles of stellar evolution and nucleosynthesis*. 1968.

D. D. Clayton. Nuclear cosmochronology within analytic models of the chemical evolution of the solar neighbourhood. *Monthly Notices of the Royal Astronomical Society*, 234:1–36, September 1988.

D. D. Clayton and M. E. Rassbach. Termination of the s-PROCESS. *ApJ*, 148:69, April 1967. doi: 10.1086/149128.

P. Coelho, G. Bruzual, S. Charlot, A. Weiss, B. Barbuy, and J. W. Ferguson. Spectral models for solar-scaled and α-enhanced stellar populations. *Monthly Notices of the*

Royal Astronomical Society, 382:498–514, December 2007. doi: 10.1111/j.1365-2966.2007.12364.x.

M. Cohen. *In darkness born. The story of star formation.* 1988.

S. A. Colgate and R. H. White. The Hydrodynamic Behavior of Supernovae Explosions. *ApJ*, 143:626, March 1966. doi: 10.1086/148549.

R. D. D. Costa, W. J. Maciel, and A. V. Escudero. Chemical evolution of the galactic bulge: single and double infall models. 2009.

J. J. Cowan and W. K. Rose. Production of C-14 and neutrons in red giants. *ApJ*, 212: 149–158, February 1977. doi: 10.1086/155030.

J. P. Cox. *Principles of stellar structure - Vol.1: Physical principles; Vol.2: Applications to stars.* 1968.

R. H. Cyburt, B. D. Fields, and K. A. Olive. The NACRE thermonuclear reaction compilation and big bang nucleosynthesis. *New Astronomy*, 6:215–238, June 2001. doi: 10.1016/S1384-1076(01)00053-7.

R. H. Cyburt, B. D. Fields, and K. A. Olive. An update on the big bang nucleosynthesis prediction for ^{7}Li: the problem worsens. *Journal of Cosmology and Astroparticle Physics*, 11:012, November 2008. doi: 10.1088/1475-7516/2008/11/012.

R. Diehl, N. Prantzos, and P. von Ballmoos. Astrophysical constraints from gamma-ray spectroscopy. *Nuclear Physics A*, 777:70–97, October 2006. doi: 10.1016/j.nuclphysa.2005.02.155.

I. Dillmann, R. Plag, F. K. Kappeler, and T. Rauscher. KADoNiS v0.3 - The third update of the "Karlsruhe Astrophysical Database of Nucleosynthesis in Stars". EFNUDAT Fast Neutrons - scientific workshop on neutron measurements, theory & applications, 2009. URL `http://www.kadonis.org`.

B. Edvardsson, J. Andersen, B. Gustafsson, D. L. Lambert, P. E. Nissen, and J. Tomkin. The Chemical Evolution of the Galactic Disk - Part One - Analysis and Results. *Astronomy & Astrophysics*, 275:101, August 1993.

J. J. Eldridge and C. A. Tout. The progenitors of core-collapse supernovae. *Monthly Notices of the Royal Astronomical Society*, 353:87–97, September 2004. doi: 10.1111/j.1365-2966.2004.08041.x.

S. Feltzing, J. Holmberg, and J. R. Hurley. The solar neighbourhood age-metallicity relation - Does it exist? *Astronomy & Astrophysics*, 377:911–924, October 2001. doi: 10.1051/0004-6361:20011119.

B. D. Fields. Big bang nucleosynthesis in the new cosmology. *European Physical Journal A*, 27:3–14, March 2006. doi: 10.1140/epja/i2006-08-001-2.

M. Forestini, S. Goriely, A. Jorissen, and M. Arnould. Fluorine production in thermal pulses on the asymptotic giant branch. *Astronomy and Astrophysics*, 261:157–163, July 1992.

A. Frebel. Stellar archaeology: Exploring the Universe with metal-poor stars. *Astronomische Nachrichten*, 331:474–488, May 2010. doi: 10.1002/asna.201011362.

U. Frischknecht, R. Hirschi, T. Rauscher, and F. K. Thielemann. Effects of rotation on the weak s process. In *Nuclei in the Cosmos*, 2010.

C. Fröhlich, G. Martínez-Pinedo, M. Liebendörfer, F.-K. Thielemann, E. Bravo, W. R. Hix, K. Langanke, and N. T. Zinner. Neutrino-Induced Nucleosynthesis of A¿64 Nuclei: The νp Process. *Physical Review Letters*, 96(14):142502, April 2006. doi: 10.1103/PhysRevLett.96.142502.

F. Fusi-Pecci and A. Renzini. On mass loss by stellar wind in population II red giants. *Astronomy & Astrophysics*, 39:413–419, March 1975.

R. Gallino, C. Arlandini, M. Busso, M. Lugaro, C. Travaglio, O. Straniero, A. Chieffi, and M. Limongi. Evolution and Nucleosynthesis in Low-Mass Asymptotic Giant Branch Stars. II. Neutron Capture and the s-Process. *ApJ*, 497:388, April 1998. doi: 10.1086/305437.

R. D. Gehrz, J. W. Truran, R. E. Williams, and S. Starrfield. Nucleosynthesis in Classical Novae and Its Contribution to the Interstellar Medium. *Publications of the Astronomical Society of the Pacific*, 110:3–26, January 1998. doi: 10.1086/316107.

H. J. Habing and H. Olofsson, editors. *Asymptotic giant branch stars*, 2003.

M. J. Harris, D. L. Lambert, and V. V. Smith. Oxygen isotopic abundances in evolved stars. IV - Five K giants. *ApJ*, 325:768–775, February 1988. doi: 10.1086/166047.

D. H. Hartmann, W. C. Haxton, R. D. Hoffman, and S. E. Woosley. Neutrino-induced nucleosynthesis in core-collapse supernovae. *Nuclear Physics A*, 527:663–668, May 1991. doi: 10.1016/0375-9474(91)90176-7.

A. Heger. *The Presupernova Evolution of Rotating Massive Stars.* PhD thesis, Ph.D. Dissertation, Max-Planck-Institut für Astrophysik, unpublished (1998), 1998.

A. Heger and S. E. Woosley. The Nucleosynthetic Signature of Population III. *ApJ*, 567:532–543, March 2002. doi: 10.1086/338487.

A. Heger and S. E. Woosley. Nucleosynthesis and Evolution of Massive Metal-free Stars. *ApJ*, 724:341–373, November 2010. doi: 10.1088/0004-637X/724/1/341.

A. Heger, S. E. Woosley, G. Martínez-Pinedo, and K. Langanke. Presupernova Evolution with Improved Rates for Weak Interactions. *ApJ*, 560:307–325, October 2001. doi: 10.1086/324092.

A. Heger, C. L. Fryer, S. E. Woosley, N. Langer, and D. H. Hartmann. How Massive Single Stars End Their Life. *ApJ*, 591:288–300, July 2003. doi: 10.1086/375341.

A. Heger, E. Kolbe, W. C. Haxton, K. Langanke, G. Martínez-Pinedo, and S. E. Woosley. Neutrino nucleosynthesis. *Physics Letters B*, 606:258–264, January 2005. doi: 10.1016/j.physletb.2004.12.017.

A. Heger, S. Woosley, R. Hoffman, C. Joggerst, and W. Zhang. Presupernova Evolution of Massive Stars. In *Progenitors and Environments of Stellar Explosions*, June 2010.

M. Heil, F. Käppeler, E. Uberseder, R. Gallino, and M. Pignatari. The s process in massive stars. *Progress in Particle and Nuclear Physics*, 59:174–182, July 2007. doi: 10.1016/j.ppnp.2006.12.013.

M. Heil, F. Käppeler, E. Uberseder, R. Gallino, S. Bisterzo, and M. Pignatari. Stellar (n,γ) cross sections for Br and Rb: Matching the weak and main s-process components. *Physical Review C*, 78(2):025802, August 2008. doi: 10.1103/PhysRevC.78.025802.

R. B. C. Henry, J. J. Cowan, and J. Sobeck. Empirically Derived Integrated Stellar Yields of Fe-Peak Elements. *ApJ*, 709:715–724, February 2010. doi: 10.1088/0004-637X/709/2/715.

F. Herwig, M. Pignatari, P. R. Woodward, D. H. Porter, G. Rockefeller, C. L. Fryer, M. Bennett, and R. Hirschi. Convective-reactive Proton-^{12}C Combustion in Sakurai's Object (V4334 Sagittarii) and Implications for the Evolution and Yields from the First Generations of Stars. *ApJ*, 727:89, February 2011. doi: 10.1088/0004-637X/727/2/89.

W. Hillebrandt and J. C. Niemeyer. Type IA Supernova Explosion Models. *Annual Review of Astron and Astrophys*, 38:191–230, 2000. doi: 10.1146/annurev.astro.38.1.191.

W. Hillebrandt, F. K. Thielemann, H. V. Klapdor, and T. Oda. The r-process during explosive helium burning in supernovae. *Astronomy & Astrophysics*, 99:195–198, June 1981.

R. D. Hoffman, S. E. Woosley, and Y.-Z. Qian. Model Independent r-Process Nucleosynthesis - Constraints on the Key Parameters. *Nuclear Physics A*, 621:397–400, February 1997. doi: 10.1016/S0375-9474(97)00278-9.

F. Hoyle. The synthesis of the elements from hydrogen. *Monthly Notices of the RAS*, 106:343, 1946.

F. Hoyle and W. A. Fowler. Nucleosynthesis in Supernovae. *ApJ*, 132:565, November 1960. doi: 10.1086/146963.

I. Iben, Jr. Thermal pulses; p-capture, alpha-capture, s-process nucleosynthesis; and convective mixing in a star of intermediate mass. *ApJ*, 196:525–547, March 1975. doi: 10.1086/153433.

I. Iben, Jr. Thermal pulse and interpulse properties of intermediate-mass stellar models with carbon-oxygen cores of mass 0.96, 1.16, and 1.36 solar masses. *ApJ*, 217:788–798, November 1977. doi: 10.1086/155626.

I. Iben, Jr. and A. Renzini. The role of semiconvection in bringing carbon to the surface of asymptotic giant branch stars of small core mass. *ApJL*, 259:L79–L83, August 1982a. doi: 10.1086/183852.

I. Iben, Jr. and A. Renzini. On the formation of carbon star characteristics and the production of neutron-rich isotopes in asymptotic giant branch stars of small core mass. *ApJL*, 263:L23–L27, December 1982b. doi: 10.1086/183916.

I. Iben, Jr. and A. V. Tutukov. Supernovae of type I as end products of the evolution of binaries with components of moderate initial mass (M not greater than about 9 solar masses). *ApJS*, 54:335–372, February 1984. doi: 10.1086/190932.

C. Iliadis. *Nuclear Physics of Stars*. Wiley-VCH Verlag, 2007.

C. Iliadis, A. Champagne, A. Chieffi, and M. Limongi. The Effects of Thermonuclear Reaction Rate Variations on ^{26}Al Production in Massive Stars: A Sensitivity Study. *ApJs*, 193:16, March 2011. doi: 10.1088/0067-0049/193/1/16.

H. R. Jacobson and E. D. Friel. Open Cluster Neutron Capture Element Abundances and Milky Way Disk Evolution. In *American Astronomical Society Meeting Abstracts #219*, volume 219 of *American Astronomical Society Meeting Abstracts*, page 152.09, January 2012.

E. Jehin, P. Magain, C. Neuforge, A. Noels, G. Parmentier, and A. A. Thoul. Abundance correlations in mildly metal-poor stars. *Astronomy and Astrophysics*, 341:241–255, January 1999.

C. L. Jiang, K. E. Rehm, B. B. Back, and R. V. F. Janssens. Expectations for C12 and O16 induced fusion cross sections at energies of astrophysical interest. *Physical Review C*, 75(1):015803, January 2007. doi: 10.1103/PhysRevC.75.015803.

C. C. Joggerst, A. Heger, and S. E. Woosley. Multidimensional Simulations of Mixing in Zero- and Solar-Metallicity SNe. In B. W. O'Shea and A. Heger, editors, *First Stars*

III, volume 990 of *American Institute of Physics Conference Series*, pages 257–259, March 2008. doi: 10.1063/1.2905557.

J. L. Johnson, D. J. Whalen, W. Even, C. L. Fryer, A. Heger, J. Smidt, and K.-J. Chen. The Biggest Explosions in the Universe. *ApJ*, 775:107, October 2013. doi: 10.1088/0004-637X/775/2/107.

J. José and M. Hernanz. TOPICAL REVIEW: Nucleosynthesis in classical nova explosions. *Journal of Physics G Nuclear Physics*, 34:431, December 2007. doi: 10.1088/0954-3899/34/12/R01.

J. José and M. Hernanz. Nucleosynthetic imprints from classical nova explosions: past to present. In *Nuclei in the Cosmos (NIC X)*, 2008.

F. Käppeler, H. Beer, and K. Wisshak. s-process nucleosynthesis-nuclear physics and the classical model. *Reports on Progress in Physics*, 52:945–1013, August 1989. doi: 10.1088/0034-4885/52/8/002.

F. Käppeler, R. Gallino, M. Busso, G. Picchio, and C. M. Raiteri. S-process nucleosynthesis - Classical approach and asymptotic giant branch models for low-mass stars. *ApJ*, 354:630–643, May 1990. doi: 10.1086/168720.

F. Käppeler, R. Gallino, S. Bisterzo, and W. Aoki. The s process: Nuclear physics, stellar models, and observations. *Reviews of Modern Physics*, 83:157–194, January 2011a. doi: 10.1103/RevModPhys.83.157.

F. Käppeler, R. Gallino, S. Bisterzo, and W. Aoki. The s process: Nuclear physics, stellar models, and observations. *Reviews of Modern Physics*, 83:157–194, January 2011b. doi: 10.1103/RevModPhys.83.157.

S. Kato. Overstable Convection in a Medium Stratified in Mean Molecular Weight. *Publications of the Astronomical Society of Japan*, 18:374, 1966.

R. Kippenhahn and A. Weigert. *Stellar Structure and Evolution*. 1990.

M. D. Kistler, K. Z. Stanek, C. S. Kochanek, J. L. Prieto, and T. A. Thompson. The Impact of Metallicity on the Rate of Type Ia Supernovae. *ApJ*, 770:88, June 2013. doi: 10.1088/0004-637X/770/2/88.

C. Kobayashi, H. Umeda, K. Nomoto, N. Tominaga, and T. Ohkubo. Galactic Chemical Evolution: Carbon through Zinc. *ApJ*, 653:1145–1171, December 2006. doi: 10.1086/508914.

S. A. Lamb, W. M. Howard, J. W. Truran, and I. Iben, Jr. Neutron-capture nucleosynthesis in the helium-burning cores of massive stars. *ApJ*, 217:213–221, October 1977. doi: 10.1086/155571.

D. L. Lambert. Observational Effects of Nucleosynthesis in Evolved Stars. In M. G. Edmunds and R. Terlevich, editors, *Elements and the Cosmos*, page 92, 1992.

L. D. Landau and E. M. Lifshitz. *Fluid mechanics*. 1959.

J. C. Lattanzio and M. A. Lugaro. What we do and do not know about the s-process in AGB stars. *Nuclear Physics A*, 758:477–484, July 2005. doi: 10.1016/j.nuclphysa.2005.05.088.

J. M. Lattimer and M. Prakash. Neutron Star Structure and the Equation of State. *ApJ*, 550:426–442, March 2001. doi: 10.1086/319702.

J. M. Lattimer and M. Prakash. What a Two Solar Mass Neutron Star Really Means. *ArXiv e-prints*, December 2010.

H. H. B. Lau, C. L. Doherty, P. Gil-Pons, and J. C. Lattanzio. S-process Nucleosynthesis in SAGB Stars. In F. Kerschbaum, T. Lebzelter, and R. F. Wing, editors, *Why Galaxies Care about AGB Stars II: Shining Examples and Common Inhabitants*, volume 445 of *Astronomical Society of the Pacific Conference Series*, page 45, September 2011.

H. H. B. Lau, C. L. Doherty, P. Gil-Pons, and J. C. Lattanzio. Lithium production in SAGB stars. *Memorie della Societa Astronomica Italiana Supplementi*, 22:247–254, 2012.

M. Leising and R. Diehl. Gamma-Ray Line Studies of Nuclei in the Cosmos. *ArXiv e-prints*, March 2009.

J. Li, B. Liang, and W. Fan. The age-metallicity relation in the thin disk. In L. Deng and K. L. Chan, editors, *IAU Symposium*, volume 252 of *IAU Symposium*, pages 265–266, October 2008. doi: 10.1017/S1743921308022989.

M. Livio. The Progenitors of Type Ia Supernovae. In J. C. Niemeyer and J. W. Truran, editors, *Type Ia Supernovae, Theory and Cosmology*, page 33, 2000.

K. Lodders. Solar System Abundances and Condensation Temperatures of the Elements. *ApJ*, 591:1220–1247, July 2003. doi: 10.1086/375492.

K. Lodders. Solar System Abundances of the Elements. In A. Goswami and B. E. Reddy, editors, *Principles and Perspectives in Cosmochemistry*, page 379, 2010.

R. Longland, C. Iliadis, and A. I. Karakas. Reaction rates for the s-process neutron source ^{22}Ne + α. *Physical Review C*, 85(6):065809, June 2012. doi: 10.1103/PhysRevC.85.065809.

K. Maeda, F. K. Röpke, M. Fink, W. Hillebrandt, C. Travaglio, and F.-K. Thielemann. Nucleosynthesis in Two-Dimensional Delayed Detonation Models of Type Ia Supernova Explosions. *ApJ*, 712:624–638, March 2010. doi: 10.1088/0004-637X/712/1/624.

E. Maiorca, S. Randich, M. Busso, L. Magrini, and S. Palmerini. s-processing in the Galactic Disk. I. Super-solar Abundances of Y, Zr, La, and Ce in Young Open Clusters. *ApJ*, 736:120, August 2011. doi: 10.1088/0004-637X/736/2/120.

E. Maiorca, L. Magrini, M. Busso, S. Randich, S. Palmerini, and O. Trippella. News on the s Process from Young Open Clusters. *ApJ*, 747:53, March 2012. doi: 10.1088/0004-637X/747/1/53.

A. Makinaga, H. Utsunomiya, S. Goriely, T. Kaihori, S. Goko, H. Akimune, T. Yamagata, H. Toyokawa, T. Matsumoto, H. Harano, H. Harada, F. Kitatani, Y. K. Hara, S. Hohara, and Y.-W. Lui. Photodisintegration of Se80: Implications for the s-process branching at Se79. *Physical Review C*, 79(2):025801, February 2009. doi: 10.1103/PhysRevC.79.025801.

F. Mannucci, M. Della Valle, and N. Panagia. Two populations of progenitors for

Type Ia supernovae? *Monthly Notices of the RAS*, 370:773–783, August 2006. doi: 10.1111/j.1365-2966.2006.10501.x.

A. Marek and H.-T. Janka. Delayed Neutrino-Driven Supernova Explosions Aided by the Standing Accretion-Shock Instability. *ApJ*, 694:664–696, March 2009. doi: 10.1088/0004-637X/694/1/664.

G. Martinez-Pinedo, A. Kelic, K. Langanke, K.-H. Schmidt, D. Mocelj, C. Fröhlich, F.-K. Thielemann, I. Panov, T. Rauscher, M. Liebendörfer, N. T. Zinner, B. Pfeiffer, R. Buras, and H.-T. Janka. Weak interaction rates. In *International Symposium on Nuclear Astrophysics - Nuclei in the Cosmos*, 2006.

L. Mashonkina and T. Gehren. Heavy element abundances in cool dwarf stars: An implication for the evolution of the Galaxy. *Astronomy and Astrophysics*, 376:232–247, September 2001. doi: 10.1051/0004-6361:20010965.

L. I. Mashonkina, A. B. Vinogradova, D. A. Ptitsyn, V. S. Khokhlova, and T. A. Chernetsova. Neutron-capture elements in halo, thick-disk, and thin-disk stars. Strontium, yttrium, zirconium, cerium. *Astronomy Reports*, 51:903–919, November 2007. doi: 10.1134/S1063772907110042.

J. Meléndez, L. Casagrande, I. Ramírez, and M. Asplund. Precise Li abundances in metal-poor stars: depletion in the Spite plateau. In K. Cunha, M. Spite, and B. Barbuy, editors, *IAU Symposium*, volume 265 of *IAU Symposium*, pages 71–72, March 2010a. doi: 10.1017/S1743921310000220.

J. Meléndez, L. Casagrande, I. Ramírez, M. Asplund, and W. J. Schuster. Observational signatures for depletion in the Spite plateau: solving the cosmological Li discrepancy? In C. Charbonnel, M. Tosi, F. Primas, and C. Chiappini, editors, *IAU Symposium*, volume 268 of *IAU Symposium*, pages 211–214, April 2010b. doi: 10.1017/S174392131000414X.

J. Meléndez, L. Casagrande, I. Ramírez, M. Asplund, and W. J. Schuster. Observational evidence for a broken Li Spite plateau and mass-dependent Li depletion. *Astronomy & Astrophysics*, 515:L3, June 2010c. doi: 10.1051/0004-6361/200913047.

M. Meneguzzi, J. Audouze, and H. Reeves. The production of the elements Li, Be, B by galactic cosmic rays in space and its relation with stellar observations. *Astronomy and Astrophysics*, 15:337–359, 1971.

N. Mennekens, D. Vanbeveren, J. P. De Greve, and E. De Donder. The delay-time distribution of Type Ia supernovae: a comparison between theory and observation. *Astronomy & Astrophysics*, 515:A89, June 2010. doi: 10.1051/0004-6361/201014115.

B. S. Meyer, T. D. Krishnan, and D. D. Clayton. Theory of Quasi-Equilibrium Nucleosynthesis and Applications to Matter Expanding from High Temperature and Density. *ApJ*, 498:808, May 1998. doi: 10.1086/305562.

G. Meynet and M. Arnould. Synthesis of ^{19}F in Wolf-Rayet stars. *Astronomy and Astrophysics*, 355:176–180, March 2000.

G. Meynet, S. Ekström, and A. Maeder. The early star generations: the dominant effect of rotation on the CNO yields. *Astronomy and Astrophysics*, 447:623–639, February 2006. doi: 10.1051/0004-6361:20053070.

Y. Momany, I. Saviane, A. Smette, A. Bayo, L. Girardi, G. Marconi, A. P. Milone, and A. Bressan. The VLT/VISIR mid-IR view of 47 Tucanae. A further step in solving the puzzle of RGB mass loss. *Astronomy & Astrophysics*, 537:A2, January 2012. doi: 10.1051/0004-6361/201117223.

N. B. Nguyen, F. M. Nunes, I. J. Thompson, and E. F. Brown. Low-Temperature Triple-Alpha Rate in a Full Three-Body Nuclear Model. *Physical Review Letters*, 109 (14):141101, October 2012. doi: 10.1103/PhysRevLett.109.141101.

H. Ning, Y.-Z. Qian, and B. S. Meyer. r-Process Nucleosynthesis in Shocked Surface Layers of O-Ne-Mg Cores. *ApJl*, 667:L159–L162, October 2007. doi: 10.1086/522372.

K. Nomoto, K. Iwamoto, N. Nakasato, F.-K. Thielemann, F. Brachwitz, T. Tsujimoto, Y. Kubo, and N. Kishimoto. Nucleosynthesis in type Ia supernovae. *Nuclear Physics A*, 621:467–476, February 1997. doi: 10.1016/S0375-9474(97)00291-1.

K. Nomoto, Y. Kamiya, and N. Nakasato. Type Ia Supernova Models and Progenitor Scenarios. In R. Di Stefano, M. Orio, and M. Moe, editors, *IAU Symposium*, volume 281 of *IAU Symposium*, pages 253–260, January 2013. doi: 10.1017/S1743921312015165.

M. Notani, H. Esbensen, X. Fang, B. Bucher, P. Davies, C. L. Jiang, L. Lamm, C. J. Lin, C. Ma, E. Martin, K. E. Rehm, W. P. Tan, S. Thomas, X. D. Tang, and E. Brown. Correlation between the ^{12}c+^{12}c, ^{12}c+^{13}c, and ^{13}c+^{13}c fusion cross sections. *Phys. Rev. C*, 85:014607, Jan 2012. doi: 10.1103/PhysRevC.85.014607. URL `http://link.aps.org/doi/10.1103/PhysRevC.85.014607`.

T. Nugis and H. J. G. L. M. Lamers. Mass-loss rates of Wolf-Rayet stars as a function of stellar parameters. *Astronomy and Astrophysics*, 360:227–244, August 2000.

E. O'Connor and C. D. Ott. Black Hole Formation in Failing Core-Collapse Supernovae. *ApJ*, 730:70, April 2011. doi: 10.1088/0004-637X/730/2/70.

B. E. J. Pagel. *Nucleosynthesis and Chemical Evolution of Galaxies*. October 1997.

B. Paxton, L. Bildsten, A. Dotter, F. Herwig, P. Lesaffre, and F. Timmes. Modules for Experiments in Stellar Astrophysics (MESA). *ApJs*, 192:3, January 2011. doi: 10.1088/0067-0049/192/1/3.

M. Pignatari, R. Gallino, G. Meynet, R. Hirschi, F. Herwig, and M. Wiescher. The s-Process in Massive Stars at Low Metallicity: The Effect of Primary ^{14}N from Fast Rotating Stars. *ApJl*, 687:L95–L98, November 2008. doi: 10.1086/593350.

M. Pignatari, R. Gallino, M. Heil, M. Wiescher, F. Käppeler, F. Herwig, and S. Bisterzo. The Weak s-Process in Massive Stars and its Dependence on the Neutron Capture Cross Sections. *ApJ*, 710:1557, February 2010. doi: 10.1088/0004-637X/710/2/1557.

M. Pignatari, R. Hirschi, M. Wiescher, R. Gallino, M. Bennett, M. Beard, C. Fryer, F. Herwig, G. Rockefeller, and F. X. Timmes. The ^{12}C + ^{12}C Reaction and the Impact on Nucleosynthesis in Massive Stars. *ApJ*, 762:31, January 2013. doi: 10.1088/0004-637X/762/1/31.

N. Prantzos. Stellar Yields and their Role in Chemical Evolution. In D. Friedli, M. Edmunds, C. Robert, and L. Drissen, editors, *Abundance Profiles: Diagnostic Tools for Galaxy History*, volume 147 of *Astronomical Society of the Pacific Conference Series*, page 171, 1998.

N. Prantzos. Evolution of CNO Abundances in the Universe (invited review). In C. Charbonnel, D. Schaerer, and G. Meynet, editors, *CNO in the Universe*, volume 304 of *Astronomical Society of the Pacific Conference Series*, page 361, 2003.

N. Prantzos. Origin and Evolution of the Light Nuclides. *Space Science Reviews*, 130: 27–42, June 2007. doi: 10.1007/s11214-007-9183-5.

N. Prantzos. Origin of cosmic rays and evolution of spallogenic nuclides Li, Be and B. In C. Charbonnel, M. Tosi, F. Primas, and C. Chiappini, editors, *IAU Symposium*, volume 268 of *IAU Symposium*, pages 473–482, April 2010a. doi: 10.1017/S1743921310004655.

N. Prantzos. Topics in Galactic Chemical Evolution. In *Nuclei in the Cosmos*, 2010b.

N. Prantzos. Production and evolution of Li, Be, and B isotopes in the Galaxy. *Astronomy & Astrophysics*, 542:A67, June 2012. doi: 10.1051/0004-6361/201219043.

J. X. Prochaska, E. Gawiser, A. M. Wolfe, S. Castro, and S. G. Djorgovski. The Age-Metallicity Relation of the Universe in Neutral Gas: The First 100 Damped Lyα Systems. *ApJL*, 595:L9–L12, September 2003. doi: 10.1086/378945.

Y.-Z. Qian. The origin of the heavy elements: Recent progress in the understanding of the r-process [review article]. *Progress in Particle and Nuclear Physics*, 50:153–199, 2003. doi: 10.1016/S0146-6410(02)00178-3.

Y.-Z. Qian. Astrophysical models of r-process nucleosynthesis: An update. In S. Kubono, T. Hayakawa, T. Kajino, H. Miyatake, T. Motobayashi, and K. Nomoto, editors, *American Institute of Physics Conference Series*, volume 1484 of *American Institute of Physics Conference Series*, pages 201–208, November 2012. doi: 10.1063/1.4763396.

Y.-Z. Qian and G. J. Wasserburg. A Model for Abundances in Metal-poor Stars. *ApJ*, 559:925–941, October 2001. doi: 10.1086/322367.

Y.-Z. Qian and G. J. Wasserburg. Where, oh where has the r-process gone? *Physics Reports*, 442:237–268, April 2007. doi: 10.1016/j.physrep.2007.02.006.

C. M. Raiteri, R. Gallino, M. Busso, D. Neuberger, and F. Käppeler. The Weak s-Component and Nucleosynthesis in Massive Stars. *ApJ*, 419:207, December 1993. doi: 10.1086/173476.

T. Rauscher, A. Heger, R. D. Hoffman, and S. E. Woosley. Nucleosynthesis in Massive Stars with Improved Nuclear and Stellar Physics. *ApJ*, 576:323–348, September 2002. doi: 10.1086/341728.

T. Rauscher, N. Dauphas, I. Dillmann, C. Fröhlich, Z. Fülöp, and G. Gyürky. Constraining the astrophysical origin of the p-nuclei through nuclear physics and meteoritic data. *Reports on Progress in Physics*, 76(6):066201, June 2013. doi: 10.1088/0034-4885/76/6/066201.

M. Rayet and M.-a. Hashimoto. The s-process efficiency in massive stars. *Astronomy and Astrophysics*, 354:740–748, February 2000.

M. Rayet, M. Arnould, and N. Prantzos. The p-process revisited. *Astronomy and Astrophysics*, 227:271–281, January 1990.

H. Reeves. Galactic Cosmic Ray Origin of Li, Be and B in Stars. *Nature*, 226:727–729, May 1970. doi: 10.1038/226727a0.

C. E. Rolfs and W. S. Rodney. *Cauldrons in the cosmos: Nuclear astrophysics*. 1988.

A. J. Ruiter, K. Belczynski, S. A. Sim, W. Hillebrandt, M. Fink, and M. Kromer. Type Ia Supernovae and Accretion Induced Collapse. In V. Kologera and M. van der Sluys, editors, *American Institute of Physics Conference Series*, volume 1314 of *American Institute of Physics Conference Series*, pages 233–238, December 2010. doi: 10.1063/1.3536375.

I.-J. Sackmann and S. P. S. Anand. Structure and Evolution of Rapidly Rotating B-Type Stars. *ApJ*, 162:105, October 1970. doi: 10.1086/150637.

B. Salasnich, L. Girardi, A. Weiss, and C. Chiosi. Evolution models for α-enhanced stars (Salasnich+ 2000). *VizieR Online Data Catalog*, 336:11023, November 2000.

M. J. Seaton. *The opacity project*. 1995.

P. A. Seeger, W. A. Fowler, and D. D. Clayton. Nucleosynthesis of Heavy Elements by Neutron Capture. *ApJS*, 11:121, February 1965. doi: 10.1086/190111.

S. L. Shapiro and S. A. Teukolsky. *Black holes, white dwarfs, and neutron stars: The physics of compact objects*. 1983.

M. D. Shetrone, C. Sneden, and C. A. Pilachowski. Carbon isotope ratios and lithium abundances in old disk giants. *Publications of the Astronomical Society of the Pacific*, 105:337–349, April 1993. doi: 10.1086/133160.

M. Shibata and S. L. Shapiro. Collapse of a Rotating Supermassive Star to a Supermassive Black Hole: Fully Relativistic Simulations. *ApJl*, 572:L39–L43, June 2002. doi: 10.1086/341516.

L. Siess. Evolution of massive AGB stars. II. model properties at non-solar metallicity and the fate of Super-AGB stars. *Astronomy & Astrophysics*, 476:893–909, December 2007. doi: 10.1051/0004-6361:20078132.

L. Siess. The most massive AGB stars. In L. Deng and K. L. Chan, editors, *IAU Symposium*, volume 252 of *IAU Symposium*, pages 297–307, October 2008. doi: 10.1017/S1743921308023077.

N. Soker, M. Catelan, R. T. Rood, and A. Harpaz. A Superwind from Early Post-Red Giant Stars? *ApJ*, 563:L69–L72, December 2001. doi: 10.1086/338443.

C. Soubiran and P. Girard. Abundance trends in kinematical groups of the Milky Way's disk. *Astronomy and Astrophysics*, 438:139–151, July 2005. doi: 10.1051/0004-6361:20042390.

T. Spillane, F. Raiola, C. Rolfs, D. Schürmann, F. Strieder, S. Zeng, H.-W. Becker, C. Bordeanu, L. Gialanella, M. Romano, and J. Schweitzer. C12+C12 Fusion Reactions near the Gamow Energy. *Physical Review Letters*, 98(12):122501, March 2007. doi: 10.1103/PhysRevLett.98.122501.

F. Spite and M. Spite. Abundance of lithium in unevolved halo stars and old disk stars - Interpretation and consequences. *Astronomy and Astrophysics*, 115:357–366, November 1982.

S. Starrfield. Thermonuclear processes and the classical nova outburst. In M. F. Bode and A. Evans, editors, *Classical Novae*, pages 39–60, 1989.

T. Sukhbold and S. Woosley. The Compactness of Presupernova Stellar Cores. *ArXiv e-prints*, November 2013.

K. Takahashi and K. Yokoi. Beta-Decay Rates of Highly Ionized Heavy Atoms in Stellar Interiors. *Atomic Data and Nuclear Data Tables*, 36:375, 1987. doi: 10.1016/0092-640X(87)90010-6.

S. F. Taylor, J. A. Harvin, and H. A. McAlister. The CHARA Catalog of Orbital Elements of Spectroscopic Binary Stars. *Publications of the Astronomical Society of the Pacific*, 115:609–617, May 2003. doi: 10.1086/374759.

F. K. Thielemann and W. D. Arnett. Hydrostatic Nucleosynthesis - Part Two - Core Neon to Silicon Burning and Presupernova Abundance Yields of Massive Stars. *ApJ*, 295:604, August 1985. doi: 10.1086/163403.

F.-K. Thielemann, I. Dillmann, K. Farouqi, T. Fischer, C. Fröhlich, A. Kelic-Heil, I. Korneev, K.-L. Kratz, K. Langanke, M. Liebendörfer, I. V. Panov, G. Martinez-Pinedo, and T. Rauscher. The r-, p-, and νp-Process. *Journal of Physics Conference Series*, 202(1):012006, January 2010. doi: 10.1088/1742-6596/202/1/012006.

F. X. Timmes, S. E. Woosley, and T. A. Weaver. Galactic chemical evolution: Hydrogen through zinc. *ApJs*, 98:617–658, June 1995. doi: 10.1086/192172.

F. X. Timmes, S. E. Woosley, and T. A. Weaver. The Neutron Star and Black Hole Initial Mass Function. *ApJ*, 457:834, February 1996. doi: 10.1086/176778.

F. X. Timmes, E. F. Brown, and J. W. Truran. On Variations in the Peak Luminosity of Type Ia Supernovae. *ApJl*, 590:L83–L86, June 2003. doi: 10.1086/376721.

Y. S. Ting, K. C. Freeman, C. Kobayashi, G. M. de Silva, and J. Bland-Hawthorn. Principal component analysis on chemical abundances spaces. *Monthly Notices of the RAS*, 421:1231–1255, April 2012. doi: 10.1111/j.1365-2966.2011.20387.x.

B. M. Tinsley. Evolution of the Stars and Gas in Galaxies. *Fundamental Cosmic Physics*, 5:287–388, 1980.

L. Tolos, I. Sagert, D. Chatterjee, J. Schaffner-Bielich, and C. Sturm. Implications for compact stars of a soft nuclear equation of state from heavy-ion data. *ArXiv e-prints*, November 2012.

S. Toonen, G. Nelemans, and S. Portegies Zwart. Supernova Type Ia progenitors from merging double white dwarfs. Using a new population synthesis model. *Astronomy & Astrophysics*, 546:A70, October 2012. doi: 10.1051/0004-6361/201218966.

T. Totani, T. Morokuma, T. Oda, M. Doi, and N. Yasuda. Delay Time Distribution Measurement of Type Ia Supernovae by the Subaru/XMM-Newton Deep Survey and Implications for the Progenitor. *Publications of the Astronomical Society of Japan*, 60:1327–, December 2008.

C. Travaglio, D. Galli, R. Gallino, M. Busso, F. Ferrini, and O. Straniero. Galactic Chemical Evolution of Heavy Elements: From Barium to Europium. *ApJ*, 521:691–702, August 1999. doi: 10.1086/307571.

C. Travaglio, R. Gallino, E. Arnone, J. Cowan, F. Jordan, and C. Sneden. Galactic Evolution of Sr, Y, And Zr: A Multiplicity of Nucleosynthetic Processes. *ApJ*, 601: 864–884, February 2004a. doi: 10.1086/380507.

C. Travaglio, W. Hillebrandt, M. Reinecke, and F.-K. Thielemann. Nucleosynthesis in multi-dimensional SN Ia explosions. *Astronomy and Astrophysics*, 425:1029–1040, October 2004b. doi: 10.1051/0004-6361:20041108.

J. W. Truran. A new interpretation of the heavy element abundances in metal-deficient stars. *Astronomy and Astrophysics*, 97:391–393, April 1981.

J. W. Truran. Nuclear Theory of Novae. In C. A. Barnes, D. D. Clayton, and D. N. Schramm, editors, *Essays in Nuclear Astrophysics*, page 467, 1982.

J. W. Truran and W. D. Arnett. Nucleosynthesis in Explosive Oxygen Burning. *ApJ*, 160:181, April 1970. doi: 10.1086/150415.

J. W. Truran and J. J. Cowan. On the Site of the Weak r-Process Component. In W. Hillebrandt and E. Müller, editors, *Nuclear Astrophysics, 2000*, page 64, 2000.

J. W. Truran and I. Iben, Jr. On s-process nucleosynthesis in thermally pulsing stars. *ApJ*, 216:797–810, September 1977. doi: 10.1086/155523.

J. W. Truran, J. J. Cowan, and A. G. W. Cameron. The helium-driven r-process in supernovae. *ApJL*, 222:L63–L67, June 1978. doi: 10.1086/182693.

J. Tumlinson. Chemical Evolution in Hierarchical Models of Cosmic Structure. I. Constraints on the Early Stellar Initial Mass Function. *ApJ*, 641:1–20, April 2006. doi: 10.1086/500383.

C. Tur, A. Heger, and S. M. Austin. On the Sensitivity of Massive Star Nucleosynthesis and Evolution to Solar Abundances and to Uncertainties in Helium-Burning Reaction Rates. *ApJ*, 671:821–827, December 2007. doi: 10.1086/523095.

C. Tur, A. Heger, and S. M. Austin. Dependence of s-Process Nucleosynthesis in Massive Stars on Triple-Alpha and ^{12}C(α, γ)^{16}O Reaction Rate Uncertainties. *ApJ*, 702:1068–1077, September 2009. doi: 10.1088/0004-637X/702/2/1068.

C. Tur, A. Heger, and S. M. Austin. Production of ^{26}Al, ^{44}Ti, and ^{60}Fe in Core-collapse Supernovae: Sensitivity to the Rates of the Triple Alpha and ^{12}C(α, γ)^{16}O Reactions. *ApJ*, 718:357–367, July 2010. doi: 10.1088/0004-637X/718/1/357.

M. Ugliano, H.-T. Janka, A. Marek, and A. Arcones. Progenitor-explosion Connection and Remnant Birth Masses for Neutrino-driven Supernovae of Iron-core Progenitors. *ApJ*, 757:69, September 2012. doi: 10.1088/0004-637X/757/1/69.

H. Umeda and K. Nomoto. Nucleosynthesis of Zinc and Iron Peak Elements in Population III Type II Supernovae: Comparison with Abundances of Very Metal Poor Halo Stars. *ApJ*, 565:385–404, January 2002. doi: 10.1086/323946.

G. Walter, H. Beer, F. Käppeler, G. Reffo, and F. Fabbri. The s-process branching at Se-79. *Astronomy and Astrophysics*, 167:186–199, October 1986.

S. Wanajo, K. Nomoto, H.-T. Janka, F. S. Kitaura, and B. Müller. Nucleosynthesis in Electron Capture Supernovae of Asymptotic Giant Branch Stars. *ApJ*, 695:208–220, April 2009. doi: 10.1088/0004-637X/695/1/208.

B. Wang and Z. Han. Progenitors of type Ia supernovae. *New Astronomy*, 56:122–141, June 2012. doi: 10.1016/j.newar.2012.04.001.

T. A. Weaver, G. B. Zimmerman, and S. E. Woosley. Presupernova evolution of massive stars. *ApJ*, 225:1021–1029, November 1978. doi: 10.1086/156569.

J. C. Wheeler, C. Sneden, and J. W. Truran, Jr. Abundance ratios as a function of metallicity. *Annual review of astronomy and astrophysics*, 27:279–349, 1989. doi: 10.1146/annurev.aa.27.090189.001431.

J. R. Wilson. Supernovae and Post-Collapse Behavior. In J. M. Centrella, J. M. Leblanc, and R. L. Bowers, editors, *Numerical Astrophysics*, page 422, 1985.

S. E. Woosley. Neutrino-induced nucleosynthesis and deuterium. *Nature*, 269:42–44, September 1977. doi: 10.1038/269042a0.

S. E. Woosley. Models for type Ia supernovae. *Nuclear Physics A*, 688:9–16, May 2001. doi: 10.1016/S0375-9474(01)00659-5.

S. E. Woosley and W. C. Haxton. Supernova neutrinos, neutral currents and the origin of fluorine. *Nature*, 334:45–47, July 1988. doi: 10.1038/334045a0.

S. E. Woosley and A. Heger. Nucleosynthesis and remnants in massive stars of solar metallicity. *Physics Reports*, 442:269–283, April 2007. doi: 10.1016/j.physrep.2007.02.009.

S. E. Woosley and W. M. Howard. The p-process in supernovae. *ApJs*, 36:285–304, February 1978. doi: 10.1086/190501.

S. E. Woosley and T. A. Weaver. Presupernova models: sensitivity to convective algorithm and Coulomb corrections. *Physics Reports*, 163:79–94, 1988. doi: 10.1016/0370-1573(88)90037-3.

S. E. Woosley and T. A. Weaver. The Evolution and Explosion of Massive Stars. II. Explosive Hydrodynamics and Nucleosynthesis. *ApJs*, 101:181, November 1995. doi: 10.1086/192237.

S. E. Woosley, D. H. Hartmann, R. D. Hoffman, and W. C. Haxton. The nu-process. *ApJ*, 356:272–301, June 1990. doi: 10.1086/168839.

S. E. Woosley, A. Heger, and T. A. Weaver. The evolution and explosion of massive stars. *Reviews of Modern Physics*, 74:1015–1071, November 2002. doi: 10.1103/RevModPhys.74.1015.

S. E. Woosley, A. Heger, T. Rauscher, and R. D. Hoffman. Nuclear data needs for the study of nucleosynthesis in massive stars. *Nuclear Physics A*, 718:3–12, May 2003. doi: 10.1016/S0375-9474(03)00673-0.

W.-M. Yao, C. Amsler, D. Asner, R. M. Barnett, J. Beringer, P. R. Burchat, C. D. Carone, C. Caso, O. Dahl, G. D'Ambrosio, A. De Gouvea, M. Doser, S. Eidelman, J. L. Feng, T. Gherghetta, M. Goodman, C. Grab, D. E. Groom, A. Gurtu, K. Hagiwara, K. G. Hayes, J. J. Hernández-Rey, K. Hikasa, H. Jawahery, C. Kolda, Y. Kwon, M. L. Mangano, A. V. Manohar, A. Masoni, R. Miquel, K. Mönig, H. Murayama, K. Nakamura, S. Navas, K. A. Olive, L. Pape, C. Patrignani, A. Piepke, G. Punzi, G. Raffelt, J. G. Smith, M. Tanabashi, J. Terning, N. A. Törnqvist, T. G. sTrippe, P. Vogel, T. Watari, C. G. Wohl, R. L. Workman, P. A. Zyla, B. Armstrong, G. Harper, V. S. Lugovsky, P. Schaffner, M. Artuso, K. S. Babu, H. R. Band, E. Barberio, M. Battaglia, H. Bichsel, O. Biebel, P. Bloch, E. Blucher, R. N. Cahn, D. Casper, A. Cattai, A. Ceccucci, D. Chakraborty, R. S. Chivukula, G. Cowan, T. Damour, T. DeGrand, K. Desler, M. A. Dobbs, M. Drees, A. Edwards, D. A. Edwards, V. D. Elvira, J. Erler, V. V. Ezhela, W. Fetscher, B. D. Fields, B. Foster, D. Froidevaux, T. K. Gaisser, L. Garren, H.-J. Gerber, G. Gerbier, L. Gibbons, F. J. Gilman, G. F. Giudice, A. V. Gritsan, M. Grünewald, H. E. Haber, C. Hagmann, I. Hinchliffe, A. Höcker, P. Igo-Kemenes, J. D. JAckson, K. F. Johnson, D. Karlen, B. Kayser, D. Kirkby, S. R. Klein, K. Kleinknecht, I. G. Knowles, R. V. Kowalewski, P. Kreitz, B. Kursche, Y. V. Kuyanov, O. Lahav, P. Langacker, A. Liddle, Z. Ligeti, T. M. Liss, L. Littenberg, J. C. Liu, K. S. Lugovsky, s. B. Lugovsky, T. Mannel,

D. M. Manley, W. J. Marciano, A. D. Martin, D. Milstead, M. Narain, P. Nason, Y. Nir, J. A. Peacock, S. A. Prell, A. Quadt, S. Raby, B. N. Ratcliff, E. A. Razuvaev, B. Renk, P. Richardson, S. Roesler, G. Rolandi, M. T. Ronan, L. J. Rosenberg, C. T. Sachrajda, Y. Sakai, S. Sarkar, M. Schmitt, O. Schneider, D. Scott, T. Sjöstrand, G. F. Smoot, P. Sokolsky, S. Spanier, H. Spieler, A. Stahl, T. Stanev, R. E. Streitmatter, T. Sumiyoshi, N. P. Tkachenko, G. H. Trilling, G. Valencia, K. van Bibber, M. G. Vincter, D. R. Ward, B. R. Webber, J. D. Wells, M. Whalley, L. Wolfenstsein, J. Womersley, C. L. Woody, A. Yamamoto, O. V. Zenin, J. Zhang, and R.-Y. Zhu. Review of Particle Physics. *Journal of Physics G Nuclear Physics*, 33:1–1232, July 2006. doi: 10.1088/0954-3899/33/1/001.

T. Yoshida, M. Terasawa, T. Kajino, and K. Sumiyoshi. Nucleosynthesis of Light Elements and Heavy r-Process Elements through the ν-Process in Supernova Explosions. *ApJ*, 600:204–213, January 2004. doi: 10.1086/379766.

W. Zhang, S. E. Woosley, and A. Heger. Fallback and Black Hole Production in Massive Stars. *ApJ*, 679:639–654, May 2008. doi: 10.1086/526404.

J. Zickefoose. *Carbon-12 + Carbon-12 Fusion: Measurement and Advances Toward the Gamow Energy.* PhD thesis, University of Connecticut, 2011.

Appendix A

Fitting Algorithm

In this section, we explain the general algorithm for constructing elemental ratios [X/Fe] from the isotopic scaling functions, and fitting to data. We then provide a specific example for illustation. The algorithm has the following steps.

A) For each isotope i of element X, write the scaling function, $X_i(\xi)$, for all processes that contribute to the solar abundance of X_i, using Equations 3.5 - 3.14 and the solar abundance decomposition in Section 3.2. This gives a scaling relation for the isotope as a function of ξ, with one or more free parameters.

B) Sum the isotopic scaling relations to give an elemental scaling relation,

$$X(\xi) = \sum_{i}^{n} X_i(\xi), \tag{A.1}$$

where n is the number of isotopes that comprise element X. The resulting elemental scaling is a function of ξ, and one or more free parameters.

C) Repeat steps A) and B) for the isotopes of Fe and H.

D) The ratios [X/Fe] and [Fe/H] can now be constructed, which are functions of ξ with

one or more free parameters. For any free parameter values chosen, a curve can be plotted in the [X/Fe] and [Fe/H] plane. This curve is generated by evaluating the ratios across $\xi \in [0, 1]$.

E) Observational data is then plotted on the [X/Fe] and [Fe/H] plane, and each data point is assigned a gaussian spread (Equation 3.15), and the gaussian contributions in x- and y-axes are binned and averaged (Section 3.4).

F) A χ^2_r analysis is performed for the free parameter values in [X/Fe] and [Fe/H]: for each free parameter value a curve generated for [X/Fe] vs. [Fe/H], and a best-fit parameter value is chosen that minimizes the χ^2_r between the curve and the averaged data. This defines a unique curve for [X/Fe] against [Fe/H], and hence also gives unique functions for the elemental *and isotopic* scaling relations.

We now give a specific example of the above steps A) - C), for constructing the elemental ratios [Au/Fe] and [Fe/H]. Note the above steps D) - F) are discussed in Section 3.4 for the elements Mg, Eu, Ba, Sr, and Pb.

To construct [Au/Fe] and [Fe/H], we first consider Au. This element has only one stable isotope, ^{197}Au. The solar abundance for ^{197}Au has *hs*-process and *r*-process components (Section 3.2), hence these abundances scale as follows (using Equations 3.9 and 3.11):

$$^{197}\mathrm{Au}(\xi) = {}^{197}\mathrm{Au}^{\mathrm{s}}_{\odot} \cdot (\xi)^h + {}^{197}\mathrm{Au}^{\mathrm{r}}_{\odot} \cdot (\xi)^p, \tag{A.2}$$

where $^{197}\mathrm{Au}^{\mathrm{s}}_{\odot}$ is the portion of the solar abundance of ^{197}Au from the *hs*-process. Similarly, $^{197}\mathrm{Au}^{\mathrm{r}}_{\odot}$ is the portion of the solar abundance of ^{197}Au from the *r*-process. For illustration, we can evaluate $^{197}\mathrm{Au}(\xi)$ at $\xi = 0, 1$:

$$^{197}\mathrm{Au}(\xi = 0) = 0, \tag{A.3}$$

$$^{197}\mathrm{Au}(\xi = 1) = {}^{197}\mathrm{Au}^{\mathrm{s}}_{\odot} + {}^{197}\mathrm{Au}^{\mathrm{r}}_{\odot} = {}^{197}\mathrm{Au}_{\odot}. \tag{A.4}$$

Observe that Equation A.3 gives the BBN abundance of ^{197}Au, whereas Equation A.4

gives the solar abundance. When ξ takes a value in between 0 and 1, we get a ^{197}Au abundance that is in between BBN and solar. This holds for all elemental scalings (all scaling functions are monotonic). We now have a scaling relation for ^{197}Au using the continuous technical parameter ξ. Note the function $^{197}\mathrm{Au}(\mathrm{Z}/\mathrm{Z}_{\odot})$ also must go from BBN to solar for $Z/Z_{\odot} \in [0,1]$. Since Au is a mono-isotopic element, the function of its isotope is also the function of its element, $^{197}\mathrm{Au}(\xi) = \mathrm{Au}(\xi)$.

The 4 stable isotopes of Fe have massive, Type Ia, and weak s-process contributions (found using Equations 3.5, 3.6, and 3.10),

$$^{54}\mathrm{Fe}(\xi) = {}^{54}\mathrm{Fe}_{\odot}^{\mathrm{Ia}} \cdot \xi \cdot [\tanh(a \cdot \xi - b) + \tanh(b)]/[\tanh(a - b) + \tanh(b)] + \\ + 10^{m_{\mathrm{Fe54}} \cdot (\log(\xi) - \log(\xi_{low})) + \log\left(X_{\mathrm{Fe54}}^{\mathrm{sim}}\right)}, \tag{A.5}$$

$$^{56}\mathrm{Fe}(\xi) = {}^{56}\mathrm{Fe}_{\odot}^{\mathrm{Ia}} \cdot \xi \cdot [\tanh(a \cdot \xi - b) + \tanh(b)]/[\tanh(a - b) + \tanh(b)] + \\ + 10^{m_{\mathrm{Fe56}} \cdot (\log(\xi) - \log(\xi_{low})) + \log\left(X_{\mathrm{Fe56}}^{\mathrm{sim}}\right)}, \tag{A.6}$$

$$^{57}\mathrm{Fe}(\xi) = {}^{57}\mathrm{Fe}_{\odot}^{\mathrm{ws}} \cdot \xi^{w} + 10^{m_{\mathrm{Fe57}} \cdot (\log(\xi) - \log(\xi_{low})) + \log\left(X_{\mathrm{Fe57}}^{\mathrm{sim}}\right)}, \tag{A.7}$$

$$^{58}\mathrm{Fe}(\xi) = {}^{58}\mathrm{Fe}_{\odot}^{\mathrm{ws}} \cdot \xi^{w} + 10^{m_{\mathrm{Fe58}} \cdot (\log(\xi) - \log(\xi_{low})) + \log\left(X_{\mathrm{Fe58}}^{\mathrm{sim}}\right)}. \tag{A.8}$$

We then find the function for elemental Fe, given by the sum of isotopic functions, $\mathrm{Fe}(\xi) = {}^{54}\mathrm{Fe}(\xi) + {}^{56}\mathrm{Fe}(\xi) + {}^{57}\mathrm{Fe}(\xi) + {}^{58}\mathrm{Fe}(\xi)$.

The ratio $[\mathrm{Au/Fe}] = \log(\mathrm{Au}(\xi)/\mathrm{Au}_{\odot}) - \log(\mathrm{Fe}(\xi)/\mathrm{Fe}_{\odot})$ can then be constructed (which is a function of ξ). To find [Fe/H], we need the scaling functions for deuterium and ^{1}H (using Equations 3.11 and 3.14:

$$\mathrm{D}(\xi) = (\mathrm{D}_{\odot} - \mathrm{D}_{\mathrm{BBN}}) \cdot \xi^{p} + \mathrm{D}_{\mathrm{BBN}}, \tag{A.9}$$

$$^{1}\mathrm{H}(\xi) = {}^{1}\mathrm{H}_{\odot} \cdot [1.0 - \xi \cdot Z_{\odot} - \mathrm{Y}(\xi) - \mathrm{D}(\xi)], \tag{A.10}$$

where D_{BBN} is the BBN abundance of deuterium. The helium function, $Y(\xi)$, is the sum of the isotopic scalings of its two stable isotopes (found using Equation 3.11 with BBN offsets):

$$^3\mathrm{He}(\xi) = (^3\mathrm{He}_\odot - {}^3\mathrm{He}_{\mathrm{BBN}}) \cdot \xi^p + {}^3\mathrm{He}_{\mathrm{BBN}}, \tag{A.11}$$

$$^4\mathrm{He}(\xi) = (^4\mathrm{He}_\odot - {}^4\mathrm{He}_{\mathrm{BBN}}) \cdot \xi^p + {}^4\mathrm{He}_{\mathrm{BBN}}. \tag{A.12}$$

The elemental function for H is then, $\mathrm{H}\,(\xi) = {}^1\mathrm{H}(\xi) + \mathrm{D}(\xi)$, and [Fe/H] can be found. The specific values used for the free parameters h, p, a, b, and w are given in Section B.1. All free parameter values are determined by fitting the elemental functions [Mg/Fe], [Eu/Fe], [Ba/Fe], [Sr/Fe], and [Pb/Fe] to observational data (Section 3.4). We then have defined a unique curve in the [Au/Fe] vs. [Fe/H] plane. Using Equations 3.5 - 3.14, Table B.1, and Table B.2, all isotopic functions and elemental ratios can be evaluated in this manner.

Appendix B

Tables

Table B.1 summarizes the optimized parameter values found by fitting to data.
Table B.2 gives the solar abundance pattern decomposition for all stable isotopes into the various astrophysical processes employed by the scaling model: Big Bang Nucleosynthesis, ν-process/primary galactic cosmic ray spallation/novae yields (together in a single category), secondary galactic cosmic ray spallation, massive star yields (includes CCSNe, stellar winds, ν-process, and r-process contributions from carbon through zinc), Type Ia SNe yields, main s-process (which include all of "strong", ls, and hs components), weak s-process, νp-process, γ-process, and the r-process (from zinc through uranium). The solar abundances in column 2 are from Lodders (2010) and are in units of mole fractions. The various astrophysical processes in columns 3-12 show the fraction of the solar abundance attributed to each process, and these fractions can be used to decompose any desired solar abundance pattern. The fraction values are rounded to three significant figures. Note that the remaining helium not made in BBN is from hydrogen burning, which not explicitly shown in the the table.
Table B.3 shows the ratios of the isotopic abundances given by our scaling model over a simple linear interpolation of abundances between BBN and solar. Ratios for all isotopes are given at two different metallicities: $[Z] = -1$, and $[Z] = -3$.

Table B.1. Optimized Parameter Values Used in Scaling Model

Parameter	Best-fit Value	Description
a	5.024	Type Ia tanh Scaling Factor
b	2.722	Type Ia tanh Shifting Factor
f	0.693	Fraction of Solar ^{56}Fe from Type Ia
p	0.938	Primary Process Exponent
h	1.509	hs-process Exponent
l	1.227	ls-process Exponent
w	1.230	Weak s-process Exponent
d	140	"Strong" tanh Scaling Factor
g	-0.05	"Strong" tanh Shift Factor

Table B.2: Solar Abundance Decomposition

Ion	Solar	Main s	Weak s	r-proc	νp-proc	γ-proc	SNIa	Massive	GCR	ν/Novae/GCR	BBN
H1	7.0571E-01	···	···	···	···	···	···	···	···	···	1.06
H2	1.3691E-05	···	···	···	···	···	···	···	···	···	1.57
He3	1.1343E-05	···	···	···	···	···	···	···	···	···	6.23E-01
He4	6.8306E-02	···	···	···	···	···	···	···	···	···	9.10E-01
Li6	1.1479E-10	···	···	···	···	···	···	···	3.00E-01	7.00E-01	···
Li7	1.3978E-09	···	···	···	···	···	···	···	3.00E-01	5.05E-01	1.95E-01
Be9	1.6640E-11	···	···	···	···	···	···	···	2.50E-01	7.50E-01	···
B10	1.0146E-10	···	···	···	···	···	···	···	2.50E-01	7.50E-01	···
B11	4.1043E-10	···	···	···	···	···	···	···	2.50E-01	7.50E-01	···
C12	1.9355E-04	···	···	···	···	···	1.12E-02	9.89E-01	···	···	···
C13	2.1747E-06	···	···	···	···	···	2.19E-05	1.00	···	···	···
N14	5.7550E-05	···	···	···	···	···	4.56E-06	1.00	···	···	···
N15	2.1158E-07	···	···	···	···	···	3.38E-06	1.00	···	···	···
O16	4.2717E-04	···	···	···	···	···	9.46E-03	9.91E-01	···	···	···
O17	1.5929E-07	···	···	···	···	···	6.27E-05	1.00	···	···	···
O18	8.5638E-07	···	···	···	···	···	8.13E-05	1.00	···	···	···
F19	2.1877E-08	···	···	···	···	···	4.42E-06	1.00	···	···	···
Ne20	8.3148E-05	···	···	···	···	···	8.22E-04	9.99E-01	···	···	···
Ne21	1.9932E-07	···	···	···	···	···	3.65E-03	9.96E-01	···	···	···
Ne22	6.1139E-06	···	···	···	···	···	3.81E-01	6.19E-01	···	···	···
Na23	1.5705E-06	···	···	···	···	···	5.08E-03	9.95E-01	···	···	···
Mg24	2.2036E-05	···	···	···	···	···	1.63E-02	9.84E-01	···	···	···
Mg25	2.7905E-06	···	···	···	···	···	5.23E-03	9.95E-01	···	···	···
Mg26	3.0701E-06	···	···	···	···	···	3.58E-03	9.96E-01	···	···	···
Al27	2.3014E-06	···	···	···	···	···	7.35E-02	9.26E-01	···	···	···

Table B.2 – Continued

Ion	Solar	Main s	Weak s	r-proc	νp-proc	γ-proc	SNIa	Massive	GCR	ν/Novae/GCR	BBN
Si28	2.5093E-05	···	···	···	···	···	2.51E-01	7.49E-01	···	···	···
Si29	1.2741E-06	···	···	···	···	···	2.65E-01	7.35E-01	···	···	···
Si30	8.3992E-07	···	···	···	···	···	4.28E-01	5.72E-01	···	···	···
P31	2.2592E-07	···	···	···	···	···	1.73E-01	8.27E-01	···	···	···
S32	1.0890E-05	···	···	···	···	···	2.16E-01	7.84E-01	···	···	···
S33	8.5956E-08	···	···	···	···	···	2.28E-01	7.72E-01	···	···	···
S34	4.8307E-07	···	···	···	···	···	3.93E-01	6.07E-01	···	···	···
S36	1.9483E-09	···	···	···	···	···	4.86E-01	5.14E-01	···	···	···
Cl35	1.0653E-07	···	···	···	···	···	8.18E-02	9.18E-01	···	···	···
Cl37	3.4066E-08	···	···	···	···	···	1.16E-01	8.84E-01	···	···	···
Ar36	2.1329E-06	···	···	···	···	···	2.14E-01	7.86E-01	···	···	···
Ar38	3.8781E-07	···	···	···	···	···	2.81E-01	7.19E-01	···	···	···
Ar40	6.0578E-10	···	···	···	···	···	3.98E-01	6.02E-01	···	···	···
K39	9.5342E-08	···	···	···	···	···	5.10E-02	9.49E-01	···	···	···
K40	1.5000E-10	···	···	···	···	···	···	1.00	···	···	···
K41	6.8806E-09	···	···	···	···	···	6.07E-02	9.39E-01	···	···	···
Ca40	1.5925E-06	···	···	···	···	···	2.97E-01	7.03E-01	···	···	···
Ca42	1.0629E-08	···	···	···	···	···	1.93E-01	8.07E-01	···	···	···
Ca43	2.2179E-09	···	···	···	···	···	1.71E-02	9.83E-01	···	···	···
Ca44	3.4270E-08	···	···	···	···	···	5.79E-02	9.42E-01	···	···	···
Ca46	6.5714E-11	···	···	···	···	···	9.58E-01	4.23E-02	···	···	···
Ca48	3.0721E-09	···	···	···	···	···	3.16E-01	6.84E-01	···	···	···
Sc45	9.3722E-10	···	···	···	···	···	3.26E-02	9.67E-01	···	···	···
Ti46	5.5503E-09	···	···	···	···	···	3.51E-01	6.49E-01	···	···	···
Ti47	5.0040E-09	···	···	···	···	···	5.00E-02	9.50E-01	···	···	···

Table B.2 – Continued

Ion	Solar	Main s	Weak s	r-proc	νp-proc	γ-proc	SNIa	Massive	GCR	ν/Novae/GCR	BBN
Ti48	4.9602E-08	···	···	···	···	···	2.65E-01	7.35E-01	···	···	···
Ti49	3.6394E-09	···	···	···	···	···	3.53E-01	6.47E-01	···	···	···
Ti50	3.4887E-09	···	···	···	···	···	1.00	8.27E-05	···	···	···
V50	1.9458E-11	···	···	···	···	···	1.78E-01	8.22E-01	···	···	···
V51	7.7732E-09	···	···	···	···	···	4.23E-01	5.77E-01	···	···	···
Cr50	1.5469E-08	···	···	···	···	···	7.65E-01	2.35E-01	···	···	···
Cr52	2.9829E-07	···	···	···	···	···	5.64E-01	4.36E-01	···	···	···
Cr53	3.3822E-08	···	···	···	···	···	7.29E-01	2.71E-01	···	···	···
Cr54	8.4184E-09	···	···	···	···	···	9.91E-01	8.88E-03	···	···	···
Mn55	2.5088E-07	···	···	···	···	···	8.69E-01	1.31E-01	···	···	···
Fe54	1.3481E-06	···	···	···	···	···	9.66E-01	3.35E-02	···	···	···
Fe56	2.1162E-05	···	···	···	···	···	6.94E-01	3.07E-01	···	···	···
Fe57	4.8876E-07	···	1.40E-04	···	···	···	···	1.00	···	···	···
Fe58	6.5018E-08	···	1.79E-02	···	···	···	···	9.82E-01	···	···	···
Co59	6.3817E-08	···	8.97E-03	···	···	···	···	9.91E-01	···	···	···
Ni58	9.0816E-07	···	···	···	···	···	···	1.00	···	···	···
Ni60	3.4988E-07	···	3.80E-03	···	···	···	···	9.96E-01	···	···	···
Ni61	1.5206E-08	···	3.74E-02	···	···	···	···	9.63E-01	···	···	···
Ni62	4.8485E-08	···	7.33E-02	···	···	···	···	9.27E-01	···	···	···
Ni64	1.2348E-08	···	2.81E-01	···	···	···	···	7.19E-01	···	···	···
Cu63	1.0184E-08	7.00E-03	1.61E-01	···	···	···	···	8.32E-01	···	···	···
Cu65	4.5381E-09	1.90E-02	7.27E-01	···	···	···	···	2.54E-01	···	···	···
Zn64	1.7153E-08	1.00E-03	6.67E-02	···	···	···	···	9.32E-01	···	···	···
Zn66	9.8409E-09	9.00E-03	2.70E-01	···	···	···	···	7.21E-01	···	···	···
Zn67	1.4461E-09	1.40E-02	4.08E-01	···	···	···	···	5.78E-01	···	···	···

Table B.2 – Continued

Ion	Solar	Main s	Weak s	r-proc	νp-proc	γ-proc	SNIa	Massive	GCR	ν/Novae/GCR	BBN
Zn68	6.6135E-09	2.00E-02	5.19E-01	···	···	···	···	4.61E-01	···	···	···
Zn70	2.1869E-10	1.00E-03	···	9.99E-01	···	···	···	···	···	···	···
Ga69	5.9779E-10	3.20E-02	7.41E-01	2.27E-01	···	···	···	···	···	···	···
Ga71	3.9674E-10	5.30E-02	9.47E-01	···	···	···	···	···	···	···	···
Ge70	6.6233E-10	5.40E-02	9.46E-01	···	···	···	···	···	···	···	···
Ge72	8.6283E-10	7.00E-02	6.80E-01	2.50E-01	···	···	···	···	···	···	···
Ge73	2.4071E-10	6.70E-02	6.88E-01	2.45E-01	···	···	···	···	···	···	···
Ge74	1.1211E-09	8.10E-02	6.73E-01	2.46E-01	···	···	···	···	···	···	···
Ge76	2.3219E-10	1.00E-03	···	9.99E-01	···	···	···	···	···	···	···
As75	1.6585E-10	5.50E-02	4.47E-01	4.98E-01	···	···	···	···	···	···	···
Se74	1.6322E-11	···	5.00E-01	···	5.00E-01	···	···	···	···	···	···
Se76	1.7196E-10	1.45E-01	8.55E-01	···	···	···	···	···	···	···	···
Se77	1.4018E-10	6.80E-02	3.91E-01	5.41E-01	···	···	···	···	···	···	···
Se78	4.3645E-10	1.53E-01	6.58E-01	1.89E-01	···	···	···	···	···	···	···
Se80	9.1077E-10	8.90E-02	9.14E-03	9.02E-01	···	···	···	···	···	···	···
Se82	1.6030E-10	1.00E-03	···	9.99E-01	···	···	···	···	···	···	···
Br79	1.4768E-10	7.40E-02	1.78E-01	7.48E-01	···	···	···	···	···	···	···
Br81	1.4368E-10	9.30E-02	3.99E-01	5.08E-01	···	···	···	···	···	···	···
Kr78	5.5028E-12	···	5.00E-01	···	5.00E-01	···	···	···	···	···	···
Kr80	3.5341E-11	9.80E-02	7.52E-01	···	1.50E-01	···	···	···	···	···	···
Kr82	1.7707E-10	2.87E-01	6.83E-01	···	3.00E-02	···	···	···	···	···	···
Kr83	1.7542E-10	1.07E-01	2.56E-01	6.37E-01	···	···	···	···	···	···	···
Kr84	8.6451E-10	1.38E-01	1.71E-01	6.91E-01	···	···	···	···	···	···	···
Kr86	2.6143E-10	1.89E-01	···	8.11E-01	···	···	···	···	···	···	···
Rb85	1.3932E-10	1.75E-01	3.16E-01	5.09E-01	···	···	···	···	···	···	···

Table B.2 – Continued

Ion	Solar	Main s	Weak s	r-proc	νp-proc	γ-proc	SNIa	Massive	GCR	ν/Novae/GCR	BBN
Rb87	5.7339E-11	2.80E-01	···	7.20E-01	···	···	···	···	···	···	···
Sr84	3.5322E-12	···	5.00E-01	···	5.00E-01	···	···	···	···	···	···
Sr86	6.2461E-11	5.60E-01	4.40E-01	···	···	···	···	···	···	···	···
Sr87	4.3651E-11	5.53E-01	4.47E-01	···	···	···	···	···	···	···	···
Sr88	5.2333E-10	1.00	···	···	···	···	···	···	···	···	···
Y89	1.2610E-10	9.81E-01	1.90E-02	···	···	···	···	···	···	···	···
Zr90	1.5089E-10	7.65E-01	1.49E-02	2.20E-01	···	···	···	···	···	···	···
Zr91	3.2913E-11	9.52E-01	1.27E-02	3.53E-02	···	···	···	···	···	···	···
Zr92	5.0282E-11	9.05E-01	6.81E-03	8.82E-02	···	···	···	···	···	···	···
Zr94	5.0969E-11	1.00	···	···	···	···	···	···	···	···	···
Zr96	8.2083E-12	4.63E-01	···	5.37E-01	···	···	···	···	···	···	···
Nb93	2.1209E-11	9.14E-01	3.37E-03	8.26E-02	···	···	···	···	···	···	···
Mo92	1.0075E-11	···	···	···	1.00	···	···	···	···	···	···
Mo94	6.3478E-12	8.00E-03	···	···	9.92E-01	···	···	···	···	···	···
Mo95	1.0986E-11	6.61E-01	3.59E-03	3.35E-01	···	···	···	···	···	···	···
Mo96	1.1564E-11	1.00	···	···	···	···	···	···	···	···	···
Mo97	6.6583E-12	6.11E-01	5.55E-03	3.83E-01	···	···	···	···	···	···	···
Mo98	1.6919E-11	7.94E-01	8.62E-03	1.97E-01	···	···	···	···	···	···	···
Mo100	6.8143E-12	4.30E-02	···	9.57E-01	···	···	···	···	···	···	···
Ru96	2.6864E-12	···	···	···	1.00	···	···	···	···	···	···
Ru98	9.0586E-13	···	···	···	1.00	···	···	···	···	···	···
Ru99	6.1841E-12	3.04E-01	3.65E-03	6.92E-01	···	···	···	···	···	···	···
Ru100	6.1068E-12	1.00	···	···	···	···	···	···	···	···	···
Ru101	8.2694E-12	1.63E-01	2.31E-03	8.35E-01	···	···	···	···	···	···	···
Ru102	1.5294E-11	4.57E-01	···	5.43E-01	···	···	···	···	···	···	···

Table B.2 – Continued

Ion	Solar	Main s	Weak s	r-proc	νp-proc	γ-proc	SNIa	Massive	GCR	ν/Novae/GCR	BBN
Ru104	9.0261E-12	2.20E-02	···	9.78E-01	···	···	···	···	···	···	···
Rh103	1.0078E-11	1.57E-01	···	8.43E-01	···	···	···	···	···	···	···
Pd102	3.7684E-13	···	···	···	2.50E-01	7.50E-01	···	···	···	···	···
Pd104	4.1157E-12	1.00	···	···	···	···	···	···	···	···	···
Pd105	8.2499E-12	1.46E-01	···	8.54E-01	···	···	···	···	···	···	···
Pd106	1.0097E-11	5.45E-01	···	4.55E-01	···	···	···	···	···	···	···
Pd108	9.7757E-12	6.95E-01	···	3.05E-01	···	···	···	···	···	···	···
Pd110	4.3300E-12	2.80E-02	···	9.72E-01	···	···	···	···	···	···	···
Ag107	6.8982E-12	1.59E-01	···	8.41E-01	···	···	···	···	···	···	···
Ag109	6.4087E-12	2.71E-01	···	7.29E-01	···	···	···	···	···	···	···
Cd106	5.3522E-13	···	···	···	···	1.00	···	···	···	···	···
Cd108	3.8108E-13	4.00E-03	···	···	···	9.96E-01	···	···	···	···	···
Cd110	5.3479E-12	1.00	···	···	···	···	···	···	···	···	···
Cd111	5.4807E-12	3.54E-01	···	6.46E-01	···	···	···	···	···	···	···
Cd112	1.0332E-11	7.00E-01	···	3.00E-01	···	···	···	···	···	···	···
Cd113	5.2323E-12	4.02E-01	···	5.98E-01	···	···	···	···	···	···	···
Cd114	1.2302E-11	8.37E-01	···	1.63E-01	···	···	···	···	···	···	···
Cd116	3.2070E-12	1.58E-01	···	8.42E-01	···	···	···	···	···	···	···
In113	2.0749E-13	···	···	···	···	1.00	···	···	···	···	···
In115	4.6314E-12	4.09E-01	···	5.91E-01	···	···	···	···	···	···	···
Sn112	9.5212E-13	···	···	···	···	1.00	···	···	···	···	···
Sn114	6.4619E-13	···	···	···	···	1.00	···	···	···	···	···
Sn115	3.3241E-13	2.50E-02	···	···	···	9.75E-01	···	···	···	···	···
Sn116	1.4253E-11	1.00	···	···	···	···	···	···	···	···	···
Sn117	7.5268E-12	5.14E-01	···	4.86E-01	···	···	···	···	···	···	···

Table B.2 – Continued

Ion	Solar	Main s	Weak s	r-proc	νp-proc	γ-proc	SNIa	Massive	GCR	ν/Novae/GCR	BBN
Sn118	2.3752E-11	7.27E-01	···	2.73E-01	···	···	···	···	···	···	···
Sn119	8.4181E-12	5.88E-01	···	4.12E-01	···	···	···	···	···	···	···
Sn120	3.1959E-11	7.62E-01	···	2.38E-01	···	···	···	···	···	···	···
Sn122	4.5390E-12	4.20E-01	···	5.80E-01	···	···	···	···	···	···	···
Sn124	5.6765E-12	···	···	1.00	···	···	···	···	···	···	···
Sb121	4.8656E-12	3.99E-01	···	6.01E-01	···	···	···	···	···	···	···
Sb123	3.6387E-12	6.30E-02	···	9.37E-01	···	···	···	···	···	···	···
Te120	1.2251E-13	···	···	···	···	1.00	···	···	···	···	···
Te122	3.3219E-12	1.00	···	···	···	···	···	···	···	···	···
Te123	1.1588E-12	1.00	···	···	···	···	···	···	···	···	···
Te124	6.1460E-12	1.00	···	···	···	···	···	···	···	···	···
Te125	9.1106E-12	2.08E-01	···	7.92E-01	···	···	···	···	···	···	···
Te126	2.4186E-11	4.20E-01	···	5.80E-01	···	···	···	···	···	···	···
Te128	4.0438E-11	3.60E-02	···	9.64E-01	···	···	···	···	···	···	···
Te130	4.3133E-11	···	···	1.00	···	···	···	···	···	···	···
I127	2.9825E-11	5.50E-02	···	9.45E-01	···	···	···	···	···	···	···
Xe124	1.9108E-13	···	···	···	···	1.00	···	···	···	···	···
Xe126	1.6569E-13	···	···	···	···	1.00	···	···	···	···	···
Xe128	3.3162E-12	1.00	···	···	···	···	···	···	···	···	···
Xe129	4.0773E-11	3.20E-02	···	9.68E-01	···	···	···	···	···	···	···
Xe130	6.4998E-12	1.00	···	···	···	···	···	···	···	···	···
Xe131	3.2369E-11	7.40E-02	···	9.26E-01	···	···	···	···	···	···	···
Xe132	3.9129E-11	3.00E-01	···	7.00E-01	···	···	···	···	···	···	···
Xe134	1.4344E-11	4.00E-02	···	9.60E-01	···	···	···	···	···	···	···
Xe136	1.1681E-11	···	···	1.00	···	···	···	···	···	···	···

Table B.2 – Continued

Ion	Solar	Main s	Weak s	r-proc	νp-proc	γ-proc	SNIa	Massive	GCR	ν/Novae/GCR	BBN
Cs133	1.0102E-11	1.49E-01	···	8.51E-01	···	···	···	···	···	···	···
Ba130	1.2868E-13	···	···	···	···	1.00	···	···	···	···	···
Ba132	1.2309E-13	···	···	···	···	1.00	···	···	···	···	···
Ba134	2.9398E-12	1.00	···	···	···	···	···	···	···	···	···
Ba135	8.0178E-12	2.87E-01	···	7.13E-01	···	···	···	···	···	···	···
Ba136	9.5515E-12	1.00	···	···	···	···	···	···	···	···	···
Ba137	1.3661E-11	6.41E-01	···	3.59E-01	···	···	···	···	···	···	···
Ba138	8.7207E-11	8.95E-01	···	1.05E-01	···	···	···	···	···	···	···
La138	1.1371E-14	···	···	···	···	1.00	···	···	···	···	···
La139	1.2430E-11	6.96E-01	···	3.04E-01	···	···	···	···	···	···	···
Ce136	5.9690E-14	···	···	···	···	1.00	···	···	···	···	···
Ce138	8.0227E-14	···	···	···	···	1.00	···	···	···	···	···
Ce140	2.8385E-11	8.87E-01	···	1.13E-01	···	···	···	···	···	···	···
Ce142	3.5666E-12	1.92E-01	···	8.08E-01	···	···	···	···	···	···	···
Pr141	4.6912E-12	5.08E-01	···	4.92E-01	···	···	···	···	···	···	···
Nd142	6.2977E-12	1.00	···	···	···	···	···	···	···	···	···
Nd143	2.7997E-12	3.22E-01	···	6.78E-01	···	···	···	···	···	···	···
Nd144	5.5255E-12	5.13E-01	···	4.87E-01	···	···	···	···	···	···	···
Nd145	2.0265E-12	2.74E-01	···	7.26E-01	···	···	···	···	···	···	···
Nd146	3.9348E-12	6.47E-01	···	3.53E-01	···	···	···	···	···	···	···
Nd148	1.3132E-12	1.88E-01	···	8.12E-01	···	···	···	···	···	···	···
Nd150	1.3482E-12	···	···	1.00	···	···	···	···	···	···	···
Sm144	2.2234E-13	···	···	···	···	1.00	···	···	···	···	···
Sm147	1.1171E-12	2.57E-01	···	7.43E-01	···	···	···	···	···	···	···
Sm148	8.1212E-13	1.00	···	···	···	···	···	···	···	···	···

Table B.2 – Continued

Ion	Solar	Main s	Weak s	r-proc	νp-proc	γ-proc	SNIa	Massive	GCR	ν/Novae/GCR	BBN
Sm149	9.9837E-13	1.25E-01	···	8.75E-01	···	···	···	···	···	···	···
Sm150	5.3059E-13	1.00	···	···	···	···	···	···	···	···	···
Sm152	1.9303E-12	2.27E-01	···	7.73E-01	···	···	···	···	···	···	···
Sm154	1.6408E-12	2.70E-02	···	9.73E-01	···	···	···	···	···	···	···
Eu151	1.2804E-12	5.80E-02	···	9.42E-01	···	···	···	···	···	···	···
Eu153	1.3977E-12	5.70E-02	···	9.43E-01	···	···	···	···	···	···	···
Gd152	1.9865E-14	7.14E-01	···	···	···	2.86E-01	···	···	···	···	···
Gd154	2.1352E-13	1.00	···	···	···	···	···	···	···	···	···
Gd155	1.4490E-12	5.90E-02	···	9.41E-01	···	···	···	···	···	···	···
Gd156	2.0038E-12	1.75E-01	···	8.25E-01	···	···	···	···	···	···	···
Gd157	1.5324E-12	1.11E-01	···	8.89E-01	···	···	···	···	···	···	···
Gd158	2.4315E-12	2.82E-01	···	7.18E-01	···	···	···	···	···	···	···
Gd160	2.1406E-12	6.00E-03	···	9.94E-01	···	···	···	···	···	···	···
Tb159	1.7255E-12	8.50E-02	···	9.15E-01	···	···	···	···	···	···	···
Dy156	6.1493E-15	···	···	···	···	1.00	···	···	···	···	···
Dy158	1.0432E-14	···	···	···	···	1.00	···	···	···	···	···
Dy160	2.5575E-13	1.00	···	···	···	···	···	···	···	···	···
Dy161	2.0742E-12	5.10E-02	···	9.49E-01	···	···	···	···	···	···	···
Dy162	2.7974E-12	1.56E-01	···	8.44E-01	···	···	···	···	···	···	···
Dy163	2.7338E-12	4.20E-02	···	9.58E-01	···	···	···	···	···	···	···
Dy164	3.1032E-12	2.26E-01	···	7.74E-01	···	···	···	···	···	···	···
Ho165	2.4767E-12	8.00E-02	···	9.20E-01	···	···	···	···	···	···	···
Er162	9.8904E-15	···	···	···	···	1.00	···	···	···	···	···
Er164	1.1392E-13	7.40E-01	···	···	···	2.60E-01	···	···	···	···	···
Er166	2.3839E-12	1.59E-01	···	8.41E-01	···	···	···	···	···	···	···

Table B.2 – Continued

Ion	Solar	Main s	Weak s	r-proc	νp-proc	γ-proc	SNIa	Massive	GCR	ν/Novae/GCR	BBN
Er167	1.6272E-12	9.10E-02	···	9.09E-01	···	···	···	···	···	···	···
Er168	1.9196E-12	2.89E-01	···	7.11E-01	···	···	···	···	···	···	···
Er170	1.0609E-12	1.23E-01	···	8.77E-01	···	···	···	···	···	···	···
Tm169	1.1033E-12	1.25E-01	···	8.75E-01	···	···	···	···	···	···	···
Yb168	8.5919E-15	···	···	···	···	1.00	···	···	···	···	···
Yb170	2.0796E-13	1.00	···	···	···	···	···	···	···	···	···
Yb171	9.8235E-13	2.03E-01	···	7.97E-01	···	···	···	···	···	···	···
Yb172	1.5124E-12	4.29E-01	···	5.71E-01	···	···	···	···	···	···	···
Yb173	1.1230E-12	2.65E-01	···	7.35E-01	···	···	···	···	···	···	···
Yb174	2.2334E-12	6.02E-01	···	3.98E-01	···	···	···	···	···	···	···
Yb176	9.0626E-13	8.30E-02	···	9.17E-01	···	···	···	···	···	···	···
Lu175	1.0058E-12	1.77E-01	···	8.23E-01	···	···	···	···	···	···	···
Lu176	2.9191E-14	1.00	···	···	···	···	···	···	···	···	···
Hf174	6.8707E-15	···	···	···	···	1.00	···	···	···	···	···
Hf176	2.2066E-13	1.00	···	···	···	···	···	···	···	···	···
Hf177	7.8866E-13	1.66E-01	···	8.34E-01	···	···	···	···	···	···	···
Hf178	1.1570E-12	5.66E-01	···	4.34E-01	···	···	···	···	···	···	···
Hf179	5.7769E-13	3.96E-01	···	6.04E-01	···	···	···	···	···	···	···
Hf180	1.4878E-12	8.57E-01	···	1.43E-01	···	···	···	···	···	···	···
Ta180	7.0387E-17	···	···	···	···	1.00	···	···	···	···	···
Ta181	5.7218E-13	4.51E-01	···	5.49E-01	···	···	···	···	···	···	···
W180	4.4674E-15	···	···	···	···	1.00	···	···	···	···	···
W182	9.8815E-13	6.01E-01	···	3.99E-01	···	···	···	···	···	···	···
W183	5.3377E-13	5.70E-01	···	4.30E-01	···	···	···	···	···	···	···
W184	1.1427E-12	7.64E-01	···	2.36E-01	···	···	···	···	···	···	···

Table B.2 – Continued

Ion	Solar	Main s	Weak s	r-proc	νp-proc	γ-proc	SNIa	Massive	GCR	ν/Novae/GCR	BBN
W186	1.0600E-12	5.74E-01	···	4.26E-01	···	···	···	···	···	···	···
Re185	5.6366E-13	2.81E-01	···	7.19E-01	···	···	···	···	···	···	···
Re187	1.0169E-12	1.02E-01	···	8.98E-01	···	···	···	···	···	···	···
Os184	3.6631E-15	···	···	···	···	1.00	···	···	···	···	···
Os186	2.9457E-13	1.00	···	···	···	···	···	···	···	···	···
Os187	2.3429E-13	4.06E-01	···	···	···	5.94E-01	···	···	···	···	···
Os188	2.4584E-12	2.85E-01	···	7.15E-01	···	···	···	···	···	···	···
Os189	2.9974E-12	4.30E-02	···	9.57E-01	···	···	···	···	···	···	···
Os190	4.8745E-12	1.40E-01	···	8.60E-01	···	···	···	···	···	···	···
Os192	7.5705E-12	3.40E-02	···	9.66E-01	···	···	···	···	···	···	···
Ir191	6.8116E-12	1.90E-02	···	9.81E-01	···	···	···	···	···	···	···
Ir193	1.1464E-11	1.30E-02	···	9.87E-01	···	···	···	···	···	···	···
Pt190	4.7599E-15	···	···	···	···	1.00	···	···	···	···	···
Pt192	2.7132E-13	7.92E-01	···	···	···	2.08E-01	···	···	···	···	···
Pt194	1.1429E-11	6.00E-02	···	9.40E-01	···	···	···	···	···	···	···
Pt195	1.1728E-11	2.30E-02	···	9.77E-01	···	···	···	···	···	···	···
Pt196	8.7505E-12	1.21E-01	···	8.79E-01	···	···	···	···	···	···	···
Pt198	2.4834E-12	···	···	1.00	···	···	···	···	···	···	···
Au197	5.2934E-12	5.90E-02	···	9.41E-01	···	···	···	···	···	···	···
Hg196	1.9119E-14	···	···	···	···	1.00	···	···	···	···	···
Hg198	1.2420E-12	1.00	···	···	···	···	···	···	···	···	···
Hg199	2.1024E-12	2.78E-01	···	7.22E-01	···	···	···	···	···	···	···
Hg200	2.8778E-12	6.75E-01	···	3.25E-01	···	···	···	···	···	···	···
Hg201	1.6423E-12	5.07E-01	···	4.93E-01	···	···	···	···	···	···	···
Hg202	3.7209E-12	8.41E-01	···	1.59E-01	···	···	···	···	···	···	···

Table B.2 – Continued

Ion	Solar	Main s	Weak s	r-proc	νp-proc	γ-proc	SNIa	Massive	GCR	ν/Novae/GCR	BBN
Hg204	8.5538E-13	1.02E-01	···	8.98E-01	···	···	···	···	···	···	···
Tl203	1.4648E-12	7.90E-01	···	2.10E-01	···	···	···	···	···	···	···
Tl205	3.4967E-12	5.96E-01	···	4.04E-01	···	···	···	···	···	···	···
Pb204	1.7961E-12	1.00	···	···	···	···	···	···	···	···	···
Pb206	1.6714E-11	6.59E-01	···	3.41E-01	···	···	···	···	···	···	···
Pb207	1.8496E-11	5.83E-01	···	4.17E-01	···	···	···	···	···	···	···
Pb208	5.2941E-11	4.23E-01	···	5.77E-01	···	···	···	···	···	···	···
Bi209	3.7589E-12	5.80E-02	···	9.42E-01	···	···	···	···	···	···	···
Th232	1.1959E-12	···	···	1.00	···	···	···	···	···	···	···
U234	1.3317E-17	···	···	1.00	···	···	···	···	···	···	···
U235	1.5716E-13	···	···	1.00	···	···	···	···	···	···	···
U238	4.8994E-13	···	···	1.00	···	···	···	···	···	···	···

Table B.3: Abundance Ratios (Scaling Model/Linear Interpolations) at different [Z]

Isotope	[Z]=-1	[Z]=-3	Isotope	[Z]=-1	[Z]=-3	Isotope	[Z]=-1	[Z]=-3
H1	0.9995	1.0000	Mg24	1.0980	1.3675	Ca42	0.6347	0.3899
H2	0.9942	0.9998	Mg25	0.4635	0.1006	Ca43	0.3651	0.0503
He3	1.0088	1.0003	Mg26	0.4644	0.1009	Ca44	0.4238	0.0855
He4	1.0015	1.0001	Al27	0.5634	0.2077	Ca46	0.0097	0.0001
Li6	0.9003	1.0831	Si28	0.7892	0.8704	Ca48	0.0038	0.0000
Li7	0.9530	0.9999	Si29	0.3133	0.0559	Sc45	0.5466	0.1743
Be9	0.9425	1.1584	Si30	0.3129	0.0908	Ti46	0.3777	0.1252
B10	0.9425	1.1584	P31	0.6071	0.3252	Ti47	0.3253	0.0380
B11	0.9425	1.1584	S32	0.9211	1.2657	Ti48	0.5270	0.2676
C12	1.4204	2.9308	S33	0.7507	0.7052	Ti49	0.4319	0.1889
C13	1.5575	3.7785	S34	0.4206	0.1976	Ti50	0.0075	0.0000
N14	0.7076	0.3543	S36	0.0920	0.0026	V50	0.2747	0.0302
N15	0.4852	0.1142	Cl35	0.7423	0.4839	V51	0.4066	0.1976
O16	1.5271	3.6295	Cl37	0.5896	0.2614	Cr50	0.1986	0.1301
O17	0.5994	0.2154	Ar36	0.8476	0.9812	Cr52	0.4000	0.3266
O18	0.0598	0.0002	Ar38	0.4697	0.1978	Cr53	0.2532	0.2076
F19	0.7012	0.3448	Ar40	0.0504	0.0003	Cr54	0.0145	0.0045
Ne20	1.3117	2.2605	K39	0.7738	0.5137	Mn55	0.1331	0.1181
Ne21	0.8830	0.6934	K40	0.8825	0.6874	Fe54	0.0512	0.0759
Ne22	0.2099	0.0232	K41	0.7554	0.4877	Fe56	0.3112	0.3051
Na23	0.7288	0.3911	Ca40	0.6662	0.5927	Fe57	0.7367	0.3999
Fe58	0.0508	0.0037	As75	0.8701	0.8665	Y89	0.5928	0.2084
Co59	0.6743	0.3067	Se74	0.8711	0.8694	Zr90	0.7162	0.5002
Ni58	0.3176	0.0320	Se76	0.5894	0.2048	Zr91	0.6126	0.2552
Ni60	0.8105	0.5328	Se77	0.8948	0.9248	Zr92	0.6423	0.3254
Ni61	0.7482	0.4210	Se78	0.6964	0.4568	Zr94	0.5929	0.2084
Ni62	0.7784	0.4777	Se80	1.0984	1.4044	Zr96	0.8939	0.9206
Ni64	0.1666	0.0574	Se82	1.1529	1.5333	Nb93	0.6392	0.3180

Table B.3 – Continued

Isotope	[Z]=-1	[Z]=-3	Isotope	[Z]=-1	[Z]=-3	Isotope	[Z]=-1	[Z]=-3
Cu63	0.7444	0.4228	Br79	1.0115	1.1997	Mo92	1.1535	1.5346
Cu65	0.5393	0.1679	Br81	0.8762	0.8808	Mo94	1.1490	1.5240
Zn64	0.7622	0.4474	Kr78	0.8711	0.8694	Mo95	0.7809	0.6532
Zn66	0.4529	0.1032	Kr80	0.6739	0.4042	Mo96	0.5929	0.2084
Zn67	0.3895	0.0946	Kr82	0.6070	0.2453	Mo97	0.8078	0.7169
Zn68	0.3867	0.1117	Kr83	0.9487	1.0517	Mo98	0.7035	0.4702
Zn70	1.1529	1.5333	Kr84	0.9793	1.1234	Mo100	1.1294	1.4776
Ga69	0.7171	0.5062	Kr86	1.0475	1.2840	Ru96	1.1535	1.5346
Ga71	0.5891	0.2044	Rb85	0.8771	0.8825	Ru98	1.1535	1.5346
Ge70	0.5891	0.2044	Rb87	0.9965	1.1633	Ru99	0.9810	1.1266
Ge72	0.7302	0.5370	Sr84	0.8711	0.8694	Ru100	0.5929	0.2084
Ge73	0.7275	0.5305	Sr86	0.5911	0.2066	Ru101	1.0608	1.3154
Ge74	0.7280	0.5315	Sr87	0.5911	0.2065	Ru102	0.8973	0.9286
Ge76	1.1529	1.5333	Sr88	0.5929	0.2084	Ru104	1.1411	1.5054
Rh103	1.0655	1.3264	Sn115	0.5976	0.2134	Xe128	0.5929	0.2084
Pd102	0.7367	0.5438	Sn116	0.5929	0.2084	Xe129	1.1355	1.4922
Pd104	0.5929	0.2084	Sn117	0.8653	0.8530	Xe130	0.5929	0.2084
Pd105	1.0716	1.3410	Sn118	0.7459	0.5705	Xe131	1.1120	1.4365
Pd106	0.8480	0.8119	Sn119	0.8239	0.7548	Xe132	0.9853	1.1368
Pd108	0.7639	0.6129	Sn120	0.7263	0.5241	Xe134	1.1310	1.4816
Pd110	1.1378	1.4975	Sn122	0.9180	0.9776	Xe136	1.1535	1.5346
Ag107	1.0643	1.3238	Sn124	1.1535	1.5346	Cs133	1.0699	1.3370
Ag109	1.0016	1.1752	Sb121	0.9298	1.0055	Ba130	0.5977	0.2136
Cd106	0.5977	0.2136	Sb123	1.1181	1.4511	Ba132	0.5977	0.2136
Cd108	0.5977	0.2135	Te120	0.5977	0.2136	Ba134	0.3097	0.0297
Cd110	0.5929	0.2084	Te122	0.5929	0.2084	Ba135	0.9113	1.1027
Cd111	0.9550	1.0652	Te123	0.5929	0.2084	Ba136	0.3097	0.0297
Cd112	0.7611	0.6063	Te124	0.5929	0.2084	Ba137	0.6126	0.5700

Table B.3 – Continued

Isotope	[Z]=-1	[Z]=-3	Isotope	[Z]=-1	[Z]=-3	Isotope	[Z]=-1	[Z]=-3
Cd113	0.9281	1.0015	Te125	1.0369	1.2588	Ba138	0.3983	0.1877
Cd114	0.6843	0.4246	Te126	0.9180	0.9776	La138	0.5977	0.2136
Cd116	1.0649	1.3251	Te128	1.1333	1.4869	La139	0.5662	0.4872
In113	0.5977	0.2136	Te130	1.1535	1.5346	Ce136	0.5977	0.2136
In115	0.9242	0.9922	I127	1.1226	1.4617	Ce138	0.5977	0.2136
Sn112	0.5977	0.2136	Xe124	0.5977	0.2136	Ce140	0.4051	0.1998
Sn114	0.5977	0.2136	Xe126	0.5977	0.2136	Ce142	0.9915	1.2457
Pr141	0.7248	0.7701	Gd157	1.0598	1.3676	Yb171	0.9822	1.2291
Nd142	0.3097	0.0297	Gd158	0.9155	1.1102	Yb172	0.7915	0.8890
Nd143	0.8818	1.0500	Gd160	1.1484	1.5256	Yb173	0.9299	1.1358
Nd144	0.7206	0.7626	Tb159	1.0817	1.4067	Yb174	0.6455	0.6287
Nd145	0.9223	1.1223	Dy156	0.5977	0.2136	Yb176	1.0834	1.4097
Nd146	0.6076	0.5609	Dy158	0.5977	0.2136	Lu175	1.0041	1.2682
Nd148	0.9948	1.2517	Dy160	0.3097	0.0297	Lu176	0.3097	0.0297
Nd150	1.1535	1.5346	Dy161	1.1104	1.4579	Hf174	0.5977	0.2136
Sm144	0.5977	0.2136	Dy162	1.0218	1.2999	Hf176	0.3097	0.0297
Sm147	0.9366	1.1479	Dy163	1.1180	1.4714	Hf177	1.0134	1.2848
Sm148	0.3097	0.0297	Dy164	0.9628	1.1945	Hf178	0.6759	0.6828
Sm149	1.0480	1.3465	Ho165	1.0860	1.4142	Hf179	0.8193	0.9387
Sm150	0.3097	0.0297	Er162	0.5977	0.2136	Hf180	0.4304	0.2449
Sm152	0.9619	1.1930	Er164	0.3846	0.0775	Ta180	0.5977	0.2136
Sm154	1.1307	1.4940	Er166	1.0193	1.2953	Ta181	0.7729	0.8559
Eu151	1.1045	1.4473	Er167	1.0767	1.3977	W180	0.5977	0.2136
Eu153	1.1054	1.4488	Er168	0.9096	1.0997	W182	0.6464	0.6302
Gd152	0.3921	0.0823	Er170	1.0497	1.3495	W183	0.6725	0.6768
Gd154	0.3097	0.0297	Tm169	1.0480	1.3465	W184	0.5089	0.3849
Gd155	1.1037	1.4458	Yb168	0.5977	0.2136	W186	0.6692	0.6708
Gd156	1.0058	1.2713	Yb170	0.3097	0.0297	Re185	0.9164	1.1117

Table B.3 – Continued

Isotope	[Z]=-1	[Z]=-3	Isotope	[Z]=-1	[Z]=-3	Isotope	[Z]=-1	[Z]=-3
Re187	1.0674	1.3811	Pt194	1.1028	1.4443	Tl203	0.4869	0.3457
Os184	0.5977	0.2136	Pt195	1.1340	1.5000	Tl205	0.6506	0.6377
Os186	0.3097	0.0297	Pt196	1.0514	1.3525	Pb204	10	1000
Os187	0.4808	0.1389	Pt198	1.1535	1.5346	Pb206	6.9833	659.52
Os188	0.9130	1.1057	Au197	1.1037	1.4458	Pb207	6.3110	583.64
Os189	1.1172	1.4699	Hg196	0.5977	0.2136	Pb208	4.8955	423.89
Os190	1.0353	1.3239	Hg198	0.3097	0.0297	Bi209	1.6666	59.446
Os192	1.1248	1.4835	Hg199	0.9189	1.1163	Th232	1.1535	1.5346
Ir191	1.1374	1.5060	Hg200	0.5839	0.5188	U234	1.1535	1.5346
Ir193	1.1425	1.5151	Hg201	0.7257	0.7716	U235	1.1535	1.5346
Pt190	0.5977	0.2136	Hg202	0.4439	0.2690	U238	1.1535	1.5346
Pt192	0.3696	0.0680	Hg204	1.0674	1.3811			

Appendix C

Solar Abundance Decomposition

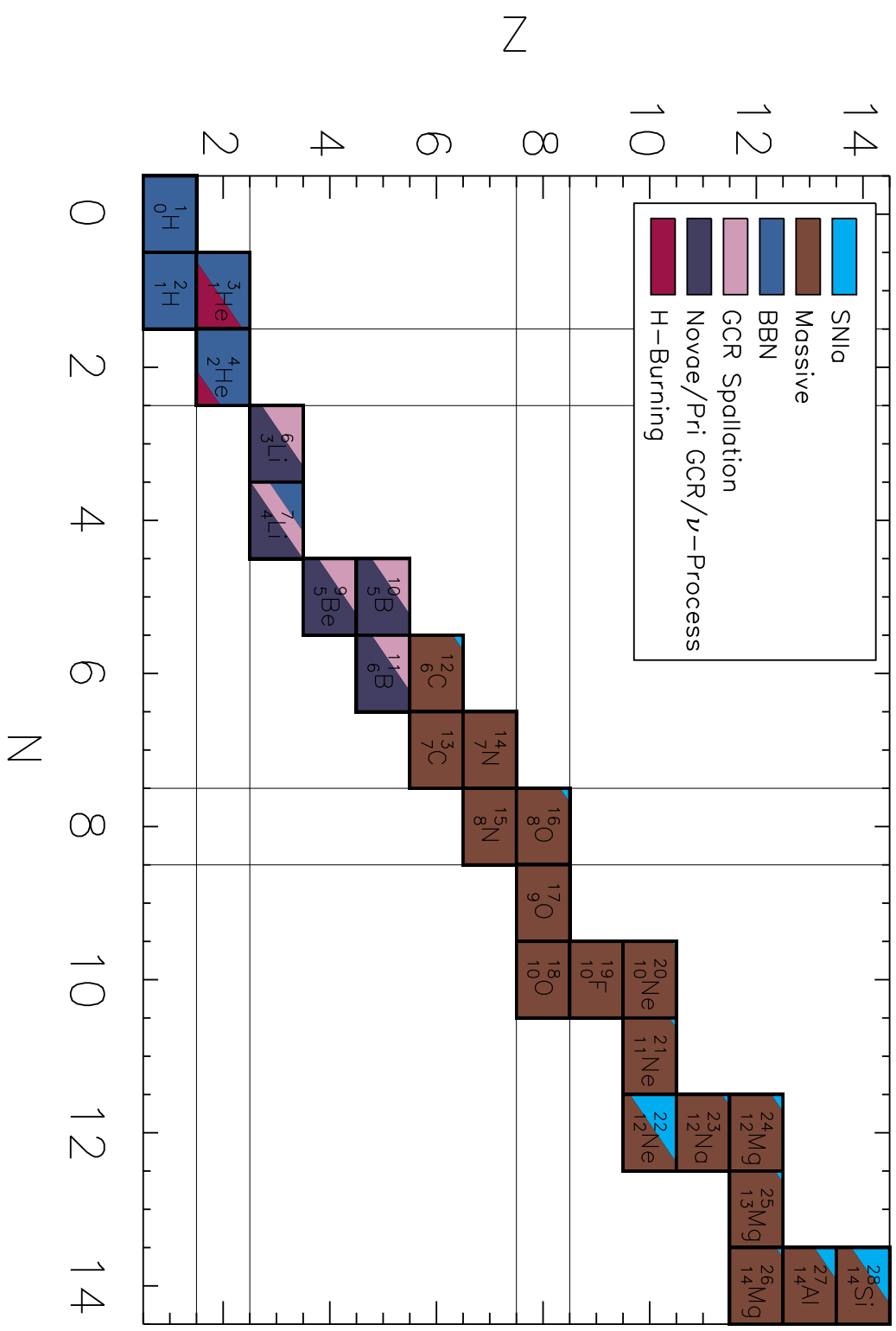

Figure C.1: Solar Abundance Decomposition for $1 \leq A \leq 28$. Contributions above about 1% can be identified.

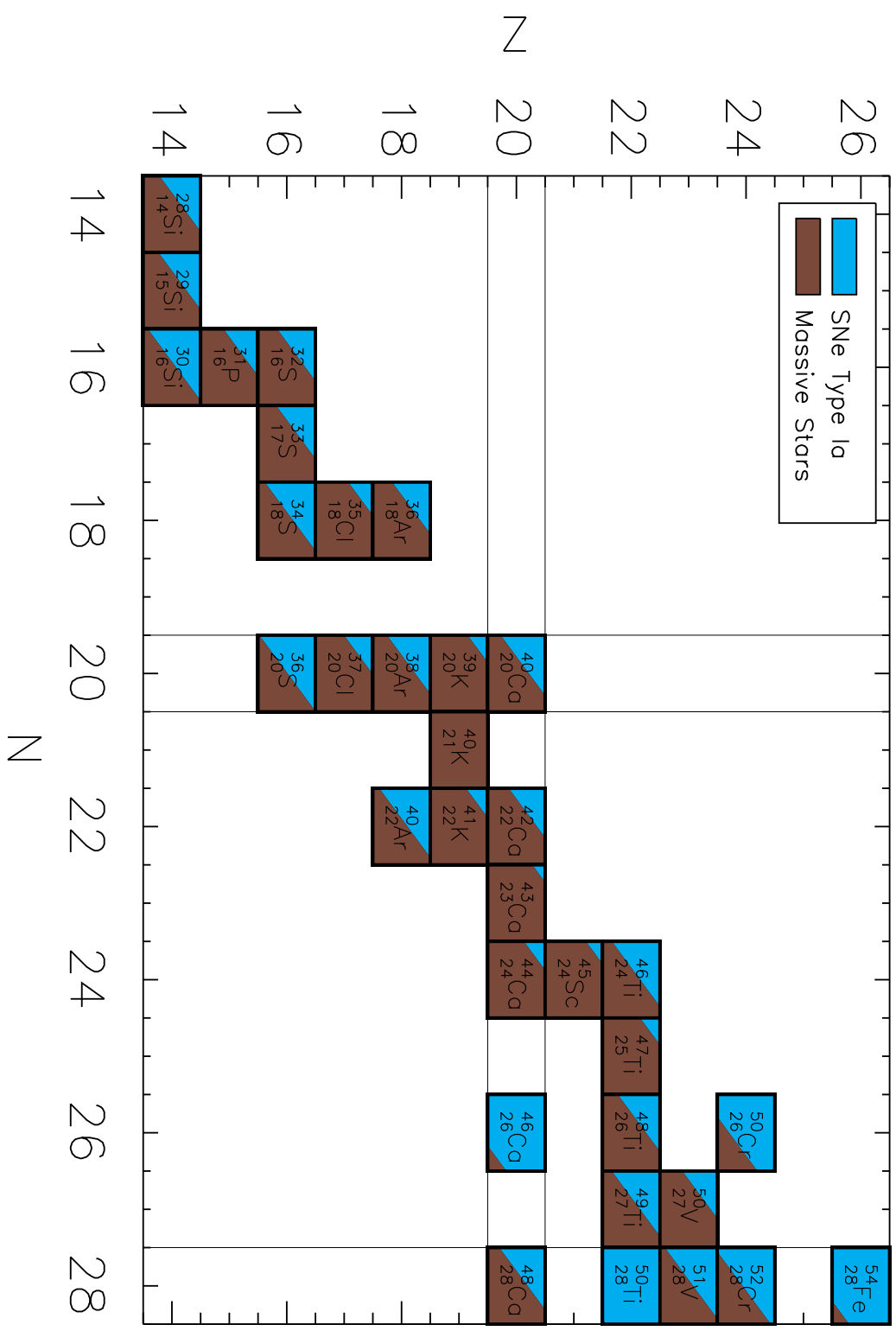

Figure C.2: Solar Abundance Decomposition for $28 \leq A \leq 54$. Contributions above about 1% can be identified.

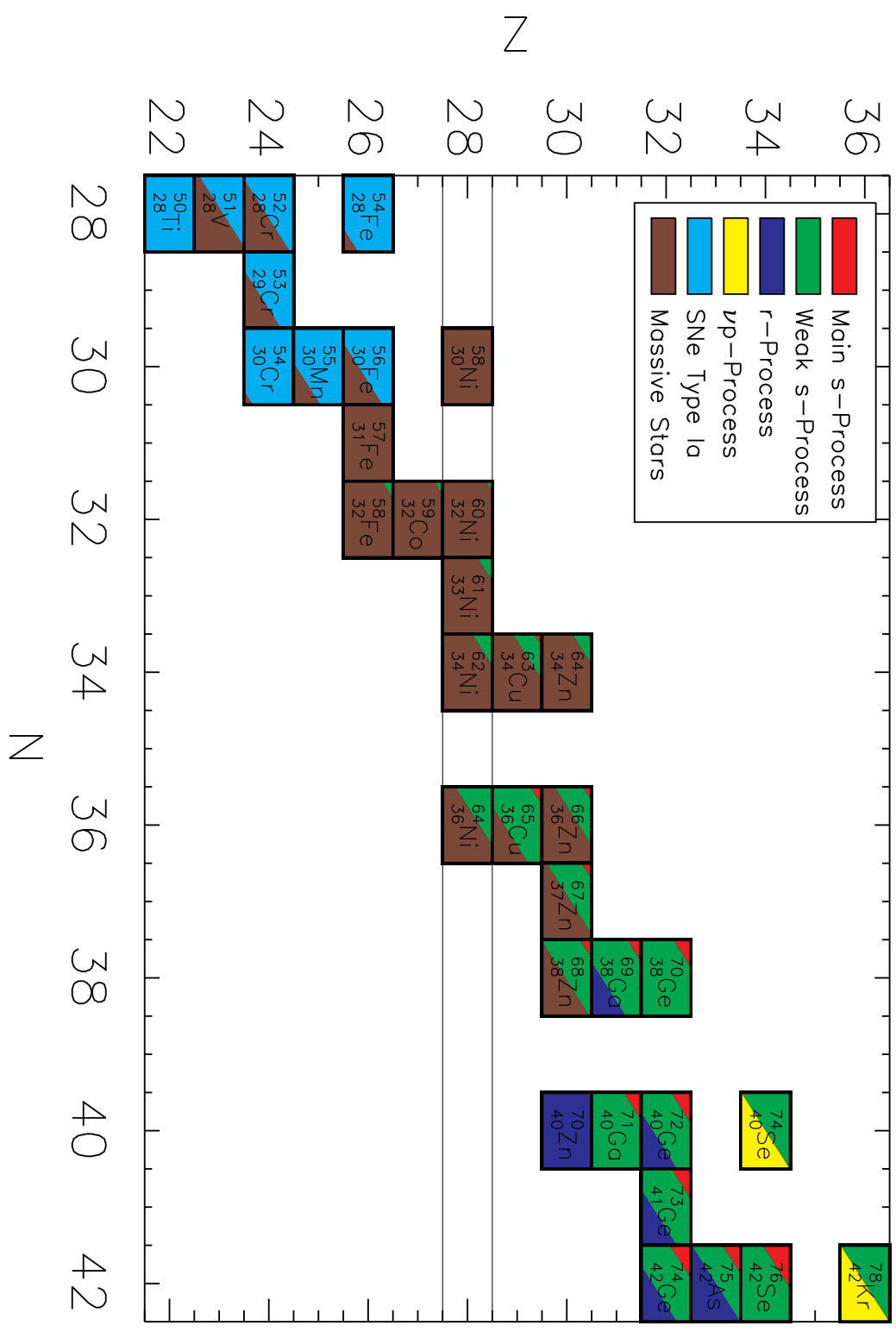

Figure C.3: Solar Abundance Decomposition for $50 \leq A \leq 78$. Contributions above about 1% can be identified.

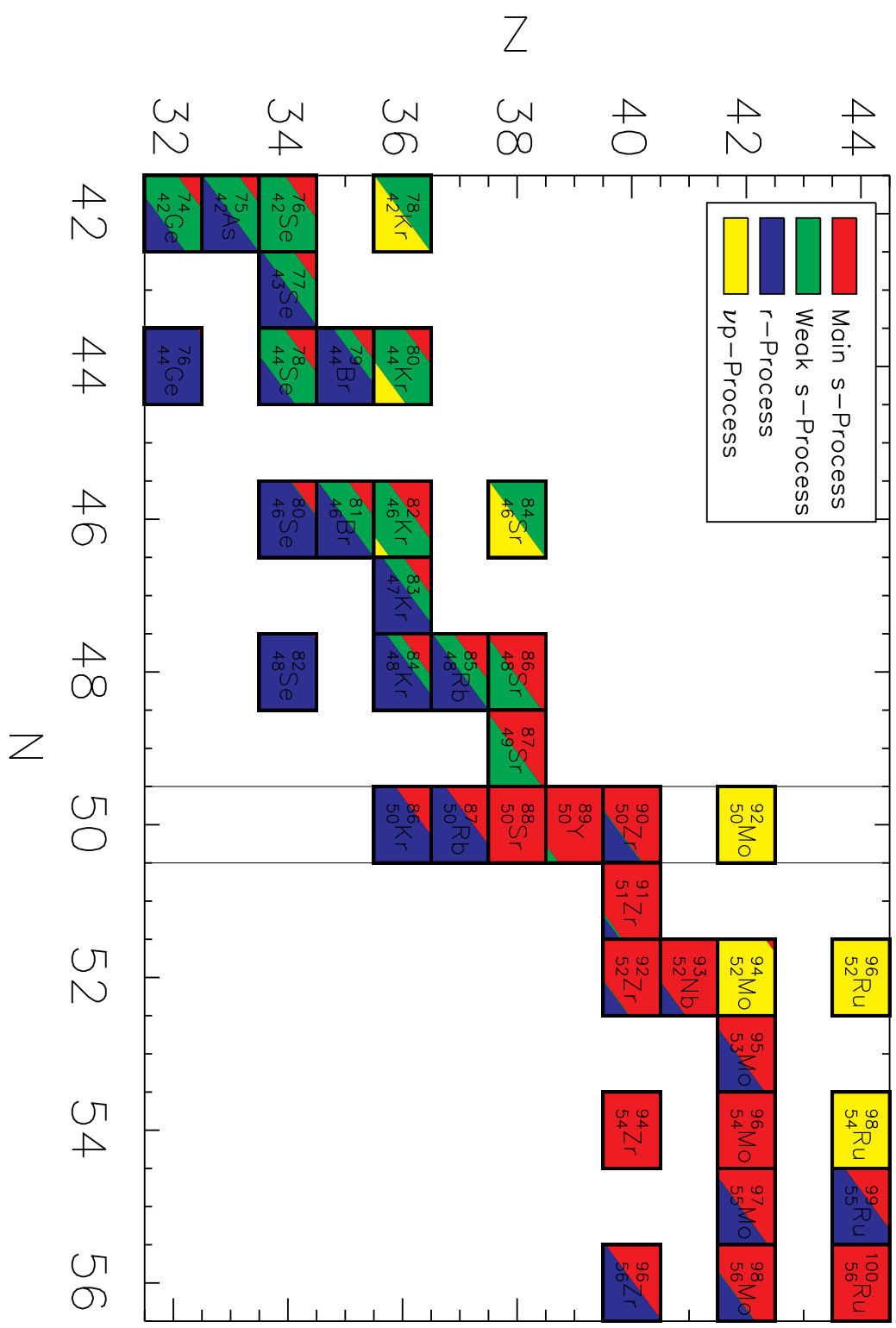

Figure C.4: Solar Abundance Decomposition for $74 \leq A \leq 100$. Contributions above about 1% can be identified.

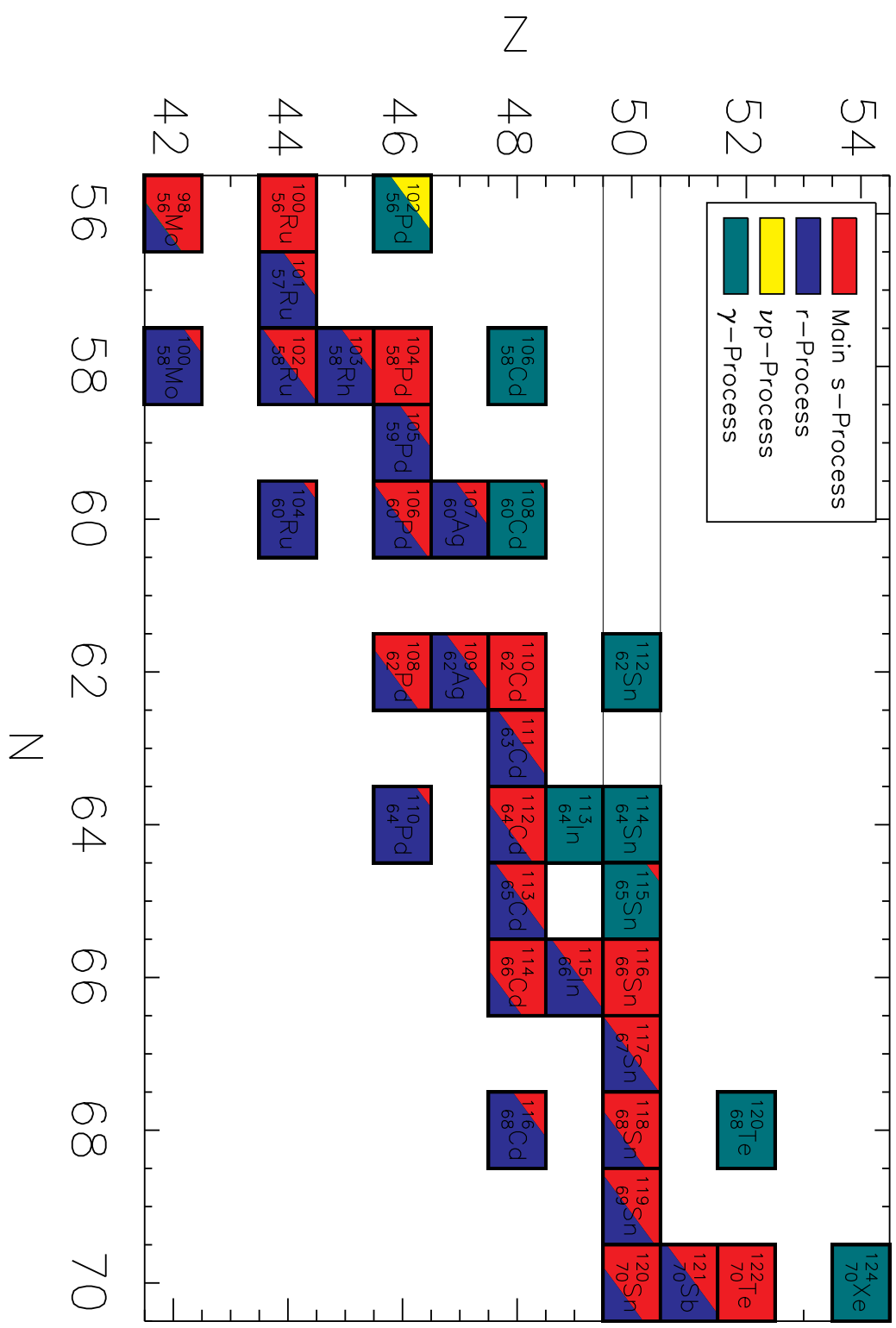

Figure C.5: Solar Abundance Decomposition for $98 \leq A \leq 124$. Contributions above about 1% can be identified.

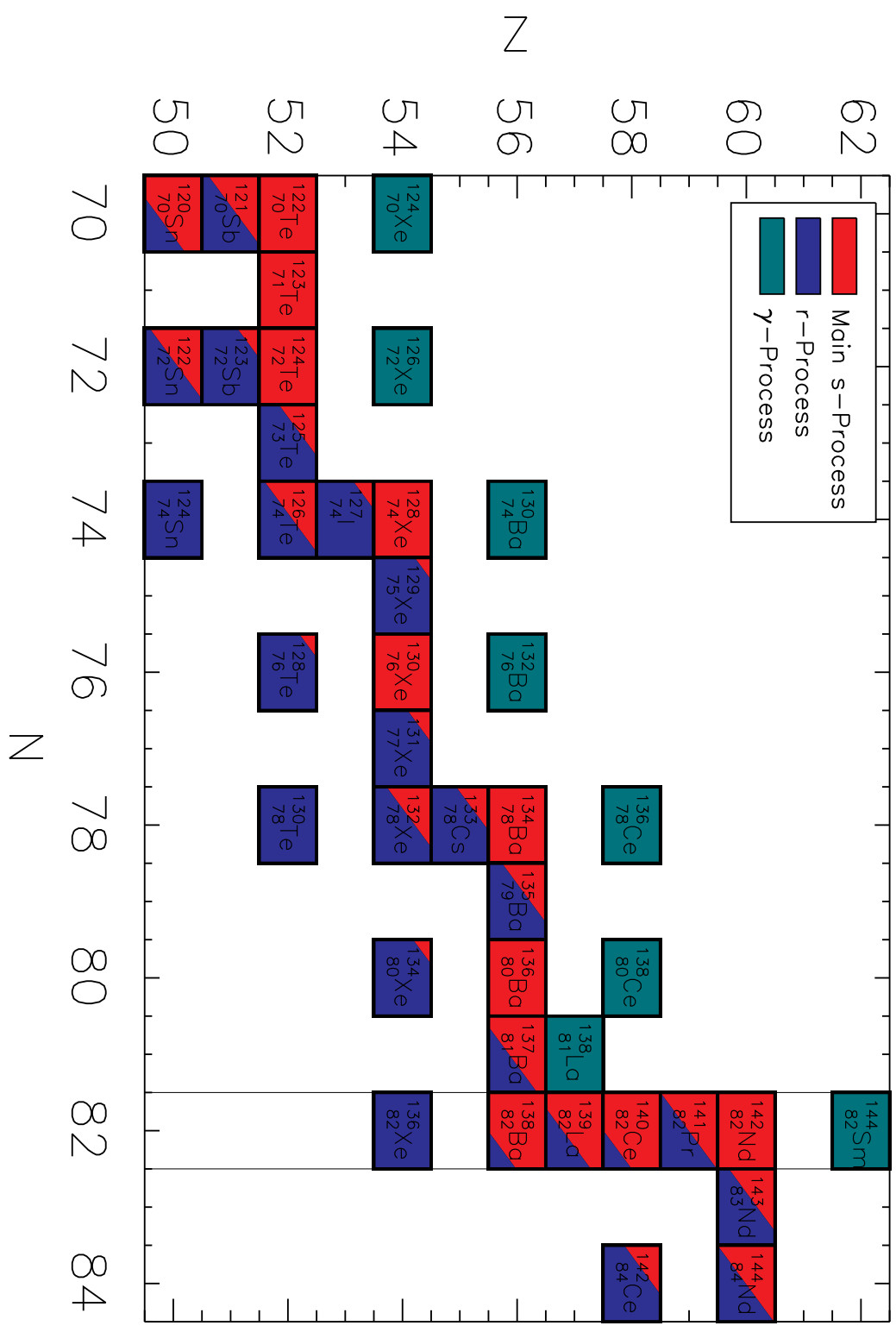

Figure C.6: Solar Abundance Decomposition for $120 \leq A \leq 144$. Contributions above about 1% can be identified.

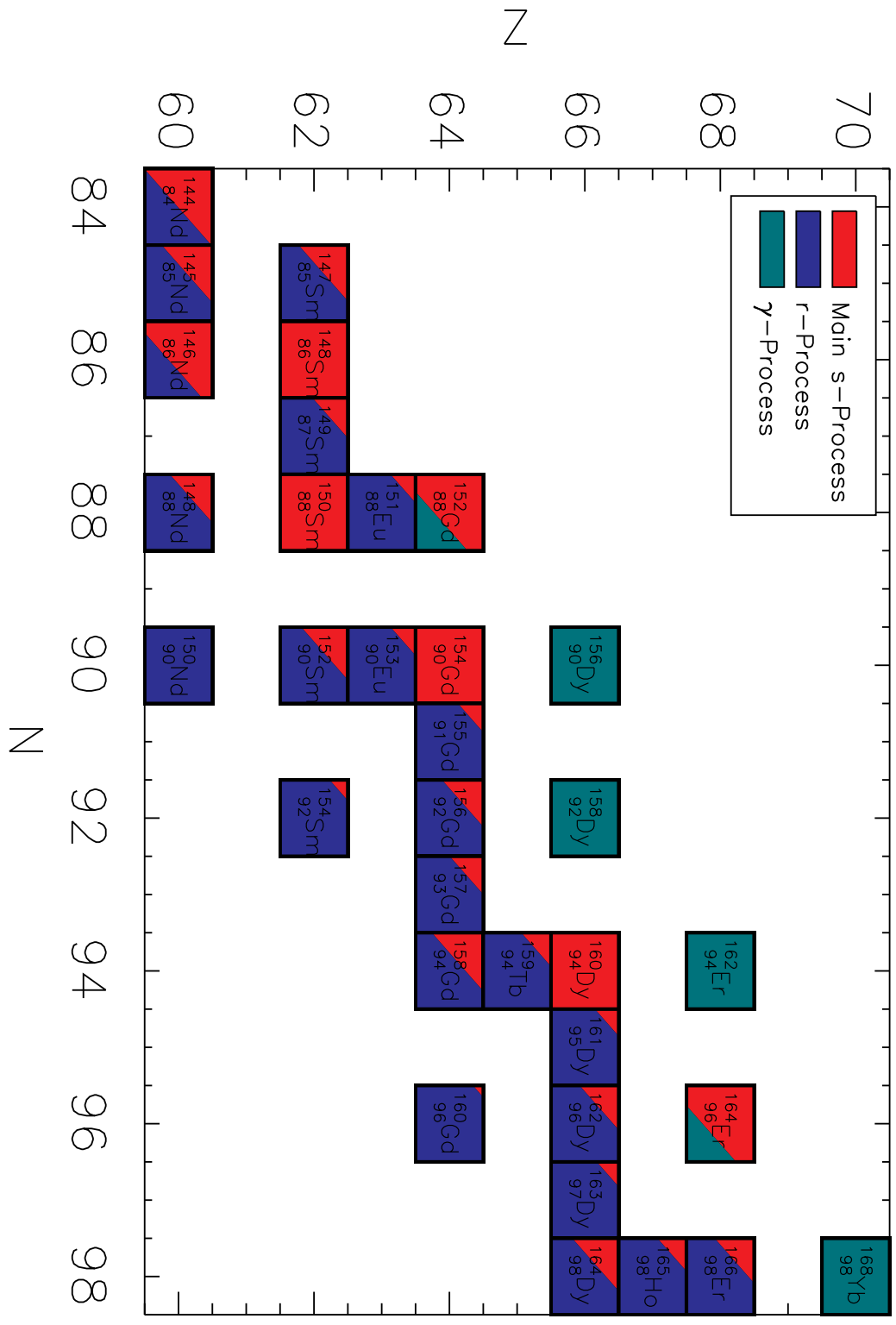

Figure C.7: Solar Abundance Decomposition for $144 \leq A \leq 168$. Contributions above about 1% can be identified.

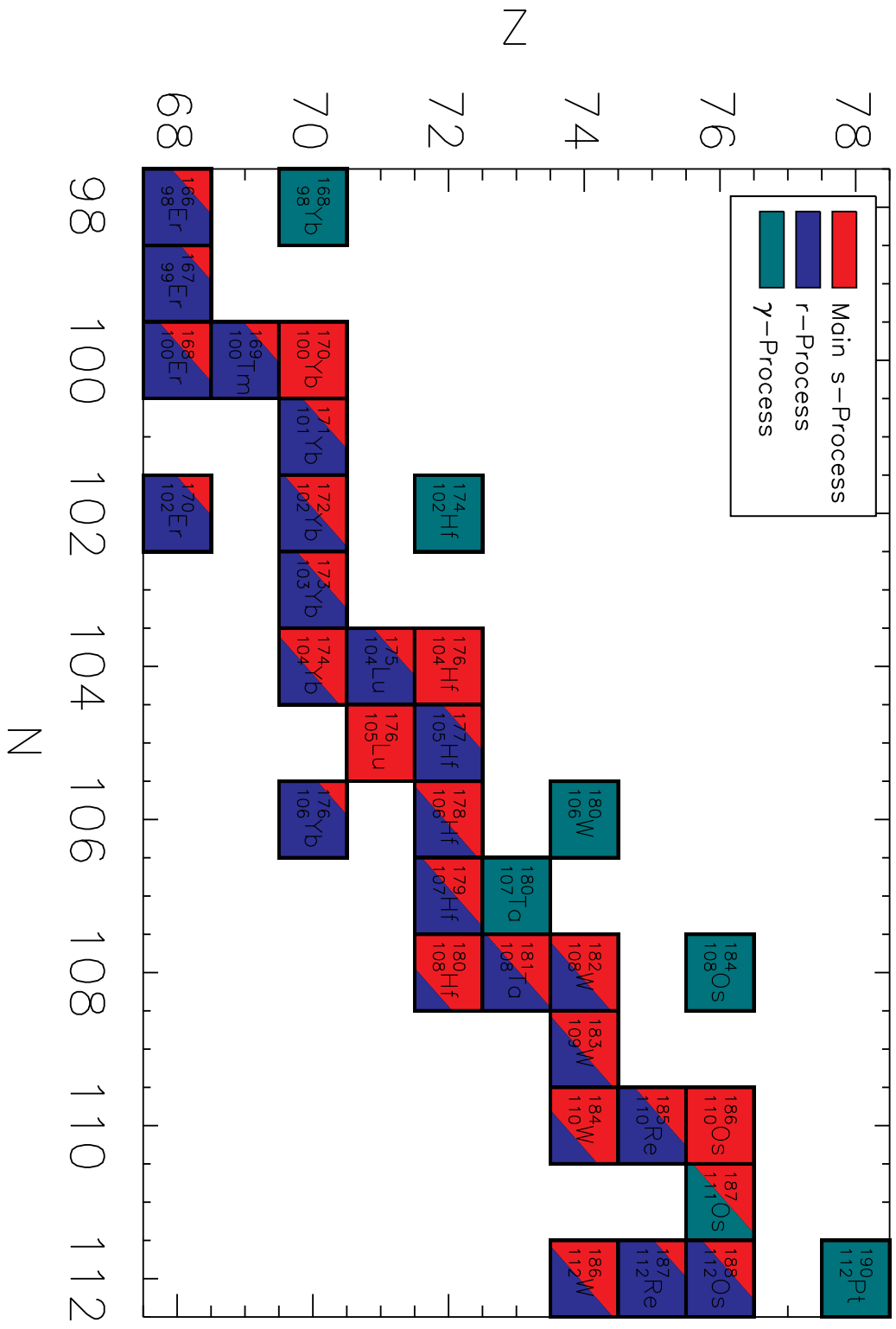

Figure C.8: Solar Abundance Decomposition for $166 \leq A \leq 190$. Contributions above about 1% can be identified.

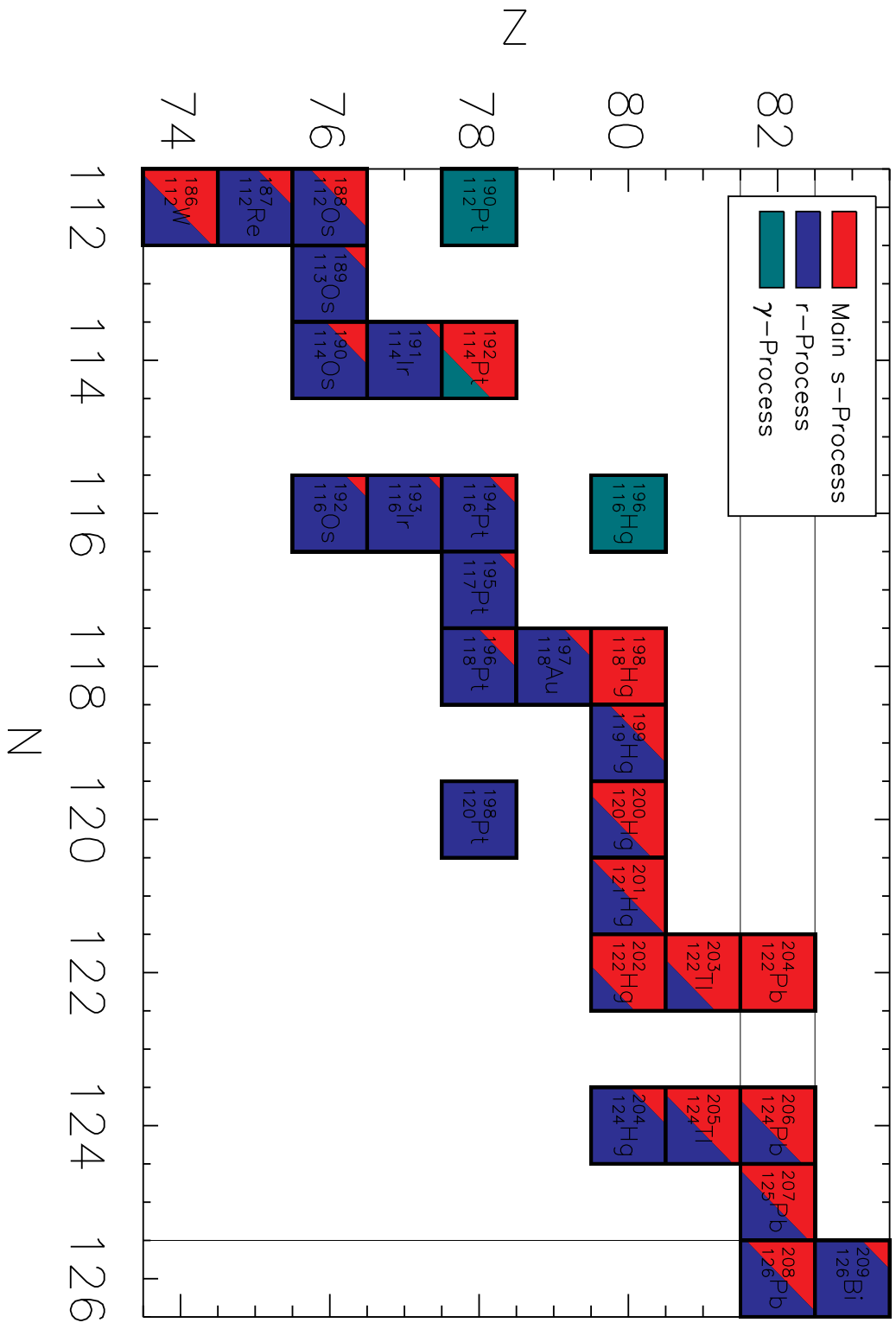

Figure C.9: Solar Abundance Decomposition for $186 \leq A \leq 209$. Contributions above about 1% can be identified.

Appendix D

Initial Composition Plots

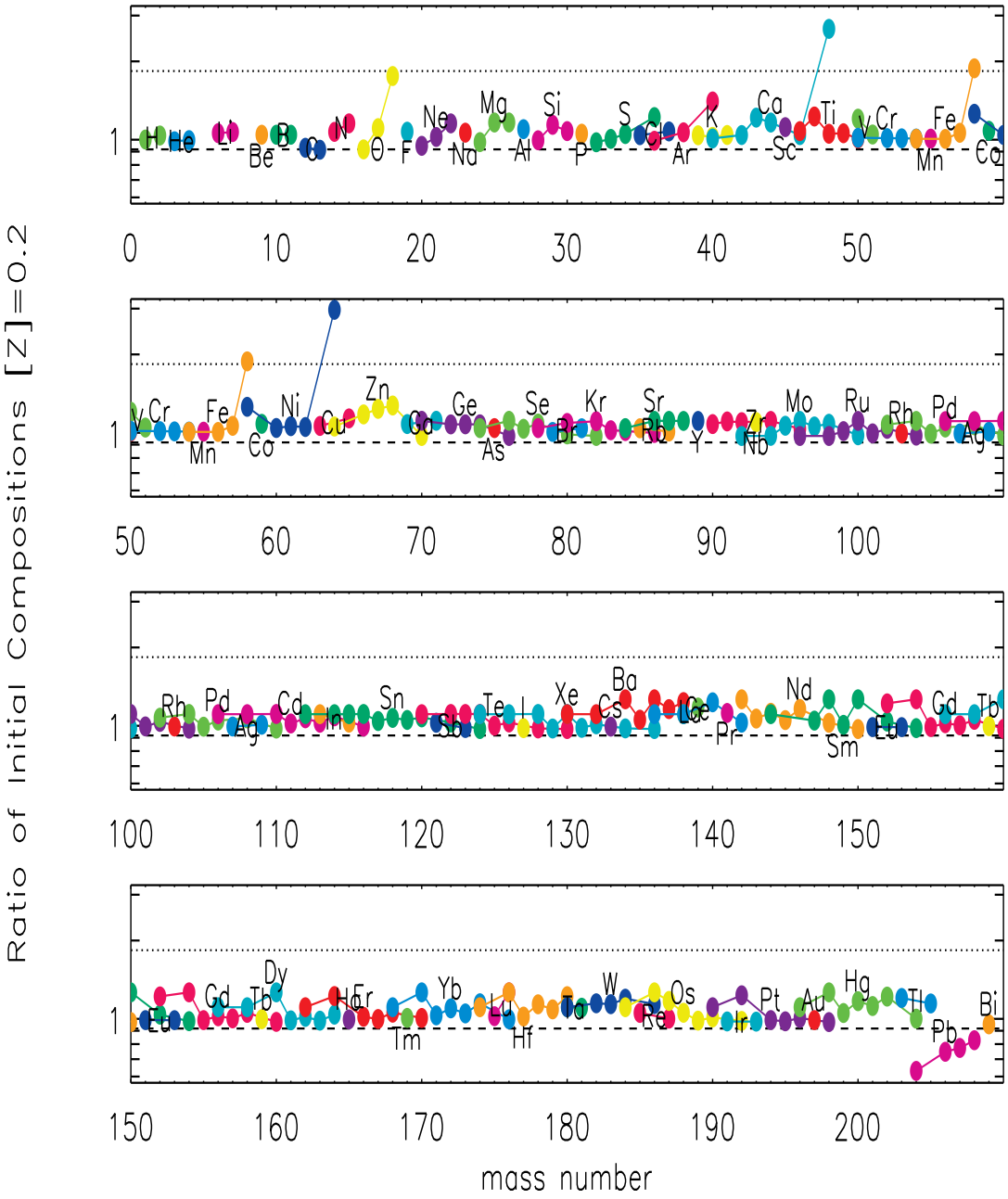

Figure D.1: The ratio of initial compositions (GG/SS) at a initial metallicity of [Z]=+0.2 for all isotopes.

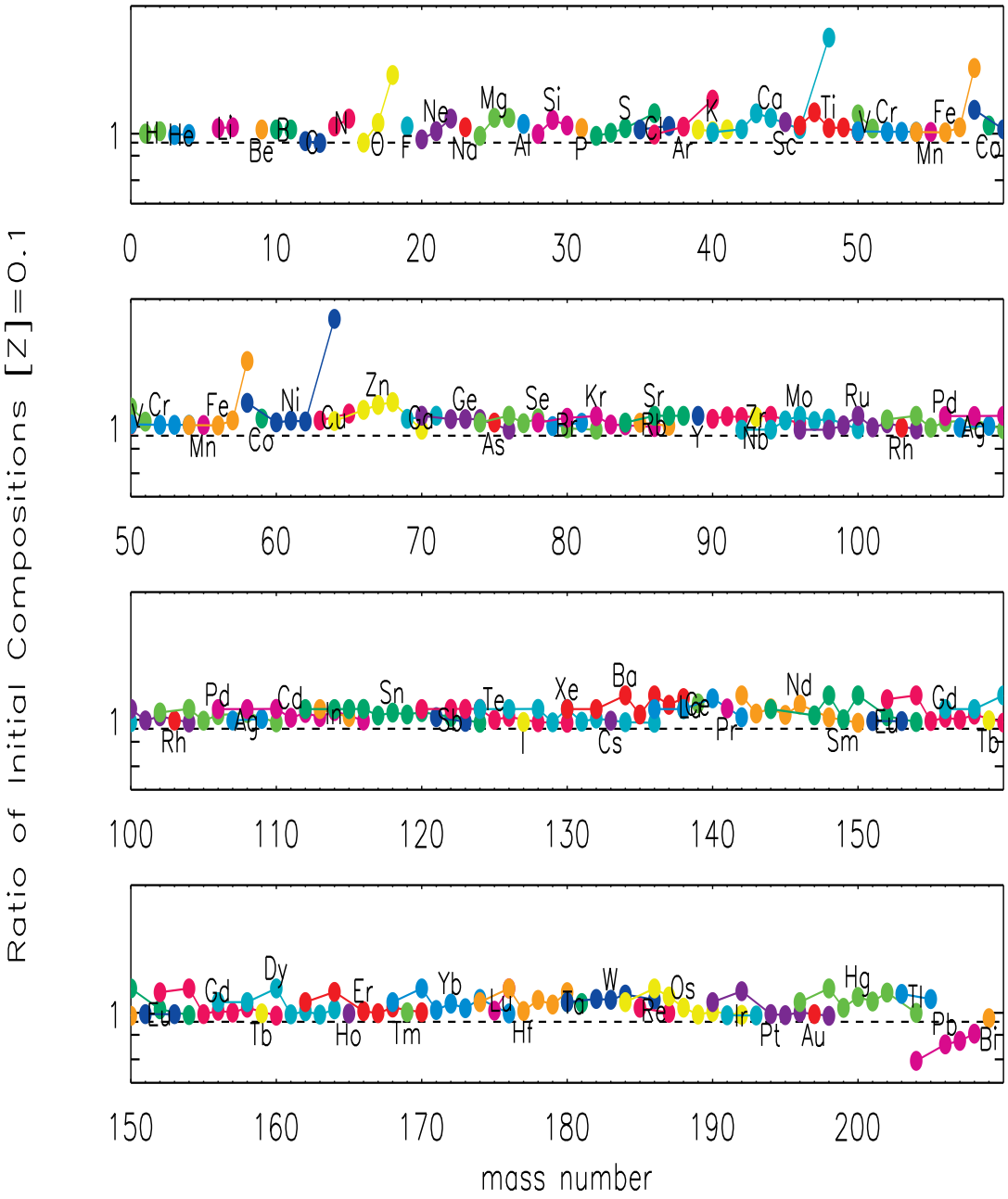

Figure D.2: The ratio of initial compositions (GG/SS) at a initial metallicity of [Z]=+0.1 for all isotopes.

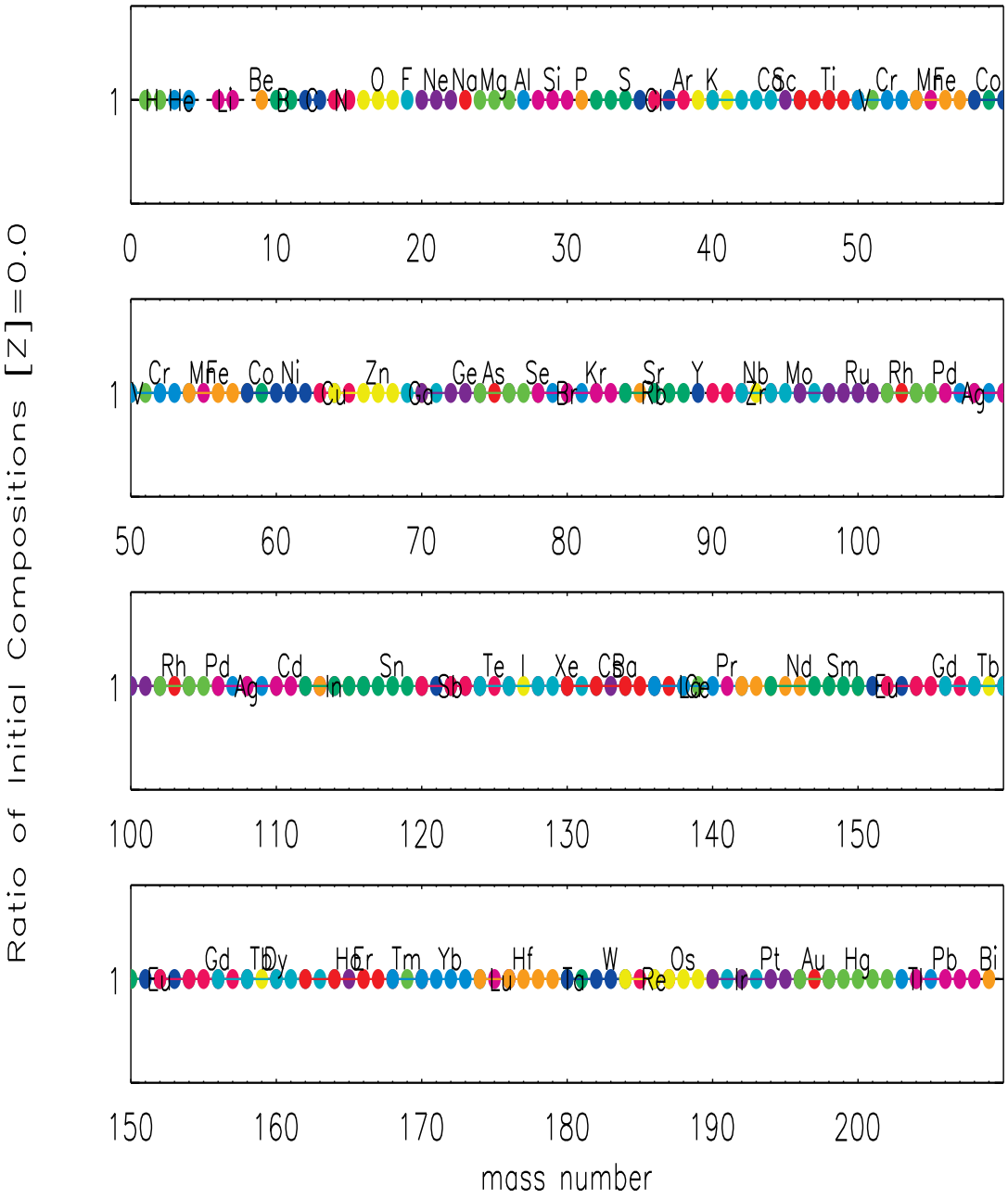

Figure D.3: The ratio of initial compositions (GG/SS) at a initial metallicity of [Z]=0 for all isotopes.

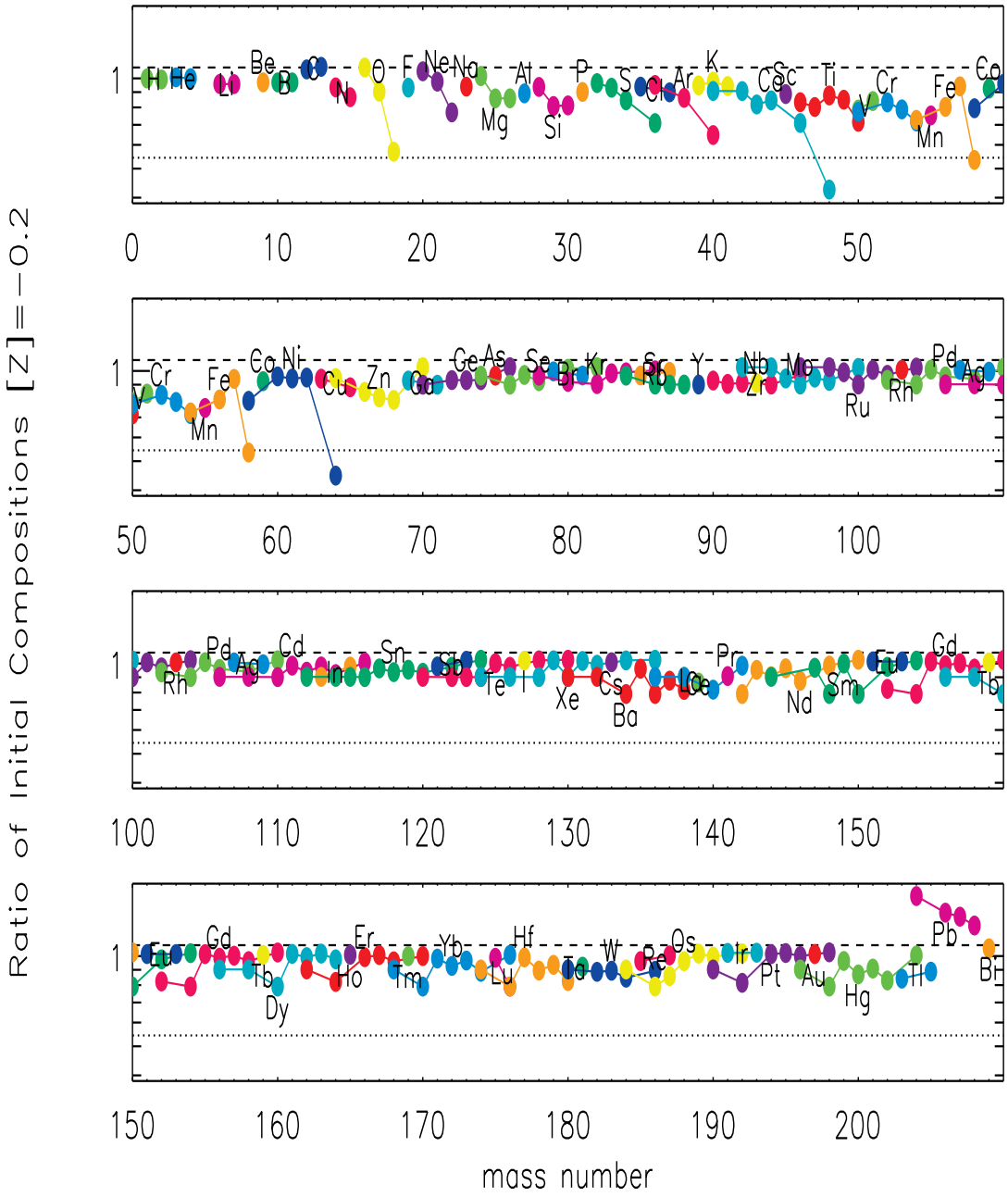

Figure D.4: The ratio of initial compositions (GG/SS) at a initial metallicity of [Z]=-0.2 for all isotopes.

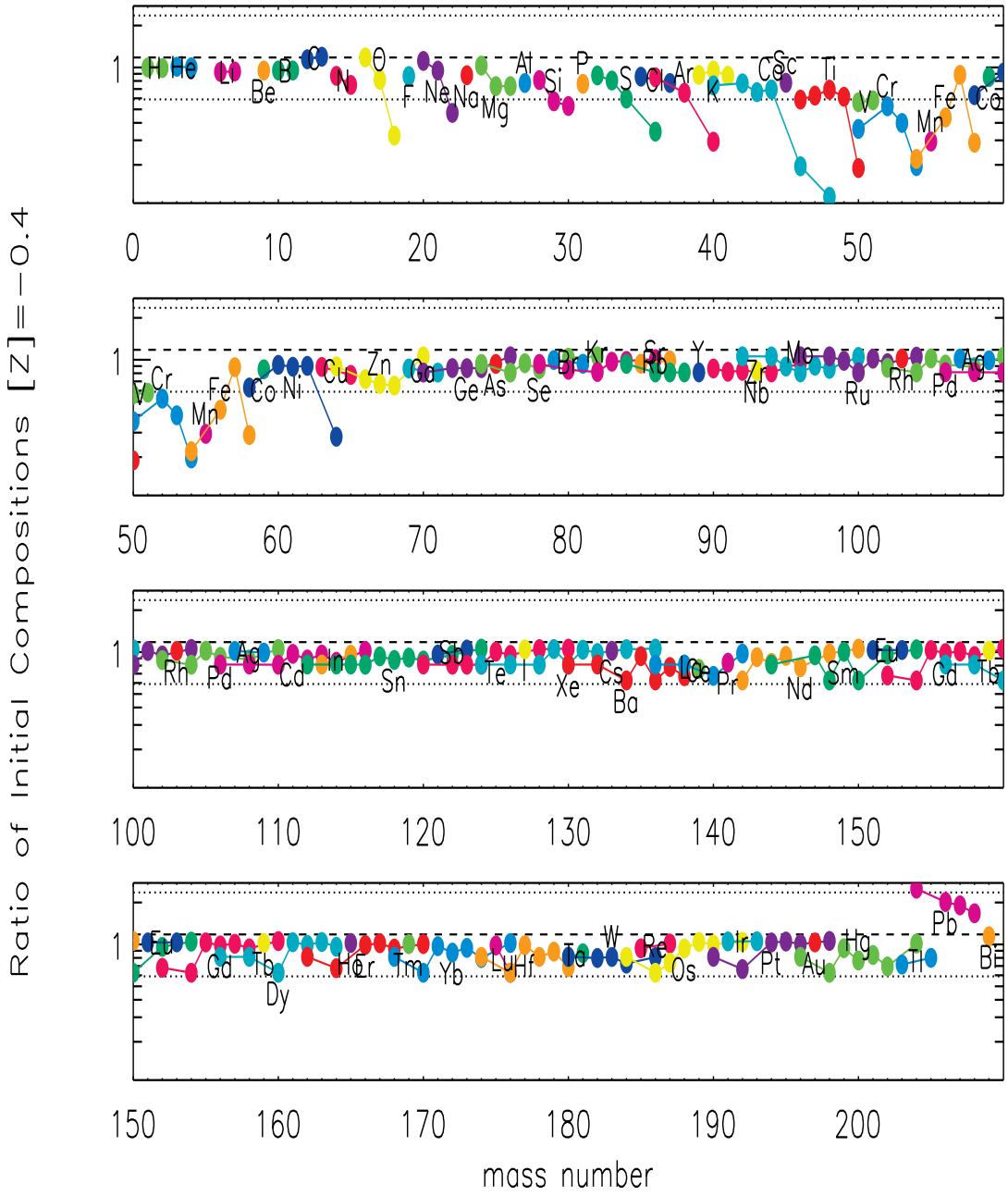

Figure D.5: The ratio of initial compositions (GG/SS) at a initial metallicity of [Z]=-0.4 for all isotopes.

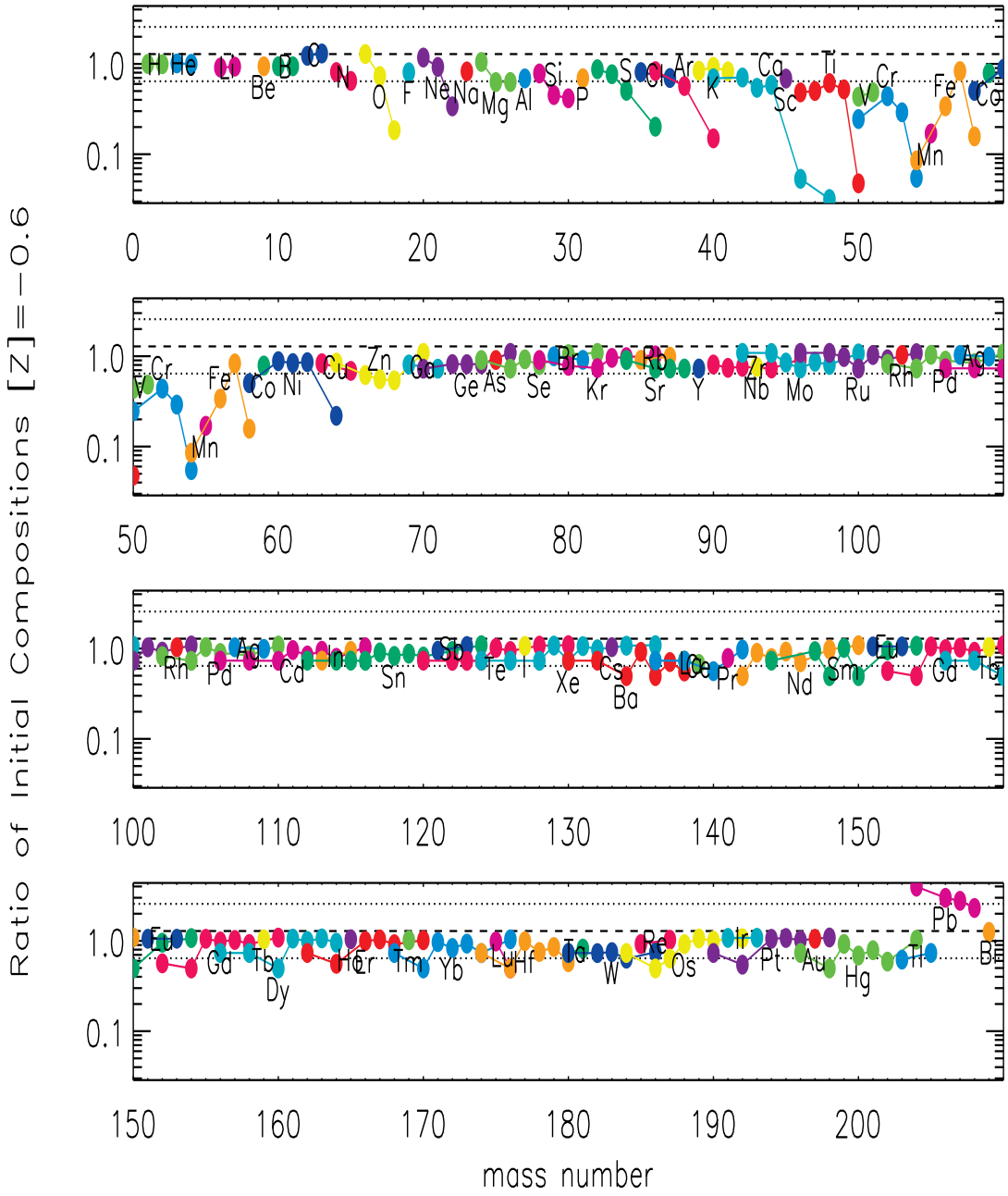

Figure D.6: The ratio of initial compositions (GG/SS) at a initial metallicity of [Z]=-0.6 for all isotopes.

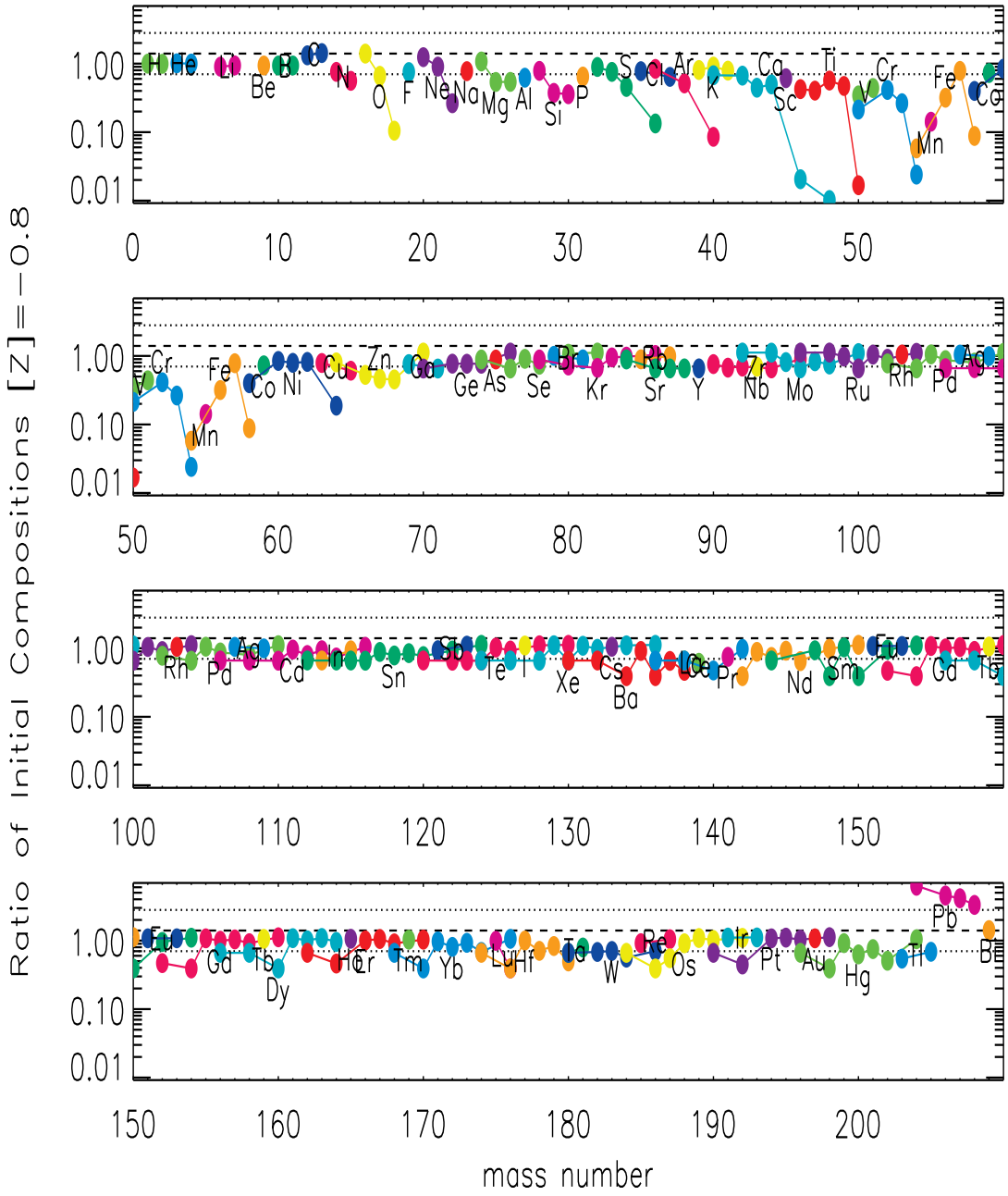

Figure D.7: The ratio of initial compositions (GG/SS) at a initial metallicity of [Z]=-0.8 for all isotopes.

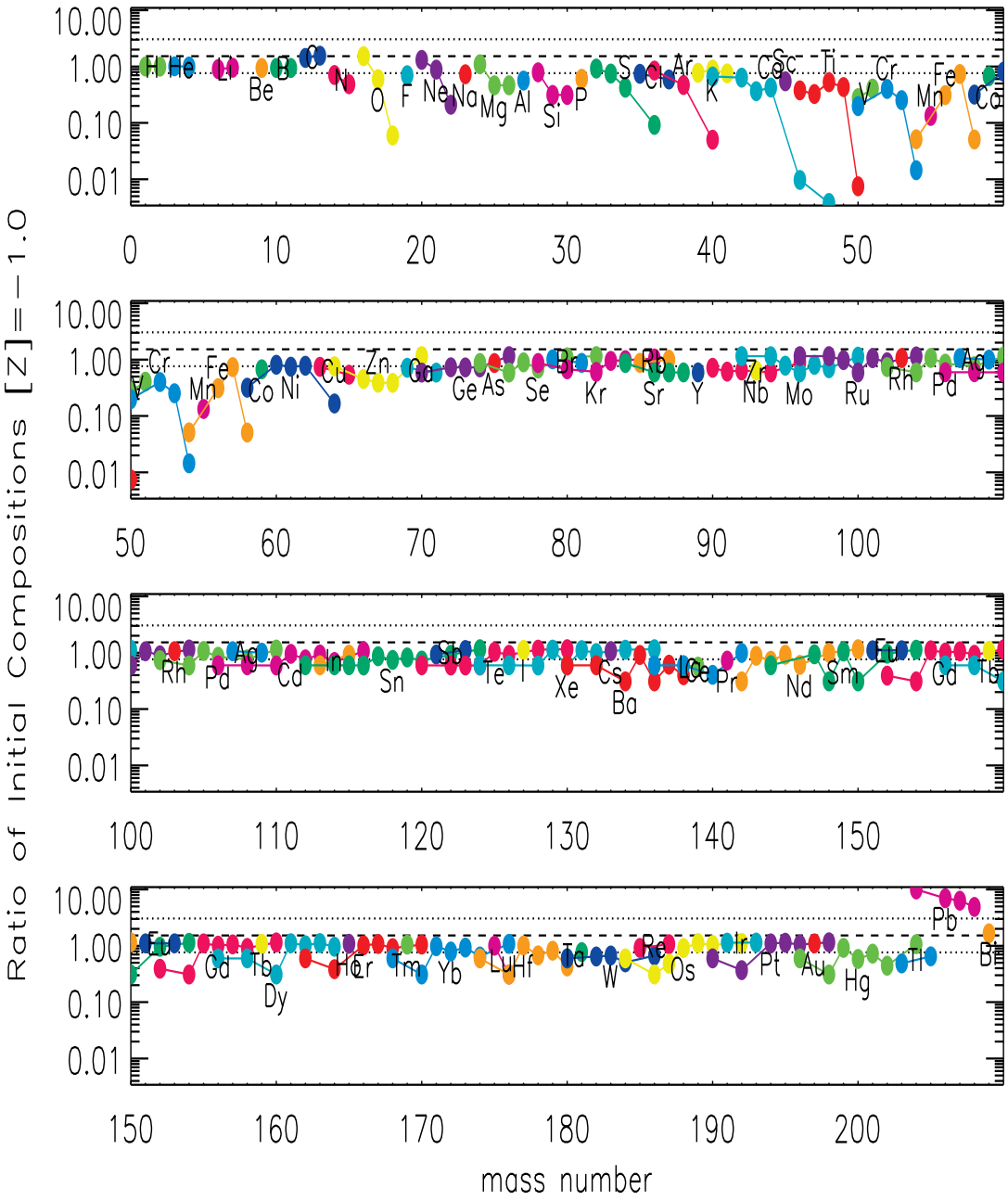

Figure D.8: The ratio of initial compositions (GG/SS) at a initial metallicity of [Z]=-1 for all isotopes.

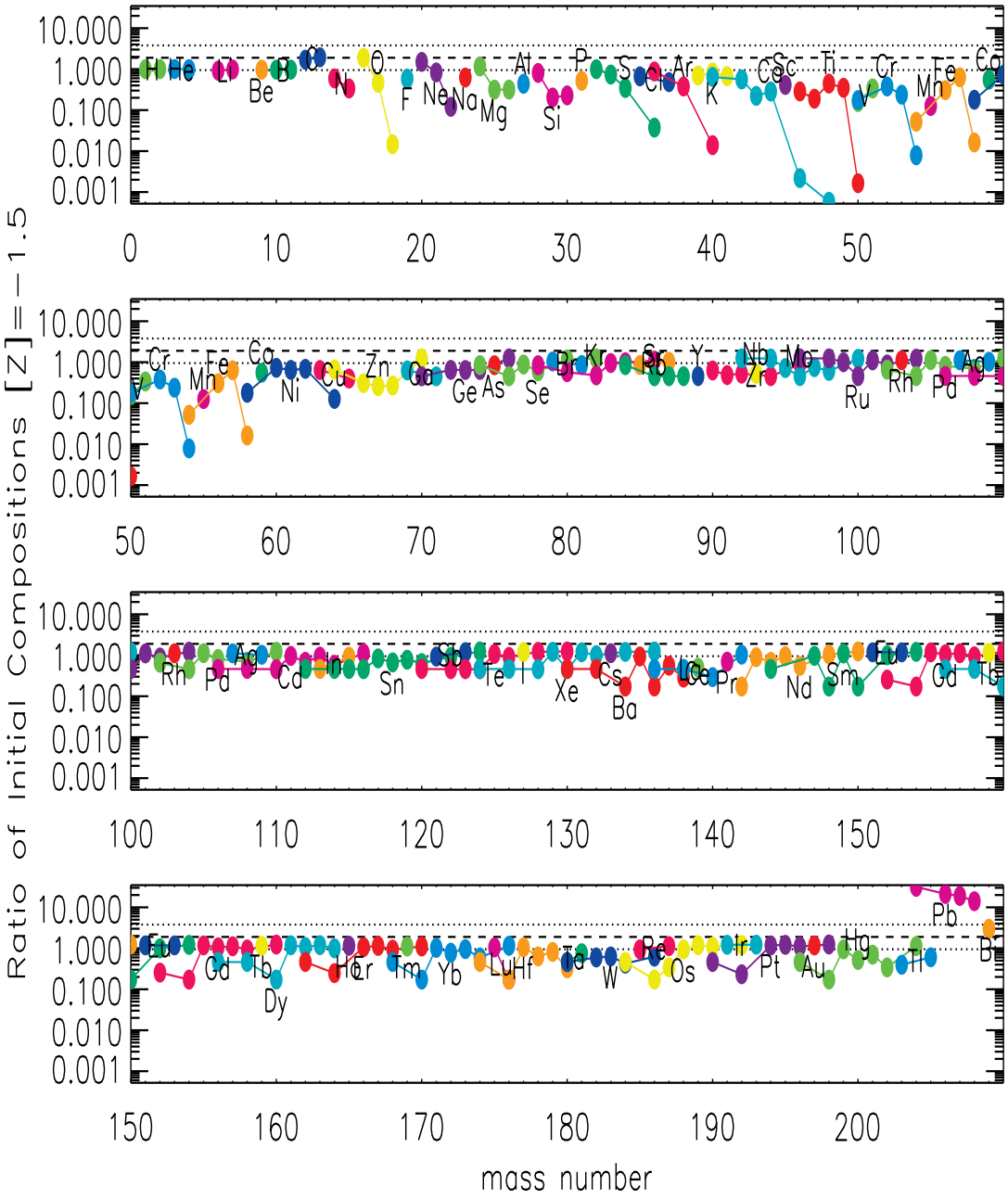

Figure D.9: The ratio of initial compositions (GG/SS) at a initial metallicity of [Z]=-1.5 for all isotopes.

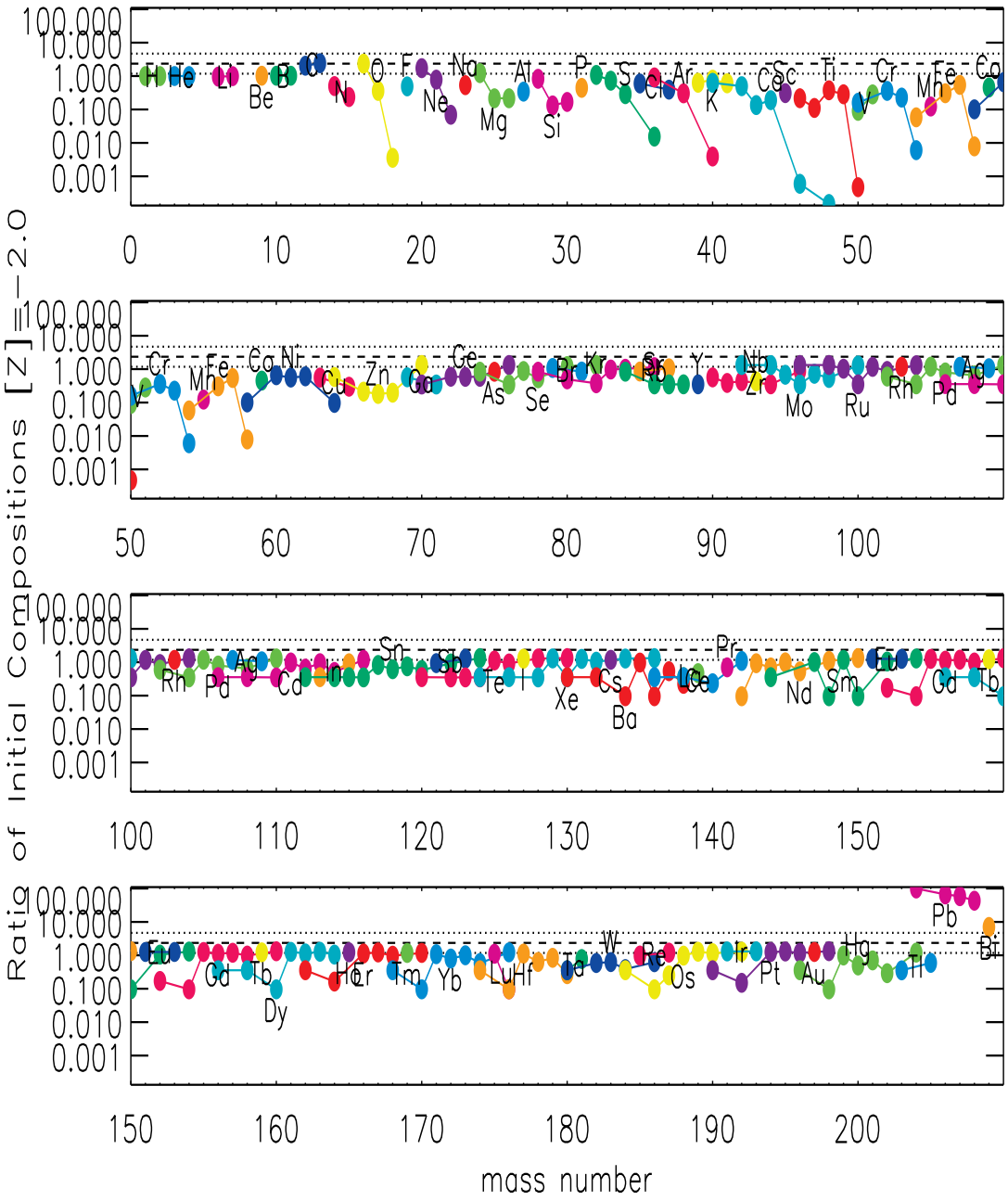

Figure D.10: The ratio of initial compositions (GG/SS) at a initial metallicity of [Z]=-2 for all isotopes.

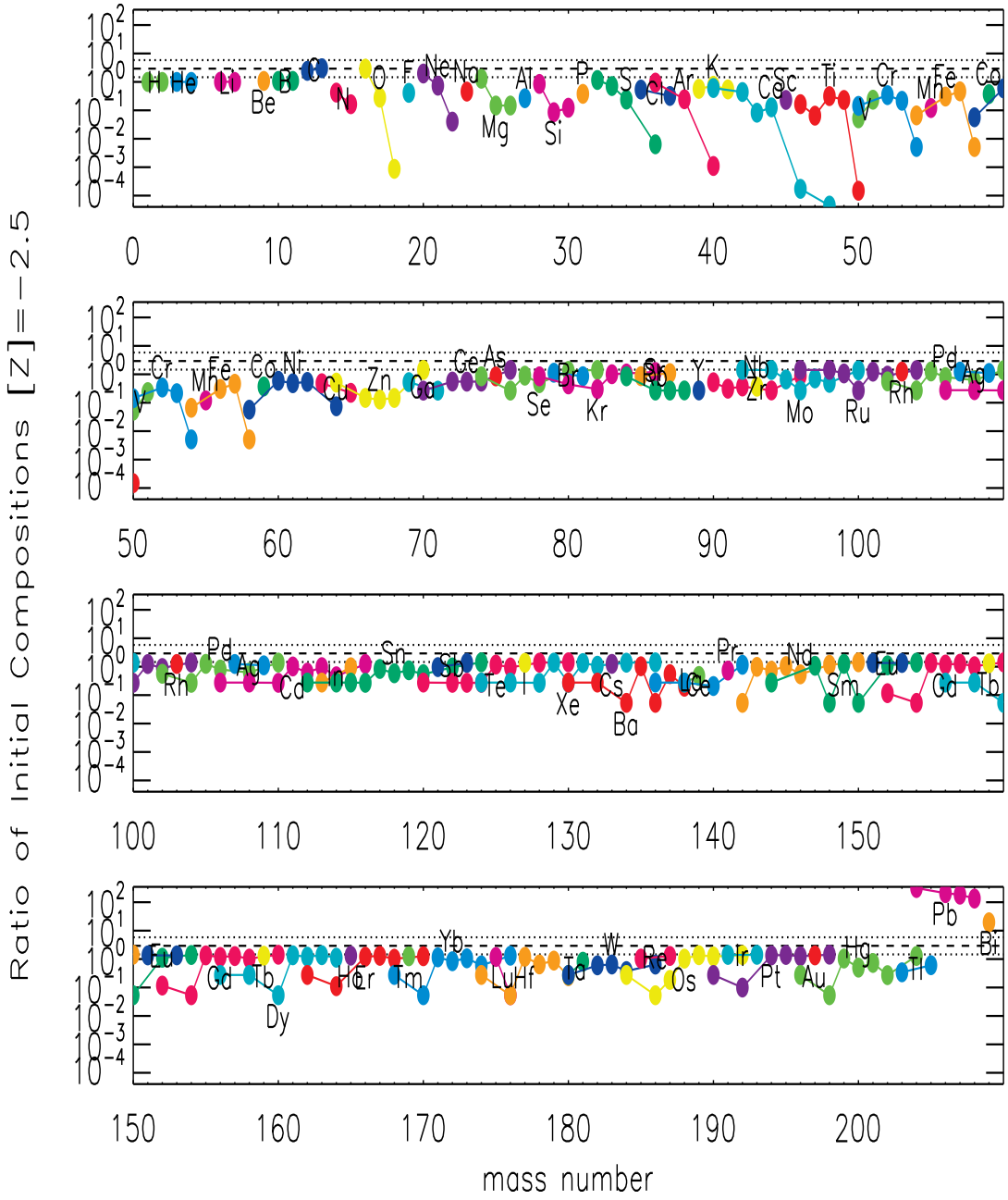

Figure D.11: The ratio of initial compositions (GG/SS) at a initial metallicity of [Z]=-2.5 for all isotopes.

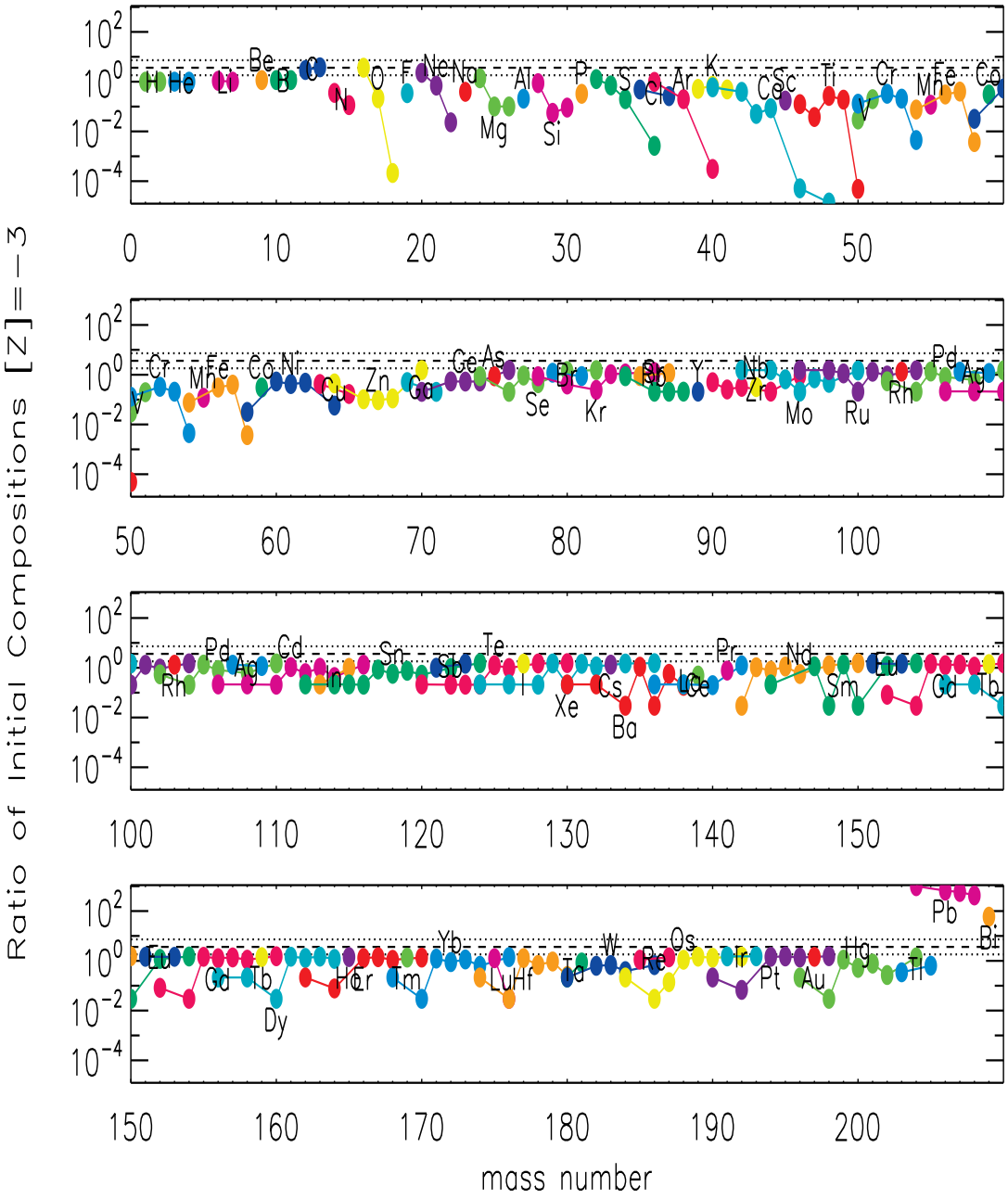

Figure D.12: The ratio of initial compositions (GG/SS) at a initial metallicity of [Z]=-3 for all isotopes.

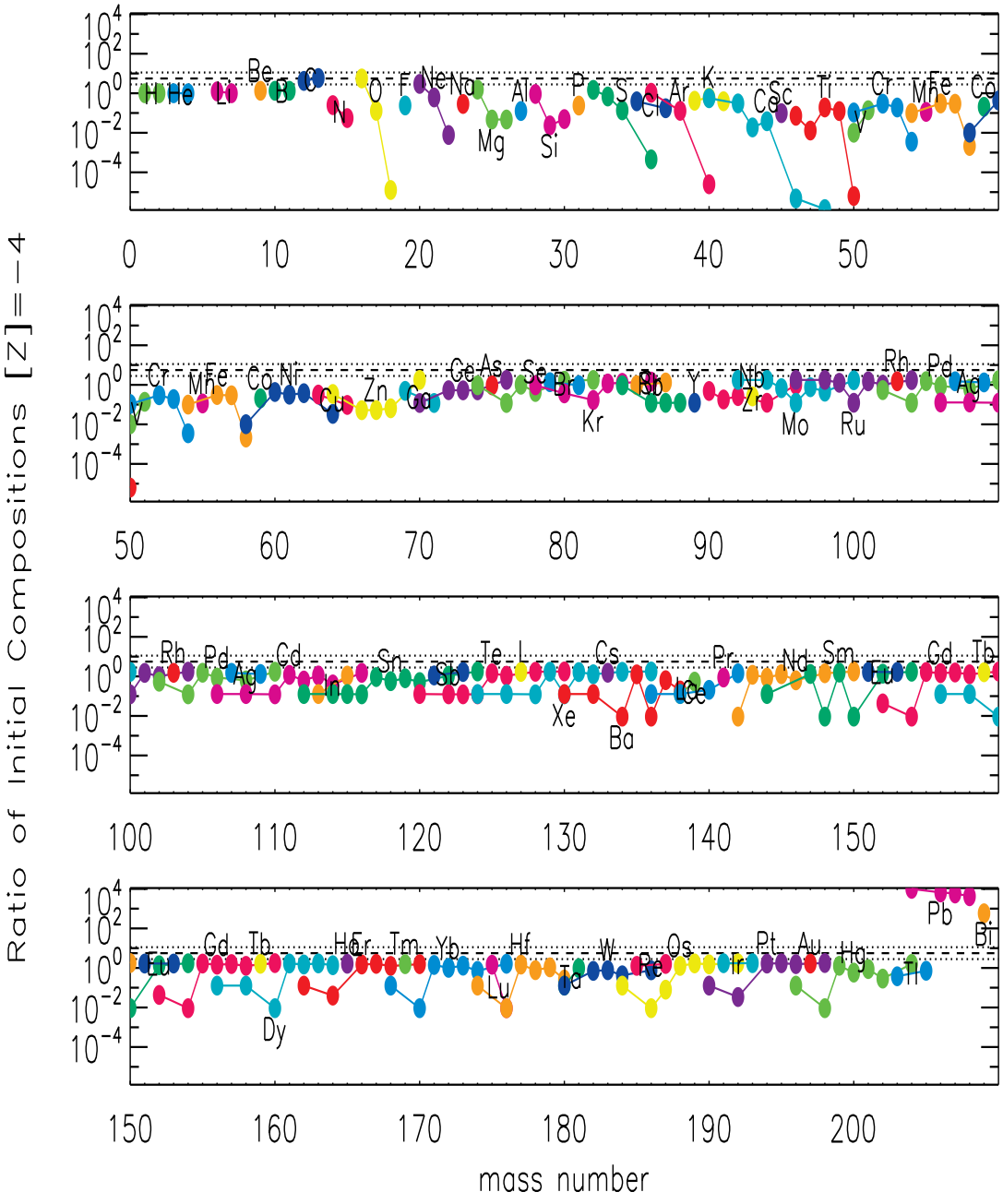

Figure D.13: The ratio of initial compositions (GG/SS) at a initial metallicity of [Z]=-4 for all isotopes.

Appendix E

Helium Reaction Rate Plots

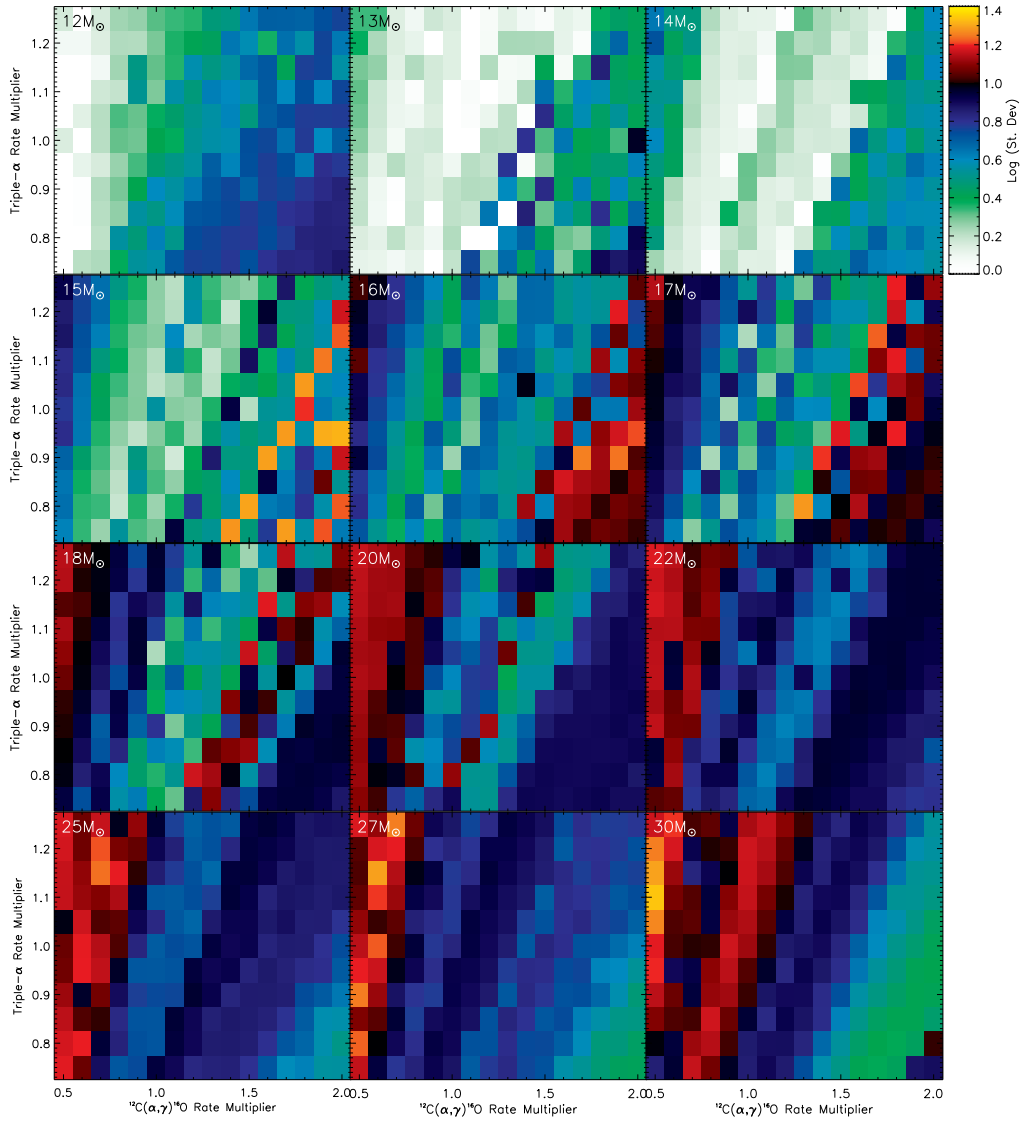

Figure E.1: Standard deviations of the production factors of intermediate-mass isotopes for all models as a function of the $R_{3\alpha}$ and $R_{\alpha,12}$ multipliers. The horizontal axis gives the $R_{\alpha,12}$ multiplier, the vertical axis gives the $R_{3\alpha}$ multiplier, and the color scale gives the logarithm of the standard deviations.

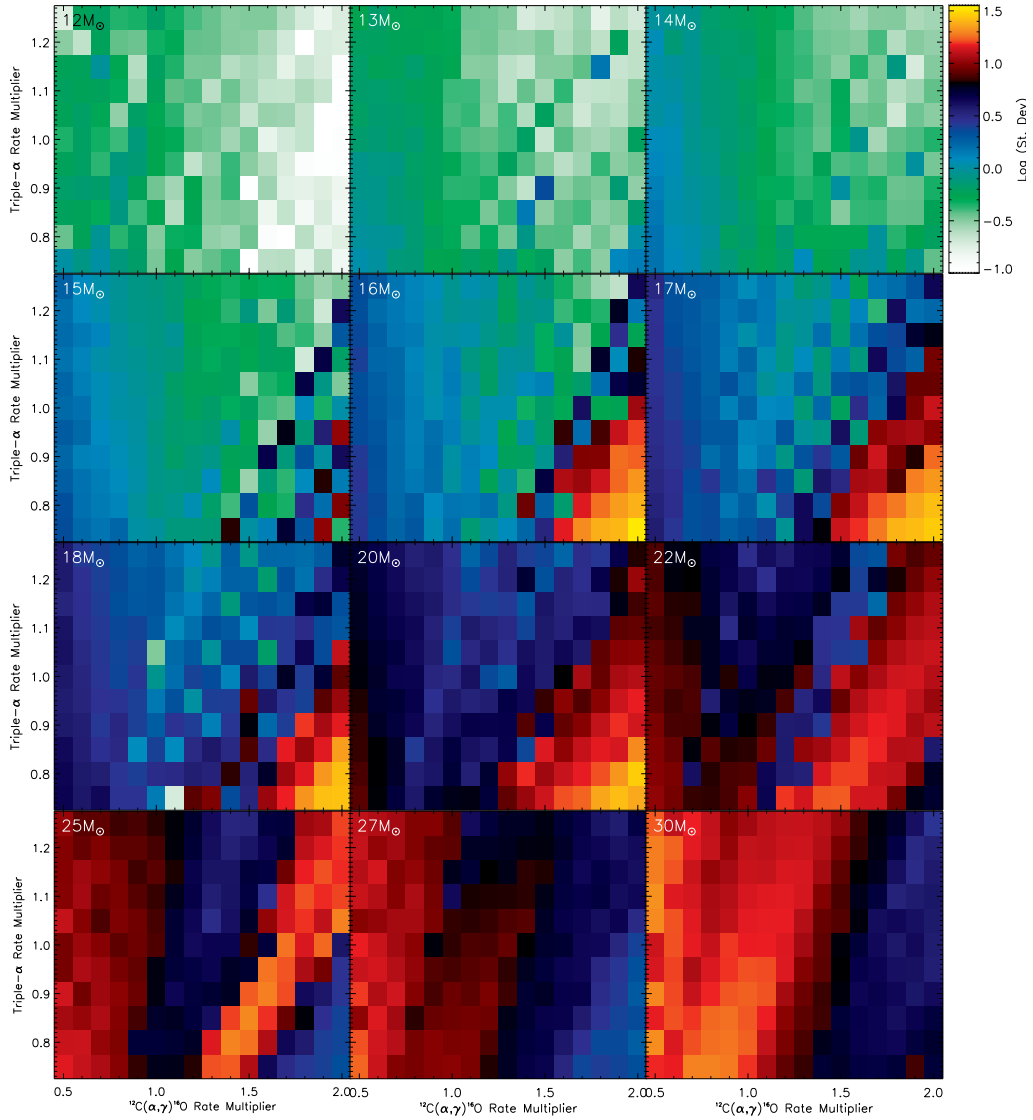

Figure E.2: Standard deviations of the production factors of weak s-only isotopes for all models as a function of the $R_{3\alpha}$ and $R_{\alpha,12}$ multipliers. The figure follows the convention of Fig. E.1.

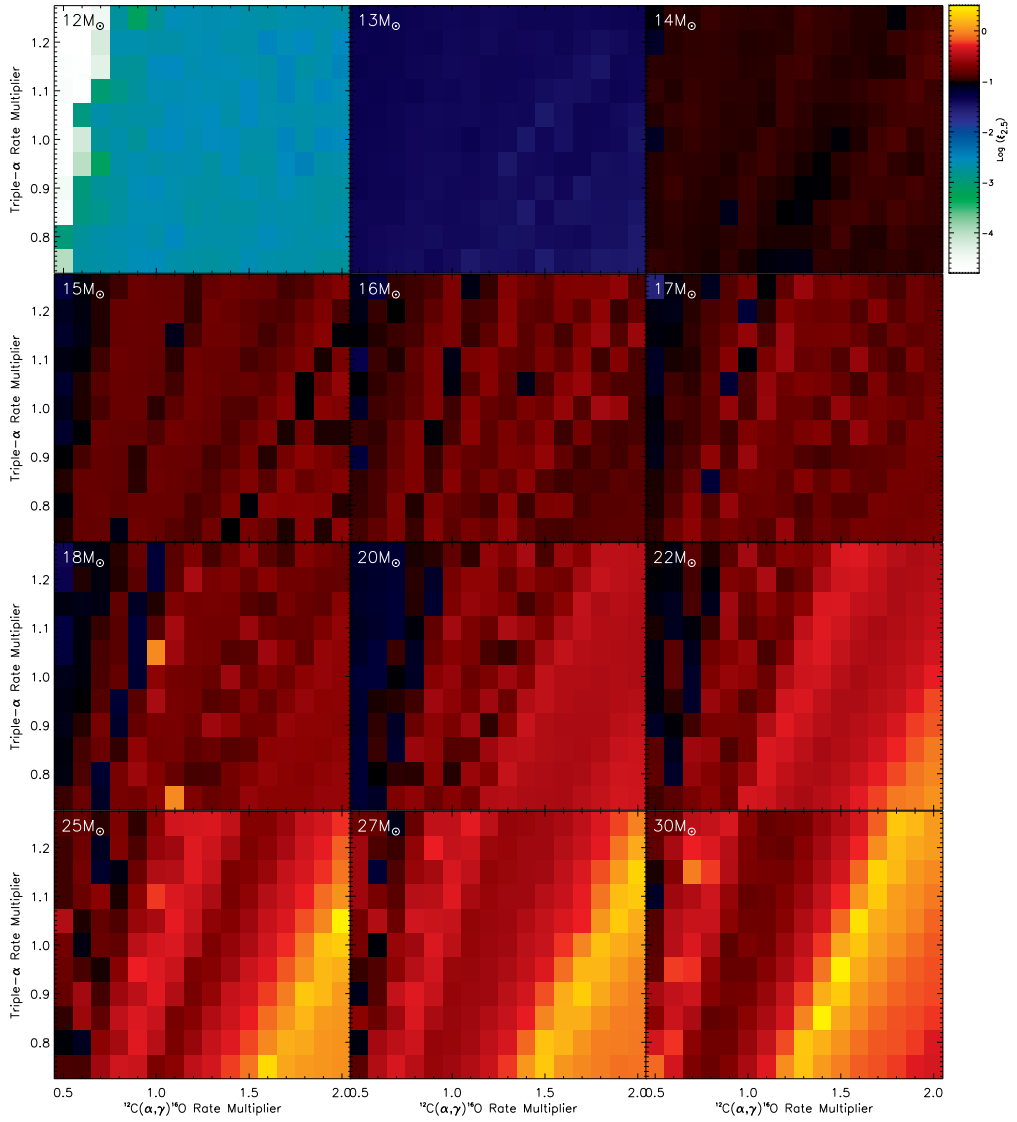

Figure E.3: Compactness parameter values for all models as a function of the $R_{3\alpha}$ and $R_{\alpha,12}$ multipliers. The color scale gives the logarithm of the compactness parameter, and the rest of the figure follows the convention of Fig. E.1.

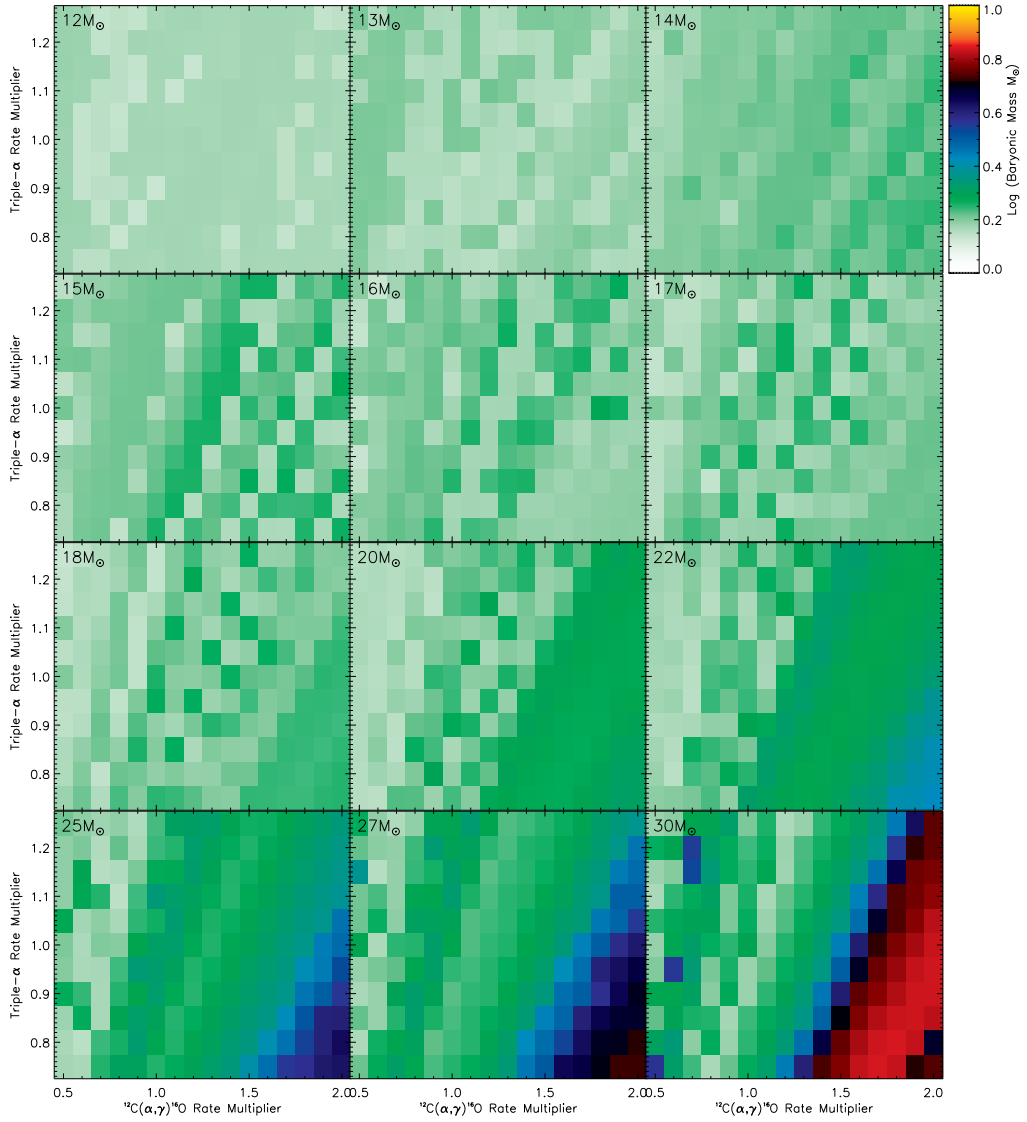

Figure E.4: Baryonic mass of the progenitors ($M_\odot$) for all models as a function of the $R_{3\alpha}$ and $R_{\alpha,12}$ multipliers. The color scale gives the logarithm of the baryonic mass, and the rest of the figure follows the convention of Fig. E.1.

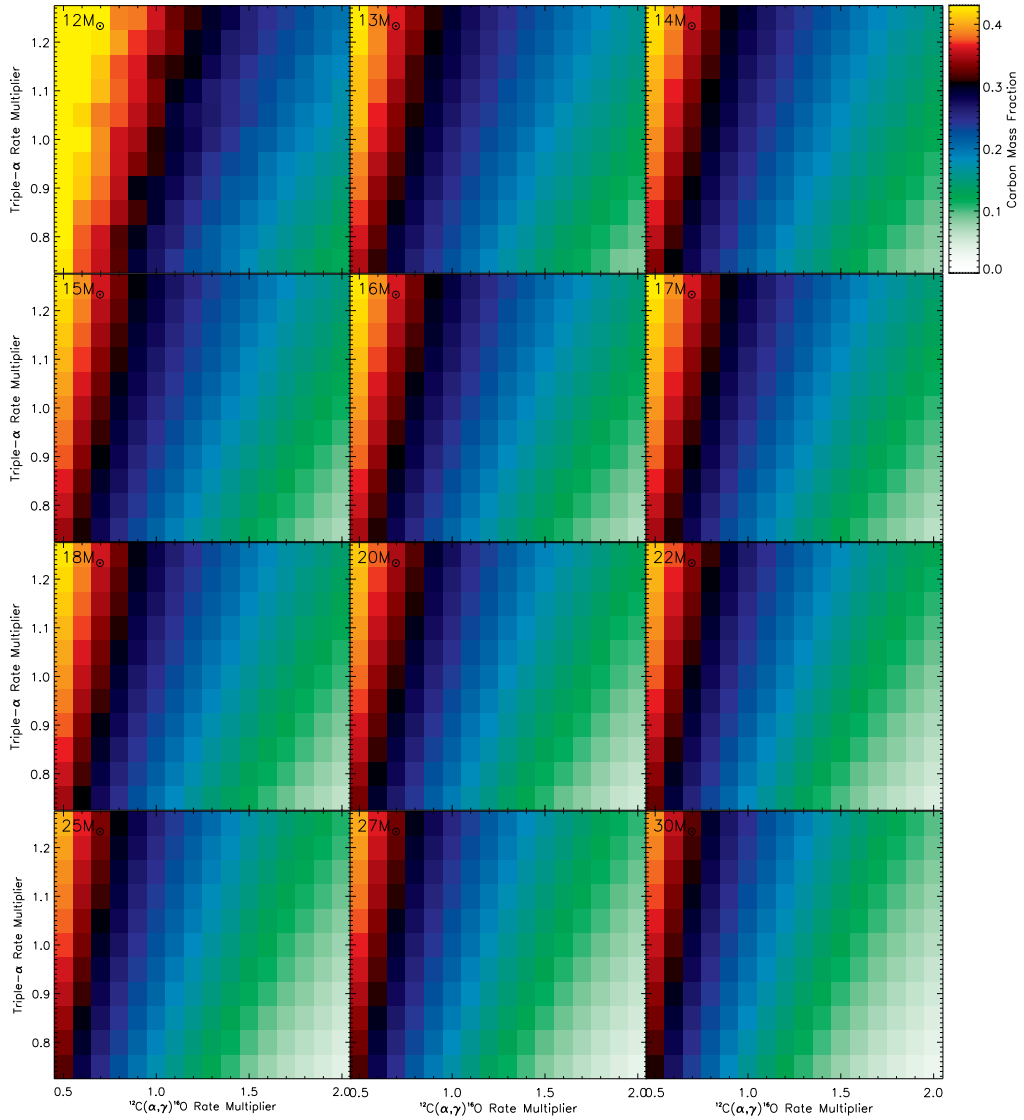

Figure E.5: Central carbon mass fractions at the end of core-He burning for all models as a function of the $R_{3\alpha}$ and $R_{\alpha,12}$ multipliers. The color scale gives the carbon mass fraction, and the rest of the figure follows the convention of Fig. E.1.